

**UCLA**

**UCLA Electronic Theses and Dissertations**

**Title**

Catalysis for C1 Chemistry: Oxidative Coupling of Methane using Nanofiber Catalysts and Discovery of Catalysts for Atmospheric Reduction of CO<sub>2</sub> to Methanol

**Permalink**

<https://escholarship.org/uc/item/7v58t830>

**Author**

Zohour, Bahman

**Publication Date**

2017

Peer reviewed|Thesis/dissertation

UNIVERSITY OF CALIFORNIA

Los Angeles

Catalysis for C<sub>1</sub> Chemistry:

Oxidative Coupling of Methane using Nanofiber Catalysts

and

Discovery of Catalysts for Atmospheric Reduction of CO<sub>2</sub> to Methanol

A dissertation submitted in partial satisfaction of the

requirements for the degree Doctor of Philosophy

in Chemical Engineering

by

Bahman Zohour

2017

© Copyright by

Bahman Zohour

2017

# ABSTRACT OF THE DISSERTATION

Catalysis for C<sub>1</sub> Chemistry:

Oxidative Coupling of Methane using Nanofiber Catalysts

and

Discovery of Catalysts for Atmospheric Reduction of CO<sub>2</sub> to Methanol

by

Bahman Zohour

Doctor of Philosophy in Chemical Engineering

University of California, Los Angeles, 2017

Professor Selim M. Senkan, Chair

The goal of this research is to explore novel catalytic material and systems for effective conversion of C<sub>1</sub> feed. Catalysis of C<sub>1</sub> chemistry is of critical importance for the clean production of fuels and chemicals and future energy sustainability. Herein, two processes were studied: In the first section, a comprehensive study of oxidative coupling of methane (OCM) using novel nanofiber catalysts of mixed metal oxides was undertaken and in the second section, direct catalytic conversion of carbon dioxide (CO<sub>2</sub>) to methanol was studied, which resulted in discovery of a superior catalytic system for CO<sub>2</sub> hydrogenation to methanol.



Section 1: Utilization of natural gas as an alternate chemical feedstock to petroleum has been a highly desirable but difficult goal in industrial catalysis. Accordingly, there has been a substantial interest in the oxidative coupling of methane (OCM), which allows for the direct catalytic conversion of methane into economically valuable  $C_{2+}$  hydrocarbons. OCM is a complex reaction process involving heterogeneous catalysis intricately coupled with gas phase reactions; hence, despite decades' worth of research, it has yet to be commercialized. The lack of progress in OCM is primarily due to the following reasons: 1. The absence of a highly active and robust catalyst that can operate at lower temperatures; and 2. Our inadequate understanding of the underlying detailed chemical kinetics mechanism (DCKM) of the OCM process, which impedes the undertaking of quantitative simulations of novel reactor configurations and/or operating strategies. To address these issues, we undertook the following program of studies: 1. Further improved the synthesis of novel nanofiber catalysts by electrospinning, building on the early discovery that  $La_2O_3-CeO_2$  nanofibers were highly active and robust OCM catalysts; 2. Applied our novel microprobe sampling system to OCM reactors for the acquisition of spatially resolved species concentration and temperatures profiles within the catalytic zone. Our novel sampling approach led to the important discovery that  $H_2$  is produced very early in the OCM catalytic zone, an observation that was completely missed in all prior studies. The application of our novel microprobe system to a dual-bed OCM reactor also demonstrated the feasibility to significantly improve  $C_{2+}$  product yields to 21% (from 16% for single bed) which we plan to further improve by considering more sequential beds; 3. Outlined development and validation of new generation of DCKM for the OCM process using the high-information content of spatial concentration profiles obtained in part 2. Most importantly, to improve the current DCKM literature by considering surface reactions that result in early  $H_2$  formation. Validated DCKM represent highly

valuable numerical tools that allow for the prediction of the OCM performance of different reactor configurations operating under a broad range of conditions, e.g. high pressures, porous wall reactors etc. Consequently, this new generation of comprehensive DCKM based on the sampling profiles, detailed in this report, will be of considerable use in improving the yields of useful products in the OCM process; 4. Explore novel conditions that include oxygen-feed distributed packed bed OCM reactors and coupled catalytic and non-thermal plasma OCM reactors, again to further push the yields for useful  $C_{2+}$  products. The details of the proposed approach for implementing such reactor configurations and development of a new generation of DCKM for the OCM process is outlined in the future work, Chapter 4, of section 1 of the report.

Section 2: Direct catalytic conversion of carbon dioxide to liquid fuels and basic chemicals, such as methanol, using solar-derived hydrogen at or near ambient pressure is a highly desirable goal in heterogeneous catalysis. When realized, this technology will pave the way for a sustainable society together with decentralized power generation. Here we report a novel class of holmium (Ho) containing multi-metal oxide Cu catalysts discovered through the application of high-throughput methods. In particular, ternary systems of  $Cu-GaO_x-HoO_y > Cu-CeO_x-HoO_y \sim Cu-LaO_x-HoO_y$  supported on  $\gamma-Al_2O_3$  exhibited superior methanol production (10x) with less CO formation than previously reported catalysts at atmospheric pressure. Holmium was shown to be highly dispersed as few-atom clusters, suggesting that the formation of tri-metallic sites could be the key for the promotion of methanol synthesis by Ho.

The dissertation of Bahman Zohour is approved.

Dante A. Simonetti

Vasilios Manousiouthakis

Louis Bouchard

Selim M. Senkan, Committee Chair

University of California, Los Angeles

2017

Dedicated to my family for their unconditional love and support

My beautiful wife, Mehrnaz

My dear mom and dad

My three great brothers

## Table of Contents

ABSTRACT OF THE DISSERTATION .....	ii
Acknowledgments.....	xiv
Vita.....	xv
SUBJECT 1. OXIDATIVE COUPLING OF METHANE (OCM) .....	1
CHAPTER 1.1. Introduction.....	2
1.1. Natural Gas.....	2
1.1.1. Natural Gas Resources.....	2
1.1.2. Utilizing Natural Gas.....	5
1.2. Ethylene and Its Applications.....	8
1.3. Oxidative Coupling of Methane (OCM) .....	11
1.3.1. Process Description and Challenges .....	12
1.3.2. Research Background .....	16
1.4. Research Objectives .....	22
CHAPTER 1.2. Experimental Set-Up .....	24
2.1. Catalyst System and Synthesis.....	24
2.1.1. Electrospinning Principle and Challenges.....	25
2.1.2. La <sub>2</sub> O <sub>3</sub> -CeO <sub>2</sub> Fiber Catalysts Synthesis .....	26
2.2. Set-up and Testing.....	29
2.2.1. Feed Gas Control System .....	29
2.2.2. Gas Chromatography System .....	30
2.2.3. Single-bed Reactor .....	31
2.2.3.1. Performance Analysis Set-up.....	31
2.2.3.2. Axial Temperature Profiles.....	32
2.2.3.3. Spatial Reactor Profiles.....	33
2.2.4. Dual-bed Reactor.....	35
CHAPTER 1.3. Results and Discussions.....	38
3.1. Characterization and Performance Analysis of Nanofibers .....	38
3.1.1. La <sub>2</sub> O <sub>3</sub> -CeO <sub>2</sub> Nanofiber Catalyst System .....	38
3.1.2. Operating Conditions of La <sub>2</sub> O <sub>3</sub> -CeO <sub>2</sub> Nanofiber .....	43
3.1.2.1. Feed Temperature Hysteresis.....	43
3.1.2.2. Effect of Feed Flow rate and CH <sub>4</sub> /O <sub>2</sub> Ratio.....	46

3.1.2.3. Effect of Bed Depth and Space Velocity .....	52
3.1.2.4. Time on Stream.....	55
3.2. Spatial Concentration and Temperature Profiles .....	56
3.2.1. Single-bed.....	57
3.2.2. Dual Catalytic OCM bed .....	63
CHAPTER 1.4. Future Work.....	72
4.1. Distribution of Oxygen Feed.....	73
4.2. Non-thermal Plasma Application in OCM.....	75
4.3. Kinetic Modeling.....	79
SUBJECT 2. ATMOSPHERIC REDUCTION OF CO <sub>2</sub> TO METHANOL.....	86
CHAPTER 2.1. Introduction.....	87
1.1. Methanol: A Valuable Product of CO <sub>2</sub> Hydrogenation.....	87
1.2. Recent Advances in Catalytic CO <sub>2</sub> Hydrogenation to Methanol .....	88
CHAPTER 2.2. Experimental Set-Up .....	90
2.1. Catalysts Preparation.....	90
2.2. Catalysts Screening and Analysis .....	91
2.2.1. Components of The High Throughput screening system .....	91
CHAPTER 2.3. Results and Discussions.....	95
3.1. Initial Screening of Binary Catalytic Systems .....	95
3.2. Ternary Catalytic Systems .....	95
3.3. Superior Catalytic Systems .....	96
3.4. Characterization Studies for the Cu-Ga-Ho System .....	101
CHAPTER 2.4. Future Work.....	104
Appendices (Select Publications) .....	107
A1. New Insights into the Oxidative Coupling of Methane.....	107
A2. Spatial Concentration and Temperature Profiles in Dual-Packed-Bed Catalytic Reactors: Oxidative Coupling of Methane.....	112
A3. Oxidative Coupling of Methane with La <sub>2</sub> O <sub>3</sub> -CeO <sub>2</sub> Nanofiber Fabrics: A Reaction Engineering Study.....	119
A4. Key Mechanistic Insight into the Direct Gas-Phase Epoxidation of Propylene by the RuO <sub>2</sub> - CuO-NaCl/ SiO <sub>2</sub> Catalyst.....	126
A5. Spatial Profiles in RuO <sub>2</sub> -CuO-NaCl/SiO <sub>2</sub> Packed-Bed Propylene Epoxidation Reactors	132

A6. Discovery of Superior Cu-GaO <sub>x</sub> -HoO <sub>y</sub> Catalysts for the Reduction of Carbon Dioxide to Methanol at Atmospheric Pressure .....	138
References.....	144

## List of Figures and Tables

Figure 1.1-1. Natural gas production trend.....	4
Figure 1.1-2. Shale gas Production in the U.S.....	5
Figure 1.1-3. The chemical value chain in terms of feedstocks.....	6
Figure 1.1-4. Potential direct routes for methane conversion.....	7
Figure 1.1-5. Commercial product chain of ethylene .....	9
Figure 1.1-6. Historical price of ethylene .....	10
Figure 1.1-7. Global ethylene market distribution.....	10
Figure 1.1-8. Ethylene Production Overview .....	11
Figure 1.1-9. Global OCM reaction steps, indicating the homogeneous and/or heterogeneous characteristics.....	14
Figure 1.1-10. Basic mechanism for the reaction network of the OCM at oxides .....	15
Figure 1.1-11. Elemental compositions of OCM catalysts with significant C <sub>2</sub> yields reported in the literature .....	18
Figure 1.1-12. Periodic DFT study of methane activation over La <sub>2</sub> O <sub>3</sub> .....	20
Figure 1.1-13. Contribution analysis for the intraparticle (left panel) and interstitial phase (right panel) at the end of the catalyst bed for the reaction conditions.....	21
Figure 1.2-1. Summary of pertinent variables associated with electrospinning .....	26
Figure 1.2-2. Electrospinning setup used in the synthesis of nanofibers of metal.....	28
Figure 1.2-3. Summary of the catalysts preparation via electrospinning process .....	28
Figure 1.2-4. SEM image of fibers (diameter 70-120 nm; image magnification 30,000) .....	29
Figure 1.2-5. Mass flow controller set-up.....	30
Figure 1.2-6. Fiber catalysts packed inside quartz tube.....	31
Figure 1.2-7. Thermolyne Tube Furnace with quartz reactors inside.....	32
Figure 1.2-8. The reactor system used to acquire spatial temperature and concentration profiles. ....	34



Figure 1.2-9. The dual-bed reactor system and the complement set-up used to acquire spatial temperature and concentration profiles.....	35
Figure 1.3-1. SEM Images of: A-Left: co-spun $\text{La}_2\text{O}_3\text{-CeO}_2$ fibers (diameter $\sim 70$ nm, BET area $26 \text{ m}^2/\text{g}$ ); B-Right: co-precipitated $\text{La}_2\text{O}_3\text{-CeO}_2$ powders (BET area $10 \text{ m}^2/\text{g}$ ). Note: both images are at the same magnification of $\times 13,000$ .....	39
Figure 1.3-2. OCM performance of $\text{La}_2\text{O}_3\text{-CeO}_2$ catalytic system compared to analogous powders synthesized by Dedov et al. ....	40
Figure 1.3-3. XRD of various $\text{La}_2\text{O}_3$ and $\text{CeO}_2$ nanofibers compared to co-precipitated powders. ....	41
Figure 1.3-4. $\text{C}_{2+}$ Selectivity Curve for $\text{La}_2\text{O}_3\text{-CeO}_2$ nanofiber catalyst system by addition of Ce as dopant.....	43
Figure 1.3-5. Reactor temperature $T_{\text{rx}}$ as a function of axial distance.....	44
Figure 1.3-6. $\text{C}_{2+}$ selectivity and $\text{CH}_4$ conversion as a function of feed temperature $T_f$ .....	45
Figure 1.3-7. Ethane-to-ethylene product ratio and percent $\text{O}_2$ conversion as a function of feed temperature $T_f$ .....	46
Figure 1.3-8. Reactor temperature $T_{\text{rx}}$ as a function of axial distance in the catalytic zone for various flow rates.....	47
Figure 1.3-9. Reactor temperature $T_{\text{rx}}$ as a function of axial distance in the catalytic zone for various feed $\text{CH}_4/\text{O}_2$ ratios.....	48
Figure 1.3-10. $\text{C}_{2+}$ selectivity and $\text{CH}_4$ conversion as a function of flow rate and $\text{CH}_4/\text{O}_2$ feed ratio. ....	51
Figure 1.3-11. Ethane-to-ethylene product ratio (left axis, filled markers) and percent $\text{O}_2$ conversion (right axis, hollow markers) as a function of flow rate and $\text{CH}_4/\text{O}_2$ feed ratio. ....	52
Figure 1.3-12. $\text{C}_{2+}$ selectivity and $\text{CH}_4$ conversion as a function of space velocity $F/m_{\text{cat}}$ and catalyst weight $m_{\text{cat}}$ . ....	54
Figure 1.3-13. Ethane-to-ethylene product ratio and percent $\text{O}_2$ conversion as a function of space velocity $F/m_{\text{cat}}$ and catalyst weight $m_{\text{cat}}$ . ....	54
Figure 1.3-14. Time on stream.....	55
Figure 1.3-15. Spatial temperature and species mole percent profiles for a feed $\text{CH}_4/\text{O}_2$ ratio of 7. ....	59

Figure 1.3-16. Spatial temperature and species mole percent profiles for a feed CH <sub>4</sub> /O <sub>2</sub> ratio of 9. .....	60
Figure 1.3-17. Spatial temperature and species mole percent profiles for a feed CH <sub>4</sub> /O <sub>2</sub> ratio of 11. .....	62
Figure 1.3-18. Spatial profiles for CH <sub>4</sub> conversions and C <sub>2+</sub> selectivities for the different CH <sub>4</sub> /O <sub>2</sub> ratio of the single-bed experiments. ....	62
Figure 1.3-19. Spatial temperature and species mole percent profiles for the single-bed reactor system (SB1) with overall feed CH <sub>4</sub> /O <sub>2</sub> ratio of 4. ....	65
Figure 1.3-20. Spatial temperature and species mole percent profiles for the dual-bed reactor system (DB1) with initial feed CH <sub>4</sub> /O <sub>2</sub> ratio of 9 and overall CH <sub>4</sub> /O <sub>2</sub> ratio of 4. ....	68
Figure 1.3-21. Spatial temperature and species mole percent profiles for the dual-bed reactor system (DB2) with initial feed CH <sub>4</sub> /O <sub>2</sub> ratio of 11 and overall CH <sub>4</sub> /O <sub>2</sub> ratio of 4.4. ....	70
Figure 1.3-22. Spatial profiles for CH <sub>4</sub> conversions and C <sub>2+</sub> selectivities for the single-bed (SB1) and dual-bed (DB1, DB2) experiments. ....	71
Figure 1.4-1. OCM reactor with distributed O <sub>2</sub> feed .....	74
Figure 1.4-2. Sequential OCM catalytic bed design with distributed oxygen injection and intercooling stages .....	74
Figure 1.4-3. Overview of Plasma-Catalysis hybrid system configurations .....	78
Figure 1.4-4. Proposed DBD reactor set-up for OCM.....	78
Figure 1.4-5. Mechanism of the oxidative coupling of methane over La <sub>2</sub> O <sub>3</sub> *dark arrow: homogenous gas-phase reactions- light arrow: surface reactions.....	81
Figure 1.4-6. Overview of our approach for development of a comprehensive DCKM .....	84
Figure 2.2-1. High Throughput Screening System .....	92
Figure 2.2-2. High Throughput micro-reactor System .....	94
Figure 2.3-1. Reactor exit CH <sub>3</sub> OH, DME and CO mole % levels for the high-performing Ho-containing catalysts discovered together with some previously reported catalytic systems under atmospheric pressure at (a) 260 °C, (b) 280 °C and (c) and 300 °C. ....	99

Figure 2.3-2. Time-on-stream behavior of the Cu-GaO <sub>x</sub> -HoO <sub>y</sub> (#4) catalyst shows no significant performance change over a 10 h testing period. ....	100
Figure 2.3-3. HR-TEM image of the reduced catalyst #4 (Cu-Ga-Ho at 8-8-4 wt % metal loading and atom ratios of 5.2/4.8/1) (Fig 2.3-3a and b) and STEM-EDS images of the element maps of Ho (Fig 2.3-3c and d) Ga (Fig 2.3-3e) and Cu (Fig 2.3-3f) over $\gamma$ -Al <sub>2</sub> O <sub>3</sub> . ....	103
Table 1.3-1. Double and single bed Reaction conditions and reactor exit values for conversions, selectivities and yields .....	71
Table 1.4-1. Elementary gas-phase reactions for homogeneous oxidation of methane.....	79
Table 1.4-2. Catalytic elementary reactions considered in OCM.....	82

## **Acknowledgments**

I would like to thank my advisor, Professor Selim Senkan, whom I greatly admire, for his leadership, support, and respect; without him, I could not have reached this far.

I would also like to thank my colleagues, Mr. Aaron Miller, Dr. Anusorn Seubsai, and Dr. Daniel Noon, for their mentorship and support.

I gratefully acknowledge UCLA Dean's Graduate Fellowship and National Science Foundation Graduate Research Fellowship Program (NSFGRFP) Grant No. DGE-1144087 for providing me with funding that allowed me to pursue my Ph.D. degree at the University of California, Los Angeles.

## Vita

### Education

University of California, Los Angeles (UCLA) 2010- 2012  
B.S. in Chemical Engineering

### Research & Teaching Experience

UCLA Chemical and Biomolecular Engineering Department 2012- Present  
Graduate Student Researcher, Prof. Selim Senkan's Heterogeneous Catalysis Lab

NASA's Jet Propulsion Laboratory (JPL) 2014- 2017  
Graduate Student Intern under supervision of Dr. Sam S. Kim, Analytical Chemistry section

Teaching Fellow UCLA Chemical Engineering Department 2013- 2015

High School Student Summer Research Program (HSSRP) Lab Supervisor Summer 2013- 2014

### Awards and Honors

- National Science Foundation (NSF) Graduate Research Fellowship 2014-2017
- UCLA Dean's Graduate Fellowship 2012-2014
- Arco Fellowship 2012-2015
- UCLA Chemical Engineering Department Outstanding Bachelor of Science Award 2012
- Rhone Poulence Scholarship 2011
- Lena De Groff Scholarship 2011
- UCLA Recognition Scholarship 2010

### Peer-reviewed Journal Publications

1. D. Noon, **B. Zohour**, A. Bae, A. Seubsai, S. Senkan. "Transition from Oxidative Coupling to Partial Oxidation of Methane with Ir-Doping in  $\text{La}_2\text{O}_3\text{-CeO}_2$  Nanofiber Catalysts: Spatial Concentration and Temperature Profiles" *RSC Advances*, [Accepted](#).
2. P. Phon-in, A. Seubsai, T. Chukeaw, K. Charoen, W. Donphai, P. Prapainainar, M. Chareonpanich, D. Noon, **B. Zohour**, S. Senkan. "Direct epoxidation of propylene to propylene oxide over  $\text{RuO}_2\text{-CuO-NaCl-TeO}_2\text{-MnO}_x\text{/SiO}_2$  catalysts" *Catalysis Communications* 86 (2016): 143-147.
3. T. Chukeaw, A. Seubsai, P. Phon-in, K. Charoen, T. Witoon, W. Donphai, P. Prapainainar, M. Chareonpanich, D. Noon, **B. Zohour**, S. Senkan. "Multimetallic Catalysts of  $\text{RuO}_2\text{-CuO-Ce}_2\text{O}_3\text{-TiO}_2\text{/SiO}_2$  for Direct Gas-Phase Epoxidation of Propylene to Propylene Oxide" *RSC Advances* 6 (2016): 56116-56126.
4. **B. Zohour**, I. Yilgor, M. A. Gulgun, O. Birer, U. Unal, C. Leidholm, S. Senkan. "Discovery of Superior  $\text{Cu-GaO}_x\text{-HoO}_y$  Catalysts for the Reduction of Carbon Dioxide to Methanol at Atmospheric Pressure" *ChemCatChem* 8 (2016): 1464-1469.
5. A. Seubsai, M. Kahn, **B. Zohour**, D. Noon, M. Charoenpanich, S. Senkan. "Copper-Manganese Mixed Metal Oxide Catalysts for the Direct Epoxidation of Propylene by Molecular Oxygen" *Journal of Industrial & Engineering Chemistry* 54 (2015): 2638-2645.

6. A. Seubsai, D. Noon, T. Chukeaw, **B. Zohour**, M. Charoenpanich, S. Senkan. "Epoxidation of Propylene to Propylene Oxide with Molecular Oxygen over  $\text{Sb}_2\text{O}_3\text{-CuO-NaCl/SiO}_2$  Catalysts" *Journal of Industrial & Engineering Chemistry* 32 (2015): 292-297.
7. **B. Zohour**, D. Noon, S. Senkan. "Spatial Concentration and Temperature Profiles in Dual-Packed-Bed Catalytic Reactors: Oxidative Coupling of Methane" *ChemCatChem* 6 (2014): 2815-2820.
8. D. Noon, **B. Zohour**, S. Senkan. "Oxidative Coupling of Methane with  $\text{La}_2\text{O}_3\text{-CeO}_2$  Nanofiber Fabrics: A reaction Engineering Study" *Journal of Natural Gas Science & Engineering* 18 (2014): 406-411.
9. A. Seubsai, **B. Zohour**, D. Noon, S. Senkan. "Key Mechanistic Insight into the Direct Gas-Phase Epoxidation of Propylene by the  $\text{RuO}_2\text{-CuO-NaCl/SiO}_2$  Catalyst" *ChemCatChem* 6 (2014): 1215-1219.
10. **B. Zohour**, D. Noon, S. Senkan. "Spatial Concentration and Temperature Profiles in Packed Bed Propylene Epoxidation Reactors" *Journal of Industrial & Engineering Chemistry Research* 53 (2014): 6243-6248.
11. **B. Zohour**, D. Noon, S. Senkan. "New insight into the Oxidative Coupling of Methane from Spatially Resolved Concentration & Temperature Profiles" *ChemCatChem* 5 (2013): 2809-2812 [Cover page].
12. Miller, **B. Zohour**, A. Seubsai, D. Noon, S. Senkan. " $\text{SnO}_2\text{-CuO-NaCl/SiO}_2$  Catalysts for Propylene Epoxidation" *Journal of Industrial & Engineering Chemistry Research* 52 (2013): 9551-9555.

### Research Presentations

1. **B. Zohour**, S. Senkan, *Discovery of Superior  $\text{Cu-GaO}_x\text{-HoO}_y$  Catalysts for the Reduction of Carbon Dioxide to Methanol at Atmospheric Pressure*. Oral Presentation, 2016 American Institute of Chemical Engineers (AIChE) Annual Meeting. San Francisco, CA.
2. **B. Zohour**, S. Senkan, *Novel Dual-bed Reactor Design and Microprobe Sampling Technique to Increase  $\text{C}_{2+}$  Yields in the Oxidative Coupling of Methane*. Poster Presentation, 2015 Catalysis science & Technology summer conference, University of Liverpool, U.K., Best poster presentation award.
3. **B. Zohour**, D. Noon, S. Senkan, *Novel Reactor Design and Microprobe Sampling Technique to Increase  $\text{C}_{2+}$  Yields in the Oxidative Coupling of Methane*. Poster Presentation, 2015 UCLA Engineering Tech Forum.
4. D. Noon, **B. Zohour**, S. Senkan, *Oxidative Coupling of Methane by  $\text{La}_2\text{O}_3\text{-CeO}_2$  Nanofiber Catalysts*. Poster Presentation, 2014 UCLA Engineering Tech Forum.
5. A. Bae, **B. Zohour**, D. Noon, S. Senkan, *Optimizing Methane Conversion Using Metal-Impregnated  $\text{La}$ ,  $\text{Ce}$  Nanofiber Catalysts*. Poster Presentation, California NanoSystems Institute (CNSI) poster symposium for 2013 UCLA Engineering High School Summer Research Program (HSSRP), Best poster award.
6. **B. Zohour**, D. Noon, S. Senkan, *Spatial Species Concentration and Temperature Profiles in  $\text{La}_2\text{O}_3\text{-CeO}_2$  Nanofiber Catalytic Beds for the Oxidative Coupling of Methane Reaction*. Oral Presentation, 2013 American Institute of Chemical Engineers (AIChE) Annual Meeting. San Francisco, CA.

## **SUBJECT 1. OXIDATIVE COUPLING OF METHANE (OCM)**

## CHAPTER 1.1. Introduction

The Oxidative Coupling of Methane (OCM) as a high potential route for direct methane conversion into ethylene, which is a valuable intermediate for the chemical industry, is of particular importance. In the oxidative coupling reaction,  $\text{CH}_4$  and  $\text{O}_2$  react over a heterogeneous catalyst at elevated temperatures to form the desired products (ethylene, ethane,  $\text{C}_2$ ). The sections below will describe our pursued research motives and provide a review of previous research performed and challenges of the process.

### 1.1. Natural Gas

The known reserves for methane, major component of natural gas (NG), are enormous and rival those of liquid petroleum. Therefore, recently, natural gas has received great attention as alternative feedstock to petroleum for chemical synthesis. Besides its abundance resources, natural gas has several other advantages such as easy purification, source independent conversion, and no need for further hydrogen when converted to higher hydrocarbons which makes it a great unconventional feedstock for chemical synthesis industry. However, utilization of methane as an alternate chemical feedstock to petroleum has been an extremely difficult task in industrial catalysis [1].

#### *1.1.1. Natural Gas Resources*

Natural gas is a fossil fuel formed when layers of buried plants, gases, and animals are exposed to intense heat and pressure over thousands of years. The energy that the plants originally obtained from the sun is stored in the form of chemical bonds in natural gas. Natural gas is a nonrenewable resource because it cannot be replenished on a human time frame. Natural gas is a hydrocarbon gas mixture consisting primarily of methane, but commonly includes varying



amounts of other higher alkanes such as ethane and to a lesser percentage of carbon dioxide, nitrogen, and hydrogen sulfide. Natural gas is an energy source often used for heating, cooking, and electricity generation. It is also used as fuel for vehicles and as a chemical feedstock in the manufacture of plastics and other commercially important organic chemicals.

However, during drilling and process, some volumes of gas cannot be efficiently captured and returned to the system for processing. Moreover, due to the uneconomical liquefaction and unsafe transportation processes of natural gas and its powerful greenhouse effects (Methane ( $\text{CH}_4$ ), the main component of natural gas, is more than 20 times as potent per kilogram as  $\text{CO}_2$ ), methane is largely flared at the wells. Therefore, considering high efficiency of complete combustion of methane during flaring process, flaring methane produces fewer net greenhouse gas emissions than would result from just releasing the natural gas.

Traditionally, natural gas reserves were tied to the oil reserves which are mainly located at specific geographical regions, namely in Middle East and north-eastern part of Europe. However, recently, largely due to the shell gas technology, there is an abundance of natural gas globally and specially in U.S.

As shown in Figure 1.1-1 in the year 2013 U.S. and Russia are among the top two producers of natural gas in the world. This is considering the fact that Russia has one of the largest oil and natural gas reserves in the world.

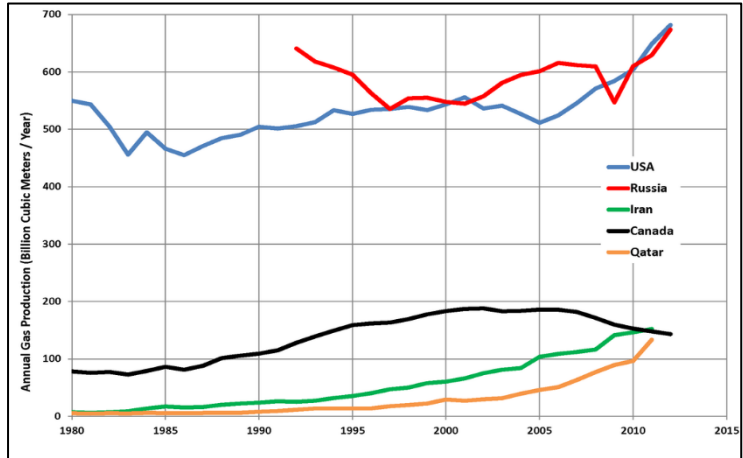


**Figure 1.1-1.** Natural gas production trend

Shale gas refers to natural gas that is trapped within shale formations. Shales are fine-grained sedimentary rocks that can be rich resources of petroleum and natural gas. Over the past decade, the combination of horizontal drilling and hydraulic fracturing has allowed access to large volumes of shale gas that were previously uneconomical to produce. The production of natural gas from shale formations has rejuvenated the natural gas industry in the United States. The report, compiled by the Energy Information Administration (EIA), estimates that there are 2,543 trillion cubic feet (Tcf) of technically recoverable natural gas in the United States. This includes undiscovered, unproved, and unconventional natural gas. According to Figure 1.1-2 (on left) Shale gas production has been rising since the year and is expected to continue its fast-increasing rate. As shown in Figure 1.1-2 (on right) shale gas production will be the driving force behind increased natural gas production, increasing from 5.0 trillion cubic feet in 2010 to 13.6 trillion cubic feet in 2035, accounting for nearly half of all domestic natural gas production.

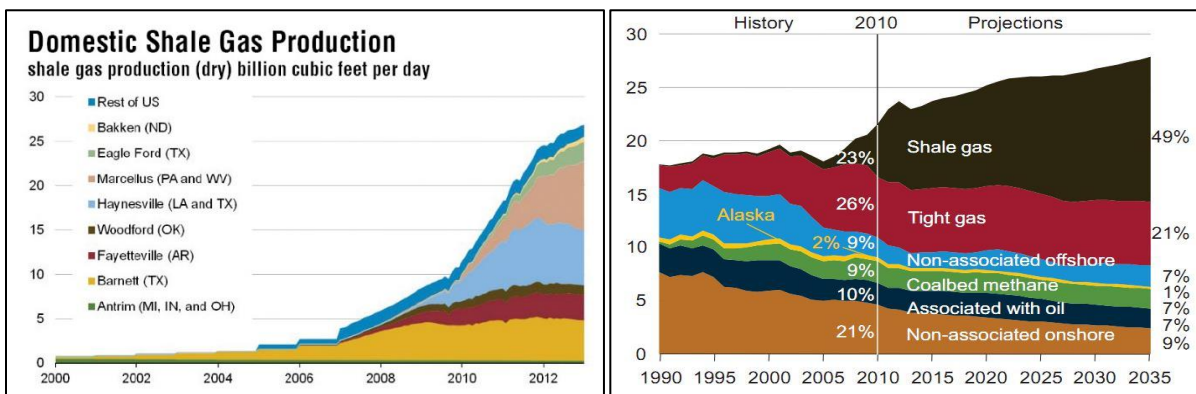


Figure 1.1-2. Shale gas Production in the U.S.

Thanks to improved technologies that are allowing energy producers to access significant and growing supplies of domestic natural gas from shale formations and other unconventional reservoirs, Over the past several years a truly game-changing event has occurred in the natural gas industry in the U.S. and worldwide. In short, shale gas is reshaping the U.S. chemical industry. However, the benefits of developing the abundant and clean natural gas energy resource in America should be realized. Subsequently, we have to be smart in utilizing the natural gas resources and take advantage of this remarkable opportunity in the best ways possible.

### 1.1.2. Utilizing Natural Gas

Recently, due to unstable petroleum market, and steadily growing concerns and requirements to environment protection, there is a need to develop alternative routes to the key raw materials, namely olefins, aromatics, synthesis gas and acetylene, Figure 1.1-3. Although many of these routes have been investigated, the commercial viability of these alternatives remains often a challenge [2]. Nevertheless, an alternative resource with high potential is methane, the major component of abundant fossil resources such as natural gas and methane hydrates given its abundance and versatility, theoretically a large number of important species may be produced via

careful construction of carbon units [2] . However, in spite of all the favorable factors and advantages of natural gas, it is still a widely underutilized feedstock.

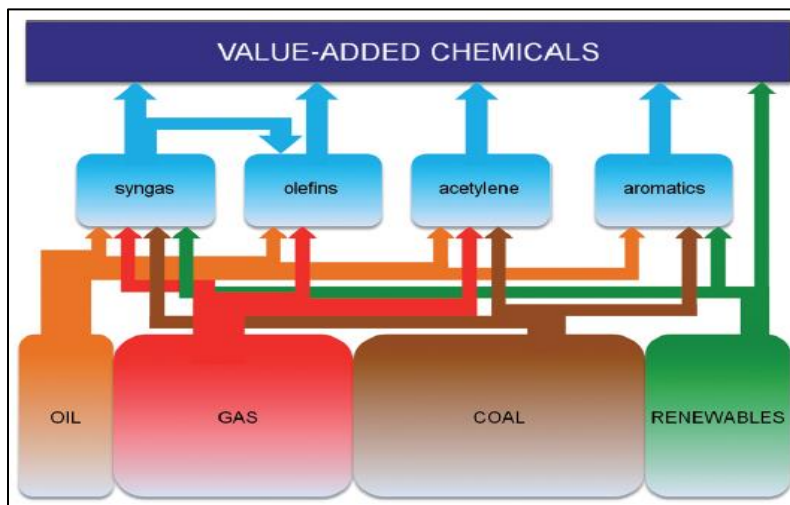


**Figure 1.1-3.** The chemical value chain in terms of feedstocks

Generally speaking, there are two possible ways of natural gas (mainly consisting of methane) transformation into value-added products (VAP) such as VA-chemicals, and synthetic transportation fuels [3]:

- a) Indirect, i.e. via synthesis gas ( $\text{CO} + \text{H}_2$  mixture)
- b) Direct, e.g. via one-step transformation to olefins (ethylene, etc.), oxygenates and aromatics.

Both of the above routes can lead to the final VAP of the same type, i.e. bulk and fine chemicals, synthetic fuels, polymers, plastics. However, at present, the syngas route is only practically implemented in natural gas processing technology [3]. Synthesis gas, as an intermediate product of indirect natural gas feedstock processing, requires subsequent processing and conversion to chemicals or fuels via Fischer-Tropsch (F-T) or hydrogenation processes. Indirect routes are extremely energy intensive due to the highly endothermic nature of the reforming step

and require a great deal of capital investment. Even more concerning, due to the resulting by-products, this method lacks to conform some of the environmental rules and regulations, which could result in making this method obsolete in the near future. Therefore, considerable interest exist in towards the development of alternative direct routes (preferably in one step) of methane conversion into VAP. Figure 1.1-4 [1] indicates some of the potential routes for direct methane upgrade.

Approach	Potential products	Major pertaining challenge(s)
partial oxidation	methanol formaldehyde formic acid methyl bisulphate	low value increases the 'selectivity challenge'
oxidative carbonylation	acetic acid	competing with the current industrial process
oxidative coupling	ethane ethylene propylene	overcoming the conversion vs. selectivity ceiling
aromatisation or alkylation	benzene toluene xylenes	thermodynamic limitations

**Figure 1.1-4.** Potential direct routes for methane conversion

Among all these potential routes of direct methane upgrade, the favorable thermodynamic and current industrial prevalence of oxidation processes ensures that these routes offer the greatest potential. Even though, there are some significant challenges with the direct oxidation of methane route, the diversity and applicability of the potential oxygenated products of this route is such that this route is a highly desirable and sought-after process which is of high potential industrial interest. Furthermore, olefins, as one of the major chemical building blocks, are typically of much greater value than alternative C<sub>1</sub>-oxygenated derivatives. Therefore, direct methane oxidation routes (i.e. oxidative coupling of methane) which have potential to directly produce C<sub>2+</sub> products such as ethylene (the intermediate chemical in production of plastics and fuels) are in significant importance.

## 1.2. Ethylene and Its Applications

Ethylene as the primary target product of the OCM reaction and because of its worldwide use as an intermediate in production of plastics and potentially fuels, represents a particularly significant opportunity.

Ethylene (IUPAC name: ethene) is a hydrocarbon with the formula  $C_2H_4$  or  $H_2C=CH_2$ . It is a colorless flammable gas with a faint "sweet and musky" odor when pure. It is the simplest alkene (a hydrocarbon with carbon-carbon double bonds), and the second simplest unsaturated hydrocarbon after acetylene ( $C_2H_2$ ). Ethylene ( $C_2H_4$ ), is the world's most widely-produced organic compound, with over 143 million metric tons produced in 2013 [4]. Ethylene is the monomer of polyethylene, the world's most popular plastic, and as shown in Figure 1.1-5 it is also used to produce other important industrial chemicals, such as polyvinylchloride, ethylene glycol, ethylene oxide, and styrene, and polystyrene. These wide range of uses makes ethylene a high-demand commodity, justifying its massive production scale. Specifically, the polymerization of ethylene accounts for the majority of end ethylene usage, followed by oxidation to ethylene glycol, an antifreeze compound, and halogenation to yield gasoline antiknock compounds; these three processes account for 90% of the world's ethylene consumption [5]. In addition, ethylene can be oligomerized into liquid hydrocarbons, thereby enabling the efficient utilization of natural gas in remote parts of the world. Other more niche uses for ethylene include its use as a plant ripening chemical. In this context, ethylene is typically formed via the catalytic decomposition of ethanol and controllably released in "gassing rooms" to hasten plant ripening and blooming. Due to the major uses of ethylene - most of which involve polymerization - it is crucial to achieve extremely high ethylene purities.

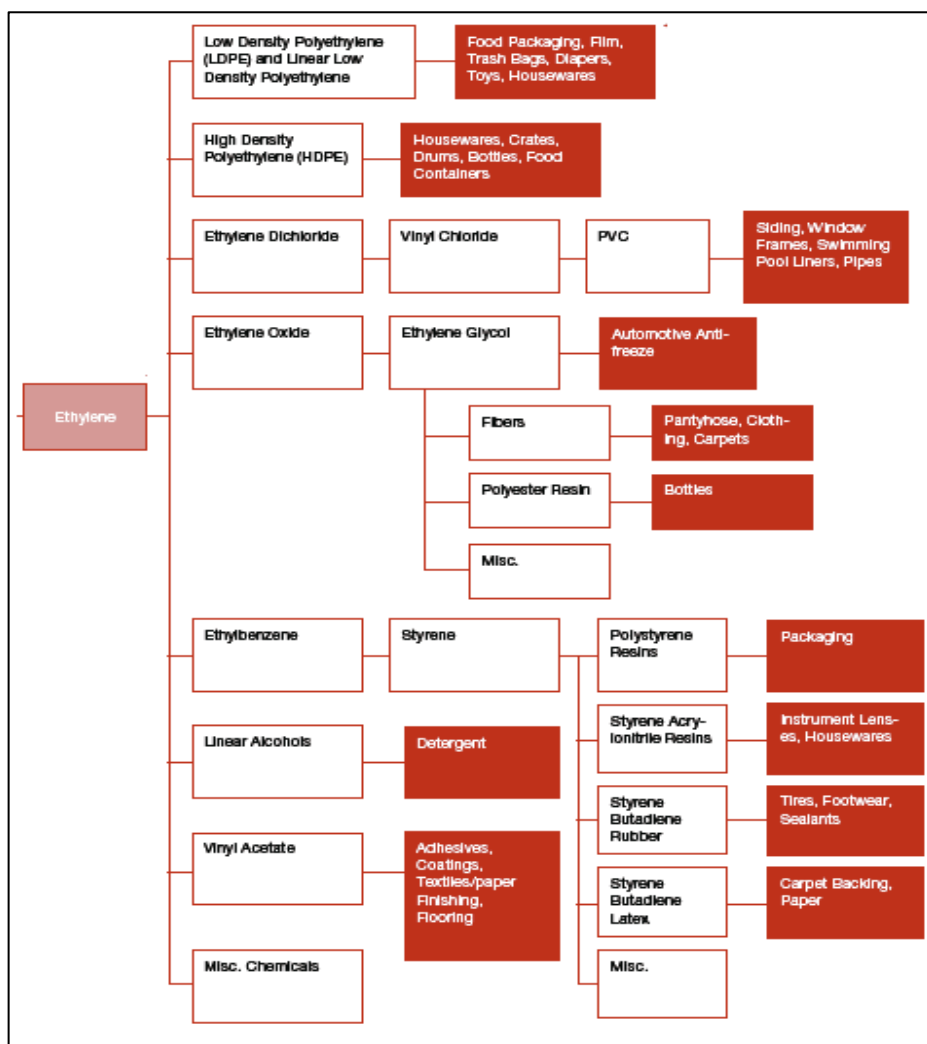


**Figure 1.1-5.** Commercial product chain of ethylene

After the drop in ethylene prices due to the global financial crisis in 2009, both the price and worldwide demand for ethylene have been steadily increasing. As shown in the graph of Figure 1.1-6 the global price of ethylene currently hovers around the average of 1300 USD/metric ton, a significant increase from the 500 USD/metric ton price in 2009, though still lower than the peak price of 1800 USD/metric ton in 2008. It is also interesting that at the writing of this prospectus, a significant change in the world energy picture is unfolding, which will likely to favorably impact the economics of using natural gas as a chemical feed stock.

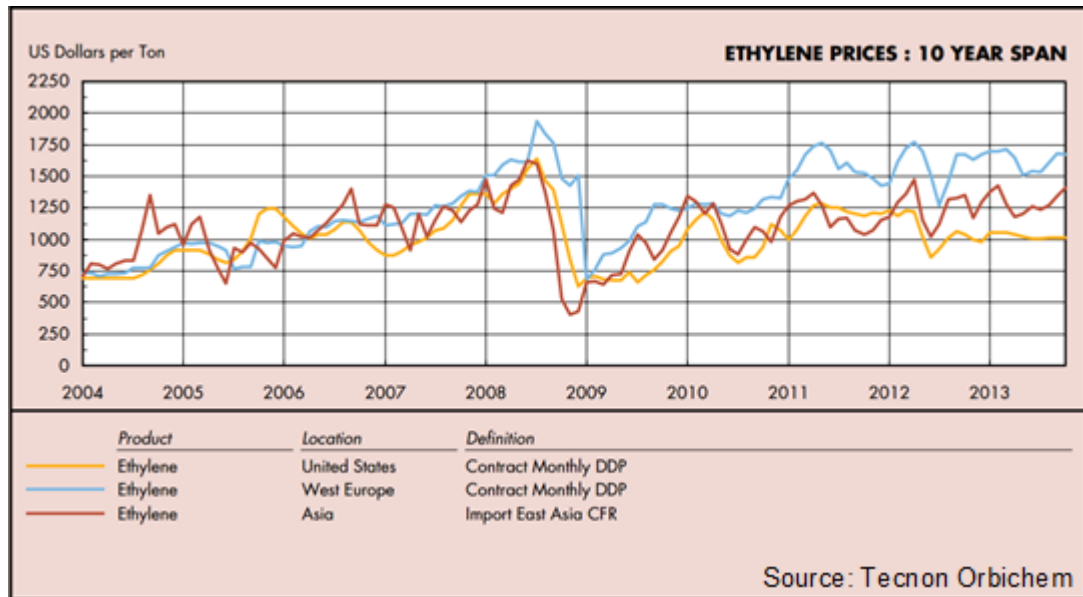


**Figure 1.1-6.** Historical price of ethylene

Global markets for ethylene are primarily concentrated in the polymer production sector. Figure 1.1-7 shows the distribution for the world consumption of ethylene. As seen in Figure 1.1-7 in 2008 Europe and the U.S. consumed about 40% of the worldwide ethylene. Since Within Europe and U.S., demand for polyethylene and PVC, both derivatives of ethylene, have been increasing as well. Predictions for the ethylene market suggest the price will continue to steadily increase over the next few years, as demand increases.

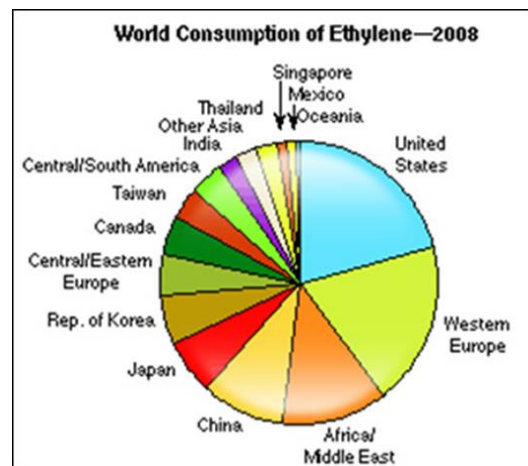


**Figure 1.1-7.** Global ethylene market distribution



Currently, the bulk of the worldwide production of ethylene is based on thermal cracking with steam [6]. The process is called pyrolysis or steam cracking in which naphtha is put through a high-temperature (~850 °C), non-catalytic process that breaks high-order hydrocarbons into smaller ones. A process diagram of cracking and separation of the various hydrocarbons involved is highly endothermic and can be split into four main sections as shown in Figure 1.1-8 [6].

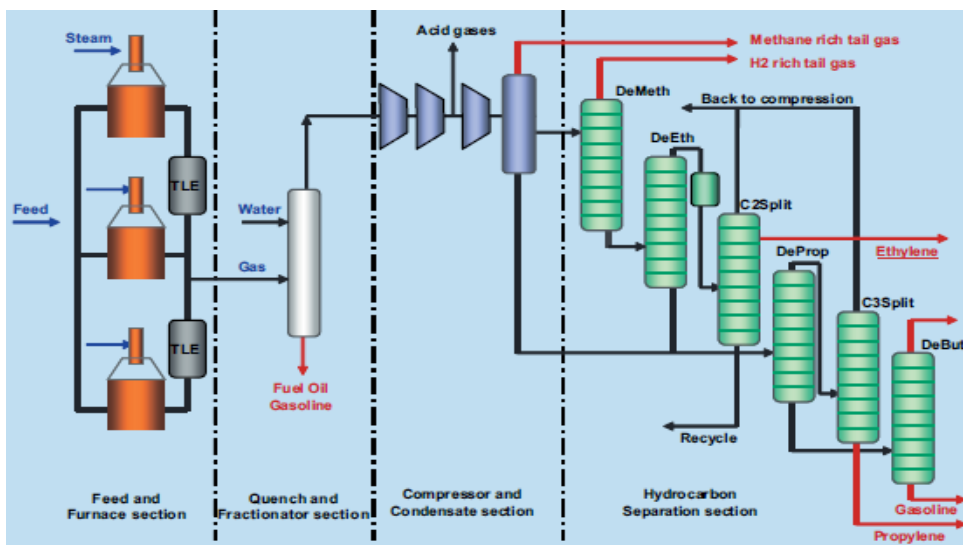


**Figure 1.1-8.** Ethylene Production Overview

This process is extremely energy intensive and produces large amounts of by-products (CO, CO<sub>2</sub>). Therefore, enhancing the direct methane conversion methods (i.e. OCM), as an effective and economically more feasible way of ethylene (and other C<sub>2</sub>) production, is highly desirable.

### 1.3. Oxidative Coupling of Methane (OCM)

All indirect NG conversion routes utilize the high temperature, endothermic and costly stream reforming as a first step, where synthesis gas (H<sub>2</sub>/CO mixtures) is produced. This is followed by the synthesis of useful products via various catalytic processes [1]. Direct methods for the conversion of methane to the desired products avoid the expensive syngas steps; however, they remain uneconomical due in part to low C<sub>2+</sub> yields. The Oxidative Coupling of Methane

(OCM) as one of the cleanest and economically more viable ways of upgrading methane is a high potential route for direct methane conversion and is in particular importance. In the oxidative coupling reaction, CH<sub>4</sub> and O<sub>2</sub> react over a heterogeneous catalyst at elevated temperatures to form the desired products. OCM is a complex surface catalysis and gas phase reaction process to transform methane into ethane, ethylene (as shown in Equation (1.1-1) and Equation (1.1-2)), and higher molecular weight hydrocarbons (C<sub>2+</sub>).



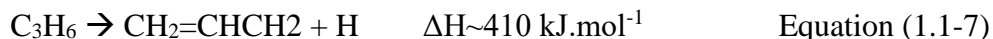
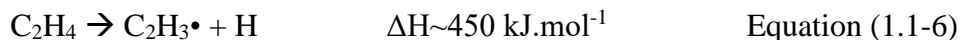
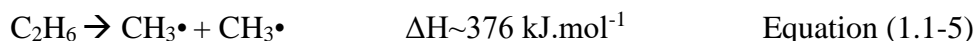
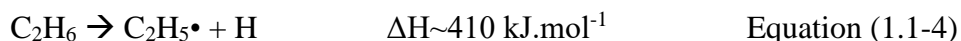
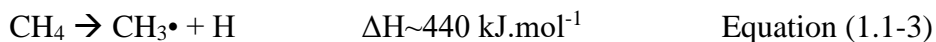
Prior research on OCM catalysis which typically involved quasi-spherically shaped nanoparticles mostly lead to deactivation and low product yield [7]. It has been suggested that there seems to be a C<sub>2+</sub> yield limit in a single pass fixed-bed OCM reactor [7]. Therefore, the development of scalable methods enabling new reactor design, or synthesis of new catalytic materials with high energy surfaces that exhibit high activity and selectivity and maintain their high performance in reactive environment is highly desirable. In this section a brief research background and process challenges of OCM are discussed. Furthermore, our research motivations and goals are discussed indicating the strategy for overcoming some of the process challenges and elucidating new insights to further improve the OCM reaction yields.

### *1.3.1. Process Description and Challenges*

Oxidative Coupling of Methane (OCM) as an effective method in the processing of natural gas offers great industrial potential. Development of an effective OCM catalytic processing system will lead to a direct process to direct transform of methane into ethane, ethylene (as shown in Equation (1.1-1) and Equation (1.1-2)), and higher molecular weight hydrocarbons (C<sub>2+</sub>), which

are considered higher-valued olefins. Consequently, the OCM reaction has been investigated for many years in laboratories around the world.

The major feed gas components of the OCM reaction are CH<sub>4</sub> and O<sub>2</sub>. Due to safety considerations and thermal control of the OCM reaction CH<sub>4</sub> is provided in excess. Typically the feed to the OCM reaction contains CH<sub>4</sub>/O<sub>2</sub> molar ratio of 3-12 with or without diluents at moderate pressures (generally atmospheric pressure). As seen from major reactions of OCM described in Equations (1.1-1) and (1.1-2), OCM is a highly exothermic reaction. Therefore, there is no thermodynamic limitations for OCM reaction. However, the reaction is typically conducted at high temperature of 900-1200 K. As shown in Equation (1.1-3), this is mainly due to the high activation energy of methane. Methane is a very stable molecule and dissociation of one hydrogen from methane molecule (CH<sub>3</sub>-H) to form methyl radical requires about 440 kJ/mol.



This has been marked as one of the major challenges of OCM reaction. As seen in Equations (1.1-3)-(1.1-7) the required activation energy for methane activation is significantly higher than most of the major products formed in the OCM reaction, which, in the absence of a selective catalyst, leads to non-selective and sequential oxidation of desired products. Therefore, high temperatures of OCM reaction over an active catalyst creates a tradeoff between conversion and products selectivity.

Furthermore, complexity in the OCM reaction process is originated from the nature of OCM reaction which contains a coupled homogenous gas phase and catalytic surface reaction network. As shown in Figure 1.1-9 [8] , in the case of OCM reaction, catalytic and gas phase reactions extensively interact with each other to form products and by-products.

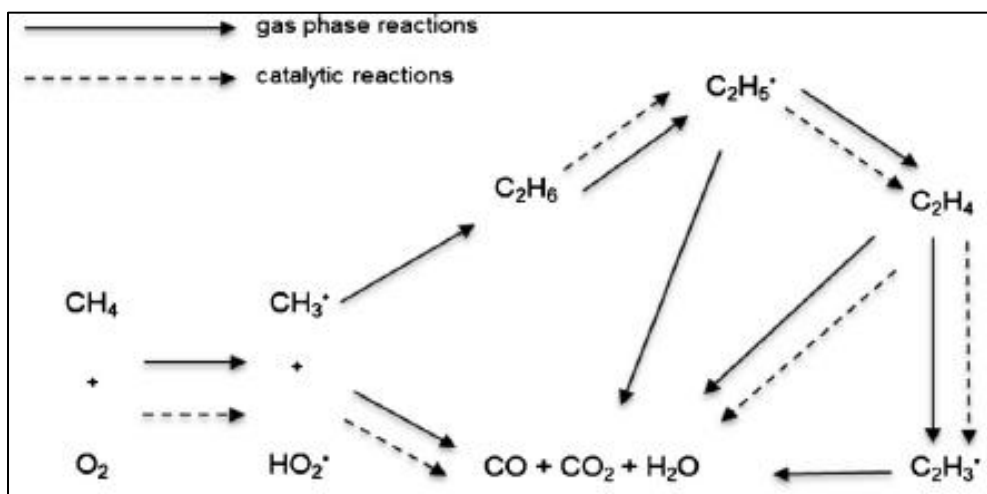


**Figure 1.1-9.** Global OCM reaction steps, indicating the homogeneous and/or heterogeneous characteristics

The OCM reaction is proposed to be initiated via the activation of methane on the surface of the metal oxide catalysts to generate methyl radicals, and the recombination of methyl radicals either on the catalyst surface or in the gas phase lead to the  $\text{C}_2$  products [9] . Although studies done by Lunsford and Luo et al. have demonstrated and confirmed the formation of gas-phase methyl radicals ( $\text{CH}_3^\bullet$ ) under OCM conditions [10], [11], which leads to a general agreement about the overall route for OCM, the particular reactive surface intermediate responsible for the initial C-H bond activation remains uncertain [10], [12]. More detailed studies conducted by isotope labeling experiments, kinetic studies, and DFT simulations done by Palmer et al. [12] suggest that  $\text{O}_2$  dissociatively adsorbs over the catalyst's oxide surface generating activated forms of surface oxygen ( $\text{O}^-$ ,  $\text{O}_2^-$ , and/or the peroxide  $\text{O}_2^{2-}$ ), which are mainly responsible for methane activation over the surface catalysts.

Based on the above studies, Figure 1.1-10 [13] shows the basic OCM mechanism, which best describes the complex nature of the OCM reaction on the catalytic solid surface.

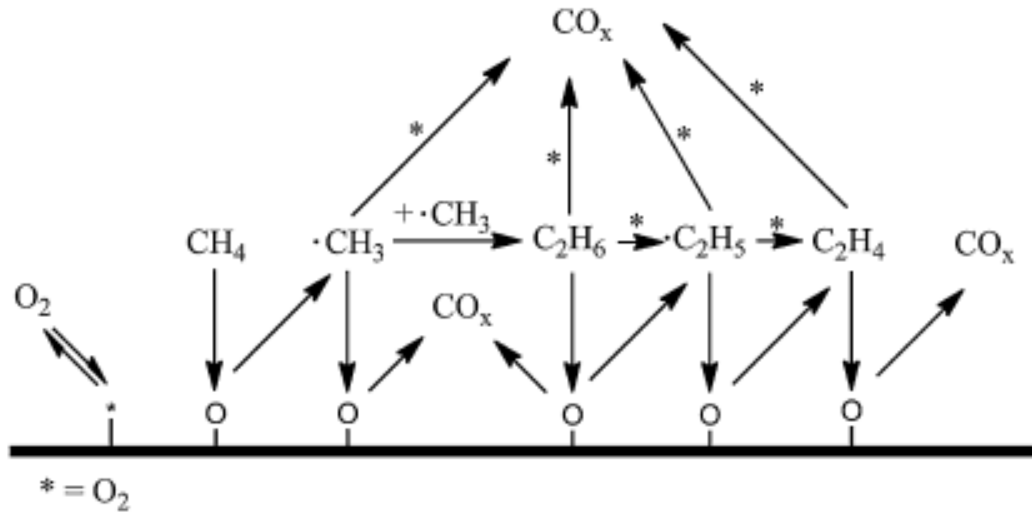


**Figure 1.1-10.** Basic mechanism for the reaction network of the OCM at oxides

Therefore, in general (Figure 1.1-10), CH<sub>4</sub> is activated on the catalyst surface by the active atomic oxygen center leading to the formation of CH<sub>3</sub>• radicals and surface [OH] [3], [14], [15], [11]. The CH<sub>3</sub>• radicals desorb then diffuse away from the catalyst surface and recombine in the gas phase producing C<sub>2</sub>H<sub>6</sub> followed by dehydrogenation to form C<sub>2</sub>H<sub>4</sub>. Some C<sub>3</sub> hydrocarbons also form by addition of CH<sub>3</sub>• to C<sub>2</sub>H<sub>4</sub>. Regeneration of the active sites is also well accepted to occur through the formation and desorption of H<sub>2</sub>O. The vacated active sites are then rapidly repopulated by O<sub>2</sub> chemisorption. . These events are summarized by the following elementary reaction set Equation (1.1-8)-(1.1-11) :





where [\*] represents a vacant catalytic surface site for oxygen chemisorption. It is likely that a dynamic equilibrium exists between gaseous O<sub>2</sub> and the various forms of surface oxygen, e.g. chemisorbed and lattice oxygen.

However, undesirable surface and gas phase combustion reactions also lead to CO and CO<sub>2</sub> (CO<sub>x</sub>). As mentioned earlier at elevated temperatures of the OCM process the intrusion of the homogenous gas phase free radical (i.e. combustion) reactions are detrimental for C<sub>2+</sub> products. Therefore, the development of novel catalysts and reactors and operating conditions that can operate at low temperatures with high methane conversion, crucial for maintaining high product yields in OCM reaction, marks another major challenge in OCM reaction.

### *1.3.2. Research Background*

The formation of C<sub>2</sub>- hydrocarbons, namely ethane was first documented in the PhD thesis of Nersessyan [16]. In the related publication [17] it was reported that methane oxidation over solid oxides (silica, alumina) is accompanied by the escape of free radicals into the gas phase [3]. This is an important fact and one of the main topics investigated in the OCM process kinetics analysis. The first publication in which the formation of higher hydrocarbons was broadly announced were the USA patent [18] and the paper by Fang and Yeh [19]. Whereas, in the former methane was transformed into ethane, ethylene, benzene, and some other condensation products over solid catalyst capable of supplying lattice oxygen to perform the process, in the latter the steady-state catalytic OCM reaction (over Th oxide) was reported for the first time [3].

However, the real “OCM boom” was initiated by the pioneering work of Keller and Bhasin [20]. This was followed by many other original works of Baerns and Hinsen [21], and Ito and Lunsford [22] . Recently, statistical analysis of the past 30 years of catalytic data on oxidative coupling of methane reaction [7] showed that these pioneering works along with many other novel experimental researches, created a huge body of data on OCM catalysts and their performance which resulted in more than 2700 research articles and about 140 patents.

Different catalyst compositions and numerous catalyst preparation techniques, namely, thermal decomposition, precipitation, impregnation, sol-gel, and spray pyrolysis, had been considered for synthesis of OCM catalysts. Figure 1.1-11 [7] summarizes the most significant elemental compositions of OCM catalysts with significant yields. All the tested materials are powder catalysts of single or mixed metal oxides and they have been tested in a fixed-bed reactor with co-feed mode under atmospheric pressure at feed gas temperatures from 943 to 1223 K. Typically, the feed to the OCM process has much less than stoichiometric oxygen ( $\text{CH}_4$  is in excess). For the processes in Figure 1.1-11  $P_{(\text{CH}_4)}/P_{(\text{O}_2)} = 1.7\text{-}9.0$ , and contact times are from 0.2 to 5.5 S. However, in most cases, the reproducibility and stability of the catalytic materials have not been reported.

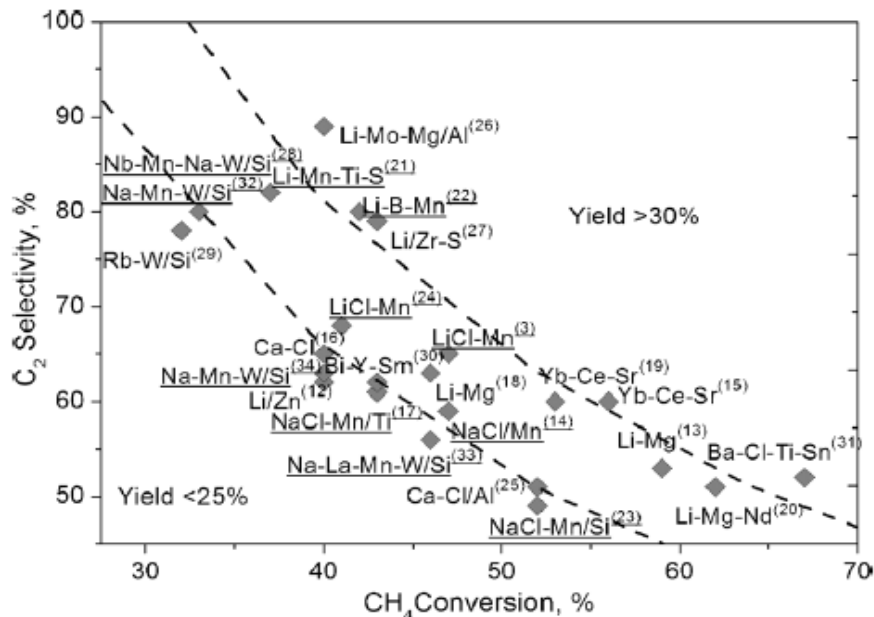


**Figure 1.1-11.** Elemental compositions of OCM catalysts with significant C<sub>2</sub> yields reported in the literature

As expected, single oxides, since the catalytic performance of single-oxide catalysts is influenced by their solid-state properties, which in turn are affected by the synthesis techniques applied for their preparation, do not exhibit high activities for OCM reaction. However, as seen in Figure 1.1-11, all the above catalysts with significant yields are mixed metal oxides (with or without supports). Therefore, it is well understood that various promoters and dopants considerably improve the catalytic performance of single-oxide catalysts for the OCM reaction. Alkaline-earth metals (Sr, Ba, Mg, Ca), lanthanide metals (La, Nd, Sm), and some other metals located in III, V, VI groups of the periodic table (Ga, Bi, Mo, W, Mn, and Re) [7] have been reported to exhibit the best activity as the host metal oxides for the OCM reaction. It has been also purposed that in multicomponent materials based on strongly basic oxides (Mg, La) dopants such as (Cs, Na, Sr, Ba, W, Cl, Ce, Mn) will show positive effects on both selectivity and catalyst activity and their synergetic effects on the host metal oxide should be considered [23].



While many experiments have been focused on optimizing the combination of the catalytic materials and enhancing the chemistry side of the reaction, many works have been focused on the reaction engineering, design, and process optimization to overcome the yield limits of the OCM process.

Simon et al. have considered pellets of lanthanum oxide at 1073-1173 K inside catalytic jet-stirred reactor [24]. However, this type of reactor showed low yields of Y ( $C_{2+}$ ) about 5% with about 30% S ( $C_{2+}$ ) selectivity. Different co-feeds, dilution of feed gas, and various oxidant substitutions such as  $CO_2$  instead of molecular oxygen were also considered to reduce or to prevent the sequential gas phase reactions [25], [26], [27], [28]. However, they all concluded unsuccessful in increasing the  $C_{2+}$  yields.

Alongside of the experimental researches, many computational studies have been deliberated for the OCM reaction system as well. At the molecular level, these studies were primarily based on the use of density functional theory (DFT) geared towards understanding the effects of dopants on the energy of surface oxygen atoms [12] and surface oxygen vacancies [29]. In addition, chemical kinetics and reactor models were also developed to better describe the OCM process [30], [31].

In the work of Palmer et al. a  $La_2O_3$  (001) surface, which is the most stable surface of lanthanum oxide, was simulated and it was exposed to oxygen atoms, Figure 1.1-12. The periodic DFT studies of methane activation over  $La_2O_3$  lead to the identification of plausible surface intermediates and the catalytic cycle of the OCM process.

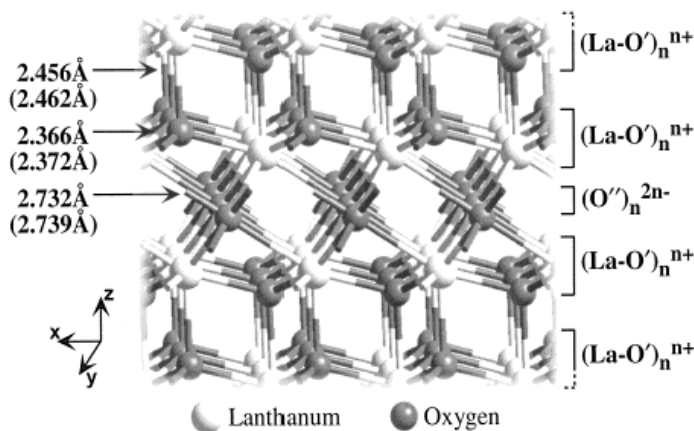


**Figure 1.1-12.** Periodic DFT study of methane activation over  $\text{La}_2\text{O}_3$

Furthermore, some simulation studies have primarily focused on kinetics modeling, and have been proven useful in establishing and improving the OCM mechanism and reactor modeling. One of the initial fixed-bed OCM reactor simulations was done by Hoebink et al. in which a two-dimensional heterogeneous model was used to successfully model the OCM reactor [30]. The concentration and temperature profiles were simulated along the fixed-bed reactor and the model predicted a 60%  $\text{C}_2$  selectivity at about 15% methane conversion [30].

Recently, Panagiotis et al. successfully simulated a catalytic fixed-bed OCM reactor accounting for the gas-phase reaction, the fundamental catalytic surface chemistry (including effects of pellet size and packing factor), and the interactions between the two [31]. In this study the concentration profiles at pellet and reactor scale were obtained for all species considered in the mechanism, leading to the simplified flow diagram shown in Figure 1.1-13 [31].

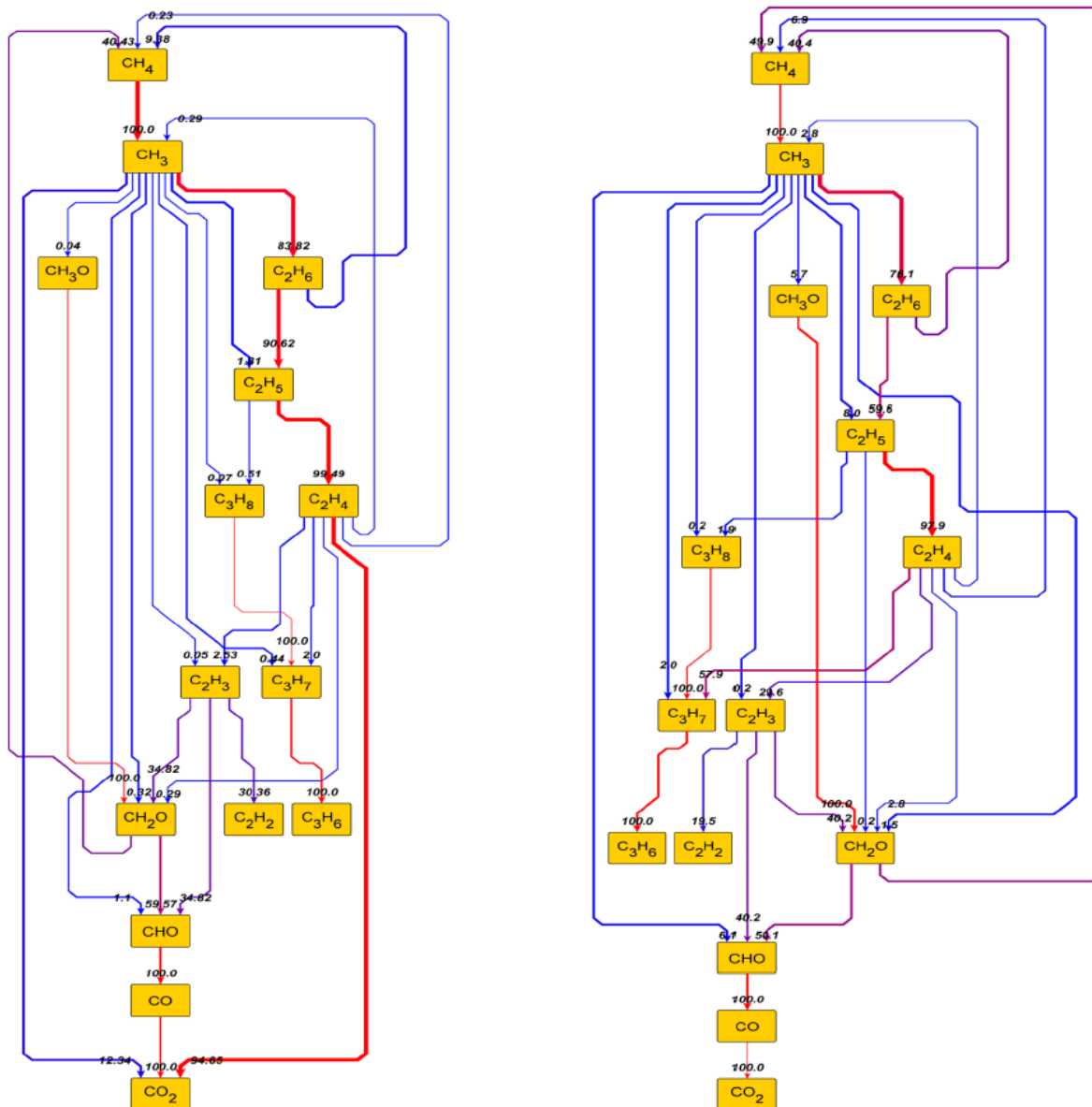


**Figure 1.1-13.** Contribution analysis for the intraparticle (left panel) and interstitial phase (right panel) at the end of the catalyst bed for the reaction conditions

Even though most OCM experiments were conducted in fixed-bed catalytic reactor, simulation of unconventional reactors such as membrane reactors were also performed [32], [33]. These simulations have shown that theoretically implementing such reactor designs, could result in C<sub>2+</sub> yields as high as 40% with a selectivity in C<sub>2</sub> products of more than 60% [33]. Simulation of fluidized bed OCM reactors with stage wise oxygen feed were shown to achieve 22% C<sub>2+</sub> yields

[34]. However, neither of these results have been demonstrated in laboratory experiments, indicating the complexity and importance of other decisive factors in the OCM reaction. Development of a systematic procedure to further pursue these simulation studies will be discussed in further detail in the proposed future work section of this report (section 4.3), as the basis for future simulations accompanied by the experimental OCM research conducted in our laboratory.

In summary, in spite of decades long research, oxidative coupling of methane (OCM) as a high potential route for direct methane conversion and highly sought-after processes in industrial chemistry, remains at the research stage. It has been suggested that  $C_{2+}$  yields of at least 30% will be necessary to render the OCM process industrially a viable technology [35].

#### 1.4. Research Objectives

The objectives of the proposed research program were to develop fundamental chemical kinetic and reactor engineering insights on the catalytic oxidative coupling of methane (OCM) process to push the  $C_{2+}$  product yields towards 30%+. These objectives were explored by undertaking a comprehensive program of studies for the OCM process as outlined below:

1. The synthesis of novel nanofiber catalysts by electrospinning, building on the early discovery from our laboratory that  $La_2O_3$ -based nanofibers were highly active and robust OCM catalysts.
2. Single bed and multi-packed bed OCM experiments were performed using our novel microprobe sampling system for the acquisition of spatially resolved species concentration and temperatures profiles within the catalytic zone. We were also able to undertake experiments under novel conditions that include oxygen-feed distributed packed bed reactors. The dual-bed OCM reactor configuration significantly improve  $C_{2+}$  product yields

to 21% (from 16% for single bed). We also plan to implement coupled catalytic and non-thermal plasma OCM reactors, to further push the yields for useful C<sub>2+</sub> products.

3. Undertake studies to outline development and validation of new generation of DCKM for the OCM process using the high-information content spatial concentration profiles obtained in this experimental program. Once developed, the DCKM will be combined with the transport models describing the reactors for the simulation of species concentration profiles in the OCM reactors. Sensitivity and reaction path analyses will be performed to identify the most influential reaction in DCKM to refine their kinetic parameters. These refinements will be performed using computational quantum chemical calculations as part of future works.

## CHAPTER 1.2. Experimental Set-Up

In this section, the synthesis of Fiber catalysts using electrospinning technique, reaction set-up, novel reactor design, and novel sampling technique applied to the oxidative coupling of methane reaction are discussed in detail.

In general, experiments were performed using a fixed-bed tubular reactor system. The 6mm diameter quartz tubular reactor was packed with nanofiber fabric catalysts that were prepared by electrospinning a viscous polymeric solution into which metal precursor/s were dissolved [36]. The experiments were performed at 1 atm. The flow rate of the reactant gases ( $\text{CH}_4$  and  $\text{O}_2$ ) was maintained (60-180  $\text{cm}^3/\text{min}$  at STP (sccm)) using electronic mass flow controllers (MFC, MKS Billerica, MA) at different  $\text{CH}_4/\text{O}_2$  feed ratio (molar feed ratio 3-7). The reaction temperature was varied according to the feed ratio to accomplish ignition at specific reaction conditions ( $T_f \sim 450$ -800  $^\circ\text{C}$ ). Gas analysis was accomplished by on line gas chromatography (Varian 4900 Mini GC, with molecular sieve 5A and Poraplot U columns). The sections of this chapter will discuss each performed synthesis method and experimental design in further detail.

### 2.1. Catalyst System and Synthesis

Our initial screening of the potential catalytic systems for the OCM reaction revealed that 40-70 nm diameter nanofibers of  $\text{La}_2\text{O}_3$  doped with  $\text{CeO}_2$  ( $\text{La}_2\text{O}_3$ - $\text{CeO}_2$ ) were superior catalytic materials for the OCM reaction compared to traditional nanoparticles [36]. Moreover, electrospinning, as a promising scalable technique for production of highly uniform catalytic nanostructures, was employed for synthesis of nanofibers. In this section, electrospinning technique and its practice for synthesis of  $\text{La}_2\text{O}_3$ - $\text{CeO}_2$  nanofibers of different diameter are discussed in further details.

### *2.1.1. Electrospinning Principle and Challenges*

There are numerous methods for fiber synthesis. However, electrospinning is a simple and relatively inexpensive mean of producing nanofibers by solidification of a polymer solution stretched by high electric field. There is a high interest in the electrospinning process and continuous nanofiber production in today's industry. Nanofiber's applications in advanced clothing, biomedical scaffolds, rechargeable batteries, and other areas are being explored and developed. Nonetheless, practice of electrospinning in heterogeneous catalysis and catalyst synthesis is a relatively new emerging field.

Electrospinning is a complex, multi-physics process involving electro-hydrodynamics, mass and heat diffusion and transfer, and solidification. Considering the fact that the polymer jet is continuously under the influence of high electrical field and mass, heat, and hydrodynamics are most likely coupled during the process, it is very difficult to accurately model the electrospinning process. Despite of these convolutions and challenges, the electrospinning process can be subdivided into several stages which include, jet initiation, steady-state jet motion, jet instabilities, and nanofiber deposition [37] . In electrospinning solvent evaporation from jet surface may lead to inhomogeneity in the radial direction in dilute polymer jets and solvent evaporation can be very fast in ultrafine jets typical for electrospinning in the order of 50 ms to 2 s. Rapid solvent evaporation accompanied by jet stretching due to electric forces and jet instabilities is ultimately responsible for final solidified nanofibers [37].

Some of the important variables that need to be considered in synthesis of catalyst fibers via electrospinning method are summarized in Figure 1.2-1. Many of these parameters could significantly affect the end result of the electrospinning process and/or diameter of the fibers produces.

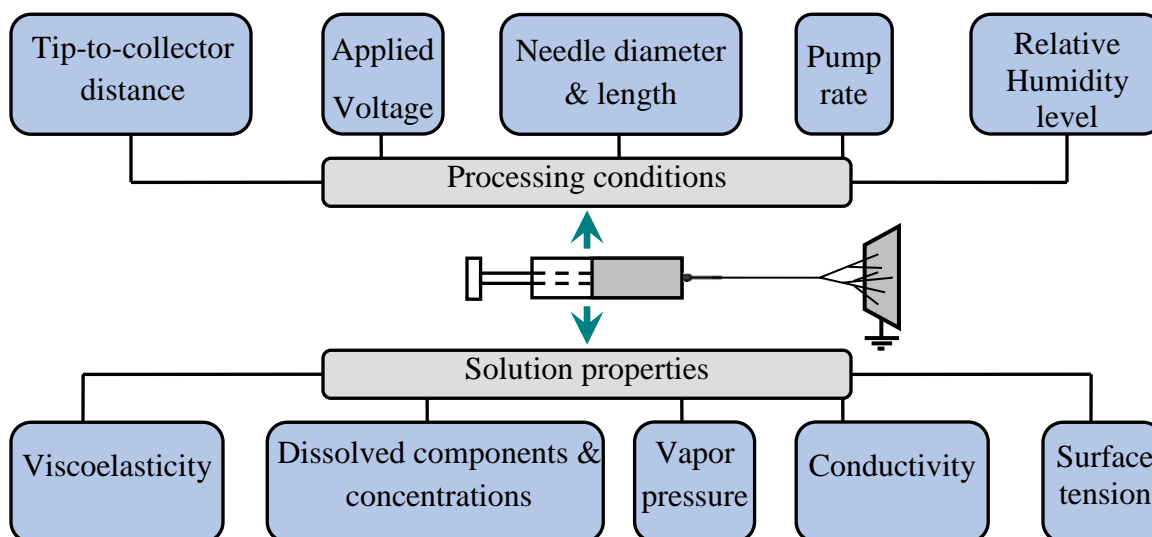


**Figure 1.2-1.** Summary of pertinent variables associated with electrospinning

The amount and type of polymer used has a strong effect on the fiber morphology. The more polymer usually will result in longer and thicker fibers due to increased entanglement in the solution. The type of solvent is also one of the major components effecting the electrospinning process and the catalyst performance. It is important to note that water is always needed as a component in the solvent to allow for complete dissolution of the metal salts. A good substitute for water could be formic acid, however, unfortunately, it catalyzes some sort of reactions when metal salts are present in the solution. However, due to the water's extremely high surface tension a multicomponent solvent system may be required to achieve uniform fibers. Moreover, since evaporation of the solvent plays a key role in producing well-defined uniform fibers, electrospinning needs to be done in a chamber with very low relative humidity level.

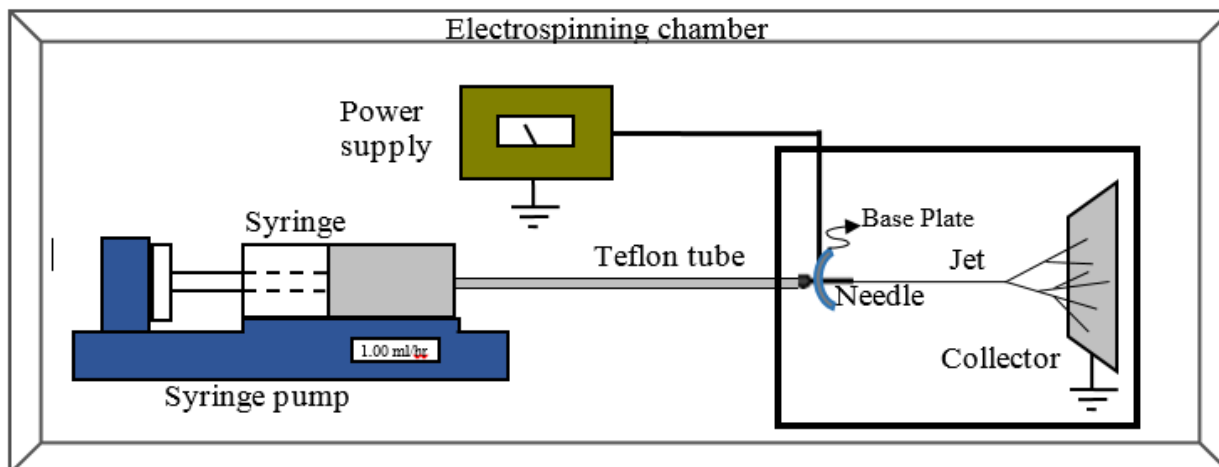
### *2.1.2. La<sub>2</sub>O<sub>3</sub>-CeO<sub>2</sub> Fiber Catalysts Synthesis*

Nanofibers will be prepared by electrospinning. In a typical experiment, polyvinylpyrrolidone (PVP; 1.3 MDa) is mixed with a solvent containing water and ethanol. To this solution, one or more metal salts are added [e.g. La(NO<sub>3</sub>)<sub>3</sub>·6H<sub>2</sub>O, Ce(NO<sub>3</sub>)<sub>3</sub>·6H<sub>2</sub>O]. Water is



necessary to allow for the mutual solubility of PVP and a metal salt while ethanol is used primarily to lower the surface tension of the solution, allowing it to be electrospun into fibers. Adjustments in the PVP concentration and metal-to-polymer ratio are made to give a desired fiber morphology and metal throughput rate. Typical values used may be 4 wt% PVP with a metal-to-polymer ratio of 0.15. Water is usually present in the solution at 30-50 wt%, with the one or more of the alcohols making up most of the remaining solvent mixture. The solution is then vigorously mixed via vortex to form a uniform viscous liquid. After 2-3 hours of mixing solution is set to rest on the side of the vial to get rid of the air bubbles formed inside the liquid.

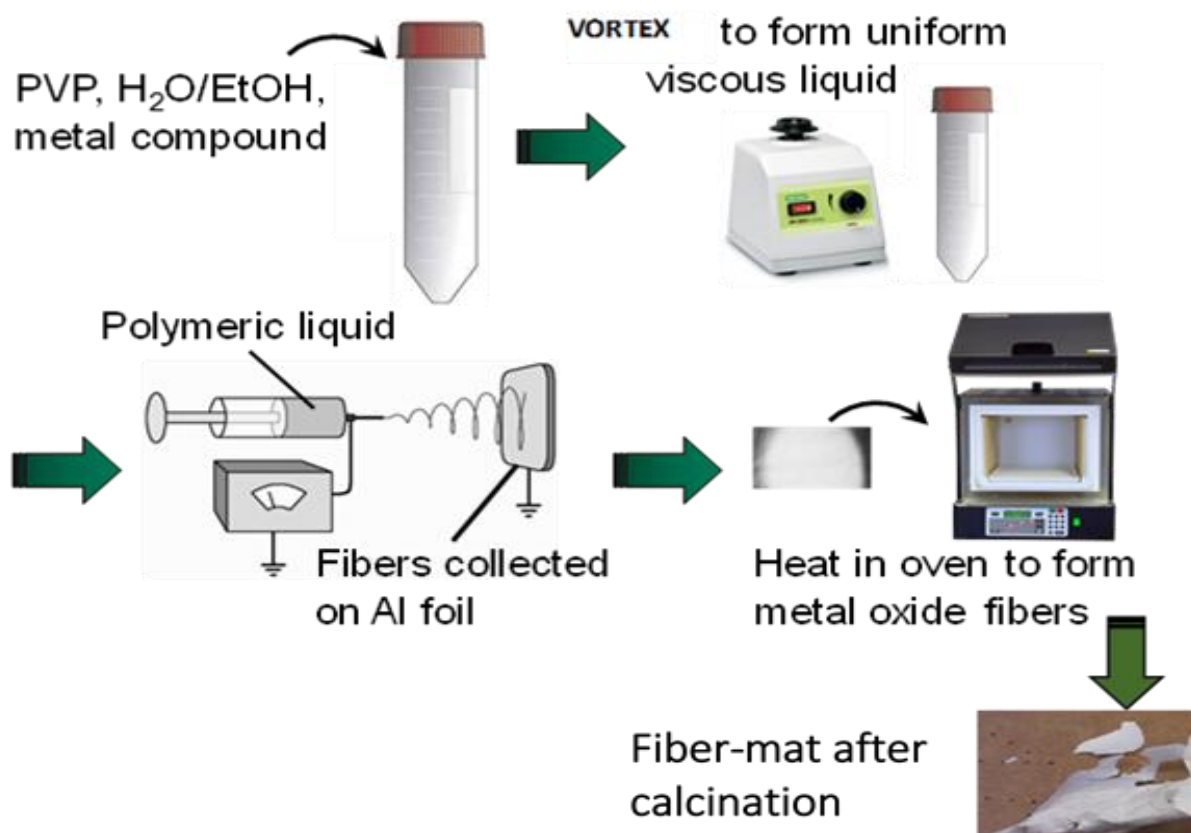
As shown in Figure 1.2-2, the electrospinning setup is contained inside a partially ventilated chamber. The solution is loaded into a syringe. Connected to the syringe is a Teflon tube, which, on its other side, is connected to a metal needle. This needle is then connected to the high voltage power supply. Aluminum foil is wrapped tightly around the collector and the fluid in the syringe is pumped to the needle. The syringe pump is programmed to then pump the fluid at a fixed rate which usually depends on the viscosity of the polymer solution (more polymer generates more viscous solution), commonly 1.0-2.0 mL/hr. In order to prevent the fibers from randomly flying everywhere in the chamber, a base plate was employed. Base plate is a simple metallic piece (preferably slightly bended) which sits on the high voltage needle. This base plate is about 1/4 of the size of the collector plate. The general purpose of using the base plate is to align and concentrate the electrical field between the needle and the collector plate. Using the base plate enhances the electrospinning yield preventing the fibers to fly all over the chamber. The base plate will guide more fibers to be collected onto the collector plate. The power supply is then set to deliver 30-50 kV and spinning ensues for 5-20 hours.



**Figure 1.2-2.** Electrospinning setup used in the synthesis of nanofibers of metal

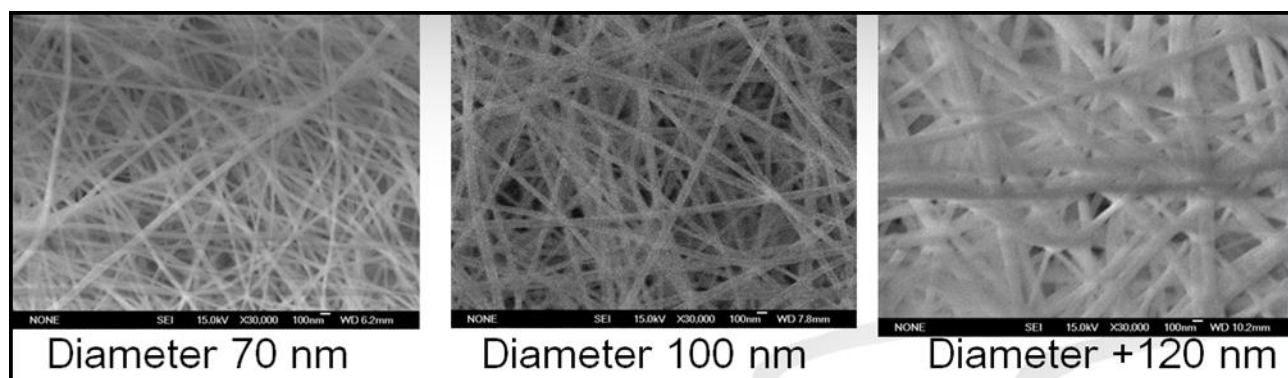
The material collected on the aluminum foil is placed inside an oven for calcination. The electrospun material was calcined at 625 °C in a furnace to form metal oxide nanofiber fabrics.

Figure 1.2-3 demonstrates a summary of the electrospinning process and some of the equipments associated with electrospinning.



**Figure 1.2-3.** Summary of the catalysts preparation via electrospinning process

SEM images of fibers after calcination Figure 1.2-4 confirmed that the nanofibers had diameters of 70-100 nm. The fabric also had a low BET area of about 20 m<sup>2</sup>/g, suggesting that the nanofibers were dense and did not possess internal porosity.



**Figure 1.2-4.** SEM image of fibers (diameter 70-120 nm; image magnification 30,000)

## 2.2. Set-up and Testing

In this section system control set-up, testing conditions, and analysis process are discussed. Furthermore, the establishment of novel sampling technique and reactor design are presented in this section.

### 2.2.1. Feed Gas Control System

Different pressurized reagent gases (e.g. methane, ethylene, ethane, hydrogen, oxygen) or inert gases (e.g. helium, argon, nitrogen) are delivered to the reactor system via mass flow controllers (MFCs from MKS, Andover, MA) as shown in Figure 1.2-5. There are 10 MFCs available for controlling the gas flow: MFCs 1-4 control the output of the gas mixture into the reactor system, and MFCs 5-10, control the gas input from the cylinders. An additional MFC (the white-colored box in Figure 1.2-5) is used to maintain the pressure of the gas output (typically at 20 psig). The CPA software operates this flow system. CPA program is used to set the gas flow

rates and subsequently specify the mixture ratio and rate of the feed gases. Practically, up to six different feed gases can be fed through MFCs no. 5-10, which then pass through a mixing zone in a tube. The gaseous mixture is then fed to the reactor system via MFCs no. 1-4. In order to achieve accurate flow rates for each MFC for a specific feed gas or gaseous mixture, the MFCs are calibrated using a bubble flow meter.



**Figure 1.2-5.** Mass flow controller set-up

### *2.2.2. Gas Chromatography System*

The effluent from the reactor setup was analyzed using gas chromatography (GC). The micro-GC (Varian, CP-4900, Middelburg, The Netherlands) is the instrument used in our work to analyze reaction products. Two GC columns are attached to the system. Column A is a molecular sieve 13X (10 m) that allows the separation of smaller molecules: H<sub>2</sub>, O<sub>2</sub>, N<sub>2</sub>, CH<sub>4</sub> and CO. Larger gas molecules are blocked by a backflushing system to prevent column pore blockage. Column B is a Porapak U column (PPU, 10m) that handles the larger gas molecules. The gas is introduced to the micro-GC system using a 500 $\mu$ m  $\times$  30cm fused silica capillary connected from the reactor to the pump. The temperature and pressure of the GC columns are adjustable, from 30 °C to 180 °C and from 7 to 21 psig. For analysis of the gas products, the micro-GC is equipped with a thermal conductivity detector (TCD). When the detector encounters a gas other than helium, it measures that gas' thermal conductivity and compares it to the thermal conductivity of helium (the reference

gas). The signals produced by the TCD represent retention times and peak areas which are then used in quantitative and qualitative analysis. All of the parameters of the micro-GC can be adjusted and the integrated peaks can be analyzed by Varian Star Workstation software.

### 2.2.3. Single-bed Reactor

Single bed experiments (fiber testing, Concentration and Temperature profiles of single bed) were performed using a fixed bed tubular reactor system as shown in Figure 1.2-6 .

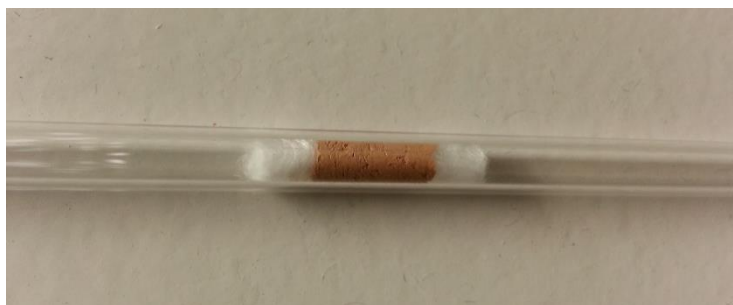


**Figure 1.2-6.** Fiber catalysts packed inside quartz tube

The reactor was packed with nanofiber fabric catalysts that were prepared by electrospinning a viscous solution of 0.60 g polyvinylpyrrolidone (PVP, 1.3 MDa), 9.5 g water-ethanol (~1:1 wt ratio) into which a total metal precursors of single and mixed metal oxides of different ratios were dissolved. 5-20 mg of this fabric was loosely packed into a 6 mm diameter quartz tube and sandwiched between 20 mg quartz wool plugs Figure 1.2-6. The bulk density and void fraction of the bed were determined to be about 0.15-0.3 g/cm<sup>3</sup> and ~0.94, for bed length of 5-10 mm, respectively.

#### 2.2.3.1. Performance Analysis Set-up

For the initial fiber performance analysis and screening experiments, a library of potential OCM catalytic materials were synthesized and systematically tested. The fibers were packed inside quartz tube reactor as shown in Figure 1.2-6. The feed gas flow rate and composition were set

using MFCs. As shown Figure 1.2-7 the quartz reactors were placed inside a cylindrical tubular furnace to preheat the feed gases and the furnace temperature is controlled to reach the desired ignition temperature.

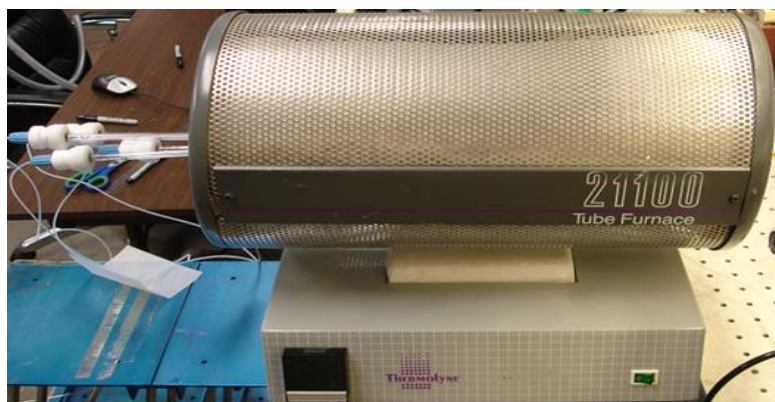


**Figure 1.2-7.** Thermolyne Tube Furnace with quartz reactors inside

Total gas flow rates of 80-320 cm<sup>3</sup>/min at STP, and feed temperatures of 300-650 °C, depending on the experiment were examined. Gas compositions were maintained between 75-87.5 mol% CH<sub>4</sub> and 12.5-25 mol% O<sub>2</sub>. In these experiments, the GC line were directly placed at the reactor exit for direct sampling followed by the gas analysis. The experiments were performed at 1 atm.

#### *2.2.3.2. Axial Temperature Profiles*

To obtain the axial temperature profiles, we examine feed gas flow rates of 80-320 cm<sup>3</sup>/min, catalyst weights of 5-20 mg and feed temperatures of 300-620 °C (corresponding to the ignition temperatures). Gas compositions were maintained between 75-87.5 mol% CH<sub>4</sub> and 12.5-25 mol% O<sub>2</sub>. Reaction products were sampled by a small glass lined tubing (water trap) and analyzed by on-line gas chromatography. A 0.25 mm diameter thermocouple is inserted tightly into a quartz capillary and placed inside the tube near the catalytic zone. The position of this thermocouple is changed incrementally using a micro-translation device (Figure 1.2-8) to quantify the axial temperature profiles during OCM catalysis for the various flow rates, feed temperatures

and feed compositions examined. The catalyst weight of 20 mg was used for experiments in which a temperature profile was measured since this weight gives sufficient depth (~1.4 cm) to the reactor to allow for precise determination of the temperature profiles along the catalyst bed. End of the reactor performance analyses were performed in separate experiments with essentially identical setups as described in section 2.2.3.1, without the use of a thermocouple probe since it was found to cause minor disturbances in the catalyst.

### *2.2.3.3. Spatial Reactor Profiles*

The complete set-up is as shown in Figure 1.2-8 . Twenty mg of this fabric was loosely packed into a 6 mm diameter quartz tube and sandwiched between two 20 mg quartz wool plugs. The bulk density and void fraction of the bed were determined to be about 0.3 g/cm<sup>3</sup> and 0.94, respectively. The reactor was placed inside a cylindrical tubular furnace to preheat the feed gases. The total flow of reactant gases was maintained at 160 cm<sup>3</sup>/min at STP in all the experiments using electronic mass flow controllers (MFC, MKS Billerica, MA). This flow rate corresponds to a nominal space time of about 66 ms. The experiments were performed at 1 atm.

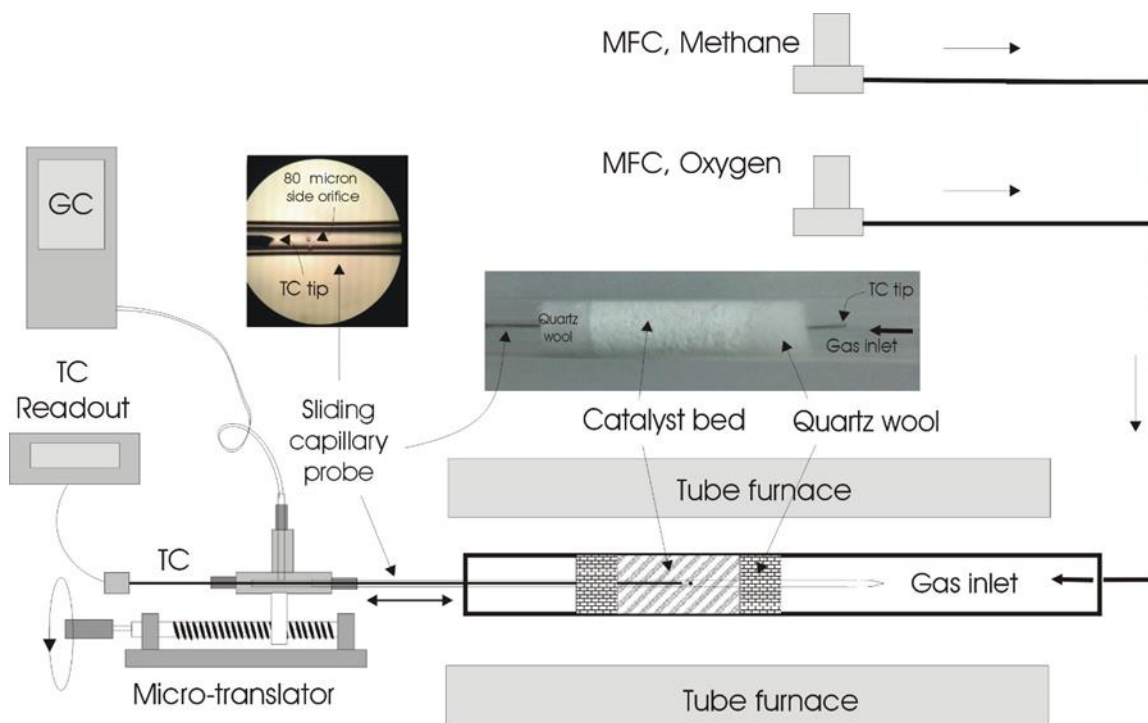


**Figure 1.2-8.** The reactor system used to acquire spatial temperature and concentration profiles

Gas sampling was accomplished by centrally inserting a conically tapered and closed end quartz capillary tube (800  $\mu\text{m}$  OD x 400  $\mu\text{m}$  ID, Friedrich and Dimock, NJ) into the packed bed followed by gas analysis by on line gas chromatography. The capillary had dual 80  $\mu\text{m}$  orifices laser drilled at 90° on its side to withdraw gases from within the bed (see insert Fig. 1.2-8). The location of the sampling orifice and the overall length of the probe was designed such that the capillary tip remained well outside packed bed at any sampling position to avoid gas bypass. The capillary probe withdrew gas samples at a rate less than 5  $\text{cm}^3/\text{min}$  at STP, thus minimally disturbing the flow within the reactor (160  $\text{cm}^3/\text{min}$  at STP). Temperature measurements were performed by placing a thin (250  $\mu\text{m}$  diameter) K-type thermocouple inside the capillary probe in the absence of gas withdrawal. The tip of the thermocouple was positioned at the sampling orifice. Temperature and concentration profiles were obtained by moving the capillary (with and without the thermocouple) in the axial direction using a micro-positioning device (Velmex, Bloomfield,



NY). Positional accuracy associated with the placement of the capillary probe within the reactor is estimated to be  $\pm 0.25$  mm. Consequently, a similar uncertainty should also exist between the temperature and concentration profiles.

#### 2.2.4. Dual-bed Reactor

Experiments were performed using a dual-fixed-bed tubular reactor system as shown in Figure 1.2-9. The reactor was sequentially packed with  $\text{La}_2\text{O}_3\text{-CeO}_2$  nanofiber fabric catalysts that were prepared by electrospinning a viscous solution of 0.60 g polyvinylpyrrolidone (PVP, 1.3 MDa), 9.5 g water-ethanol (~1:1 wt ratio) into which a total of 0.35 g metal precursor, as  $\text{La}(\text{NO}_3)_3 \cdot 6\text{H}_2\text{O}$  and  $\text{Ce}(\text{NO}_3)_3 \cdot 6\text{H}_2\text{O}$  were dissolved having a La/Ce weight ratio of 3 (identical fibers used for the single-bed experiment).

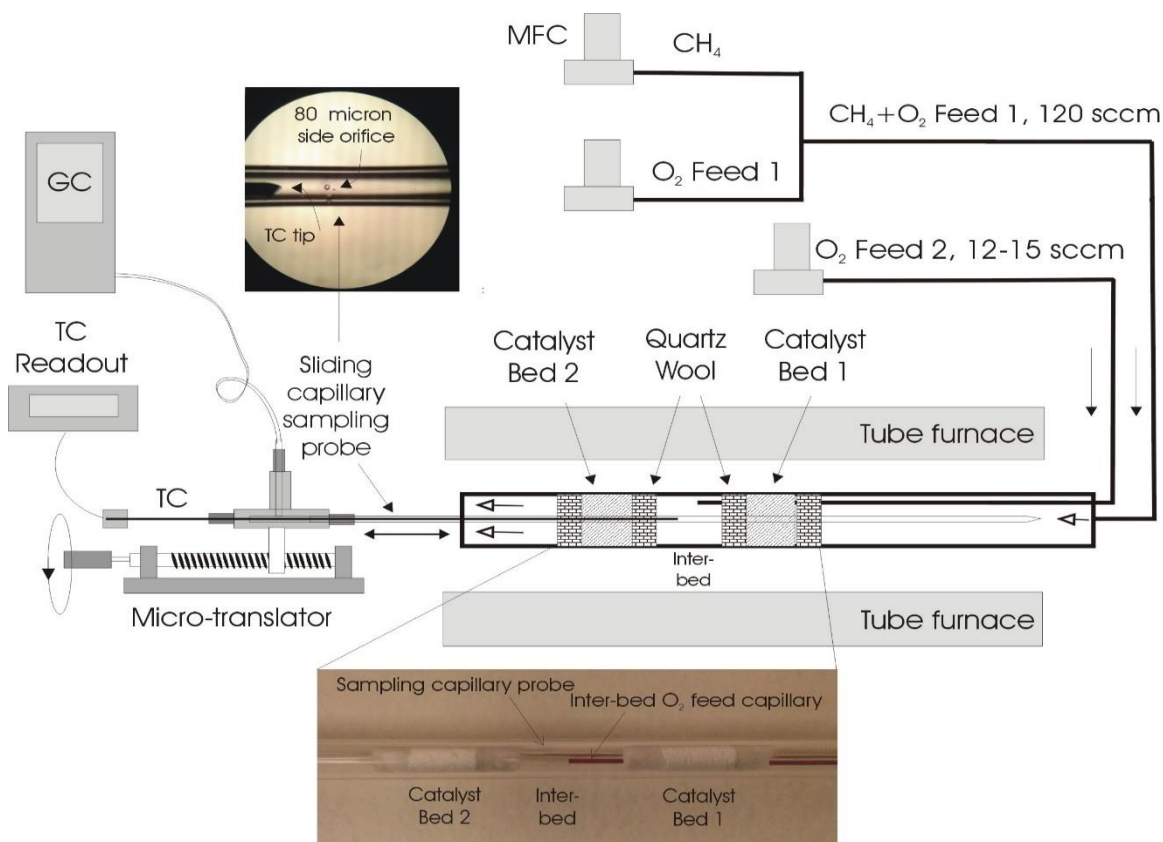


**Figure 1.2-9.** The dual-bed reactor system and the complement set-up used to acquire spatial temperature and concentration profiles

As shown in the bottom section of Figure 1.2-9, two sections each with 20 mg of fabric catalysts was loosely packed into a 6 mm diameter quartz tube (~10mm bed depth) and sandwiched between two 20 mg quartz wool plugs (~5 mm bed depth). Inter-bed spacing was about 15 mm long. The dual-bed reactor was placed inside a cylindrical tubular furnace to preheat the feed gases. In all experiments, the flow rate of the reactant gases to the first bed was maintained at 120 cm<sup>3</sup>/min at STP (sccm) using electronic mass flow controllers (MFC, MKS Billerica, MA). This flow rate corresponds to a nominal space time of about 60 ms per bed. The inter-stage O<sub>2</sub> was introduced at the middle of the inter-space, i.e. at about ~27-28 mm, using a quartz capillary feed tube (800 μm, Friedrich and Dimock, Millville, NJ) at a rate of 12-15 sccm. The experiments were performed at 1 atm.

Gas sampling was accomplished by centrally inserting a conically tapered and closed end quartz capillary tube into the packed beds followed by gas analysis by on line gas chromatography. The sampling capillary had four perpendicularly oriented 80 μm diameter orifices laser drilled on its side to withdraw gases from within the bed (see Figure 1.2-9). The location of the sampling orifice and the overall length of the probe were designed such that the capillary tip remained well outside both packed beds at any sampling position to avoid gas bypass within the beds. The sampling capillary probe withdrew gases at a rate less than 5 sccm, thus minimally perturbing the flow within the reactor (total flow ~120-135 sccm). This sampling rate corresponds to an average gas velocity of 50-100 cm/sec within the capillary (depends on the temperature), enabling the rapid removal of the gas samples from within the reactor. The fact that the measured concentration profiles remained flat, i.e. did not change with axial position within the quartz wool, the inter-stage section and reactor exits further supports the notion that reactions inside the sampling capillary were unimportant in our experiments. Temperature measurements were performed by placing a

thin (250  $\mu\text{m}$  diameter) K-type thermocouple inside the sampling capillary probe in the absence of gas withdrawal. The tip of the thermocouple was positioned at the sampling orifice. The possible presence of radial-temperature gradients was also explored by simultaneously placing multiple thermocouples at the same axial position but at different radial positions during the reaction. These measurements indicated maximum radial temperature differences in the 10-20  $^{\circ}\text{C}$  range at peak reactor temperatures of 800-1000  $^{\circ}\text{C}$ . Consequently, the treatment of the reactor as quasi 1-dimensional appears to be a reasonable assumption. Capillary sampling lines outside the reaction furnace as well as GC injection system were heated to about 100  $^{\circ}\text{C}$ , in order to prevent water condensation in the transfer lines. Water subsequently was condensed out using an ice-bath before GC analysis. Temperature and concentration profiles were obtained by moving the capillary (with and without the thermocouple) in the axial direction using a micro-positioning device (Velmex, Bloomfield, NY). Positional accuracy associated with the placement of the capillary probe within the reactor is estimated to be  $\pm 0.25$  mm. Similar uncertainty would also be expected to exist between the temperature and concentration profiles here as well.

## CHAPTER 1.3. Results and Discussions

Most of the results and discussions indicated in this section are adapted from our Laboratory work published in the following papers: “Oxidative Coupling of Methane by Nanofiber Catalysts” [36], “Oxidative coupling of methane with  $\text{La}_2\text{O}_3$ - $\text{CeO}_2$  nanofiber fabrics: A reaction engineering study” [38], “New insights into the oxidative coupling of methane from spatially resolved concentration and temperature profiles” [39], and “Spatial Concentration and Temperature Profiles in Dual-Packed-Bed Catalytic Reactors: Oxidative Coupling of Methane” [40] .

### 3.1. Characterization and Performance Analysis of Nanofibers

Our initial search for screening of the potentially high performance OCM catalysts lead to the discovery of  $\text{La}_2\text{O}_3$  nanofiber catalyst system doped with  $\text{CeO}_2$  [36]. This finding confirmed the past results reported in literature stating that the Rare-earth-metal (REM) oxides are among the most active catalysts for OCM [41], [42], [7].

#### *3.1.1. $\text{La}_2\text{O}_3$ - $\text{CeO}_2$ Nanofiber Catalyst System*

Initially, the performance of our  $\text{La}_2\text{O}_3$ - $\text{CeO}_2$  fabrics were compared to analogous powders reported in the literature, synthesized using co-precipitation [43], in terms of structure, selectivity, conversion, upstream gas temperature, gas throughput, and robustness of catalytic system under reaction conditions. Since nanofibers are produced as fabrics, they exhibit catalytic properties similar to monoliths are thus particularly suitable for high-throughput exothermic reaction schemes, such as. As evident from Figure 1.3-1 [38], the  $\text{La}_2\text{O}_3$ - $\text{CeO}_2$  nanofibers clearly exhibit significant differences from co-precipitated powders. First and foremost, nanofibers show remarkable uniformity in diameter (~70 nm) and dispersion, with a BET surface area of 20  $\text{m}^2/\text{g}$ .

This surface area is close to the geometric external surface area of 70 nm diameter solid fibers, thus suggesting that the fibers were non-porous, i.e. dense. Second, the fibers appear individually well exposed with little clustering, concomitant with the large and uniform inter-fiber space. These features provide rapid access to and from the active sites, which should be advantageous in improving the selectivity for labile products in partial oxidation reactions. In contrast, co-precipitated La-Ce powders (Figure 1.3-1-right) exhibit a high degree of agglomeration in which a significant fraction of  $\text{La}_2\text{O}_3\text{-CeO}_2$  remain inaccessible or are accessible only through crystal cracks or pores, concomitant with pore diffusion limitations and associated problems. The BET area of the powder was  $10 \text{ m}^2/\text{g}$ , suggesting low porosity.

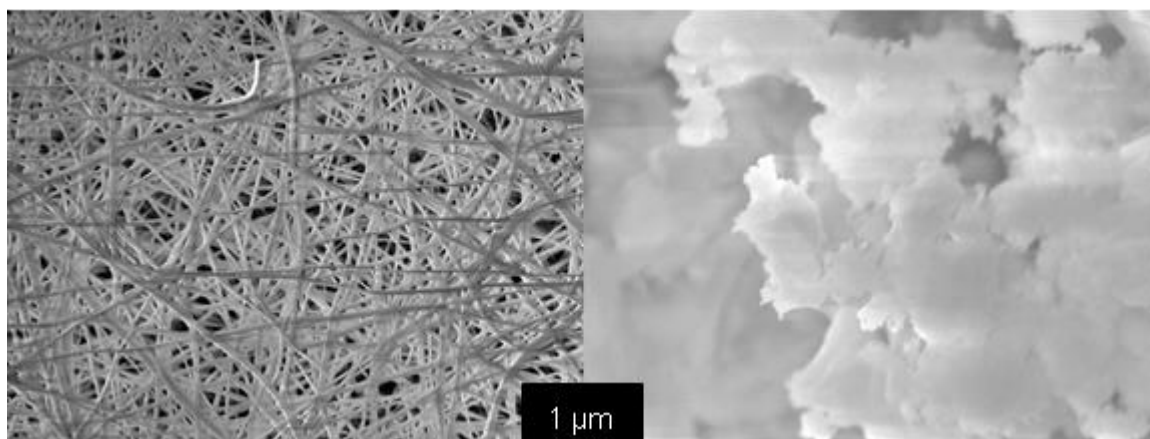


**Figure 1.3-1.** SEM Images of: A-Left: co-spun  $\text{La}_2\text{O}_3\text{-CeO}_2$  fibers (diameter  $\sim 70 \text{ nm}$ , BET area  $26 \text{ m}^2/\text{g}$ ); B-Right: co-precipitated  $\text{La}_2\text{O}_3\text{-CeO}_2$  powders (BET area  $10 \text{ m}^2/\text{g}$ ). Note: both images are at the same magnification of  $\times 13,000$

The  $\text{La}_2\text{O}_3\text{-CeO}_2$  fabrics at La/Ce ratio of about 15 were synthesized and tested. The feed gas flows at  $120 \text{ cm}^3/\text{min}$  with 8 mg of catalyst packed into the reactor, corresponding to a gas throughput of  $9.0 \times 10^5 \text{ cm}^3/\text{g-hr}$  or a contact time of 5-10 ms. The  $\text{CH}_4/\text{O}_2$  ratio is 7. For the experiments with the co-precipitated  $\text{La}_2\text{O}_3\text{-CeO}_2$  catalysts of Dedov et al., the gas throughput is  $4.4\text{-}4.8 \times 10^4 \text{ cm}^3/\text{g-hr}$  with a  $\text{CH}_4/\text{O}_2$  ratio that ranges between 5-7. As shown in Figure 1.3-2 [36], both the nanofiber fabrics and the co-precipitated powders exhibit very similar results for  $\text{C}_2+$

selectivity, CO<sub>x</sub> selectivity and CH<sub>4</sub> conversion. However, the fabrics are found to achieve this degree of performance at temperatures as low as 470 °C, or about 250-350 °C lower than the temperatures shown by Dedov et al. for their powders. Additionally, our fibers are able to achieve this performance at gas throughputs about 20-fold higher. Since pre-heating a reactor feed can incur significant energy costs, the methane activation temperatures accomplished by this work so far represent a significant step towards making OCM a viable process. Lower temperatures also help ameliorate materials issues, as even the highest quality steels may have durability problems at OCM temperatures previously reported in the literature. Furthermore, the ability to process such large volume rates of gas feed could improve process economics even further by allowing for the use of small reactors.

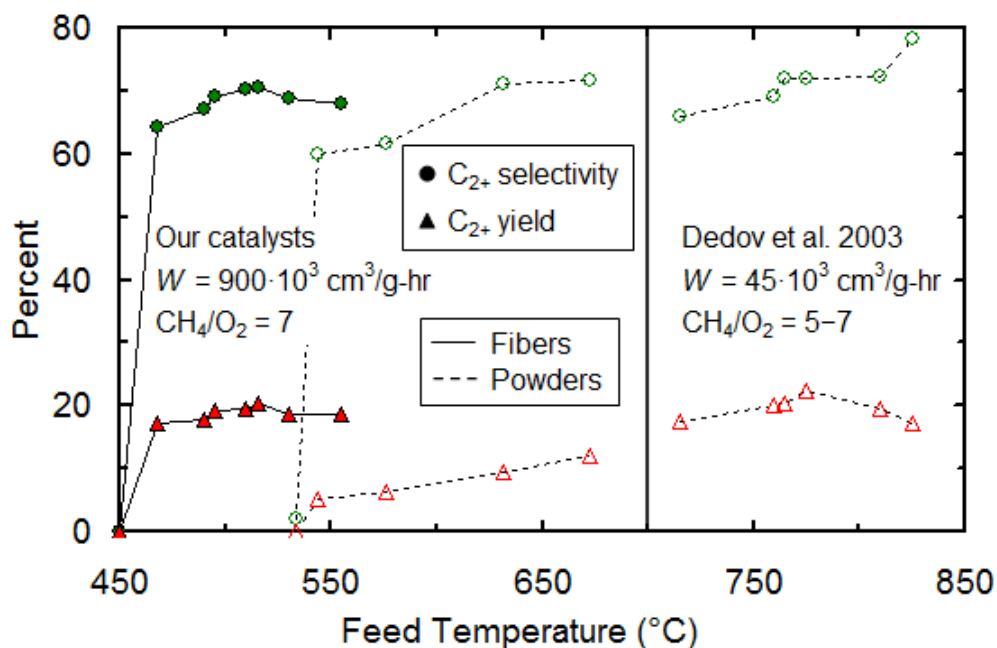


**Figure 1.3-2.** OCM performance of La<sub>2</sub>O<sub>3</sub>-CeO<sub>2</sub> catalytic system compared to analogous powders synthesized by Dedov et al.

In Figure 1.3-3, the XRD data for La<sub>2</sub>O<sub>3</sub>-CeO<sub>2</sub> nanofibers and powders (also La/Ce weight ratio of 15), both pre- and post OCM test conditions are presented (A,B and C,D), along with those

for individual  $\text{La}_2\text{O}_3$  (E) and  $\text{CeO}_2$  (F) fibers and powders. Several interesting features are revealed. First, both the  $\text{La}_2\text{O}_3$  fibers (Figure 1.3-3, E) and powders exhibit virtually identical mixed cubic (222 and 440 reflections) and hexagonal (100, 101, 102 reflections) structures [44]. Similarly, the same cubic (111, 200, 220)  $\text{CeO}_2$  phases were present in both fibers and powder [45]. However, the XRD spectrum of binary  $\text{La}_2\text{O}_3$ - $\text{CeO}_2$  nanofibers was remarkably less crystalline than  $\text{La}_2\text{O}_3$  and  $\text{CeO}_2$  fibers (Figure 1.3-3, B). This can possibly be attributed to incorporation of  $\text{La}^{+3}$  ions into the cubic lattice of  $\text{CeO}_2$  and partial reduction of ceria which is further discussed in next paragraph. Significant shortening and broadening of the  $\text{La}_2\text{O}_3$ - $\text{CeO}_2$  nanofiber peaks are also shown, indicating smaller mean crystallite dimensions compared to single metal oxide nanofibers.

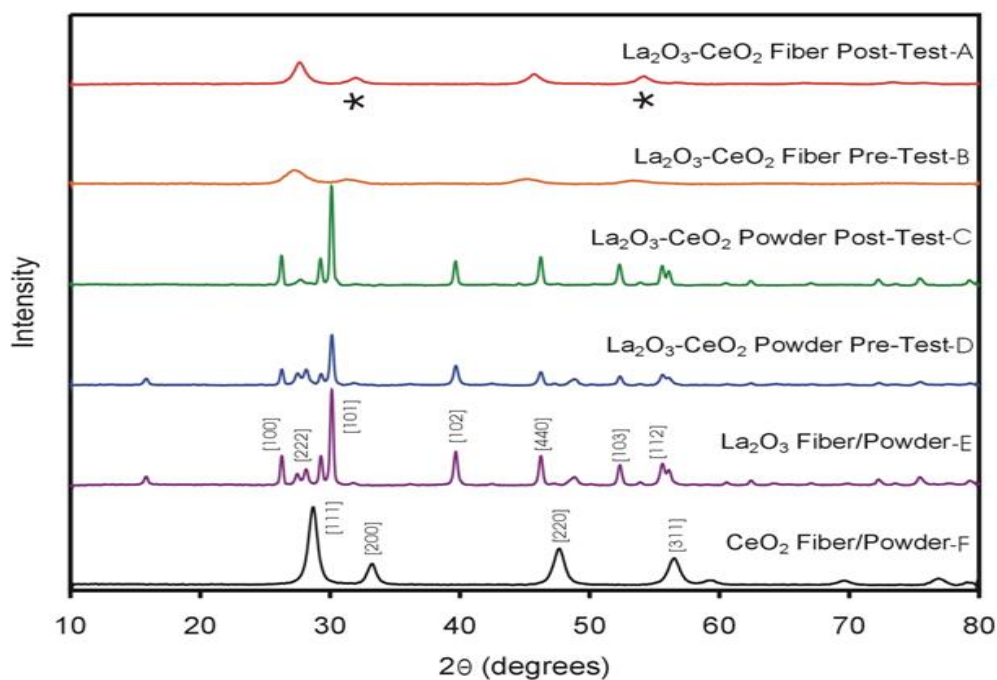


**Figure 1.3-3.** XRD of various  $\text{La}_2\text{O}_3$  and  $\text{CeO}_2$  nanofibers compared to co-precipitated powders

Furthermore,  $\text{La}_2\text{O}_3$  nanofiber catalyst system doped with  $\text{CeO}_2$  was further explored for La/Ce metal ratio. At total feed gas flow rate of 120  $\text{cm}^3/\text{min}$  with 8mg of catalyst and  $\text{CH}_4/\text{O}_2$  feed ratio of 4, As shown in Figure 1.3-4, the best result was obtained for 90-75% La doped with 10-25% Ce at  $\sim 70\%$  selectivity. Even though pure  $\text{La}_2\text{O}_3$  fibers exhibit relatively close

performance to that of the doped system at optimized La/Ce ratio, it requires higher feed gas temperature to reach ignition of the reaction. These clearly indicate some synergetic effect of using a binary system of La-Ce.

From results of the XRD (Figure 1.3-3) and  $C_{2+}$  selectivity curve (Figure 1.3-4) of the doped and undoped La nanofiber catalyst system, it is hypothesized that interaction of lanthanum with cerium on the surface may lead to the formation of  $Ce_2O_3$ . This shows that on one hand La promotes formation of  $Ce^{3+}$  and on the other hand extra La prevents Ce from being deep reduced. The charge transfer from lanthanum to ceria on the surface is facilitated and confirms the proposal of existing redox equilibrium ( $La^{2+}+Ce^{4+} \leftrightarrow La^{3+}+Ce^{3+}$ ) at some lanthanum-cerium ratios. Reduction of  $Ce^{4+}$  to  $Ce^{3+}$  is associated with formation of lattice oxygen vacancies in ceria and increase of oxygen storage capacity at the surface. This is critically important in enhancing the dissociation of methane and combination of bonds at active sites [12]. Furthermore, this confirms the simulation study of Palmer et al. that doping strontium into the  $La_2O_3$  surface via  $Sr^{2+}/La^{3+}$  exchange generates a surface oxygen site characteristic of an O- species (as noted earlier in section 1.3.1, possible candidate for methane activation), which may account for the enhanced OCM reactivity of doped  $La_2O_3$  catalysts when compared to the unpromoted system [12]. More dispersed Ce on the surface confirms the fact that more Ce are in contact with Lanthanum which helps in promotion of converting more  $Ce^{4+}$  to  $Ce^{3+}$  and which plays an important part in increasing the oxygen storage capacity of cerium and reactivity of the catalyst. As we increase the Ce concentration it is possible that more Ce on the surface is creating Ce cluster or more Ce are concentrated at the core of fiber which leads to less interaction of Ce with La on the surface and leads to less amount of  $Ce^{4+}$  conversion and therefore lower catalyst activity/selectivity. This is in agreement with the feature we see from Figure 1.3-4 and the reason for higher ignition temperature



of pure  $\text{La}_2\text{O}_3$  nanofiber catalysts. Further ensuing this hypothesis calls for supplementary characterization of the La-Ce nanofiber system by XPS (X-ray photoelectron spectroscopy), AES (Auger electron spectroscopy), TEM (Transmission electron microscopy) and other characterization methods to enable examination of the cross-section of the fibers to better explain these features.

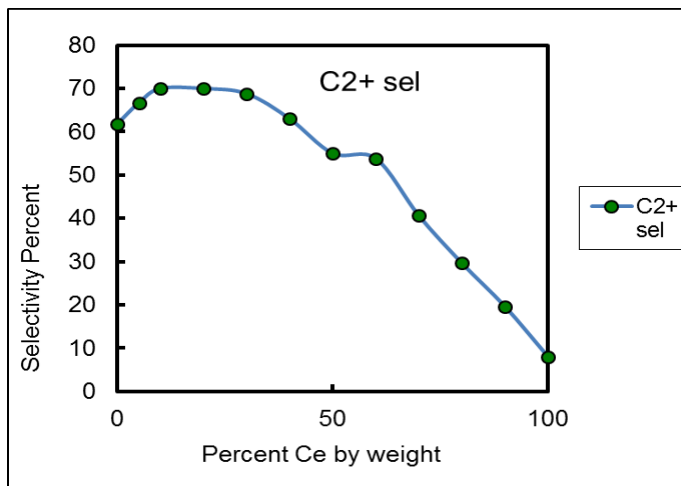


**Figure 1.3-4.**  $\text{C}_{2+}$  Selectivity Curve for  $\text{La}_2\text{O}_3\text{-CeO}_2$  nanofiber catalyst system by addition of Ce as dopant

### 3.1.2. Operating Conditions of $\text{La}_2\text{O}_3\text{-CeO}_2$ Nanofiber

In this section, the effects of changes in various operating conditions were explored on the performance of an oxidative coupling of methane (OCM) atmospheric pressure fixed bed reactor comprising  $\text{La}_2\text{O}_3\text{-CeO}_2$  nanofiber fabric catalysts at La/Ce weight ratio of 3 (refer to section 2.2.3 for synthesis of fiber). Additionally, in situ reactor temperature profiles were measured. Reactor temperature profiles as well as reactor exit conversion and product selectivities are presented as a function of feed temperature, feed flow rate and composition.

#### 3.1.2.1. Feed Temperature Hysteresis

In Figure 1.3-5, the axial temperature profiles are presented for a  $\text{CH}_4/\text{O}_2$  feed ratio of 5 and at a feed gas flow rate of  $F = 160$  standard cubic centimeters per minute (sccm) with  $m_{\text{cat}} = 20$

mg of catalyst packed into the bed at various feed gas temperatures  $T_f$ . Filled symbols represent the temperature profiles measured when the furnace temperature was stepwise heated up, while empty symbols were obtained during the stepwise cooling process. The temperature profile measurements were acquired while the reactant gases were flowing. Once the steady state temperature was reached ( $\sim 30$  min during heating and  $\sim 60$  min during cooling), the temperature profile was measured by axially moving the thermocouple. After data acquisition, the furnace temperature was readjusted to its new set point. As seen in Figure 1.3-5, the difference between the peak temperature in the catalytic zone and feed temperature  $T_f$  ranges between  $\sim 300$ - $400$  °C. This difference is at its largest at the lowest feed temperature  $T_f = 390$  °C. However, the location of the peak shifts downstream only during the cooling experiments, i.e. at values for  $T_f$  that are lower than the ignition temperature  $T_{ig}$ .

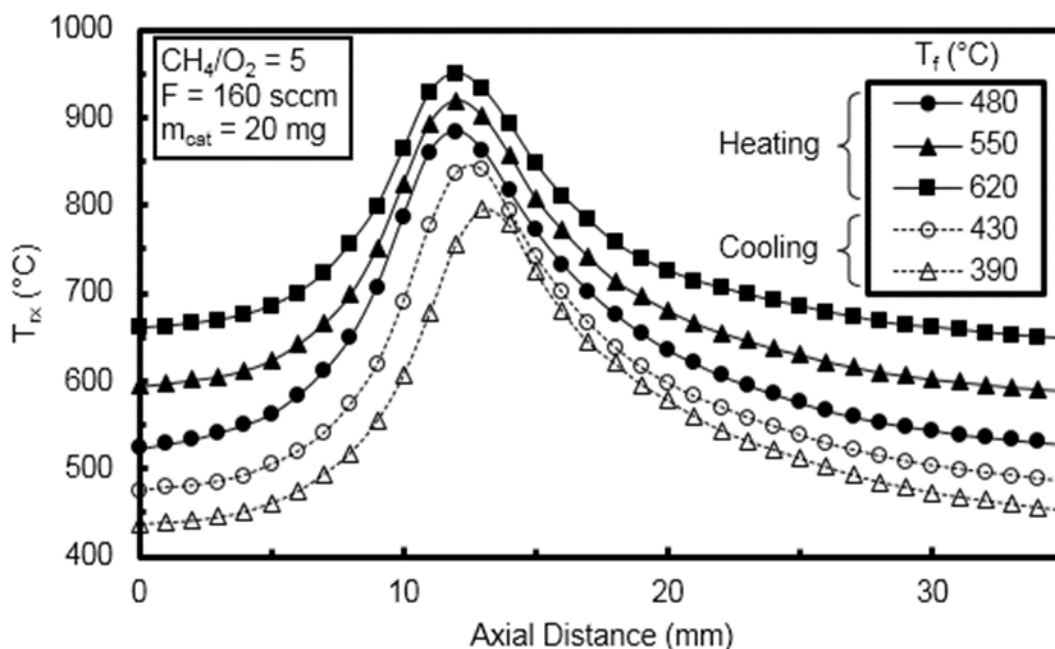


**Figure 1.3-5.** Reactor temperature  $T_{rx}$  as a function of axial distance

In Figure 1.3-6, the accompanying reactor exit  $CH_4$  conversions and  $C_{2+}$  selectivities are presented while Figure 1.3-7 shows the  $O_2$  conversions and  $C_2H_6/C_2H_4$  ratios, both as a function

of feed gas temperature  $T_f$  (where the arrows indicate the increasing or decreasing path for  $T_f$ ). As seen in Figure 1.3-5 and Figure 1.3-6, the onset of catalyst ignition was at 450 °C when increasing  $T_f$ , with a  $C_{2+}$  selectivity of 55% at 28%  $CH_4$  conversion. Oxygen was completely consumed and the  $C_2H_6/C_2H_4$  ratio was about 1 at the ignition point. For  $T_f > T_{ig}$ , the catalyst performance remains limited by the complete  $O_2$  conversion, yielding no change in the location of the peak bed temperature. As evident from Figure 1.3-5 and Figure 1.3-6, a hysteresis window was noted. On the decreasing  $T_f$  path, the  $La_2O_3-CeO_2$  nanofiber fabrics' high  $C_{2+}$  selectivity of 52-59% extended down to about 300 °C. Both the  $CH_4$  and  $O_2$  conversions steadily decreased and the  $C_2H_6/C_2H_4$  ratio increased with decreasing  $T_f$  below the ignition temperature. These results suggest that the catalyst peak temperature should also decrease and its spatial location should shift downstream with decreasing  $T_f$ . These features were indeed observed in the spatial temperature profiles presented in Figure 1.3-5.

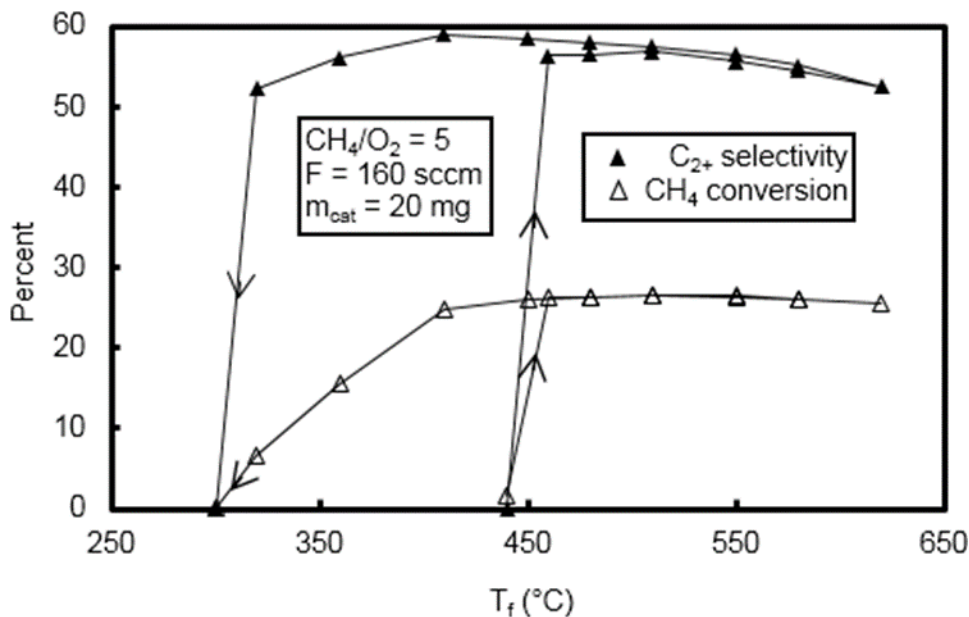


**Figure 1.3-6.**  $C_{2+}$  selectivity and  $CH_4$  conversion as a function of feed temperature  $T_f$

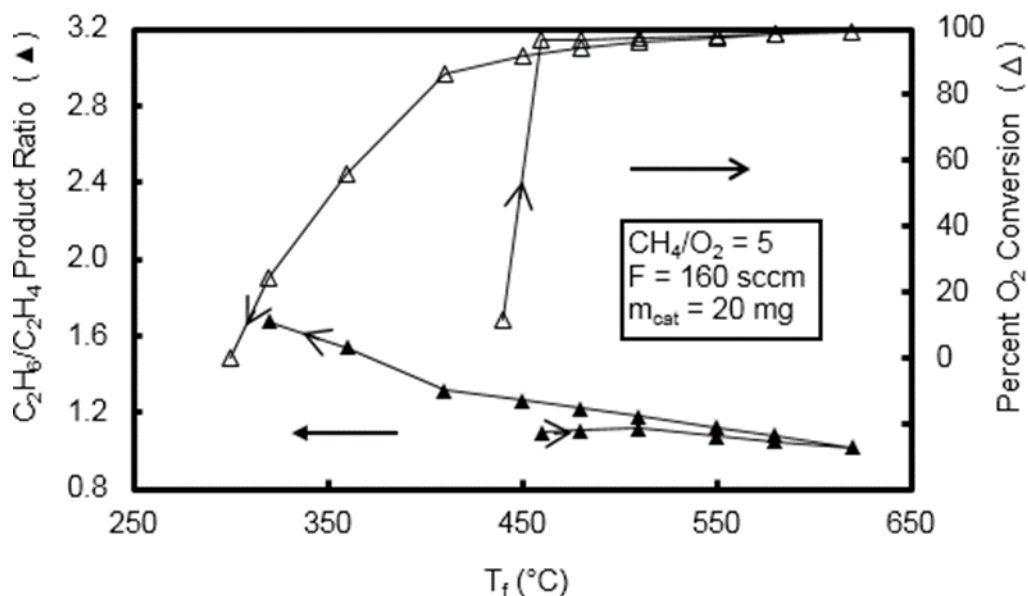


**Figure 1.3-7.** Ethane-to-ethylene product ratio and percent  $O_2$  conversion as a function of feed temperature  $T_f$

### 3.1.2.2. Effect of Feed Flow rate and $CH_4/O_2$ Ratio

In Figure 1.3-8, the effects of feed gas flow rate on the spatial temperature profiles are presented at a  $CH_4/O_2$  ratio of 5 and feed gas temperature of 570 °C. As evident from this figure, increasing feed gas flow rate dramatically increases the reactor temperature while slightly shifting the location of the maximum temperature. For example, at 80 sccm flow, the peak temperature is 825 °C at ~12 mm within the bed. In contrast, at 200 sccm, the peak temperature reached 960 °C at ~11 mm. These results clearly indicate that the rate of the OCM process under the experimental conditions investigated is also affected by mass transfer limitations [46]. For example, increased flow rates increase mass transfer coefficients and thus transport rates to the catalyst surface, thereby increasing the rates of the OCM reaction. The observation of the shift in peak temperature slightly upstream with increasing gas flow rate can readily be accounted for by the increased thermal conduction caused by the increased temperature gradient in the hot spot. An increase in the temperature gradient before the catalytic zone provides evidence of both this and of radiation originating from the catalyst. Additionally, there is competition between the increases in the

reaction rate from enhanced mass transfer, which would create a temperature rise earlier in the reactor, with axial convection pushing the reaction downstream. The overall net effect from these three factors appears to lead to the location of the temperature peak being relatively unchanged.

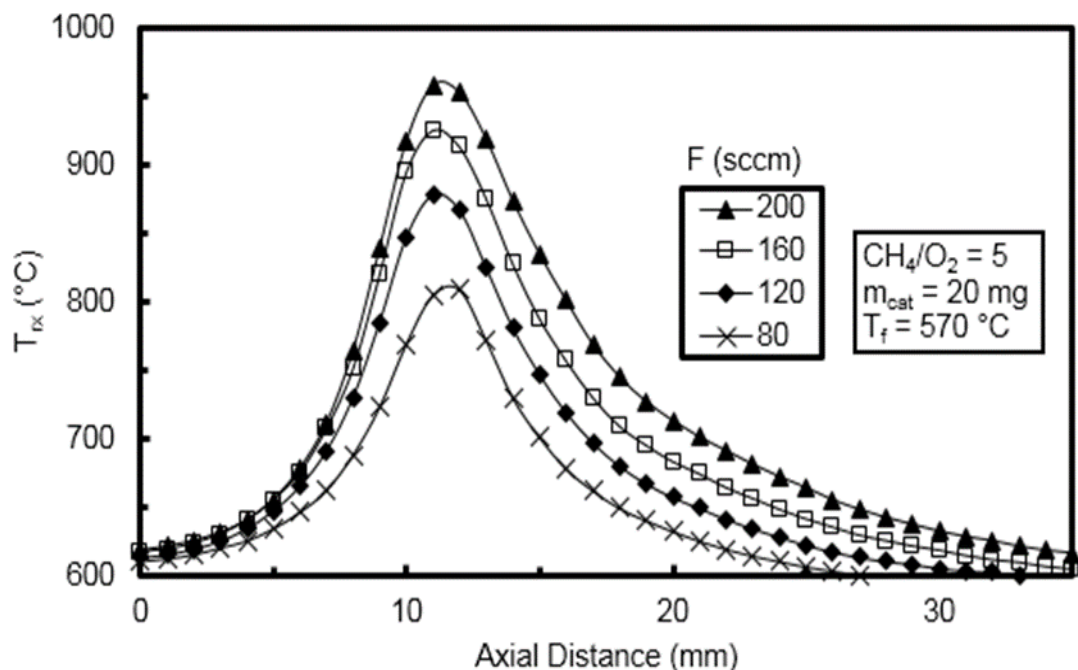


**Figure 1.3-8.** Reactor temperature  $T_{rx}$  as a function of axial distance in the catalytic zone for various flow rates

As expected, the effect of  $\text{CH}_4/\text{O}_2$  ratio on reactor temperature is also significant within the experimental conditions investigated (Figure 1.3-9). As evident from Figure 1.3-9, decreasing the  $\text{CH}_4/\text{O}_2$  ratio from 7 to 4 increases the peak reactor temperature from 850 °C to 980 °C, while shifting the peak location from 12 mm to 10.8 mm. The increase in reactor temperature is the expected consequence of decreased methane dilution in the feed gas based on the overall OCM as well as combustion reaction stoichiometries.

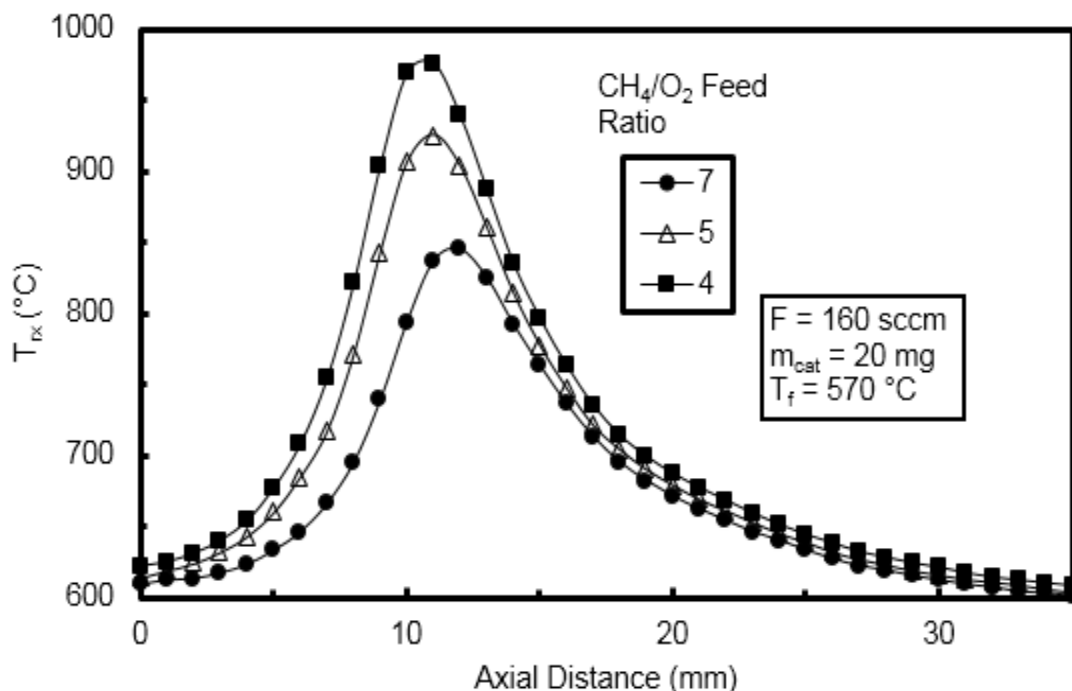


**Figure 1.3-9.** Reactor temperature  $T_{rx}$  as a function of axial distance in the catalytic zone for various feed  $CH_4/O_2$  ratios

In Figure 1.3-10 and Figure 1.3-11,  $CH_4$  and  $O_2$  conversions,  $C_{2+}$  selectivities and  $C_2H_6/C_2H_4$  ratios are presented as a function of feed gas flow rate and  $CH_4/O_2$  ratio at a feed gas temperature of  $T_f = 570$  °C. An inspection of Figure 1.3-10 reveals several interesting trends. First, increasing gas flow rates and decreasing  $CH_4/O_2$  ratios have an adverse effect on  $C_{2+}$  selectivity, which reaches as high as 70% at a  $CH_4/O_2$  feed ratio of 7 and feed flow rate of  $F = 160$  sccm. The only exception to this trend is seen at the  $CH_4/O_2$  ratio of 7 at low gas flow rates, which can be attributed to greater mass transfer limitations. Additionally, the depth of the catalyst bed could be a significant factor in creating low  $C_{2+}$  selectivities for low flow rates for the high  $CH_4/O_2$  ratio. In a previous work when using an 8 mg  $La_2O_3-CeO_2$  bed, a  $T_f$  hysteresis plot similar to that of Figure 1.3-6 here was constructed. It was found that for a  $CH_4/O_2$  feed ratio of 4 that  $C_{2+}$  selectivities reached their highest at the quench temperature of  $T_f = 230$  °C. In Fig. 5 at the quench temperature,

the  $C_{2+}$  selectivity is at one of its lowest observed values. A key difference between these two experiments is the bed depth, which could help explain why  $C_{2+}$  selectivities are sacrificed at very low flow rates at  $CH_4/O_2 = 7$ . Over our OCM catalyst, we have previously shown that  $O_2$  conversion nearly halts about one-third of the distance through a deep 20 mg  $La_2O_3-CeO_2$  bed, well before the metal oxide bed ends. This would not necessarily happen within a shallow 5 mg bed. Hence, gasses from an OCM reactor with a deep bed are exposed to additional catalyst at low temperatures, which may provide a thermodynamic driving force for adsorption that could lead to the destruction of  $C_{2+}$  products. At the highest  $CH_4/O_2$  feed ratio of 7 examined here, this is more likely to happen as the total amount of energy created is at its lowest, entailing the effluent gas that contacts the remaining catalyst will be colder and more apt to see its  $C_{2+}$  products experience a driving force for adsorption. The low flow rates seen in Figure 1.3-10 could provide the contact time necessary for the adsorption to occur.

Second, methane conversions consistently increase with decreasing  $CH_4/O_2$  ratio as a consequence of increased bed temperature by decreased methane dilution, reaching as high as 33% at a  $CH_4/O_2$  feed ratio of 4 and the lowest feed rate examined of  $F = 80$  sccm. Third, the effect of gas flow rates on methane conversions is complex. Methane conversion decreases with increasing gas flow rate for  $CH_4/O_2$  ratios of 4 and 5, but the reverse trend is observed for 7. For the  $CH_4/O_2$  ratios of 4 and 5 decreases in  $CH_4$  conversions with increase in gas flow rate can readily be accounted for by the decreases in contact/reaction times since under these conditions the catalyst is at a sufficiently high temperature. Also,  $CO_x$  selectivities tend to naturally be higher at larger flow rates due to transport and mechanistic reasons. Since pathways that produce  $CO_x$  consume more  $O_2$ , less  $O_2$  is available to convert  $CH_4$ , thus resulting in a decrease the  $CH_4$  conversion. From Figure 1.3-11, the variation in oxygen conversion with respect to flow rate is far less dramatic than

for methane conversion, supporting the rationale behind rising  $\text{CO}_x$  selectivities with flow rates being the driving factor for falling  $\text{CH}_4$  conversions as opposed to the contact time. For the  $\text{CH}_4/\text{O}_2$  ratio of 7 at 80 sccm, the catalyst temperature evidently is not hot enough resulting in increase in methane conversion slightly with increase in gas flow rate. This result is also consistent with the increased selectivity observed with increased gas flow rates noted above.

Third,  $\text{O}_2$  conversions uniformly increased with increasing gas flow and leveled off at higher flow rates for all  $\text{CH}_4/\text{O}_2$  ratios (Figure 1.3-11). Interestingly,  $\text{O}_2$  conversions leveled off earlier and to a slightly lower level at the  $\text{CH}_4/\text{O}_2$  ratio of 7. Fourth,  $\text{C}_2\text{H}_6/\text{C}_2\text{H}_4$  ratios exhibited trends that consistently decreased with increasing gas flow rates and decreasing  $\text{CH}_4/\text{O}_2$  ratios. The  $\text{C}_2\text{H}_6/\text{C}_2\text{H}_4$  ratios were significantly higher (i.e. 1.3-1.6) at the  $\text{CH}_4/\text{O}_2$  ratio of 7. For the  $\text{CH}_4/\text{O}_2$  ratio of 4, the  $\text{C}_2\text{H}_6/\text{C}_2\text{H}_4$  ratio decreased from 1.15 at 80 sccm to 0.95 at 320 sccm.

As mentioned previously, possible reasons for the counterintuitive trends for selectivity in Figure 1.3-10 are likely due to transport or mechanistic effects. Carbon dioxide, a side product dealt with in abundance, has been documented as a catalyst poison and has strong binding affinity for highly basic materials [47]. Higher flow rates may enhance the mass transfer of  $\text{CO}_2$ , created at or near the catalyst's surface, away from the  $\text{La}_2\text{O}_3\text{-CeO}_2$  fabric, potentially freeing up sites for catalysis. The catalyst clearly becomes more active at some of the higher flow rates used; hence, the desorption of  $\text{CO}_2$ , the heaviest of the major compounds seen, facilitated by larger mass transfer coefficients at higher Reynolds numbers, could be a significant factor. An additional factor related to mass transfer could be the degree of turbulence facilitating greater mixing of compounds and transport of all species between the gas and catalyst, which could help explain the increasing level of  $\text{CO}_x$  production for very large flow rates. A possible specific scenario related to rising turbulence and mass transfer is the increased rate of adsorption of  $\text{O}_2$  onto the catalyst. It is known



that larger  $O_2$  feed concentrations drive selectivity away from  $C_{2+}$  compounds and towards  $CO_x$ . Greater mixing in the reactor could likewise increase local  $O_2$  concentrations near the catalyst and thus result in a similar phenomenon in which the catalytic production of  $CO_x$  becomes favored. This could also explain the larger  $C_2H_4/C_2H_6$  ratios with increasing flow rates as collisions of  $C_2H_6$  with the catalyst would be enhanced.

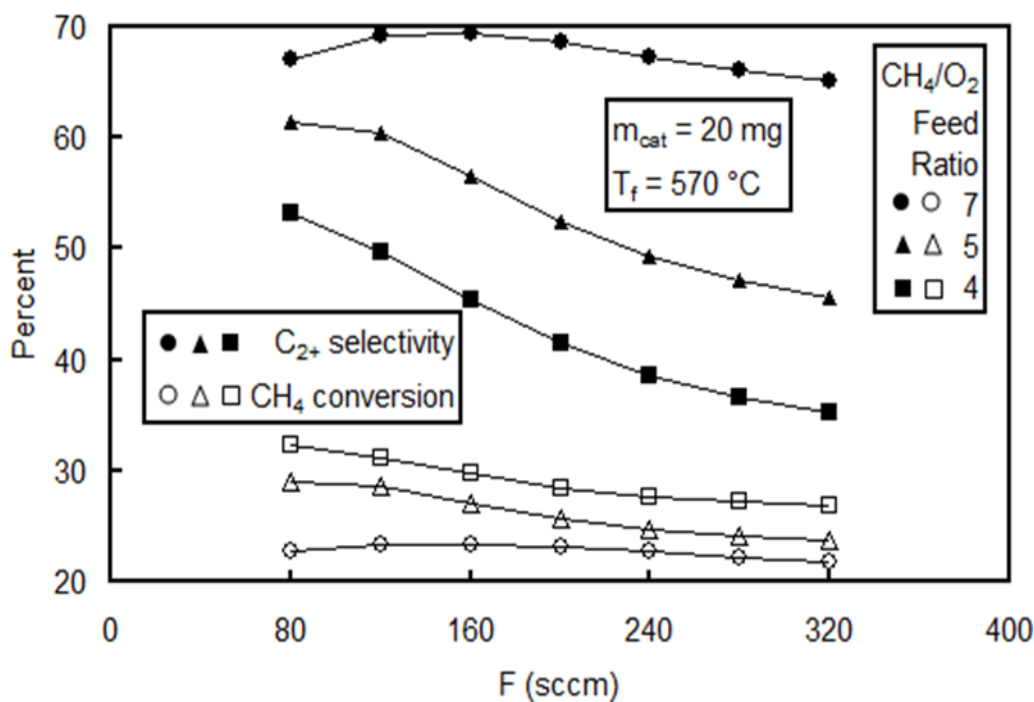


**Figure 1.3-10.**  $C_{2+}$  selectivity and  $CH_4$  conversion as a function of flow rate and  $CH_4/O_2$  feed ratio

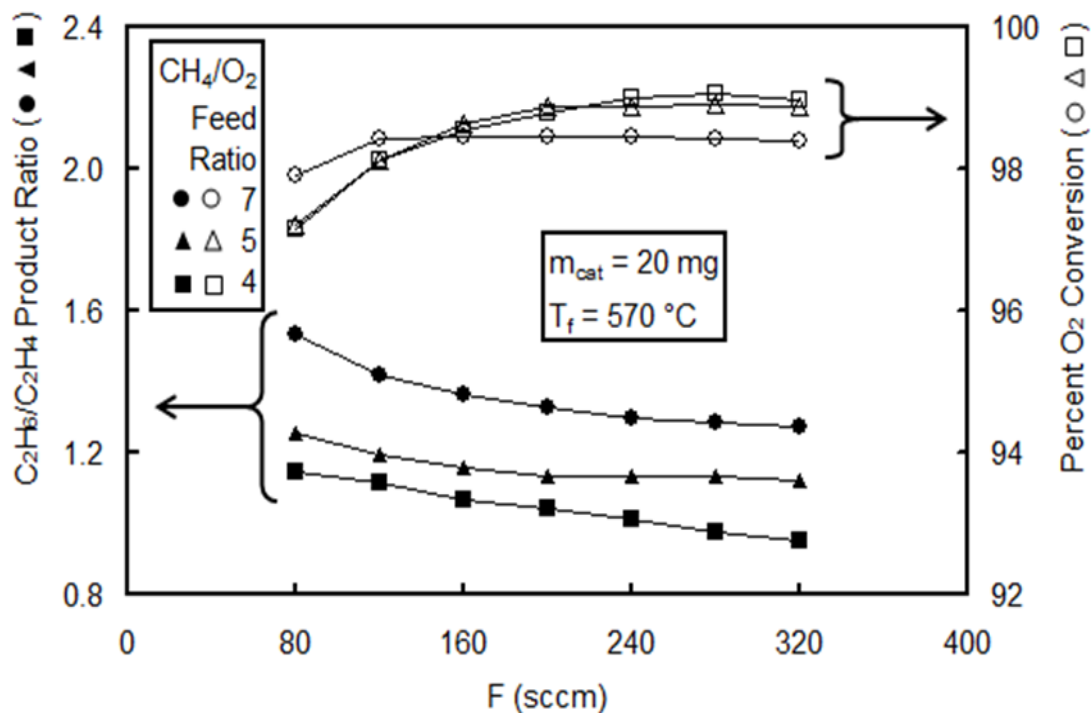


**Figure 1.3-11.** Ethane-to-ethylene product ratio (left axis, filled markers) and percent  $O_2$  conversion (right axis, hollow markers) as a function of flow rate and  $CH_4/O_2$  feed ratio

### 3.1.2.3. Effect of Bed Depth and Space Velocity

Experiments were also performed using reactor beds having different packing weights in order to better assess the relative importance of transport limitations relative to surface reactions. For this, three different packed bed weights of 5, 10 and 20 mg are investigated. In Figure 1.3-12 and Figure 1.3-13,  $CH_4$  and  $O_2$  conversions,  $C_{2+}$  selectivities and  $C_2H_6/C_2H_4$  ratios are shown as a function of space velocity, i.e. feed gas flow rate/catalyst weight, at  $CH_4/O_2$  ratio of 5 and at 570 °C feed gas temperature. An inspection of Figure 1.3-12 reveals several trends. First, both the  $C_{2+}$  selectivities and methane conversions almost uniformly decreased with space velocity for all the three beds considered. Second, methane conversions were similar (~24-29%) for all the beds at similar space velocities. In contrast,  $C_{2+}$  selectivities were dramatically different, with the smaller packed bed reactor performing the best. For example, at the 15 sccm/mg space velocity, the  $C_{2+}$

selectivities were 64%, 55% and 45%, for the 5, 10 and 20 mg catalyst bed reactors, respectively. These results clearly indicate that deeper bed reactors may be detrimental in OCM as they lead to the subsequent destruction of  $C_{2+}$  products once formed in the early part of the bed. Consequently, shallow bed reactors are desirable to maximize  $C_{2+}$  selectivities.

From Figure 1.3-13, it can be seen that  $O_2$  conversions in the shallower 5 mg bed were consistently lower at 85-93% than others both of which exhibited near complete oxygen conversions (>95%). These results are consistent with the higher  $C_{2+}$  selectivity of the 5 mg bed with its similar methane conversion (Figure 1.3-12) and the lower  $C_{2+}$  selectivities of deeper beds. In other words, the 5 mg bed utilizes the reactants more efficiently towards OCM products while the other, i.e. deeper, beds leads to the combustion of  $C_{2+}$  products.

The trends exhibited by the  $C_2H_6/C_2H_4$  ratios were all similar, decreasing with increasing space velocity as a result of increasing reactor temperatures. However, unlike  $C_{2+}$  selectivities, the deeper bed reactors were more beneficial for ethylene production. For example, at space velocity of 20 sccm/mg, the  $C_2H_6/C_2H_4$  ratios were 1.3 and 1.05 for the 5 mg and 10 mg beds, respectively. This appears to be due to increased rates of surface mediated ethane dehydrogenation through the deeper catalyst bed. If gas phase dehydrogenation processes were responsible, then the  $C_2H_6/C_2H_4$  ratios would have been similar. Such a lag is expected since  $C_2H_4$  is understood (from basic OCM mechanism Equations (1.1-8)-(1.1-11)) to be produced by the sequential catalytic dehydrogenation of  $C_2H_6$ .

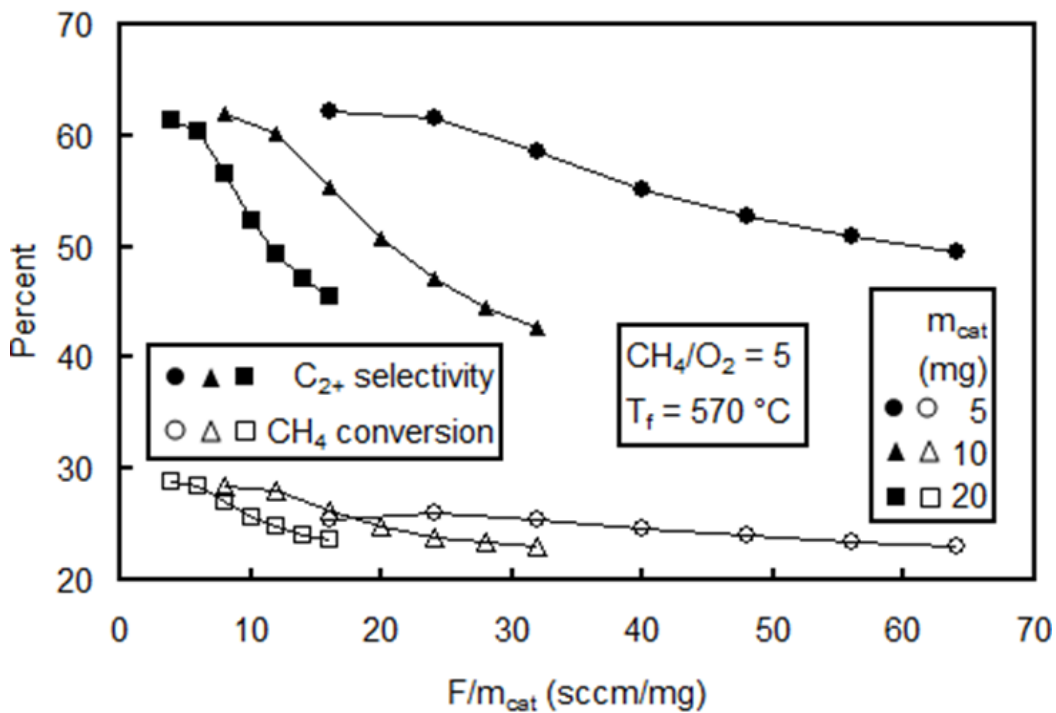


**Figure 1.3-12.**  $C_{2+}$  selectivity and  $CH_4$  conversion as a function of space velocity  $F/m_{cat}$  and catalyst weight  $m_{cat}$

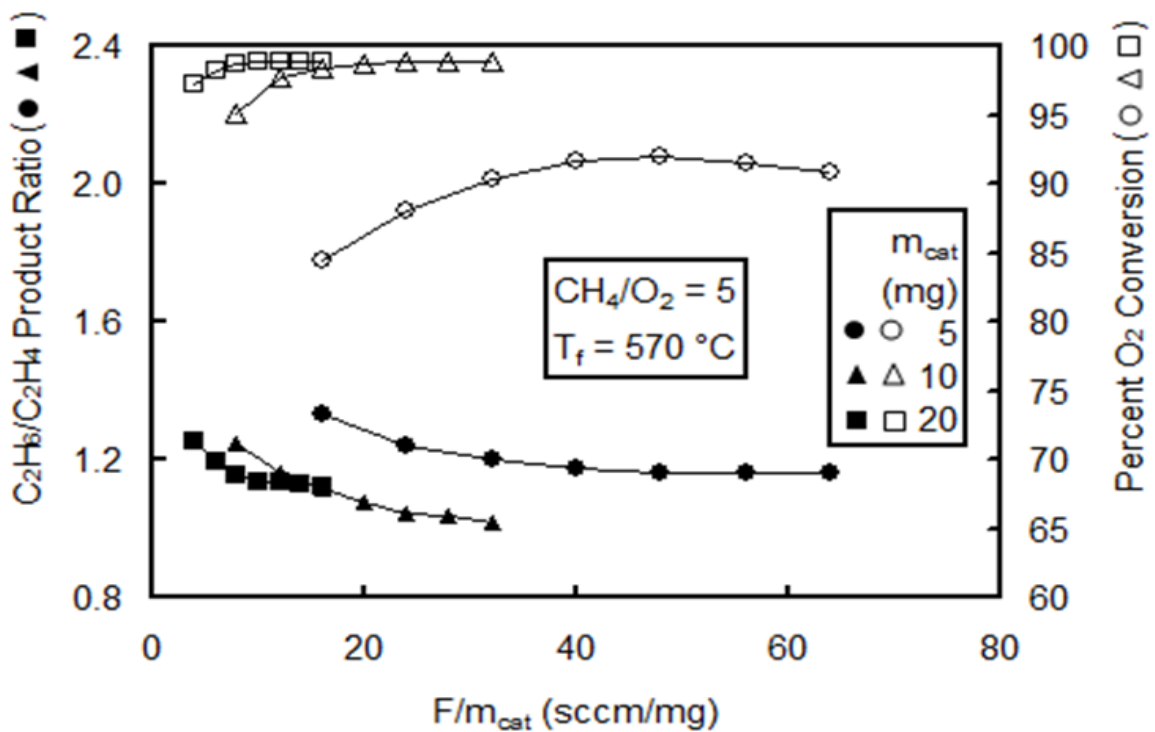


**Figure 1.3-13.** Ethane-to-ethylene product ratio and percent  $O_2$  conversion as a function of space velocity  $F/m_{cat}$  and catalyst weight  $m_{cat}$

### 3.1.2.4. Time on Stream

In Figure 1.3-14, the time on stream performance of the  $\text{La}_2\text{O}_3\text{-CeO}_2$  nanofiber fabric catalyst is presented for over a 10 hr continuous operation. The experimental conditions were: feed gas flow rate 80 sccm, 20 mg catalyst  $\text{CH}_4/\text{O}_2$  ratio of 5, feed temperature  $570^\circ\text{C}$ . As evident from this Figure, the  $\text{La}_2\text{O}_3\text{-CeO}_2$  exhibits an excellent performance, showing no deterioration in activity and selectivity, rendering it a promising practical OCM catalyst.

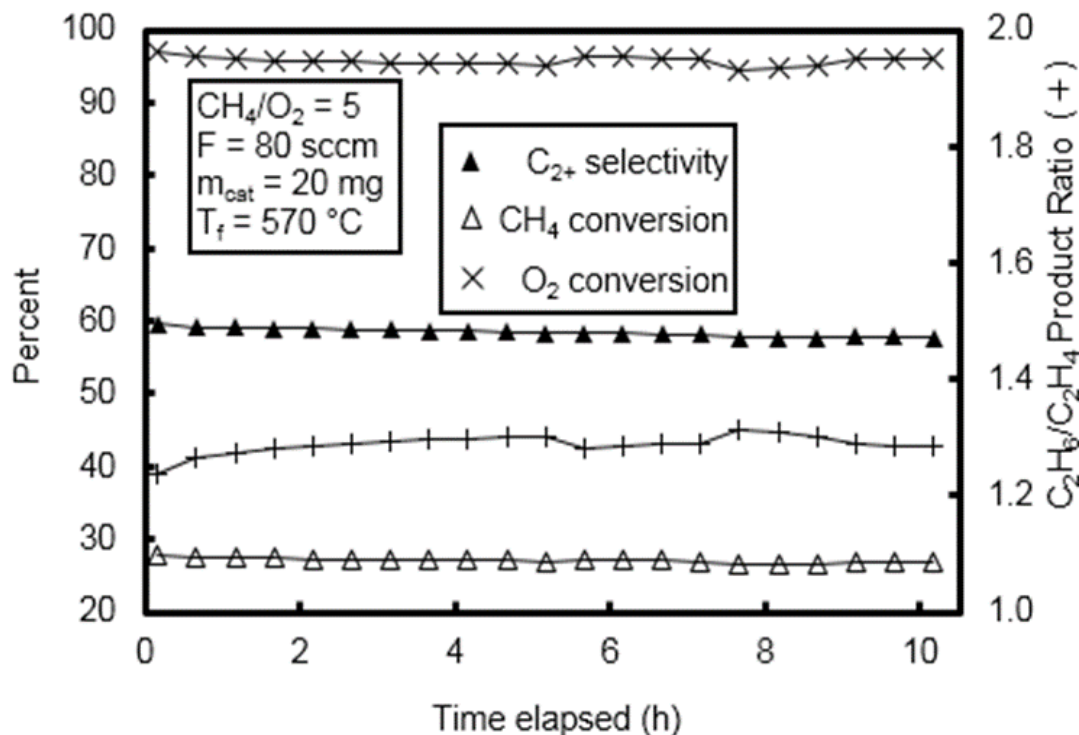


Figure 1.3-14. Time on stream

### 3.2. Spatial Concentration and Temperature Profiles

We believe that in order to make further improvement in oxidative coupling of methane (OCM) and other promising partial oxidation reactions, e.g. propylene epoxidation (PE) and partial oxidation of methane (POM), progress has to be made to develop and validate a comprehensive detailed chemical kinetic mechanisms (DCKM) for these processes. DCKMs comprise a comprehensive description of chemical transformations in terms of *irreducible* chemical events or *elementary reactions* for which independent rate coefficient parameters, frequently expressed in the form  $k=AT^n\exp(-E/RT)$ , are available from direct measurements or estimated from theoretical considerations, e.g. density functional theory (DFT) or kinetics descriptors. Once developed, DCKM can be combined with transport models to simulate the behavior of reactors. Therefore, DCKMs represent numerical tools of exceptional generality and broad utility that not only correlate available data but also predict the behavior of complex reaction systems under a very broad range of conditions, including conditions under which the acquisition of experimental data may be impractical, e.g. on the catalyst surface. With the availability of DCKMs, we will then be in a better position to identify improved OCM conditions, superior reactor configurations, and new leads for catalytic materials that are needed to exceed the 25% limit for C<sub>2+</sub> product yields. However, validation of DCKMs requires experimental data of high information content because of the presence of a large number of species participating in an even larger number of elementary reactions. Therefore, end-of-reactor measurements of concentrations, as it has been done commonly in the past, are inadequate for the validation of DCKM. Consequently, to remedy this issue, we developed a highly versatile micro-probe sampling technique for the *in-situ* acquisition of detailed species concentration profiles together with temperature profiles in catalytic reactors packed with nanofiber fabric catalysts. Here, in this section, the spatially resolved comprehensive

species concentrations and temperature profiles in a fixed-bed OCM reactor, for *nanofibers* of  $\text{La}_2\text{O}_3\text{-CeO}$ , which proven to be superior catalytic materials for the OCM reaction, are reported. A total of nine species were quantified:  $\text{CH}_4$ ,  $\text{O}_2$ ,  $\text{C}_2\text{H}_6$ ,  $\text{C}_2\text{H}_4$ ,  $\text{C}_3\text{H}_8/\text{C}_3\text{H}_6$  ( $\text{C}_3$ ),  $\text{H}_2$ ,  $\text{H}_2\text{O}$ ,  $\text{CO}$ , and  $\text{CO}_2$ . With the exception of the concentration of  $\text{H}_2\text{O}$ , which was calculated from oxygen atom balances, all of the species were quantified directly from GC measurements. Furthermore, based on our single-bed reactor findings, need for refinement of OCM mechanism is discussed and a novel reactor design (dual-bed reactor with interstage cooling) is put into practice.

### *3.2.1. Single-bed*

The single-bed experiments were conducted with total gas flow rate of 160 sccm (standard cc/min) at three different  $\text{CH}_4/\text{O}_2$  feed ratios of 7, 9, and 11. The feed temperature was set to reach ignition at each respective condition. Complete experimental set-up is as shown in Figure 1.2-8.

As seen in Figure 1.3-15, the experiment is done at  $\text{CH}_4/\text{O}_2$  ratio of 7. The feed temperature was at  $600\text{ }^\circ\text{C}$  and the peak reactor temperature, as shown by the temperature profile, reaches its peak of  $\sim 810\text{ }^\circ\text{C}$  at about 5 mm inside the catalyst bed (10 mm axial distance).

The species profiles in Figure 1.3-15 exhibit both confirmatory and new information. Most importantly, significant levels of  $\text{H}_2$  were produced very early in the catalytic zone, that is, prompt  $\text{H}_2$ ; a peak level of approximately 2.5 mol% was reached within 5 mm inside the catalyst bed (9 mm axial distance). This is an important discovery, an observation that was completely missed in all prior studies. As discussed earlier in Section 1.3.1, there is no mention of hydrogen production in the so far well-established OCM mechanism. This calls for further investigation and possible refinement of the current OCM mechanism, which will be discussed in detail, as part of the future work, in chapter 4 of this report. Prompt hydrogen formation, which is closely followed by

formation of CO<sub>2</sub> (peak at ~5 %) and CO (peak at ~1.8 %), is within the relatively low temperature zone of the reactor. Therefore, we suggest that hydrogen could be produced by surface reactions similar to those reported in the catalytic partial oxidation of methane to synthesize gas on Pt and Rh surfaces [48], [49]. Consequently, the following equations, Equation (1.3-1) - (1.3-7), may best describe the H<sub>2</sub> formation and could be incorporated into the OCM reaction mechanism for further investigation.



It is important to note that the measured concentration profiles for C<sub>2</sub>H<sub>6</sub> (~3.5 %) and H<sub>2</sub>O are consistent with the well-established OCM basic mechanism (discussed in Section 1.3.1). Moreover, as observed in Figure 1.3-15, the formation of C<sub>2</sub>H<sub>4</sub> (peak at ~2.5 %) exhibits significant lag relative to that of C<sub>2</sub>H<sub>6</sub>. This further confirms the basic OCM mechanism in which C<sub>2</sub>H<sub>4</sub> is understood to be produced by the oxidative or catalytic dehydrogenation of C<sub>2</sub>H<sub>6</sub>.

Figure 1.3-15 also shows the early formation and rapid rise in the concentration of H<sub>2</sub>O (peak at ~13 %) concomitant with a decrease in the concentration of O<sub>2</sub>. It is well recognized that the steady-state rate of the OCM reaction is controlled not by the activation of CH<sub>4</sub> and the formation of C<sub>2</sub>H<sub>6</sub> but by the reactions that lead to the formation of H<sub>2</sub>O (e.g., Equation (1.1-11)). This is because of the requirement to close the catalytic cycle [3], [14]. The data presented in here



are in agreement with this argument, for which sharp changes in species mole fraction profiles cease only after O<sub>2</sub> is largely consumed, that is, at an axial distance of approximately 10-11 mm.

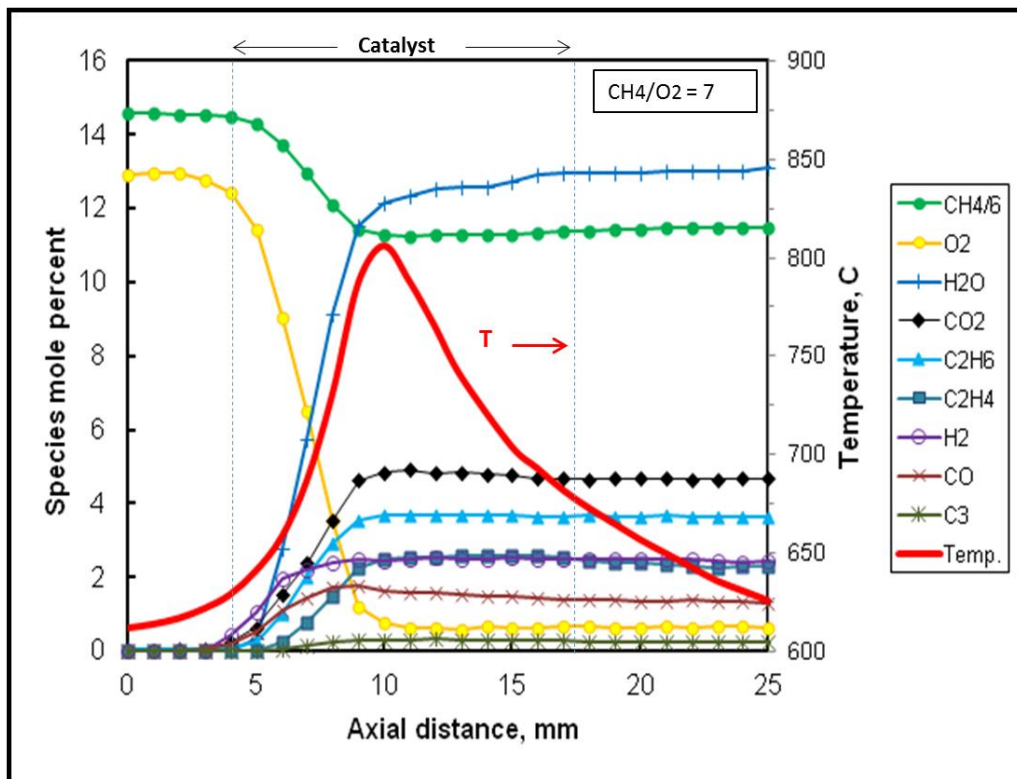


**Figure 1.3-15.** Spatial temperature and species mole percent profiles for a feed CH<sub>4</sub>/O<sub>2</sub> ratio of 7

As seen in Figure 1.3-16, the experiment is done at CH<sub>4</sub>/O<sub>2</sub> ratio of 9. The feed temperature was at 640 °C to reach ignition. The peak reactor temperature, as shown by the temperature profile, reaches its peak of ~800 °C at about 5 mm inside the catalyst bed (10 mm axial distance).

Prompt H<sub>2</sub> formation was also noted in this case, although at a slightly lower peak level of approximately 2.2 %. The production of CO<sub>2</sub> decreased and reached only 3.5 %, whereas C<sub>2</sub>H<sub>6</sub> production increased to a peak level of approximately 3.5 %. Similar to the system with CH<sub>4</sub>/O<sub>2</sub>=7, C<sub>2</sub>H<sub>4</sub> formation lagged behind C<sub>2</sub>H<sub>6</sub> formation and increased to a peak level of approximately 2.1

%). The integral  $\text{CH}_4$  conversions and  $\text{C}_{2+}$  selectivities were approximately 19 and 72%, respectively, shown in Figure 1.3-18. Water formation leveled off at approximately at ~11–12 %.

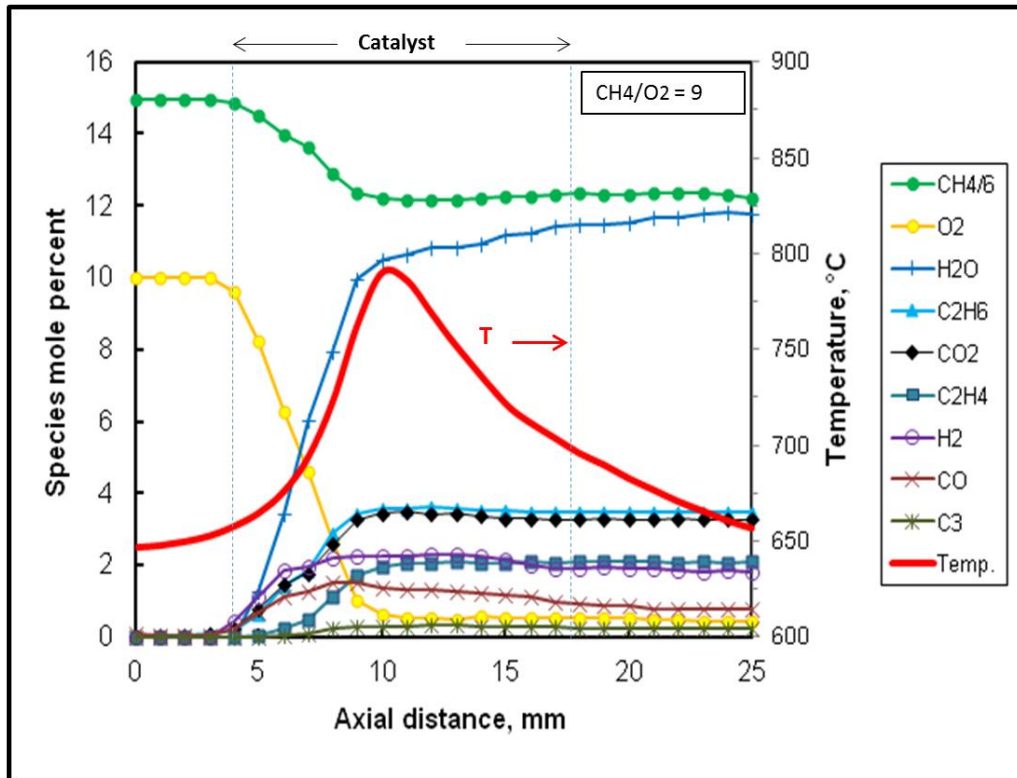


**Figure 1.3-16.** Spatial temperature and species mole percent profiles for a feed  $\text{CH}_4/\text{O}_2$  ratio of 9

As seen in Figure 1.3-17, the experiment is done at  $\text{CH}_4/\text{O}_2$  ratio of 11. The feed temperature was at 730 °C to reach ignition. The temperature profile followed a similar trend to that of the previous ones. The peak reactor temperature at this ratio, as shown by the temperature profile, reaches its peak of ~840 °C at about 5 mm inside the catalyst bed (10 mm axial distance).

Contrary to the Temperature profile, the species profiles exhibited new trends at this feed ratio. Most importantly,  $\text{C}_2\text{H}_6$  was formed very early in the catalyst bed, and significantly,  $\text{C}_2\text{H}_6$  production surpassed  $\text{H}_2$  production, which is in stark contrast to the experiments for lower  $\text{CH}_4/\text{O}_2$  ratios discussed above. Possible reason for the lag in  $\text{H}_2$  formation and the lower levels of  $\text{H}_2$

(Hydrogen levels peaked at ~1.9%) in this experiment could be attributed to the presence of lower levels of molecular oxygen, which is due to the higher CH<sub>4</sub>/O<sub>2</sub> feed ratio adapted in this experiment. As suggested by Lunsford et al. certain level of molecular oxygen is needed to maintain the high level of catalytic OCM activity [10]. Even though the exact role of O<sub>2</sub> is unclear, possibly dissociatively adsorbs over oxide catalyst surface to generate active oxygen species (O<sup>-</sup>, O<sub>2</sub><sup>-</sup>, and/or the peroxide O<sub>2</sub><sup>2-</sup>) [50], [51] [52], it is crucial in methane activation and other relevant surface reactions [12]. Consequently at low levels of O<sub>2</sub>, as the case here, much less H<sub>2</sub> is produced, which seem to be in agreement with our hypothesis that H<sub>2</sub> is perhaps produced by surface reactions, Equations (1.3-1)-(1.3-7).

Ethane also became the most abundant product (peak at ~4 %), surpassing CO<sub>2</sub> (peak at ~3 %). However, ethylene levels remained surprisingly similar to those of previous experiments and exhibited a peak concentration of only 2.2%, although the temperatures were significantly higher. As seen in Figure 1.3-17, C<sub>2</sub>H<sub>4</sub> production abruptly ceased at 6 mm into the catalyst bed (10 mm axial distance), at which point O<sub>2</sub> was entirely consumed and the temperature peaked at 840 °C. This result is consistent with the generally accepted mechanism that oxidative dehydrogenation of C<sub>2</sub>H<sub>6</sub> is the primary path for C<sub>2</sub>H<sub>4</sub> formation in OCM experiments. Similar observations were made in experiments in which lower CH<sub>4</sub>/O<sub>2</sub> ratios were studied (Figure 1.3-15 and Figure 1.3-16). Maximum water concentration of approximately 10% was also reached at 6 mm into the catalyst bed. As shown in Figure 1.3-18, exit CH<sub>4</sub> conversions were lowest at approximately 17%, whereas C<sub>2+</sub> selectivities were the highest at 77% among the three CH<sub>4</sub>/O<sub>2</sub> ratios investigated, which is expected.

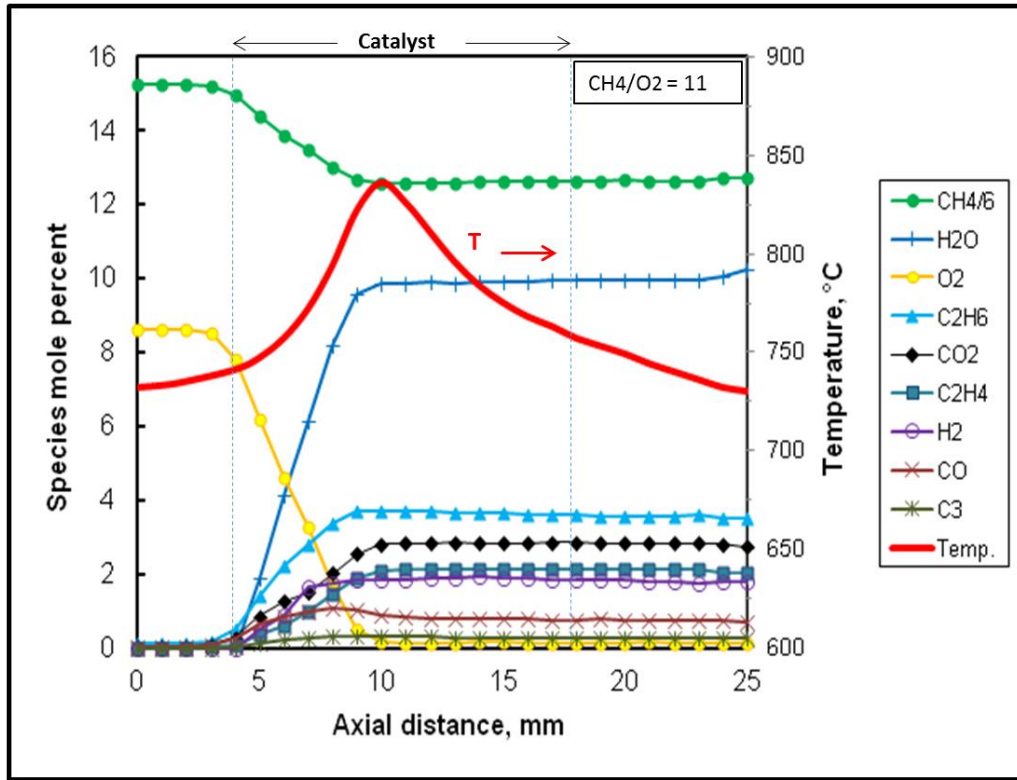


Figure 1.3-17. Spatial temperature and species mole percent profiles for a feed  $\text{CH}_4/\text{O}_2$  ratio of 11

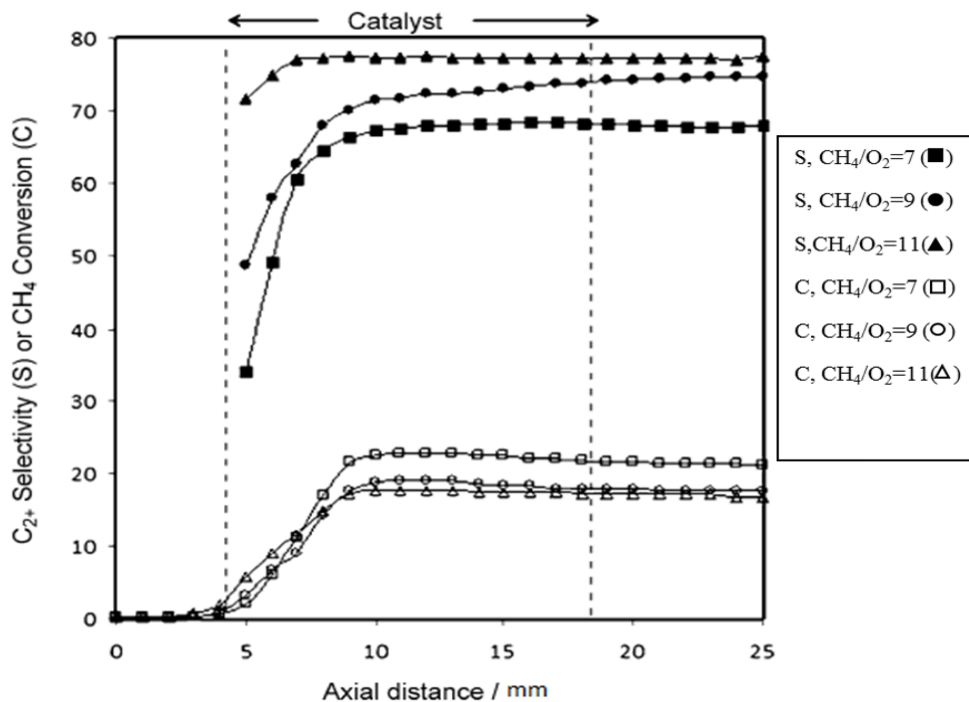


Figure 1.3-18. Spatial profiles for  $\text{CH}_4$  conversions and  $\text{C}_2+$  selectivities for the different  $\text{CH}_4/\text{O}_2$  ratio of the single-bed experiments

### 3.2.2. Dual Catalytic OCM Bed

The superior performance of our La-Ce nanofiber catalysts under OCM conditions and the results of our diligent sampling technique which provided us with some never-seen-before inside the reactor insights, motivated us to further improve and apprehend the system. Furthermore, due to complex nature of the OCM process, we realized that the catalyst design alone may not be sufficient to result in the breakthrough needed for the commercialization of the OCM process, namely to prevail the 25% C<sub>2+</sub> yield limit associated with the OCM process [53]. Consequently, a combined effort, both in catalyst development and in novel reactor systems and operating schemes are needed to advance the field.

In this regards, early reactor simulations that used global OCM reaction kinetics were particularly encouraging, as they suggested the feasibility for attaining yields for C<sub>2+</sub> products as high as +50 % if the O<sub>2</sub> feed was distributed along the reactor, that is, by using membrane-type reactors [33], [54], [55]. Although these predictions may not be realistic, as the global reaction models used are well recognized to be of limited predictive value, they nevertheless create optimism regarding the future of the OCM process. More realistic and accurate predictions of the attainable yields can be accomplished by using detailed chemical kinetic mechanism (DCKM).

Therefore, considering our system's exclusive properties, we developed a novel reactor design for dual-bed OCM reactor with interstage O<sub>2</sub> injection and inter-cooling stage to further enhance the OCM reaction's C<sub>2+</sub> yields. Furthermore, applying our novel sampling technique, information-rich spatial profiles were acquired, which provide new quantitative insight into the close coupling formation of C<sub>2+</sub> products and O<sub>2</sub> levels in OCM reactors. These information are expected to be extremely valuable for the improvement and validation of predictive models.

The dual-bed experiments were conducted with total gas flow rate of 120 sccm (standard cc/min) at overall CH<sub>4</sub>/O<sub>2</sub> feed ratios of 4 (DB1), Figure 1.3-20, and 4.4 (DB2), Figure 1.3-21. For assessment of the system improvement, a single-bed experiment with overall CH<sub>4</sub>/O<sub>2</sub> feed ratios of 4 (SB1), Figure 1.3-19, and spatial profiles for CH<sub>4</sub> conversions and C<sub>2+</sub> selectivities (Figure 1.3-22) were also conducted. The feed temperature was set to reach ignition at each respective condition. Complete experimental set-up is as shown in Figure 1.2-9.

The spatial concentration and temperature profiles for the single-bed experiment (SB1) with a CH<sub>4</sub>/O<sub>2</sub> ratio of 4 were acquired at a furnace temperature (T<sub>f</sub>) of 600 °C. As seen in Figure 1.3-19, the maximum bed temperature reached approximately 1015 °C at ~10 mm (i.e., 5 mm within the catalyst zone), concomitant with the near-complete consumption of O<sub>2</sub> and approximately 30% CH<sub>4</sub> maximum conversion and 55% C<sub>2+</sub> selectivity (see also Figure 1.3-22). These values represent a C<sub>2+</sub> yield of approximately 16%. SB1 at CH<sub>4</sub>/O<sub>2</sub> feed ratio of 4 essentially exhibits the same features as of the single bed experiment with CH<sub>4</sub>/O<sub>2</sub> feed ratio of 7. Close examination of the profiles at the upstream part of the catalyst bed reveals significant levels of H<sub>2</sub> production early in the catalytic zone, that is, prompt H<sub>2</sub>; a peak level is reached at approximately 3.7 mol% within 3 mm inside the catalyst bed (8 mm axial distance). Within this zone, the reactor temperature is still relatively low at 650–725 °C; thus, as explained earlier, we expect that H<sub>2</sub> formation is due to surface-catalyzed reactions, Equations (1.3-1)-(1.3-7). Hydrogen formation precedes H<sub>2</sub>O formation (peak 19%) and is closely followed up by CO<sub>2</sub> (9.31%) and CO (~3%) and then by C<sub>2</sub>H<sub>6</sub> (3.6 %). The measured concentration profiles for C<sub>2</sub>H<sub>6</sub> and H<sub>2</sub>O are consistent with the well-established elementary reactions leading to their formation, Equations (1.1-8)-(1.1-11). As expected, C<sub>2</sub>H<sub>4</sub> formation exhibits significant lag relative to C<sub>2</sub>H<sub>6</sub> formation, which is in agreement with our understating of basic OCM mechanism, stating that Ethylene is produced by

the oxidative or catalytic dehydrogenation of  $C_2H_6$ . Ethylene levels peaked at 3.1% at 4 mm into the catalyst bed. It is important to note that once  $O_2$  is completely consumed (~4 mm inside catalyst bed),  $H_2O$  and other major species level off and thereon no sharp changes are observed in the species profiles.

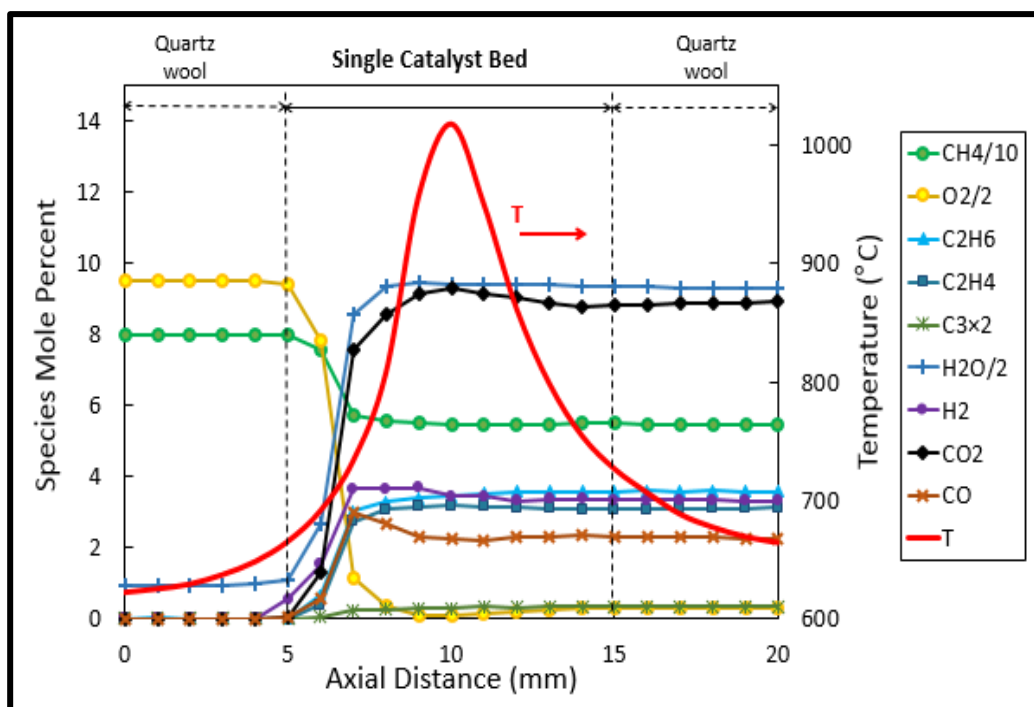


**Figure 1.3-19.** Spatial temperature and species mole percent profiles for the single-bed reactor system (SB1) with overall feed  $CH_4/O_2$  ratio of 4

The spatial concentration and temperature profiles for the dual-bed operation (DB1) for the OCM reaction at the overall  $CH_4/O_2$  ratio of 4 as presented in Figure 1.3-20 reveal several important features. First, the feed  $CH_4/O_2$  ratio of 9 used in the first catalyst bed necessitated the use of a higher  $T_f$  of approximately 750 °C for ignition. As seen in Figure 1.3-20, the bed temperatures rapidly increased within the catalytic zones and reached maximum bed temperatures of 920 °C in the first bed and 866 °C in the second bed, both at approximately 5 mm within the catalyst zones, which corresponds to complete conversion of  $O_2$ . This trend of temperature profile is similar to the SB1 and initial single-bed experiments presented in Figure 1.3-19, Figure 1.3-15,

and Figure 1.3-16 and yet gives us additional insight into the effects of temperature on  $C_{2+}$  yields in OCM. For example, the peak temperatures in each bed for the dual-bed experiments are significantly lower than those in the single-bed experiment (SB1). This was the consequence of the split introduction of oxygen and heat removal realized within the interstage zone, which collectively decreased the maximum temperature attained in the OCM reactors, in spite of the higher ignition temperature. As seen in Figure 1.3-22, a  $C_{2+}$  selectivity of 70% and an ultimate  $C_{2+}$  yield of 21% was achieved in the DB1 experiment; the latter is a value significantly higher than the 16% yield observed in the single-bed experiment at the same overall  $CH_4/O_2$  ratio of 4 (SB1). This clearly demonstrates that distributing the oxygen feed with interstage cooling is a good strategy to increase  $CH_4$  conversion, whereas adverse effects on the selectivity of  $C_{2+}$  products are minimized.

Second, although the mixing of the secondary  $O_2$  feed with the reactor gases at the point of  $O_2$  injection was not instantaneous, as evidenced by the presence of a steep axial oxygen concentration profile, a uniform composition was achieved within the interbed zone close to the upstream quartz-wool packing of the second reactor. Third, the concentrations of all the species decreased upon  $O_2$  introduction (i.e., dilution), but remained virtually unchanged along the interbed zone and within the quartz-wool packing. Furthermore, the temperature in the interbed zone remained at approximately 755 °C, close to the furnace temperature. These measurements clearly indicate both the absence of any gas-phase reactions in the interstage zone and the inert nature of the quartz wool. This is a surprising result, as packets of high  $O_2$  concentrations would be expected to cause gas-phase combustion at the indicated interbed temperatures especially if  $H_2$  is present. The OCM reaction commenced once the gases entered the second catalytic bed at approximately 40 mm.



As seen in Figure 1.3-20, CO exhibited peak concentrations of 1.2% at 9 mm in the first bed and of 2.2% at 43 mm in the second bed, which ultimately leveled off at 2.0% at the reactor exit. Hydrogen levels were 2.3 and 3.6% at the exits of beds 1 and 2, respectively. Carbon dioxide and water levels reached 3.4 and 11.5% in bed 1, respectively, and became 7 and 25.5% at the exit of the dual-bed reactor, respectively.

Hydrocarbon products generally increased monotonically within the catalytic zones with increasing methane conversions and ceased to change once O<sub>2</sub> was consumed. At the exit of the first bed, the following levels were reached: C<sub>2</sub>H<sub>6</sub> 3.7%, C<sub>2</sub>H<sub>4</sub> 2.23%, and C<sub>3</sub>H<sub>6</sub> 0.25%, whereas CH<sub>4</sub> conversion was 17%. Under these conditions, C<sub>2+</sub> selectivities corresponded to 76.6%, which represents a yield of 13%. However, at the exit of the second bed the species concentrations became: C<sub>2</sub>H<sub>6</sub> 4.4%, C<sub>2</sub>H<sub>4</sub> 4.1%, and C<sub>3</sub>H<sub>6</sub> 0.41%, whereas CH<sub>4</sub> conversion increased to approximately 30%, with a small reduction in the C<sub>2+</sub> selectivities and, hence, a 21% yield at the end of the dual-bed reactor, see also Figure 1.3-22.

Temperature and species concentration profiles within the second catalytic zone were qualitatively similar to those within the first bed, and the reactions ceased immediately after the exhaustion of O<sub>2</sub>. This is an interesting result because unlike the first reactor, the feed to the second catalyst bed possessed significant levels of H<sub>2</sub>, CO, CO<sub>2</sub>, and H<sub>2</sub>O, together with C<sub>2+</sub> products. Considering the fact that with complete consumption of oxygen in the second bed, H<sub>2</sub> and H<sub>2</sub>O production levels are consistent with our expectations from the OCM reaction and there is no sign of H<sub>2</sub>O consumption in the second bed. Therefore, as apparent from the species concentration profiles in the second bed, even in the presence of an excess amount of steam produced in the first bed, La<sub>2</sub>O<sub>3</sub>-CeO<sub>2</sub> does not promote the steam reforming of methane reaction. Moreover, the excess amounts of carbon dioxide and water fed to the second bed did not cause any apparent deactivation

of the OCM catalyst. Moreover, Analysis of the experimental data of Figure 1.3-19 and Figure 1.3-20 also indicate that the catalytic water gas shift (WGS) reaction, as shown in Equation (1.3-8) can be ruled out.



For example, the mole fraction ratios  $(Y_{\text{CO}_2} \times Y_{\text{H}_2}) / (Y_{\text{H}_2\text{O}} \times Y_{\text{CO}})$  were in the 0.4–0.6 range within the 5 mm in the catalyst beds in all the experiments. These values are significantly lower than those of the WGS reaction equilibrium constants that are in the 1.5–2.0 range under the prevailing conditions in the reactor beds.

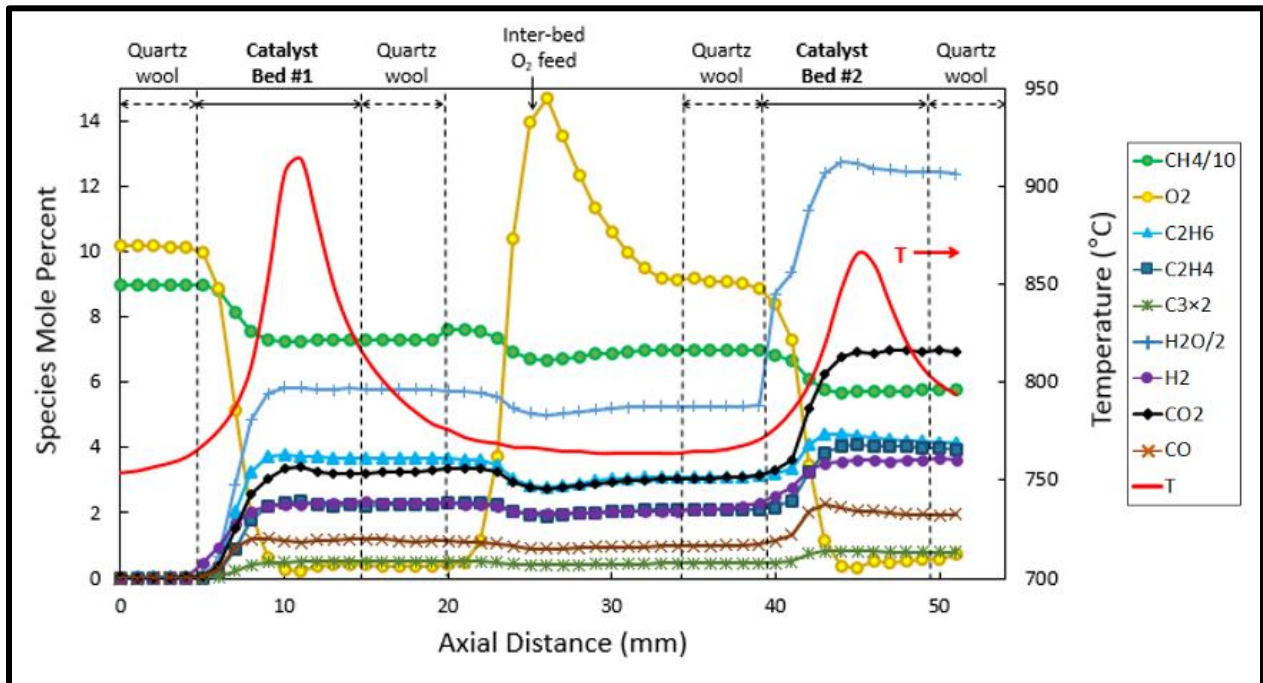


**Figure 1.3-20.** Spatial temperature and species mole percent profiles for the dual-bed reactor system (DB1) with initial feed  $\text{CH}_4/\text{O}_2$  ratio of 9 and overall  $\text{CH}_4/\text{O}_2$  ratio of 4

The profiles for the DB2 experiment at the overall  $\text{CH}_4/\text{O}_2$  ratio of 4.4 as presented in Figure 1.3-21 are in harmony with the DB1 experiment at  $\text{CH}_4/\text{O}_2=4.0$  (Figure 1.3-20), which thereby gives us confidence regarding the validity of our measurements. In the DB2 experiment, the initial feed  $\text{CH}_4/\text{O}_2$  ratio of 11 used in the first catalyst bed necessitated the use of a higher  $T_f$  of approximately  $780^\circ\text{C}$  for ignition, and the maximum bed temperatures reached  $930$  and  $910^\circ\text{C}$  in the first and second beds, respectively. These values are significantly lower than the single-bed temperature peak of  $1015^\circ\text{C}$  (Figure 1.3-19). Again, the location of the maximum temperatures corresponds to the complete conversion of  $\text{O}_2$ . Moreover, the interbed temperature remained relatively constant at approximately  $800^\circ\text{C}$ .

From Figure 1.3-21 it can be seen that CO exhibited a peak concentration of 1.0% at  $\sim 5$  mm within the first bed, and ultimately reached 1.6% at the exit of the second catalyst bed. Hydrogen levels were 2.2% and 3.5% at the exits of beds 1 and 2, respectively. Carbon dioxide and water levels reached 2.8% and 10% in bed 1, respectively, and became 6% and 24.2% at the exit of the second bed, respectively.

In the DB2 experiment, the hydrocarbon products also exhibited similar trends, which generally increased within the catalytic zones with increasing methane and oxygen conversions and which ceased to change after the complete conversion of  $\text{O}_2$ . At the exit of the first bed, the following levels were recorded:  $\text{C}_2\text{H}_6$  3.52 %,  $\text{C}_2\text{H}_4$  2.1 %, and  $\text{C}_3\text{H}_6$  0.21 %, whereas  $\text{CH}_4$  conversion was 19%. Under these conditions,  $\text{C}_{2+}$  selectivities would be 74 %, which represents a yield of 14 % (refer to Figure 1.3-22). At the second bed exit, the concentration levels became  $\text{C}_2\text{H}_6$  4.1 %,  $\text{C}_2\text{H}_4$  3.8 %, and  $\text{C}_3\text{H}_6$  0.35 %, with a maximum  $\text{CH}_4$  conversion of approximately 28%. These results correspond to a  $\text{C}_{2+}$  selectivity of 67% and represent a final yield of

approximately 19 %. This value is slightly lower than the 21% yield obtained in the DB1 experiment yet higher than the 16% yield of the single-bed experiment.

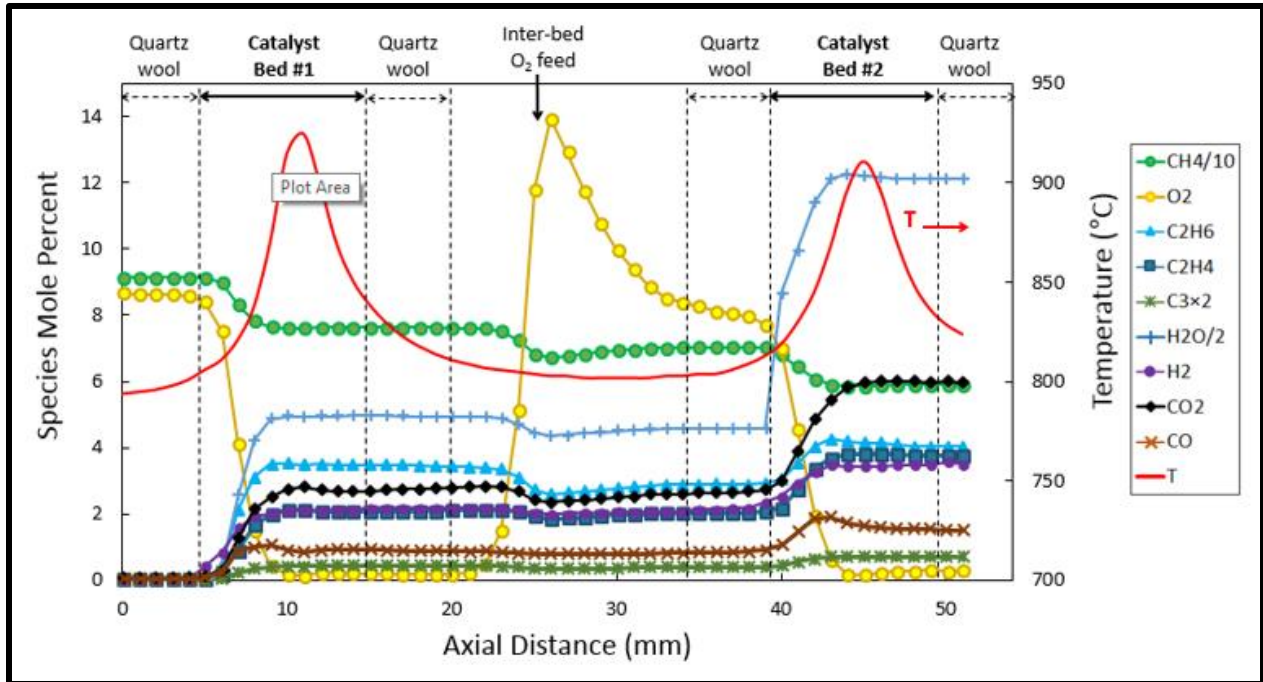


**Figure 1.3-21.** Spatial temperature and species mole percent profiles for the dual-bed reactor system (DB2) with initial feed  $\text{CH}_4/\text{O}_2$  ratio of 11 and overall  $\text{CH}_4/\text{O}_2$  ratio of 4.4

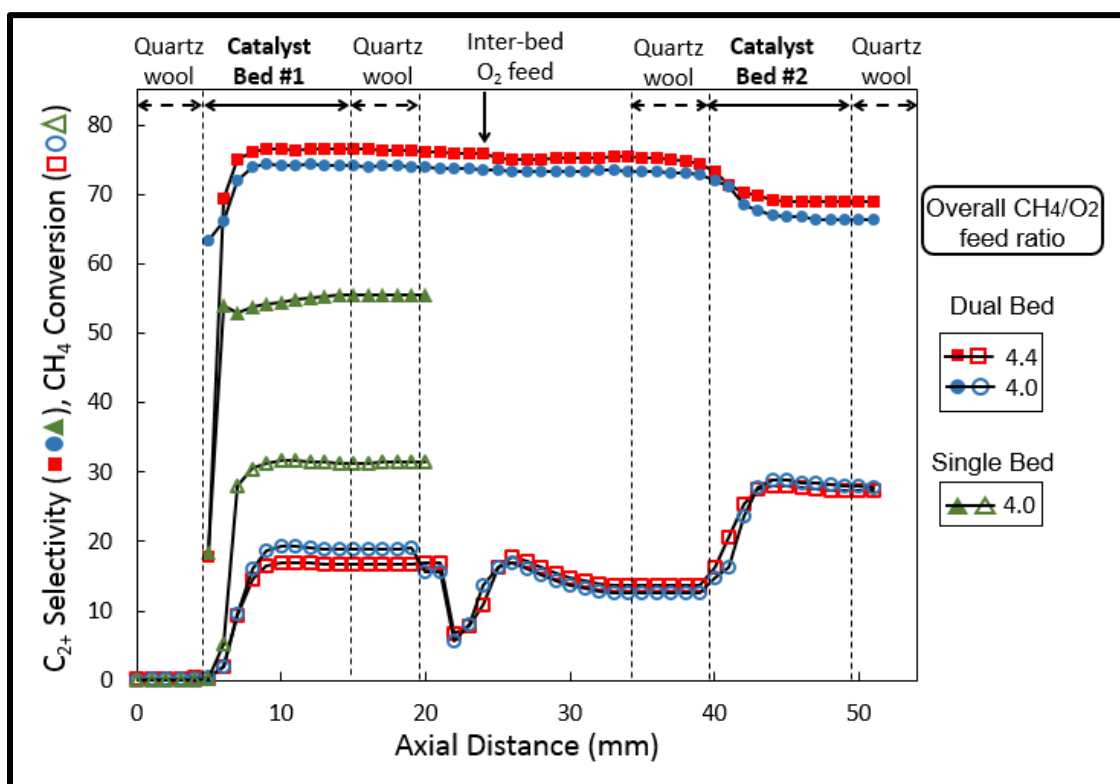


**Figure 1.3-22.** Spatial profiles for CH<sub>4</sub> conversions and C<sub>2+</sub> selectivities for the single-bed (SB1) and dual-bed (DB1, DB2) experiments

For ease of comparison, and to signify the system's improvement using a dual-bed reactor design, substantial results of the dual-bed experiment including SB1, DB1, and DB2 are summarized here in Table 1.3-1.

**Table 1.3-1.** Double and single bed Reaction conditions and reactor exit values for conversions, selectivities and yields

	Furnace, T °C	Overall CH <sub>4</sub> /O <sub>2</sub>	Peak1, T °C	Feed 1 CH <sub>4</sub> /O <sub>2</sub>	Exit1 CH <sub>4</sub> conv.	Exit1 C <sub>2+</sub> sel.	Exit1 C <sub>2+</sub> yield		Inter-bed, T °C	Peak2, T °C	Exit2 CH <sub>4</sub> conv	Exit2 C <sub>2+</sub> sel.	Exit2 C <sub>2+</sub> yield
Single-Bed, SB1	600	4	1015	4	30	55	<b>16</b>		-	-	-	-	-
Double-Bed, DB1	750	4	920	9	17	77	13		755	866	30	70	<b>21</b>
Double-Bed, DB2	780	4.4	930	11	19	74	14		800	910	28	67	19

## **CHAPTER 1.4. Future Work**

Up to this point we have developed a comprehensive understanding of characteristics and operating conditions of our La-Ce nanofiber catalyst system under OCM conditions. Moreover, with the latest advancements that we have made in our lab towards development of spatially resolved concentration and temperature profiles for single-bed and our novel dual-bed OCM reactor via novel sampling technique, we have gathered valuable insights regarding complex nature of the OCM reaction. Most notably, the information rich data, now available to us by the in-situ spatial concentration and temperature profiles, along the length of the packed-bed OCM reactor, will be particularly useful for the development and validation of DCKM.

Therefore, motivated by significance of our work, we put forth the following plans for future work, explained in this section, to further our understanding of the in-had La-Ce nanofiber catalyst system and OCM reaction. Moreover, considering our main focus of improving  $C_{2+}$  yield of OCM, we discuss possible application of other novel methods such as catalytic nonthermal plasma reactor (CNTP) in OCM reaction.

#### 4.1. Distribution of Oxygen Feed

As we have seen so far at high  $\text{CH}_4/\text{O}_2$  ratios (e.g. exit of first bed in dual-bed reactor), high  $\text{C}_{2+}$  selectivities and low methane conversions are achieved and this is reversed once we increase the  $\text{O}_2$  level in the feed. Therefore, the trade-off between  $\text{C}_{2+}$  selectivity and methane conversion in OCM seems to be inevitable. However, considering the success of our dual-bed reactor design, which showed superior performance compared to the single-bed, namely increasing the 16% yield of a single-bed OCM reactor to about 21% in dual-bed, as our platform, we realize that the distribution of feed oxygen along the catalytic OCM bed may have the potential to break the  $\text{C}_{2+}$  yield limitations.

In this regard, we propose to explore the effects of oxygen feed distribution on the OCM yield in two different types of reactor design.

The first reactor configuration is simply adapted from the concept of a membrane reactor, as shown in Figure 1.4-1. Oxygen is distributed throughout the length of the catalyst bed via a small quartz capillary feed line with a large number of orifices. The orifices are laser drilled two at each position, with  $180^\circ$  angle apart, and it is rotated  $90^\circ$  at each consecutive position to achieve well distribution of  $\text{O}_2$  feed. There are a number of design issues that can be explored to maximize the yields for  $\text{C}_{2+}$  products. First, by varying the spacing between the orifices, the  $\text{O}_2$  concentration (distribution) along the reactor can be adjusted to ultimately maximize the  $\text{C}_{2+}$  yield. However, initial experiments will be performed by using a uniform spacing of the orifices along the reactor as shown in Figure 1.4-1. It should be noted that it is crucial to achieve rapid radial mixing of  $\text{O}_2$  feed along the reactor bed, although this may be a significant challenge as we scale up the reactor.

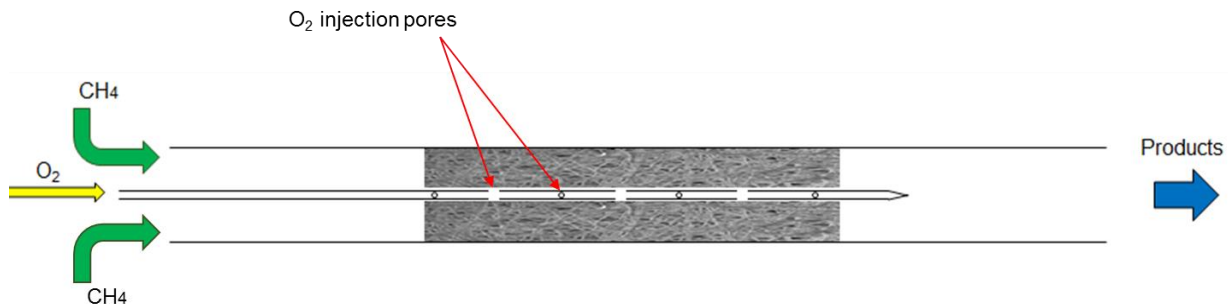


**Figure 1.4-1.** OCM reactor with distributed  $O_2$  feed

We will also explore three sequential packed-beds, see Figure 1.4-2, with space between each consecutive bed for  $O_2$  injection and inter-stage cooling. Here, the initial  $CH_4/O_2$  feed ratio which splits for each stage has to be explored and optimized. Initial experiments will be performed within the same heating furnace, thereby resulting in the establishment of the same inter-stage cooling temperature. This, however, may not be desirable to maximize the ultimate  $C_{2+}$  yield since different ignition temperatures are needed for different  $CH_4/O_2$  feed ratios. For example, a high ignition temperature needed for the first packed-bed reactor (due to its highest  $CH_4/O_2$  ratio) may be excessive for the second and third reactors, where  $CH_4$  concentrations are lower. The higher furnace temperatures promote gas phase combustion reactions in the subsequent reactors which adversely affect the  $C_{2+}$  yields. Consequently, it will be beneficial to independently control the furnace temperature for each of the catalyst bed used. For example, since the initial  $CH_4/O_2$  ratio will be higher, therefore it may be advantageous to use separate furnace for this portion to achieve the high ignition temperature without promoting catalytic gas-phase reactions inside other beds due to the elevated temperature required for ignition of the first bed.

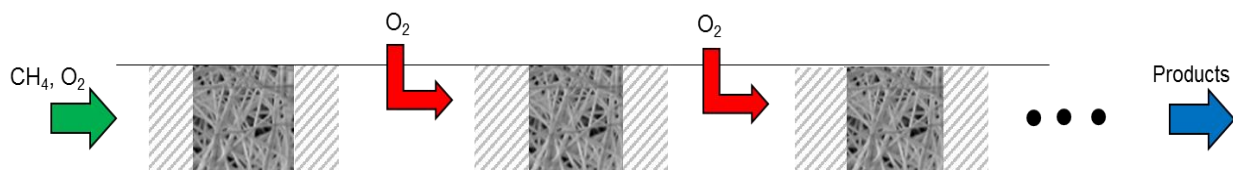


**Figure 1.4-2.** Sequential OCM catalytic bed design with distributed oxygen injection and intercooling stages



Even though the sequential OCM catalytic bed with multiple oxygen injection zones may seem very similar to a typical membrane reactor concept, it differentiates in one key aspect and that is the presence of inter-cooling stage. Since high temperatures promote homogeneous gas phase free radical reactions detrimental for  $C_{2+}$  products, the development of a reactor design with multiple heat removal zones (intercooling stages) may help remedy this issue. Therefore, as seen in the dual-bed reactor configuration, the interstage cooling, which enables the heat removal, is the primary factor that attributes to increasing the  $C_{2+}$  yields primarily by maintaining the  $C_{2+}$  product selectivity levels while stepwise injection of  $O_2$  within the catalyst beds increases  $CH_4$  conversion inside the subsequent beds.

#### 4.2. Non-thermal Plasma Application in OCM

As mentioned earlier in section 1.3.1, even though OCM is a thermodynamically favored process, it is hindered by kinetics. A major challenge in this route is the high stability of methane molecule which requires high levels of energy for activation (abstraction of one H from methane to create  $CH_3\bullet$ ). Requirement of this high level of energy then leads to high temperatures and consequent promotion of gas phase reaction which leads to low  $C_{2+}$  selectivity and thus low yields of OCM. Therefore, herein, we propose to explore the application of catalytic nonthermal plasma (CNTP) as a possible route to promote the activation of methane at low temperature and low pressure.

There are various thermal and non-thermal plasma sources such as a dielectric barrier discharge (DBD), corona, gliding arc, rotating arc, spark, microwave, glow discharge and pulsed discharge with or without a catalyst. However, in general, the atmospheric plasma can be divided

into two general classes, thermal plasma and nonthermal plasma, depending on the gas temperature. In the thermal plasma, like plasma torch, all the charged species (electrons and ions) and neutral species (atoms, molecules, radicals and excited species) are in thermal equilibrium, with typical gas temperature ranges from 1,000 to 10,000 K. On the other hand, nonthermal plasma sources, such as a dielectric barrier discharge (DBD) is not in thermal equilibrium state in which the electron temperature is much higher (10,000 ~ 100,000 K, or 1 ~ 10 eV) while the *gas* remains cold (300K).

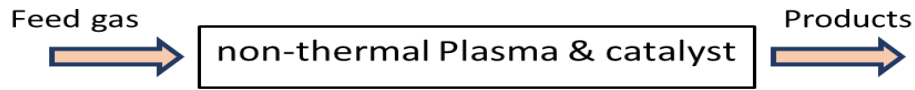
Plasma and catalysts have their own advantages and disadvantages. Catalysts are highly selective but are active only at high temperature since reactants ( $\text{CH}_4$ ) must overcome the activation barriers. On the other hand, plasma can be highly reactive even at room temperature although it is nonselective and requires the high energy [56]. Hence, the hybridization of plasma and a catalyst into one system can provide complementary or even synergistic results for the activation at low temperature [57]. Previous studies have shown the positive effect of using a plasma–catalysis combination system on various reactions such as oxidation, dissociation, reduction, and reforming [58], [59], [60].

The main advantage of nonthermal plasma process is its high chemical efficiency. As little or no heat is produced, nearly all input energy is converted to energetic electrons which produce methane activation through collision. The high energy electrons collide against neutral molecules inside the DBD reactor, producing ions, radicals, and electronically/vibrationally excited species almost independently of the reaction temperature. They are responsible for triggering low temperature conversion. This is in contrast to thermal plasmas in which the heating itself leads to higher thermal losses and thereby waste of energy.

The nonthermal plasma contains energetic electrons and a variety of chemically active species which can accelerate the OCM process. From the point of plasma chemistry, the decomposition of hydrocarbons is mainly from electron-impact dissociation and ionization. Impact ionization occurs when electrons are accelerated in a high local electric field. Thus, a higher electric field leads to a higher electron energy, favoring the electron-impact reactions responsible for the hydrocarbon activation. For CH<sub>4</sub>, the electron impact reactions induce vibrational excitation [CH<sub>4</sub> (v<sub>24</sub>, v<sub>13</sub>)], dissociation (CH<sub>3</sub>, CH<sub>2</sub>, CH, H, H<sub>2</sub>, e) and ionization (CH<sub>4</sub><sup>+</sup>, CH<sub>3</sub><sup>+</sup>, H, 2e) as shown in equations (1.4-2) - (1.4-8). Therefore, if applied properly, plasma is expected to significantly increase the C<sub>2+</sub> yield of OCM reaction.

The plasma catalysis technique can be classified as single-stage (Figure 1.4-3 a) and two-stage (Figure 1.4-3 b) depending on the position of catalyst in the DBD reactor. Single-stage type is constructed by packing catalysts within the plasma zone, and two-stage type is by placing catalysts upstream or downstream to the plasma zone. However, in order to maximize an influence of short-lived active radicals (~10 nsec, excited species, radicals and ions) on catalytic reactions, it is desirable for plasma to take place near or on the catalyst surface [56]. Here, we aim to investigate the use of both plasma configurations for OCM reactor.

**(a) Single-Stage**



**(b) two-Stage**

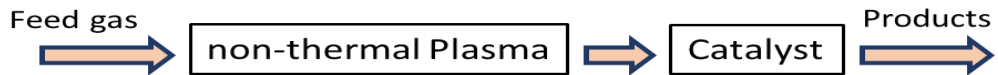


**Figure 1.4-3.** Overview of Plasma-Catalysis hybrid system configurations

Our proposed reactor configuration for the OCM CNTP reactor configuration is as shown in Figure 1.4-4; This is for the single-stage type. As expected in the CNTP application, the operating conditions, including temperature, applied voltage, frequency, feed flow rates,  $\text{CH}_4/\text{O}_2$  ratio, catalyst type and treatment, all need to be experimentally searched as variable parameters for the best result under OCM conditions.

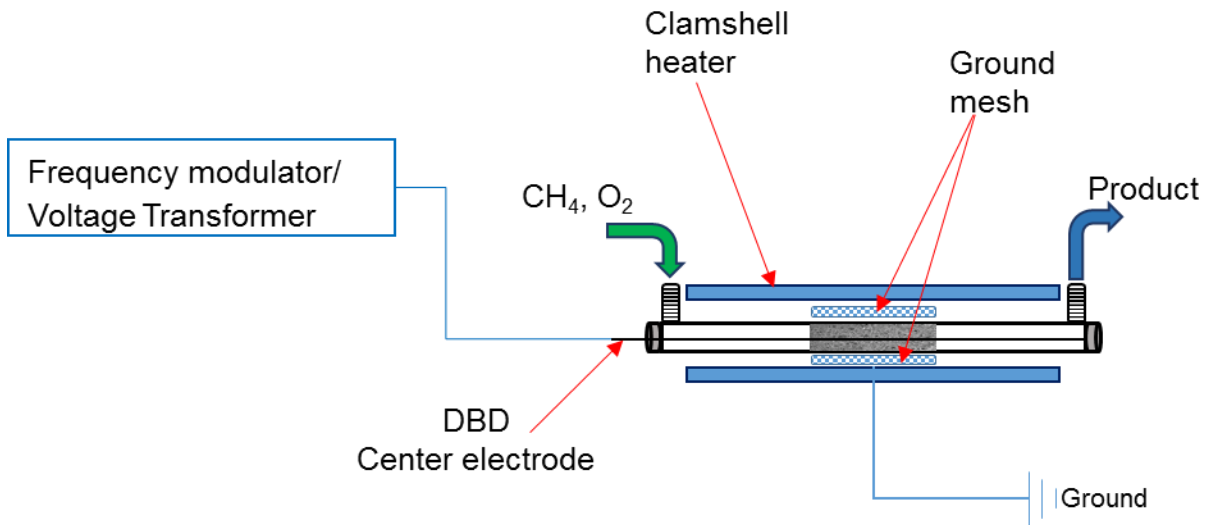


**Figure 1.4-4.** Proposed DBD reactor set-up for OCM

### 4.3. Kinetic Modeling

In this program, we will develop and validate a new generation of DCKM for the OCM process using the high-information content spatial concentration profiles obtained in the experimental program. At this stage, our primary focus will be on further understanding the La<sub>2</sub>O<sub>3</sub>-CeO<sub>2</sub> catalytic system and gaining valuable insights on the mechanism of the OCM process and the effects of operating conditions on C<sub>2+</sub> yields. The proposed numerical simulation studies will include the following four parts:

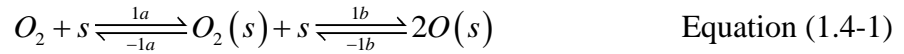
- I. Homogenous gas-phase reactions
- II. Heterogeneous surface reactions
- III. Coupled surface and gas phase reactions for reactor modeling and development of a detailed chemical kinetic mechanism DCKM
- IV. Homogeneous gas- phase under Plasma

The homogenous gas-phase mechanism is well-known and has been confirmed by vast amounts of experimental data [61]. Table 1.4-1 (no. 1'-454') shows a part of this comprehensive mechanism [61].

**Table 1.4-1.** Elementary gas-phase reactions for homogeneous oxidation of methane

no.	gas-phase reactions	$A$ (mol, cm <sup>3</sup> , s)	$n$	$E$ (cal·mol <sup>-1</sup> )
1'	CH <sub>3</sub> · + O <sub>2</sub> → HCHO + OH·	3.0 × 10 <sup>30</sup>	-4.69	36 600
2'	2CH <sub>3</sub> · + (M) → C <sub>2</sub> H <sub>6</sub> + (M)	3.61 × 10 <sup>13</sup>	0	0
3'	HCHO + H· → CHO· + H <sub>2</sub>	1.3 × 10 <sup>8</sup>	1.62	2 100
4'	HCHO + OH· → CHO· + H <sub>2</sub> O	3.4 × 10 <sup>9</sup>	1.18	0
5'	CHO· + (M) → CO + H· + (M)	1.9 × 10 <sup>16</sup>	-1	17 000
6'	CHO· + O <sub>2</sub> → CO + HO <sub>2</sub>	2.6 × 10 <sup>11</sup>	0	410
7'	CO + HO <sub>2</sub> · → CO <sub>2</sub> + OH·	1.5 × 10 <sup>15</sup>	0	23 600
8'	C <sub>2</sub> H <sub>6</sub> + CH <sub>3</sub> · → C <sub>2</sub> H <sub>5</sub> · + CH <sub>4</sub>	1.5 × 10 <sup>-7</sup>	6	5 800
9'	C <sub>2</sub> H <sub>5</sub> · + (M) → C <sub>2</sub> H <sub>4</sub> + H· + (M)	8.2 × 10 <sup>13</sup>	0	40 000
10'	C <sub>2</sub> H <sub>5</sub> · + O <sub>2</sub> → C <sub>2</sub> H <sub>4</sub> + HO <sub>2</sub> ·	8.4 × 10 <sup>11</sup>	0	3 900
11'	C <sub>2</sub> H <sub>3</sub> · + O <sub>2</sub> → CHO· + HCHO	4.5 × 10 <sup>16</sup>	-1.39	1 000
12'	C <sub>2</sub> H <sub>3</sub> · + (M) → C <sub>2</sub> H <sub>2</sub> + H· + (M)	2 × 10 <sup>14</sup>	0	39 800
13'	HO <sub>2</sub> · + CO → CO <sub>2</sub> + OH·	1015	0	23 600
⋮	⋮	⋮	⋮	⋮
454'	CO <sub>2</sub> + CH <sub>2</sub> · → HCHO + CO	2.3 × 10 <sup>10</sup>	0	0

The heterogeneous reactions of methane in the OCM process have also been explored and described previously in section 1.3 [24], [31]. As noted earlier it has generally been accepted that oxygen is dissociatively adsorbed over the oxide surface to form active atomic oxygen centers according to the following reaction, Equation (4-1):



In which  $s$  represents a surface site (O atom on the surface of the  $La_2O_3$  crystal) [24]. Then the methane molecule loses one of its hydrogen atoms to the surface O atom forming  $CH_3\bullet$  which then diffuses back to the gas phase. A set of 24 elementary reactions for the surface kinetics of the OCM process is shown in the Table 1.4-2 part (a) [24], [31]. The combination of these surface reactions (set of 24 part(a)) and the gas-phase reactions described above in Table 1.4-1 have been used in the past for kinetic modeling of OCM process. Most recently Y. Simon et al. concluded the following mechanism schematics for the OCM reaction using these set of surface and gas-phase reactions, shown in Figure 1.4-5 [24]. More recently, a similar schematic was constructed in the work of Marin et al. as shown earlier in Figure 1.1-13 [31]. Although the proposed mechanisms correctly predicted some of the features of the OCM process, they were not in quantitative agreement with the available experimental data.

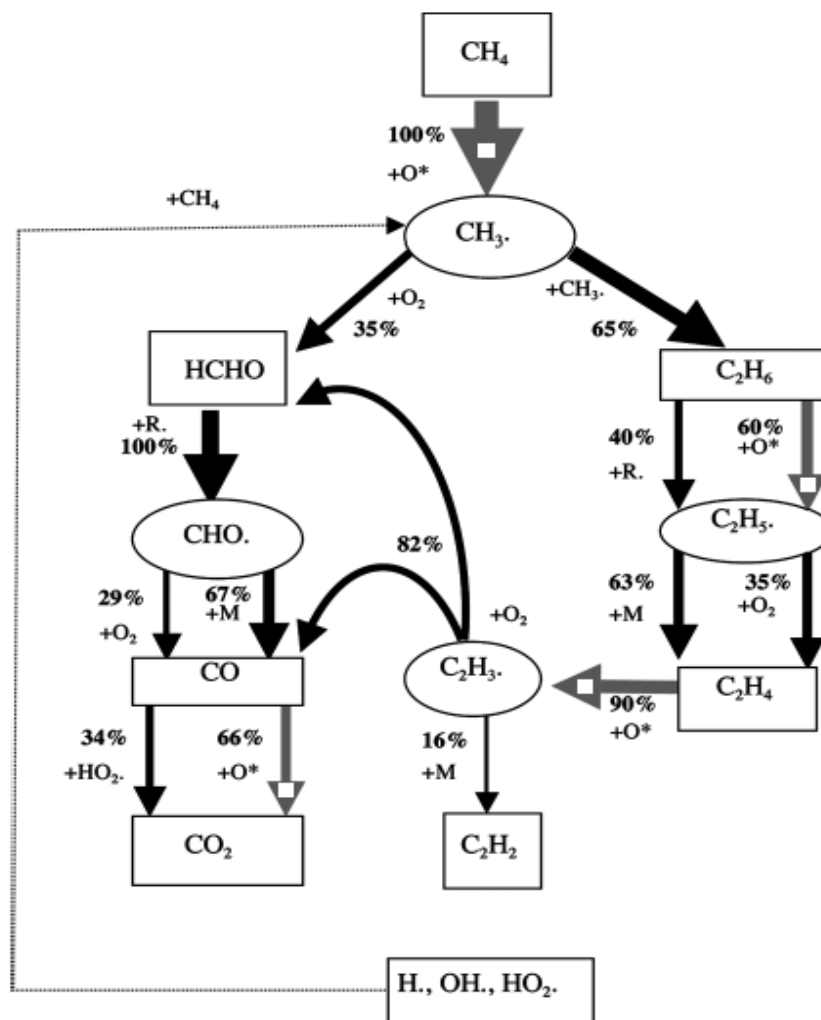


**Figure 1.4-5.** Mechanism of the oxidative coupling of methane over  $\text{La}_2\text{O}_3$   
 \*dark arrow: homogenous gas-phase reactions- light arrow: surface reactions

As noted earlier, our experimental studies of spatially resolved concentration profiles of single-bed and dual-bed OCM clearly demonstrated the early formation of  $\text{H}_2$  in the OCM process, even before  $\text{C}_2$  products. Formation of  $\text{H}_2$  which has significant mechanistic implications was missing in all the prior OCM modeling work, including the most current kinetic studies mentioned above. Consequently, we will develop a new generation of DCKM for the OCM process by including the participation of relevant surface elementary reactions of hydrogen. A preliminary set

of surface reactions we propose to be included in OCM are shown in Table 1.4-2 (25-31, part (b)).

These equations will be added to the set of 24 surface elementary steps, making it 31 total.

**Table 1.4-2.** Catalytic elementary reactions considered in OCM

no.	Surface reactions
1	$O_2 + s \rightarrow O_2(s)$
2	$O_2(s) \rightarrow O_2 + s$
3	$O_2(s) + s \rightarrow 2O(s)$
4	$2O(s) \rightarrow O_2(s) + s$
5	$CH_4 + O(s) \rightarrow CH_3 + OH$
6	$CH_3 + O(s) \rightarrow CH_2 + OH(s)$
7	$CH_2 + O(s) \rightarrow CH + OH(s)$
8	$CH + O(s) \rightarrow C + OH(s)$
9	$C + O(s) \rightarrow CO + s$
10	$C_2H_4 + O(s) \rightarrow C_2H_3 + OH(s)$
11	$C_2H_6 + O(s) \rightarrow C_2H_5 + OH(s)$
12	$C_2H_5 + O(s) \rightarrow C_2H_4 + OH(s)$
13	$C_3H_7 + O(s) \rightarrow C_3H_6 + OH(s)$
14	$CO_2 + s \rightarrow CO_2(s)$
15	$CO_2(s) \rightarrow CO_2 + s$
16	$CO + O(s) \rightarrow CO_2 + s$
17	$CH_3 + O(s) \rightarrow CH_3O(s)$
18	$CH_3O(s) + O(s) \rightarrow CH_2O + OH(s) + s$
19	$CH_2O + O(s) \rightarrow CO + OH(s)$
20	$C_2H_5 + O(s) \rightarrow C_2H_5O(s)$
21	$C_2H_5O(s) + O(s) \rightarrow CH_3CHO + OH(s) + s$
22	$OH(s) + OH(s) \rightarrow H_2O + O(s) + s$
23	$H_2O + O(s) \rightarrow OH\cdot + OH(s)$
24	$OH\cdot + O(s) \rightarrow O\cdot + OH(s)$
25	$CH_3 + OH(s) \rightarrow CH_2O(s) + H_2$
26	$CH_2O(s) \rightarrow (s) + CO + H_2$
27	$CO + O(s) \rightarrow CO_2 + (s)$
28	$CH_3 + O(s) \rightarrow CH_3O(s) \rightarrow CHO(s) + H_2$
29	$CHO(s) + O(s) \rightarrow (s) + H(s) + CO_2$
30	$CHO(s) \rightarrow H(s) + CO$
31	$H(s) + H(s) \rightarrow 2(s) + H_2$

Part (a) - Set of 24

Part (b) - Set of 7



The above mentioned set of gas-phase reactions coupled with the revised surface kinetics (i.e. involving prompt H<sub>2</sub> formation) represents the new generation of DCKM that will be the starting point in our reactor simulations. The DCKM will then be combined with the transport models describing packed-bed reactors for the simulation of species concentration profiles in the OCM reactors (both catalytic and coupled catalytic-non-thermal plasma). In all our reactor simulations, we will use experimentally acquired temperature profiles to solve the multi-component convection, diffusion and reaction equations. This approach accomplishes two major objectives: First, the energy and component balance equations are decoupled, and second heat losses are realistically accounted for. Reactor simulations will be performed using commercial software, such as Surface ChemkinPro.

Model predictions will be compared to these experimental data to assess the validity of the detailed chemical kinetic mechanism (DCKM). Sensitivity analysis will be performed to identify important elementary reactions for further studies and refinement, e.g. DFT studies. The schematics of our approach for development of a comprehensive DCKM, applicable to a broad range of reactions conditions, is shown in Figure 1.4-6.

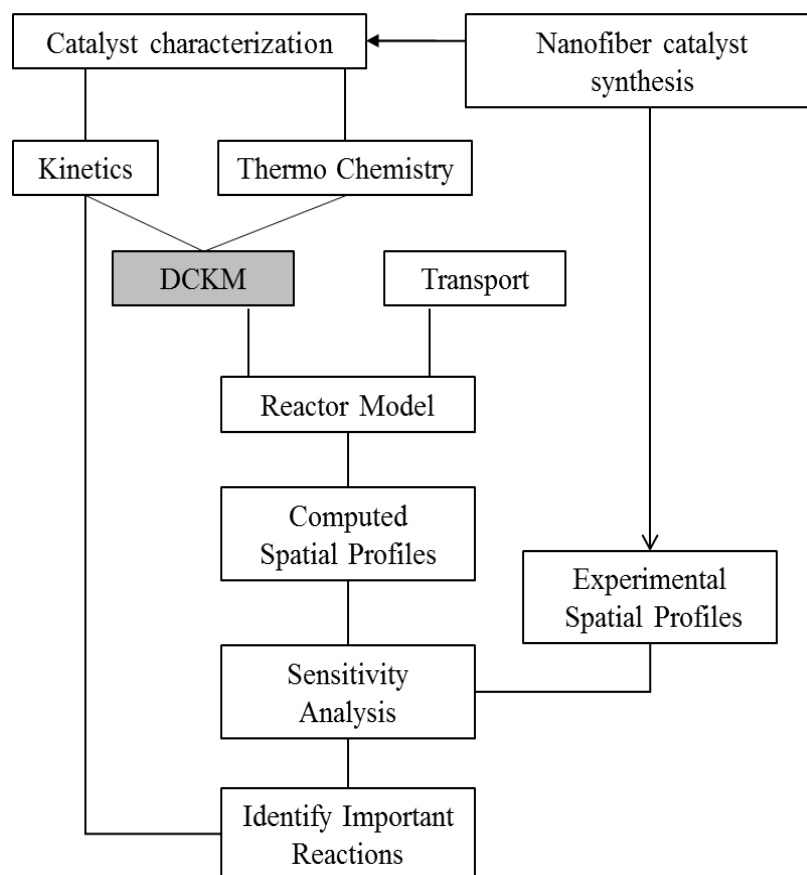
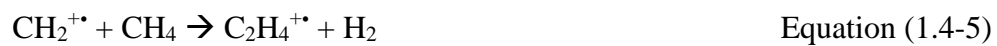
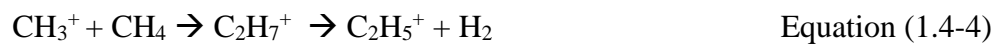


**Figure 1.4-6.** Overview of our approach for development of a comprehensive DCKM

The proposed approach will provide validated DCKMs for OCM reaction over a broad range of reaction conditions. With the availability of DCKM, we will be in a better position to identify improved reaction conditions, superior reactor configurations, and find new leads for catalytic materials that are needed to exceed the current product yield limits of OCM and possibly other applicable partial oxidation reactions.

Furthermore, we will be conducting a kinetic modeling study for OCM reactor under plasma condition. For this, additional sets of gas-phase plasma reactions for gas phase ionization, mainly described by Equations (1.4-2)-(1.4-8), will be identified, developed, and added to the existing gas-phase methane oxidation reactions.



**SUBJECT 2. ATMOSPHERIC REDUCTION OF CO<sub>2</sub> TO METHANOL**

## CHAPTER 2.1. Introduction

For the past centuries, the concentration of carbon dioxide (CO<sub>2</sub>) in the atmosphere has risen drastically. Undoubtedly, this increase in CO<sub>2</sub> emissions contributes to the climate change and health hazards. Hence, development of efficient systems and processes for capture, storage and utilization of atmospheric CO<sub>2</sub> is of great importance. As an economical, safe, and renewable carbon source, CO<sub>2</sub> turns out to be an attractive C<sub>1</sub> building block for basic chemicals and fuels. Therefore, it would be highly desirable to develop alternative fuels from CO<sub>2</sub> feed.

Methanol as an excellent fuel alternative and basic building block of many chemicals, creates a great opportunity for development of processes to utilize CO<sub>2</sub> as a chemical feedstock. Catalytic reduction of carbon dioxide (CO<sub>2</sub>), the primary product of the combustion of fossil fuels and an increasing atmospheric greenhouse gas, to methanol (CH<sub>3</sub>OH) represents an important step towards the creation of a sustainable society.

### 1.1. Methanol: A Valuable Product of CO<sub>2</sub> Hydrogenation

Methanol has been proposed both as a chemical feedstock as well as a convenient liquid medium of energy storage [62], [63], [64], [65]. Although the CO<sub>2</sub> reduction process requires molecular hydrogen, it can easily be obtained by the electrolysis of water using electricity obtained from photovoltaic cells and/or wind turbines [66], [67], [68], [69].

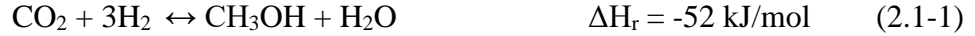
Once produced, methanol can be transformed into a wide range of useful chemicals, such as dimethyl ether (DME), ethylene, gasoline, diesel and others using established technologies [62], [63], [64]. In addition, methanol can also directly be used in combustion engines, with minimal changes to the internal combustion engines, and fuel cells thereby allowing the generation of electricity over 24/7 and enabling energy sustainability.

At present methanol is produced exclusively from syngas (CO/CO<sub>2</sub>/H<sub>2</sub>) obtained from the reforming of fossil fuels in centralized facilities, over Cu-ZnO catalysts promoted by Al<sub>2</sub>O<sub>3</sub> at 50-100 bar pressure and 200-300 °C temperature [70], [71], [72], [73], [74], [75], [76]. This catalyst is also active for the water gas shift reaction (WGSR) [77], [78], [79], [80].

## 1.2. Recent Advances in Catalytic CO<sub>2</sub> Hydrogenation to Methanol

Due to the practical importance of direct CO<sub>2</sub> hydrogenation, catalysts for methanol synthesis have been studied extensively and optimized for use with syngas at high pressures. Most catalysts investigated to date for the CO<sub>2</sub> hydrogenation reaction were based on the Cu-ZnO-Al<sub>2</sub>O<sub>3</sub> system modified by metals such as Zr, Ga, Si, Al, B, Cr, V, Ti, etc [77], [78], [79], [80]. Although high methanol yields have been reported at 360 bar pressure, [81], [82] the Cu-ZnO-Al<sub>2</sub>O<sub>3</sub> system could not efficiently be used for neat CO<sub>2</sub> reduction at low pressures, [82], [83] calling for the discovery and optimization of new and more active catalysts for methanol synthesis. Recently, Ni-Ga/SiO<sub>2</sub> system prepared by standard impregnation technique was reported to give methanol yields that were comparable to the traditional Cu-ZnO-Al<sub>2</sub>O<sub>3</sub> catalysts prepared by co-precipitation at atmospheric pressure [83]. In another recent work, also at 1 atm, CeO<sub>x</sub> deposited on Cu(111) and Cu-CeO<sub>x</sub> co-deposited on TiO<sub>2</sub>(110) surfaces (by chemical vapor deposition) produced significantly more CH<sub>3</sub>OH than the Cu-ZnO(0001) surfaces [84]. A hybrid oxide catalyst comprising MnO<sub>x</sub> nanoparticles supported on mesoporous-Co<sub>3</sub>O<sub>4</sub> was also recently reported to exhibit significant CH<sub>3</sub>OH production at a higher pressure of 4 bar, together with CO and hydrocarbon products [85].

Methanol formation from carbon dioxide and hydrogen proceeds via the following reaction:



Which is often accompanied by the reverse water gas reaction (RWGS):



In the presence of acidic surfaces, e.g. H-ZSM5 or  $\gamma\text{-Al}_2\text{O}_3$ , the  $\text{CH}_3\text{OH}$  produced is readily converted to DME by dehydration, which is also a desirable product: [70], [71], [86]



Here we report the discovery of a series of superior and novel holmium-containing catalytic materials for the low pressure reduction of  $\text{CO}_2$  to  $\text{CH}_3\text{OH}$  and DME. Using impregnation and high throughput (HT) catalyst screening technologies developed in our laboratories, [87], [88] we systematically investigated the oxides of single, binary and ternary combinations of 27 metals (total metal atom loading of 20 wt %) with several support materials in over 3000 experiments. Our studies led to the discovery of  $\gamma\text{-Al}_2\text{O}_3$  supported  $\text{Cu-GaO}_x\text{-HoO}_y$  as well as  $\text{Cu-CeO}_x\text{-HoO}_y$  and  $\text{Cu-LaO}_x\text{-HoO}_y$  systems, which exhibit superior methanol production and less CO formation than all other materials reported in the literature. The observed higher activity and selectivity of the Cu-Ga-Ho system could to be related to the formation of tri-metallic active sites.

## CHAPTER 2.2. Experimental Set-Up

In this section the synthesis, screening and analysis methods for the testing and discovery of multi-metallic catalysts for the direct reduction of CO<sub>2</sub> are discussed.

In general, the catalysts were prepared using co-impregnation method using mixture of metal salt solutions on different support materials. Catalyst screenings were performed using our sophisticated high throughput (HT) array channel micro-reactor system and the performance analysis of the catalysts were carried out using a Varian micro-GC 490 (gas chromatography) system.

### 2.1. Catalysts Preparation

Catalysts were prepared by impregnating powders of  $\gamma$ -Al<sub>2</sub>O<sub>3</sub>, CeO<sub>2</sub>, SiO<sub>2</sub>, TiO<sub>2</sub> and Y-ZrO<sub>2</sub> with single, binary and ternary mixtures of aqueous (nitrate) salt solutions of 27 metals: Li, Na, Rb, Cs, Mg, Ca and Sr, Ga, V, Cr, Mn, Co, Ni, Cu, Zn, Zr, Ru, Ir, Ag, Au, La, Ce, Pr, Dy, Ho, Er and Yb. Systematic consideration of different metal ratios and loadings necessitated the preparation of about 3000 distinct catalytic materials. For example, the tri-metallic Cu-GaO<sub>x</sub>-HoO<sub>y</sub>/ $\gamma$ -Al<sub>2</sub>O<sub>3</sub> catalysts were prepared as follows: A predetermined amount of  $\gamma$ -Al<sub>2</sub>O<sub>3</sub> support (Alfa Aesar, surface area of ~150 m<sup>2</sup>/g) was soaked in an aqueous solution of Cu(NO<sub>3</sub>)<sub>2</sub>·2.5H<sub>2</sub>O, Ga(NO<sub>3</sub>)<sub>3</sub>·6H<sub>2</sub>O and Ho(NO<sub>3</sub>)<sub>3</sub>·5H<sub>2</sub>O (Alfa Aesar) at concentrations previously determined to yield the desired metal loadings. The mixture is then dried at 120 °C while stirring and followed by calcining in air at 450 °C for 6 h. In addition, the recently reported hybrid MnO<sub>x</sub>/m-Co<sub>3</sub>O<sub>4</sub> catalyst (#16) was acquired and tested [85].



## 2.2. Catalysts Screening and Analysis

Catalyst screenings were performed using our high throughput (HT) array channel micro-reactor system, which is shown in Figure 2.2-1, details of which will be further described in the next section [87], [88]. The system allows parallel screening of up to 80 catalytic materials. High-throughput screening is one of the most efficient methodologies by which catalytic materials with useful properties may be discovered. The technique, compared to the traditional, one-by-one approach, not only accelerates the discovery process by as much as a thousand times but also reduces costs. High-throughput screening in catalysis research is sometimes referred as “combinatorial chemistry”. The HT system is controlled by a computer program (Catalysis Performance Analysis or CPA) and is used for the screening and discover of all catalytic materials considered in this Section (section 2) of the dissertation.

### *2.2.1. Components of The High Throughput screening system*

The high throughput system is as shown in Figure 2.2-1. It is consisted of four different parts:

1. Micro-reactor system assembled on top of a x-y-z motion system.
2. Heating system, which includes heating cartridges and Eurotherm PID controllers.
3. Feed Gas system, which includes several MKS flow meters, pressure regulator and mixing tube.
4. Analysis Instruments, which includes residual gas analyzer (RGA) mass spec (MS) and micro-GC 490 systems.

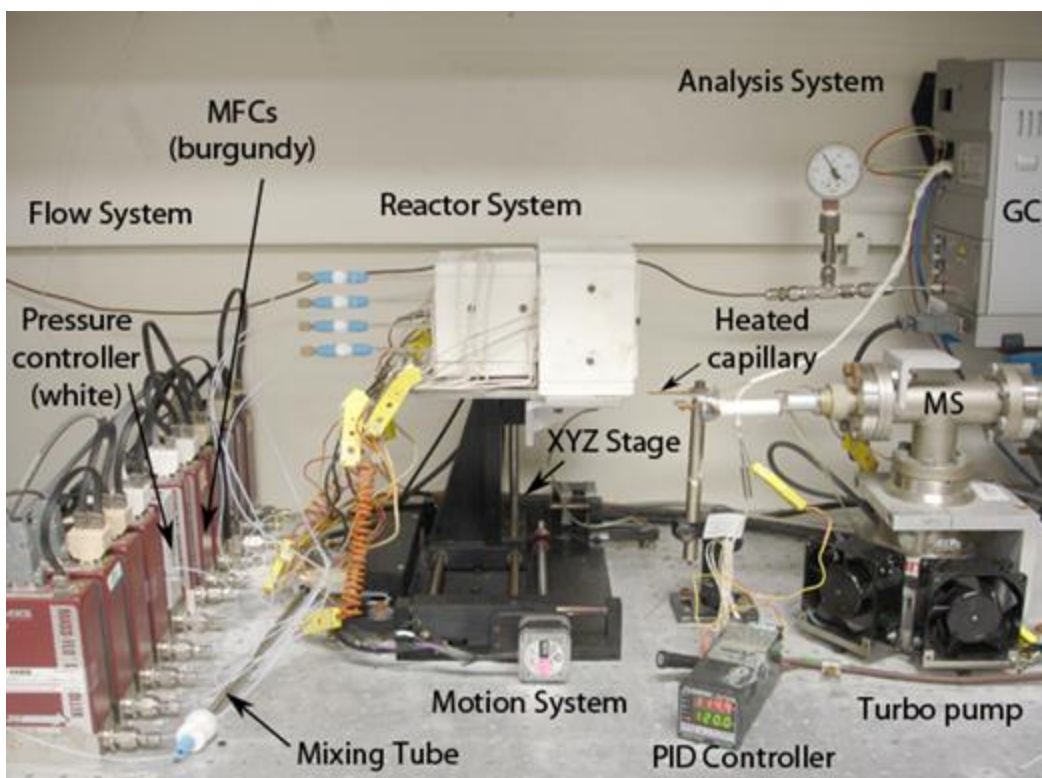


**Figure 2.2-1.** High Throughput Screening System

Components of the micro-reactor are as shown in Figure 2.2-2: A. Each reactor bank with 20 parallel channels (4 banks, total 80 channels); B. Capillary sampling probe; C. Mass spectrometer or Gas Chromatograph; D. Wells containing individual catalyst pellets or powders; E. Temperature controlled heating block with a preheat zone which is not shown; F. Insulation. The top right insert shows the reactant gas (G) flowing over the catalyst bed in the well (D) which results in minimal pressure drop. Each micro-reactor in the bank (H) are isolated by the cover plate I. The capillary probe (B) is also shown inserted into the channel for sampling. In array micro-reactors, reactant gases flow over the flat surfaces of compacted powders (20 mg of  $\gamma$ -Al<sub>2</sub>O<sub>3</sub>-based and 6 mg of SiO<sub>2</sub>-based) of catalytic materials that are placed into the wells in each reactor channel. Consequently, the majority of the gases exit the reactor while only a small fraction (~10%) participate in the catalytic reaction process [88]. This arrangement results in the establishment of

identical flow rates or contact times in every channel, which enables the rapid comparison of the catalytic performances of up to 80 catalysts in a single experiment.

The experiments were carried out in the following manner: First, the catalysts were reduced under H<sub>2</sub>/He (50/50) flow at a temperature in the range of 230-350 °C for 2 h. Catalysts were then cooled to the desired reaction temperature while still under H<sub>2</sub>/He flow, and the gas flow is switched to the reactants. The experiments were performed at 260, 280 and 300 °C, at 1 atm pressure and at gas hourly space velocity (GHSV) of about 200,000 h<sup>-1</sup>. The feed gas consisted of 25 vol% CO<sub>2</sub> (Matheson, 99.9% purity) and 75 vol% H<sub>2</sub> (Matheson, 99.99%). Gas sampling was accomplished by withdrawing reactor exit gases using a passivated 200 micron ID capillary sampling probe that was sequentially positioned into each reactor channel, followed by on-line gas analysis either by mass spectrometry (MS, Stanford Research Systems, RGA-200) or by gas chromatography (Micro-GC Varian, CP-4900). GC had dual Porapak U (10 m) and molecular sieve 13X (10 m) modules each equipped with individual thermal conductivity detectors (TCD). With MS the screening of the entire 80 catalyst library typically takes 30 min or less depending on the sampling capillary dwell time inside and outside the reactor channels and the mass range and scan rate of the MS [87], [88]. Consequently, MS was used for initial screening to rapidly identify promising leads. The leads were then studied in greater detail by gas chromatography in smaller sets of 10 to 20 catalysts to better compare them under similar time-on-stream conditions. In the present work, each GC analysis took about 2.5 min for completion including a 30 s sampling time. The following products were detected and quantified: CH<sub>3</sub>OH, CH<sub>3</sub>OCH<sub>3</sub> (DME), CO, CH<sub>4</sub>, C<sub>2</sub>S and C<sub>3</sub>S. However, only CH<sub>3</sub>OH, CH<sub>3</sub>OCH<sub>3</sub> (DME) and CO are reported in Figure 2.3-1 to prevent clutter.

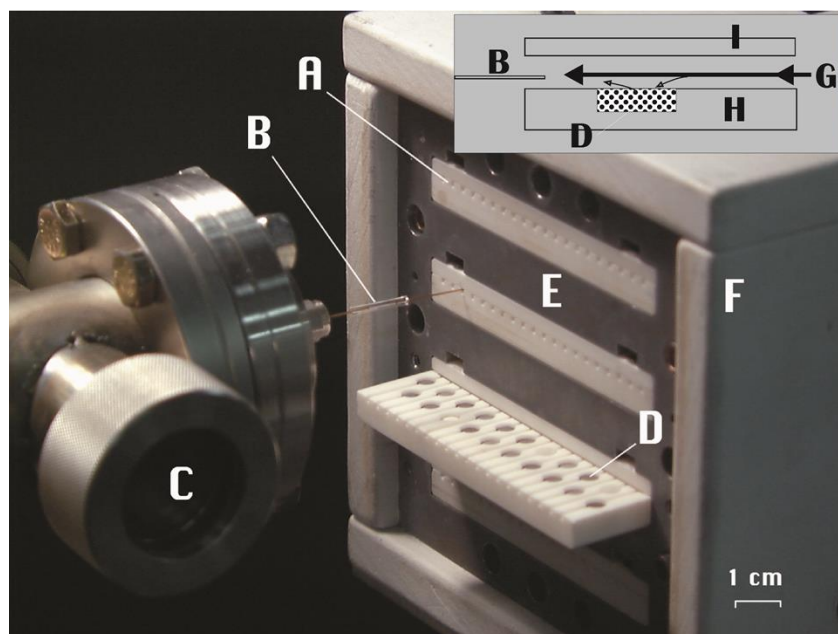


**Figure 2.2-2.** High Throughput micro-reactor System

Since the system has a fixed position capillary probe - the probe leads to a detector for analysis, as shown in Figure 2.2-2 - that has to be inserted precisely into each channel within a certain length (1-5 mm), a robotic x-y-z system (Newmark Systems Irvine, CA) is used to control the movement of the reactor. This motion can be operated through the master CPA program, so that the micro-reactor can be directed to move from one position to another position precisely. The CPA can also move the micro-reactor to a position convenient for loading the reactor arrays into the reactor block, the “loading position”. When non-operational, the reactor can be moved to a “home position”. The motion system must be calibrated once prior to use.

The Gas feed section and the micro-GC analysis systems are identical to the units described previously in section 1 of this dissertation. For more details please refer to Section 1 parts 2.2.1. Feed Gas Control System and 2.2.2. Gas Chromatography System.

## CHAPTER 2.3. Results and Discussions

### 3.1. Initial Screening of Binary Catalytic Systems

Initial screening experiments led to the determination of a number of binary systems that exhibit catalytic activity for CH<sub>3</sub>OH synthesis mostly over the  $\gamma$ -Al<sub>2</sub>O<sub>3</sub> support. These binaries, in decreasing order of CH<sub>3</sub>OH production at 260 °C were: Cu-Ga [75], [89] > Cu-La [90] ~ Cu-Ce [84] > Cu-Ho ~ Cu-Zr [76] > Ga-Ni/SiO<sub>2</sub> [83] ~ Cu-Zn [71], [73], [72] ~ Ga-Ho ~ Cu-Mg > Zn-Ir, which are consistent with the literature. The validity of our experimental approach is supported by the observation that the relative performances of our as-prepared Cu-Zn/Al<sub>2</sub>O<sub>3</sub> and Ga-Ni/SiO<sub>2</sub> catalysts are similar to one another, which is identical to results reported by Studt et al. who used co-precipitation to synthesize the traditional Cu-Zn-Al<sub>2</sub>O<sub>3</sub> catalysts [83].

### 3.2. Ternary Catalytic Systems

The higher performing binaries were then used as the basis to explore the ternary systems at different loadings and temperatures. In Figure 2.3-1, the reactor exit mole percentages for CH<sub>3</sub>OH ( $\times 10^4$ ), DME ( $\times 10^4$ ) and CO ( $\times 0.5 \times 10^3$ ) are presented for our best performing Ho-containing ternary catalysts together with select binary systems for comparison. The values presented in Figure 2.3-1 correspond to the average of three different sets of experiments that were within 10% of each other. It should be noted that CO<sub>2</sub> conversions, thus product mole fractions were small because of high gas velocities used (GHSV~200,000 h<sup>-1</sup>). This way catalysts remained isothermal, which enabled the undertaking of rigorous comparisons of their intrinsic activities. The leads reported here clearly must be studied in greater detail to better understand their structure, activities, selectivities, reaction mechanisms and optimize their performances.

From Figure 2.3-1a it can be seen that our HT experiments produced the following rank order for CH<sub>3</sub>OH production for some of the previously reported catalysts at 260 °C: Cu-Ga<sub>2</sub>O<sub>3</sub> (#3) [75], [89] > Cu-La<sub>2</sub>O<sub>3</sub> (#9) [90] > Cu-CeO<sub>2</sub> (#11) [84] > Cu-Zn-(Zr-Al<sub>2</sub>O<sub>3</sub>)(#7) [76], [91] > Cu-ZrO<sub>2</sub> (#6) [76] > Ga-Ni/SiO<sub>2</sub> (#13) [83] ~ MnO<sub>x</sub>/m-Co<sub>3</sub>O<sub>4</sub> hybrid(#16) [85] ~ Cu-ZnO<sub>2</sub>/Al<sub>2</sub>O<sub>3</sub> (#1) [71], [73], [72]. Unlike its reported high performance at 4 bar, the methanol production of the hybrid MnO<sub>x</sub>/m-Co<sub>3</sub>O<sub>4</sub> catalyst (#16) [85] was surprisingly poor at 1 atm, only on par with the as-prepared Cu-Zn/Al<sub>2</sub>O<sub>3</sub> (#1) ~ Ga-Ni/SiO<sub>2</sub> (#13) systems (see Figure 2.3-1a); nevertheless, it was a very active catalyst producing very high levels of CO and CH<sub>4</sub> along with some C<sub>2</sub>H<sub>4</sub> and higher hydrocarbons (C<sub>3+</sub>).

### 3.3. Superior Catalytic Systems

As evident from Figure 2.3-1, our  $\gamma$ -Al<sub>2</sub>O<sub>3</sub> supported ternary Cu-GaO<sub>x</sub>-HoO<sub>y</sub> catalyst (#4, Cu-Ga-Ho at 8-8-4 metal wt%) together with the Cu-LaO<sub>x</sub>-HoO<sub>y</sub> (#10, Cu-La-Ho at 10-5-5 metal wt%) and Cu-CeO<sub>x</sub>-HoO<sub>y</sub> (#12, Cu-Ce-Ho at 10-5-5 metal wt %) systems significantly outperform the previously reported systems. For example, at 260 °C (Figure 2.3-1a), the Cu-GaO<sub>x</sub>-HoO<sub>y</sub> catalyst (#4) produced CH<sub>3</sub>OH at 1.14x10<sup>-4</sup>%, which is about a factor of 10 higher than the Cu-Zn/Al<sub>2</sub>O<sub>3</sub> system (#1) of 0.112x10<sup>-4</sup>%, while producing similar levels of CO. It is also important to note that our catalyst #4 also produced significant levels of DME. In fact, if we were to add the yields for DME (2x0.42x10<sup>-4</sup>=0.84x10<sup>-4</sup>) and CH<sub>3</sub>OH (1.14x10<sup>-4</sup>) (#4), at 260 °C, the performance of our #4 catalyst would be a factor of 17 higher than the Cu-Zn/Al<sub>2</sub>O<sub>3</sub> (#1) and the Ni-Ga/SiO<sub>2</sub> (#13) catalysts. These results correspond to a CH<sub>3</sub>OH+DME selectivity of 48% for the Cu-GaO<sub>x</sub>-HoO<sub>y</sub> (#4) catalyst at 260 °C. The turnover frequency (TOF) of our Cu-GaO<sub>x</sub>-HoO<sub>y</sub> catalyst (#4) was estimated to be about 1.6x10<sup>-4</sup> s<sup>-1</sup> at 260 °C (Figure 1a) for the combined CH<sub>3</sub>OH and DME; this was calculated by assuming ~7 nm diameter spherical Cu metal clusters (~20,000 Cu atoms)

and ~3,000 surface atoms exposed for reaction and 10% reactant gas utilization [88]. Similar considerations for the Cu-Zn/Al<sub>2</sub>O<sub>3</sub> catalyst (#1) lead to a TOF value of 0.45x10<sup>-5</sup>s<sup>-1</sup>, which is in harmony with the values reported in literature [83], [85].

As seen in Figure 2.3-1, holmium also had a dramatic promotional effect on some of the reported binary CH<sub>3</sub>OH catalyst systems. For example, both CH<sub>3</sub>OH and DME production increased significantly by the Ho-doping of the Cu-Zn/Al<sub>2</sub>O<sub>3</sub> (#1) by more than a factor of two (#2) at 300 °C. For the case of the Cu-CeO<sub>2</sub>(#11), Ho-doping was also influential, increasing CH<sub>3</sub>OH levels by about a factor of two (#12) at 260 °C. However, Ho did not promote CH<sub>3</sub>OH formation in the Ga-Ni/Al<sub>2</sub>O<sub>3</sub> system (#15), while it significantly increased CO and CH<sub>4</sub> (not included in Figure 2.3-1) production.

Increasing the temperature from 260 °C to 280 °C significantly increased CH<sub>3</sub>OH production for our Cu-GaO<sub>x</sub>-HoO<sub>y</sub> (#4) catalyst. However, increasing the temperature further from 280 °C to 300 °C resulted in a smaller increase in CH<sub>3</sub>OH formation. This is not surprising in view of the equilibrium considerations of this exothermic reaction (1) [92]. On the other hand, increasing temperature increased CO production substantially, clearly calling for the need to develop low temperature catalysts for the synthesis of CH<sub>3</sub>OH from CO<sub>2</sub>.

We observed rapid decreases in CH<sub>3</sub>OH production within few hours with the Cu-Zn/Al<sub>2</sub>O<sub>3</sub> (#1) catalyst. None of the γ-Al<sub>2</sub>O<sub>3</sub> supported Cu-GaO<sub>x</sub>-HoO<sub>y</sub> (#4), Cu-LaO<sub>x</sub>-HoO<sub>y</sub> (#10) or Cu-CeO<sub>x</sub>-HoO<sub>y</sub> (#12) exhibited any significant deactivation or change in methanol selectivity during ~10 h of continuous runs and/or after repeated reduction-reaction cycles. The time-on-stream performance of the Cu-GaO<sub>x</sub>-HoO<sub>y</sub> (#4) catalyst presented in Figure 2.3-2 at 260 °C shows that

the combined selectivities for CH<sub>3</sub>OH and DME remained at about 48% for the for the entire 10 h testing period.



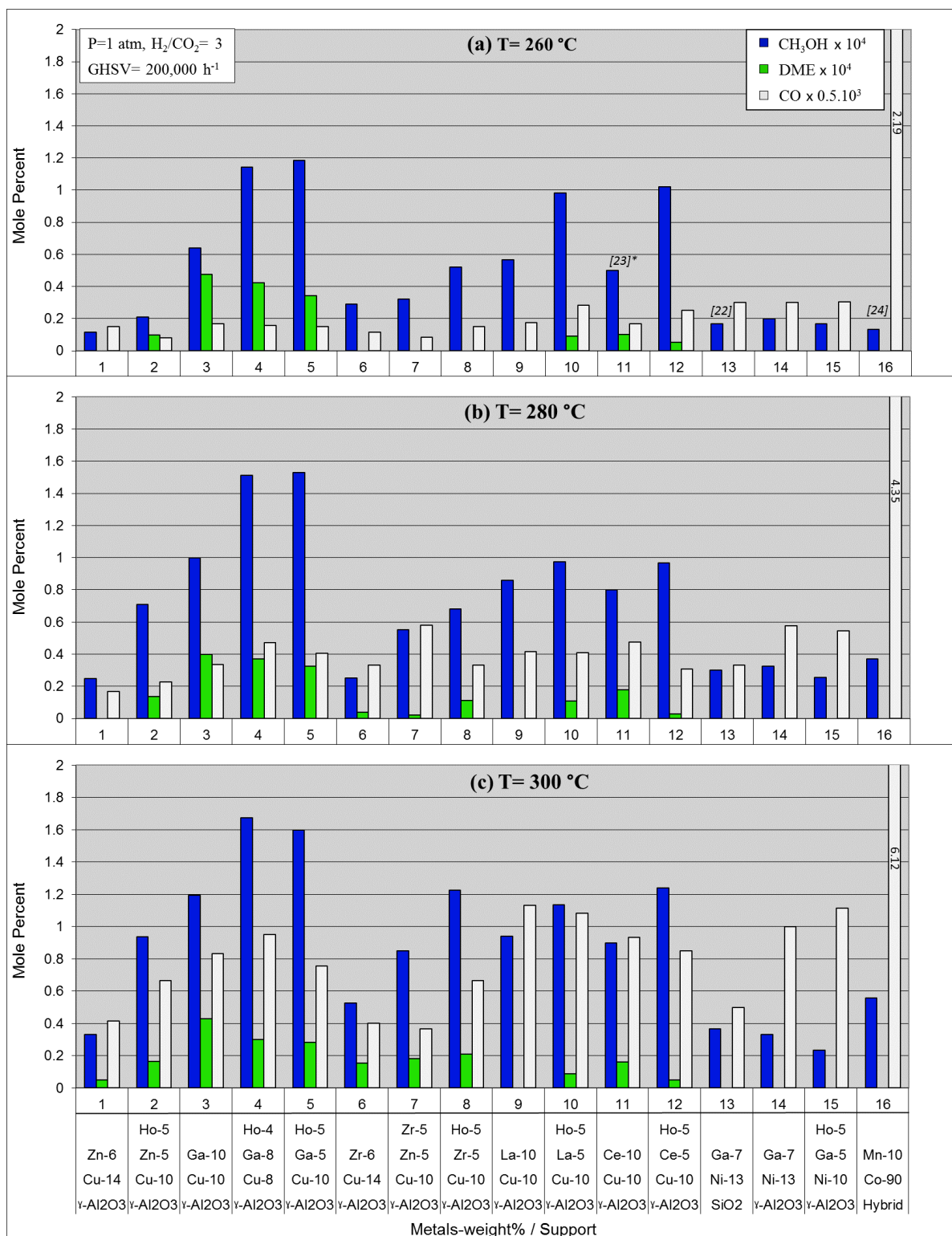


**Figure 2.3-1.** Reactor exit CH<sub>3</sub>OH, DME and CO mole % levels for the high-performing Ho-containing catalysts discovered together with some previously reported catalytic systems under atmospheric pressure at (a) 260 °C, (b) 280 °C and (c) and 300 °C

In the Cu-Zn/Al<sub>2</sub>O<sub>3</sub> system (#1), the metallic copper clusters are accepted to be the sites for methanol synthesis, while ZnO has been proposed to act both as a physical promoter (i.e. assist in the formation of a larger number of surface Cu sites) and for the Cu-ZnO synergy [72]. The same Cu-ZnO sites are also believed to be catalysts for the RWGS reaction. It is also widely accepted that CH<sub>3</sub>OH production from CO<sub>2</sub> over Cu-ZnO catalysts occur via the formation of surface formates HCOO-M → HCOOH-M → CH<sub>3</sub>O<sub>2</sub>-M → CH<sub>2</sub>O-M → CH<sub>3</sub>O-M → CH<sub>3</sub>OH-M [92].

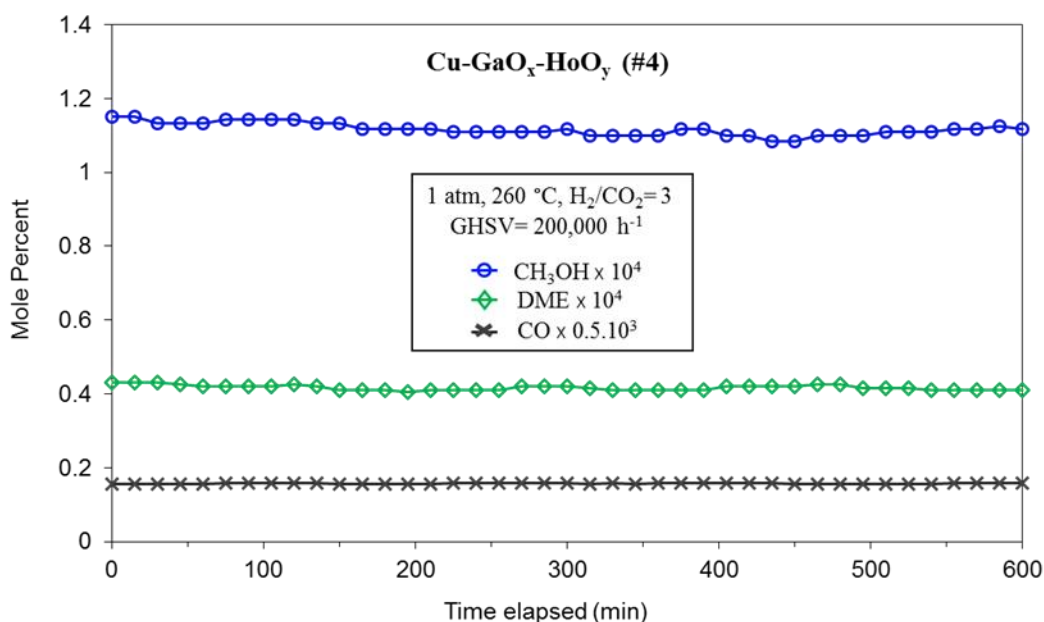


**Figure 2.3-2.** Time-on-stream behavior of the Cu-GaO<sub>x</sub>-HoO<sub>y</sub> (#4) catalyst shows no significant performance change over a 10 h testing period

As for the Ni-Ga/SiO<sub>2</sub> system (#13), the Ga-rich sites were reported to facilitate methanol synthesis, while the nickel-rich sites were suggested to be responsible for the RWGS and methanation reactions [83]. Consequently, the superior performance of our Cu-GaO<sub>x</sub>-HoO<sub>y</sub> system (#4), which contains both Cu and Ga sites, can be due, in part, to their mutual physical and

chemical promotion (#3). The remarkable effect of Ho in promoting methanol synthesis could be attributed to the formation of very small clusters that are highly dispersed. As discussed in the characterization section below, STEM images of the #4 catalyst, as shown in Figure 2.3-3, showed the presence of few atom (1-3 atom) Ho clusters. Some of these clusters also appear to be positioned along the Cu and Ga cluster interfaces or on the surfaces of their alloys, creating tri-metallic sites that could be the key for the promotion of methanol synthesis by Ho. This picture is also supported by the experimentally observed rank order of activity of the CH<sub>3</sub>OH catalysts, i.e. Cu-Ga-Ho (#4) > Cu-Ga (#3) > Cu-Ho > Ga-Ho.

#### 3.4. Characterization Studies for the Cu-Ga-Ho System

We characterized our reduced Cu-GaO<sub>x</sub>-HoO<sub>y</sub> system (#4, Cu-Ga-Ho at 8-8-4 metal wt % loading and 5.3/4.8/1 atom ratio) using BET analysis (Micromeritics ASAP 2020 using N<sub>2</sub>), scanning transmission electron microscopy (STEM, JEOL, JEM-ARM200CFEG UHR, with EDS), X-ray diffraction (XRD) (Bruker Xflash 5010) and X-ray photoelectron (XPS) (ThermoScientific K-Alpha) spectroscopy in order to develop insights on its structure and surface chemistry. BET analysis indicated a surface area of 142 m<sup>2</sup>/g for the catalyst, consistent with the alumina support. The XRD spectra (see supporting information) only showed the features of the Al<sub>2</sub>O<sub>3</sub> support, suggesting the presence of amorphous Cu, Ga and Ho moieties or their nano-size crystallites. This is also confirmed by the high resolution TEM studies (Figure 2.3-3). HR-TEM image of the reduced catalyst #4 (Cu-Ga-Ho at 8-8-4 wt % metal loading and atom ratios of 5.2/4.8/1) is provided in Figure 2.3-3a and Figure 2.3-3b. Element mapping images obtained from STEM/EDS indicate the presence of 5-7 nm Ga (2.3-3e) and Cu (Figure 2.3-3f) clusters in close proximity to one another, which also suggest the possibility of some alloy formation. On the other hand, the Ho map did not show the presence of larger particles (Figure 2.3-3c). The high angular

annual dark field (HAADF) Z-contrast ( $\sim z^2$ ) image indicated that the heavy Ho ( $z=165$ ) is highly dispersed and exists only as few-atom (1-3 atom) clusters (Figure 2.3-3d).

Ex-situ XPS studies of the reduced #4 catalyst indicated the presence of both  $\text{Cu}^0$  and  $\text{CuO}$ , while only  $\text{Ga}_2\text{O}_3$  and  $\text{Ho}_2\text{O}_3$  were observed at the surface (see Supplementary Materials). Some oxidation of Cu was observed because of exposure to the atmosphere during sample transfer to the XPS system. Consequently  $\text{Cu-Ga}_2\text{O}_3\text{-Ho}_2\text{O}_3$  could be the correct representation of the #4 catalyst. It is interesting to note that the surface concentration of Ga was higher, while those for Cu and Ho were lower than their nominal/bulk values for the  $\text{Cu-Ga}_2\text{O}_3\text{-Ho}_2\text{O}_3$  (#4) catalyst. Further characterizations as well as detailed kinetic and quantum modeling studies are underway to better understand the nature of the active site(s) and to explain the mechanism of action of our novel  $\text{Cu-Ga}_2\text{O}_3\text{-Ho}_2\text{O}_3$  system in promoting  $\text{CH}_3\text{OH}$  synthesis from  $\text{CO}_2$  and  $\text{H}_2$ .

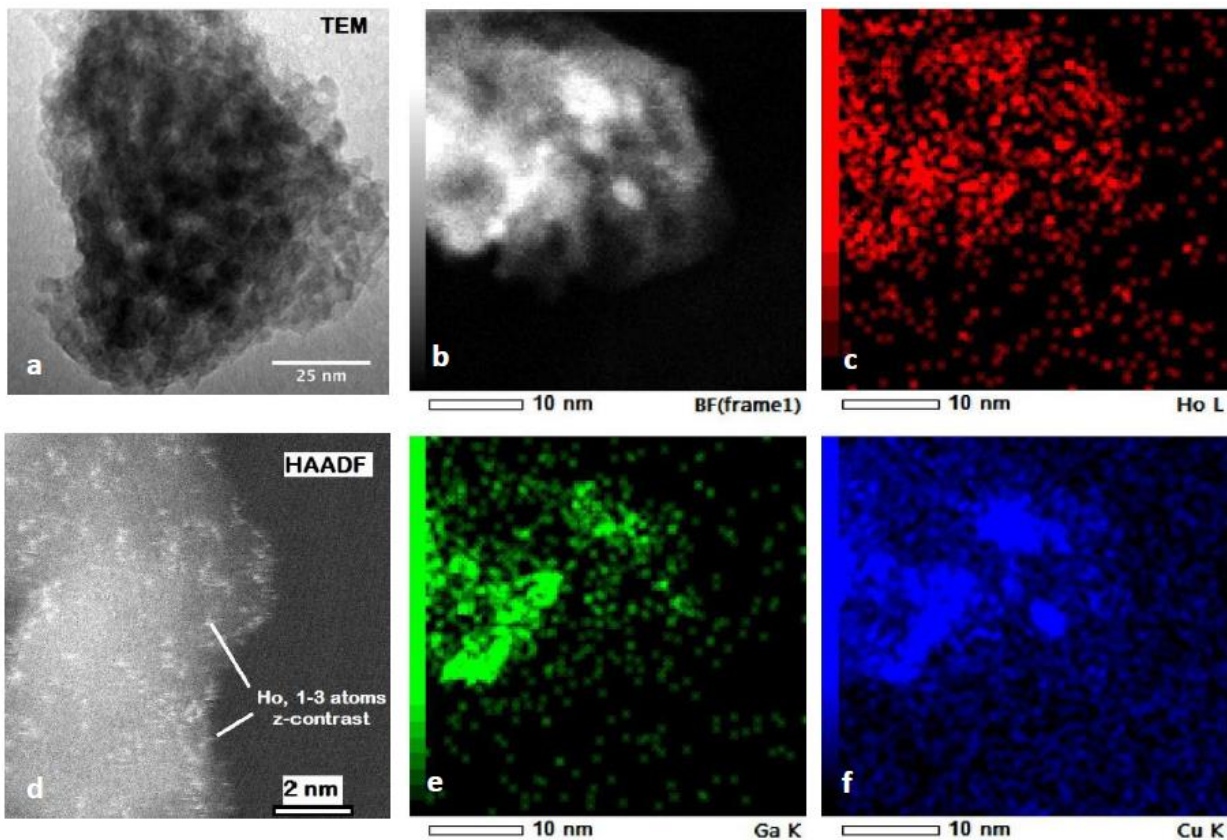


**Figure 2.3-3.** HR-TEM image of the reduced catalyst #4 (Cu-Ga-Ho at 8-8-4 wt % metal loading and atom ratios of 5.2/4.8/1) (Fig 2.3-3a and b) and STEM-EDS images of the element maps of Ho (Fig 2.3-3c and d) Ga (Fig 2.3-3e) and Cu (Fig 2.3-3f) over  $\gamma$ -Al<sub>2</sub>O<sub>3</sub>

## CHAPTER 2.4. Future Work

Development of sustainable technologies for the synthesis of Carbon-Neutral Liquid Fuels (CNLF) that can easily be stored, transported, and later converted into other chemicals and energy is of immense practical significance for the future of our civilization. Methanol ( $\text{CH}_3\text{OH}$ ), energy density of 4.6 kWh/L, and ammonia ( $\text{NH}_3$ ), energy density of 4.3 kWh/L are examples of CNLFs. Both can be synthesized from air, water and renewable energy sources such as photovoltaics and wind, as such could provide an ultimate route towards carbon-neutral economy.

Our High throughput system is capable of screening large number of catalytic systems in a short time. Therefore, it can be effectively used to screening and discovery of novel catalytic systems for complex processes such as methanol synthesis, ammonia synthesis, etc.

Therefore, as future work, I propose to undertake the following “discovery coupled with scientific feedback” research program to develop new generations of high performing catalysts for the low pressure synthesis of  $\text{CH}_3\text{OH}$  and  $\text{NH}_3$  (a subset of CNLF):

(1) High-throughput (HT) synthesis and screening of new class of catalytic material for the reduction reactions of  $\text{CO}_2$  and  $\text{N}_2$  to be used in packed bed reactor (PBRs). Although many kinds of metal-based catalysts have been examined for the synthesis of methanol and ammonia, Cu and Fe remain the main active catalyst components for the reduction of  $\text{CO}_2$  and  $\text{N}_2$ , respectively. Recently, our group made advances in the catalytic synthesis of both methanol and ammonia synthesis under atmospheric pressure. Using our novel HT screening system (parallel testing of 80 different catalysts), we discovered superior Holmium (Ho)-containing Cu-Ga-Ho/ $\text{Al}_2\text{O}_3$  and Cu-La-Ho/ $\text{Al}_2\text{O}_3$  catalysts for the reduction of  $\text{CO}_2$  into  $\text{CH}_3\text{OH}$ . The Cu-Ga-Ho catalyst system exhibited 10-17x higher activity at significantly higher selectivity than the traditional Cu-Zn- $\text{Al}_2\text{O}_3$  catalysts under the experimental conditions. Similarly, we discovered tungsten oxide

(WO<sub>3</sub>) supported Co-Ni system that exhibited similar activity for ammonia synthesis at atmospheric pressure in comparison to the commercial Ru-based catalysts, tested at 4 atm. Neither of these catalytic systems have been optimized yet. One of my future goals will be to further investigate and improve these new discoveries. The promotional effect of Ho on some of the reported binary methanol synthesis catalysts is of great interest and needs to be further investigated. Ho also plays an effective role in improving selectivity by suppressing amount of CO, which could be the result of the undesired water-gas shift reaction. The zeolite like pore structure of WO<sub>3</sub> support and its reduced form of hydrogen tungsten bronzes (HWO<sub>3</sub>), an electron-proton mixed conductor with high conductivity and chemical reactivity, also present a great potential for new class of catalytic materials for the reduction reactions.

(2) I will be collaborating with staff in the Department of Material Science and Engineering to perform characterization studies of select catalytic materials using XRD, SEM, EDX, TEM, XPS, BET, AES, TPR to better understand the physical and chemical structures of these catalytic systems to better establish active sites for catalysis, plausible surface moieties and elementary reactions and their kinetic parameters. Based on current studies, the rate-determining step for CO<sub>2</sub> reduction process on Cu surface is the formation and hydrogenation of formate (HCOO<sup>-</sup>). The rate-determining step of ammonia synthesis is cleavage of the N≡N bond, because the bond energy is extremely large (945 kJ mol<sup>-1</sup>). Therefore, understanding and controlled synthesis of the surface active sites, surface moieties and electronic nature of appropriate promoters are key to establishing the reaction mechanism and enhancing the efficiency of these processes.

(3) Built on the past literature and in conjunction with our studies in part (2) and detailed *in situ* studies (XRD, FTIR, and NMR), that will enable me to better understand the nature of surface moieties, a preliminary elementary reaction mechanism will be developed. This reaction

mechanism together with transport models, e.g. ChemkinPro, will be used to validate and optimize the experiments in a PBR reactor.

(4) I also plan to undertake computational studies (i.e. DFT studies) of select catalytic systems. DFT studies will help develop better insights for the refinement of reaction mechanisms and their associated kinetic parameters. These quantum chemical calculations together with catalyst characterizations of part (2) and (3) will help us better understand role of Ho and WO<sub>3</sub> support for synthesis and optimization of novel catalytic systems.

Based on the above mentioned newly discovered catalysts, novel reactor and process designs will also be considered to further increase yield of these reduction reactions. The yield and selectivity of the reduction reactions are usually low when using a single-stage PBR. Therefore, utilizing advanced modeling tools (such as CFD modeling as in Comsol) and established reaction mechanism in part (3) we can explore novel reactor systems. Innovative and cost-effective reactors such as membrane or electrochemical-based reactors will be considered and studied. Discovery of new class of catalytic materials, which are highly active and robust, could allow for the fabrication of effective membrane reactors, electrodes, and/or solid state cells. Using my knowledge of modern process design tools, such as HYSYS, I plan to perform relevant process simulations for the analysis and assessment of plant operations and costs analysis.



## **Appendices (Select Publications)**

### A1. New Insights into the Oxidative Coupling of Methane

# New Insights into the Oxidative Coupling of Methane from Spatially Resolved Concentration and Temperature Profiles

Bahman Zohour, Daniel Noon, and Selim Senkan<sup>\*[a]</sup>

Oxidative coupling of methane (OCM) is a high-temperature process involving the transformation of methane into ethane and ethylene, which are valuable intermediates for the chemical processing industry.<sup>[1]</sup> Despite decades of long research that has resulted in thousands of papers and hundreds of patents, OCM still remains at the research stage. Although many OCM catalysts have been reported,<sup>[2]</sup> there appears to be an upper limit for the yield of C<sub>2+</sub> products of approximately 25% per reactor pass, for which the kinetic reasons are largely unknown. It has been recognized that to make progress in the OCM an improved quantitative understanding of the underlying detailed chemical kinetic mechanisms (DCKMs) of the coupled surface and gas-phase reactions must be developed and validated over the very broad range of conditions encountered in the process.<sup>[3–6]</sup> DCKMs comprise a comprehensive description of chemical transformations in terms of irreducible chemical events or elementary reactions for which independent rate coefficient parameters, frequently expressed in the form  $k = AT^n \exp(-E/RT)$ , are either available from direct measurements or estimated from theoretical considerations.<sup>[3,5–7]</sup> DCKMs are then combined with models describing the transport phenomena for the realistic simulation of the performance of the OCM reactors.<sup>[3,5,7]</sup> With the availability of DCKMs, we will then be in a better position to identify improved OCM conditions, superior reactor configurations, and new leads for catalytic materials that are needed to exceed the 25% limit for C<sub>2+</sub> product yields.<sup>[3]</sup>

Validation of DCKMs requires experimental data of high information content because of the presence of a large number of species participating in an even larger number of elementary reactions. Although DCKMs for OCM have been reported in the past,<sup>[3,6]</sup> they were all validated by using integral reactor data, that is, reactor exit conditions. However, this is not a particularly demanding test for mechanism validation. In fact, different DCKMs can readily predict similar OCM reactor exit concentrations, as estimated kinetic parameters are used for many of the elementary reactions. Therefore, the performance of more comprehensive validation tests such as the prediction of the absolute concentration profiles of all the major and minor species within the catalytic packed-bed reactors is necessary for the development of truly predictive DCKMs for the OCM process. However, we are not aware of such information-rich data sets in the open OCM literature.

Herein, we report, for the first time, the spatially resolved comprehensive species concentrations and temperature profiles in a fixed-bed OCM reactor by using microprobe sampling. Although microprobe sampling techniques have long been used in high-temperature flame-combustion research to obtain spatial temperature and concentration profiles,<sup>[8–10]</sup> their adaptation to and use in heterogeneous catalysis is relatively recent. One of the earliest applications of microprobe sampling to catalysis was in the determination of the concentration profiles of species in the catalytic partial oxidation of methane to produce CO and H<sub>2</sub> in a Pt- and Rh-coated  $\alpha$ -Al<sub>2</sub>O<sub>3</sub> foam.<sup>[11–13]</sup>

Experiments were performed by using a fixed-bed tubular reactor system, as shown in Figure 1. The reactor was packed with La<sub>2</sub>O<sub>3</sub>-CeO<sub>2</sub> nanofiber fabric catalysts that were prepared by electrospinning a viscous solution of polyvinylpyrrolidone (PVP; 1.3 MDa, 0.60 g), water/ethanol ( $\approx$  1:1 wt ratio, 9.5 g) in which the metal precursors, as La(NO<sub>3</sub>)<sub>3</sub>·6H<sub>2</sub>O and Ce(NO<sub>3</sub>)<sub>3</sub>·6H<sub>2</sub>O (La/Ce weight ratio = 3, 0.35 g), were dissolved.<sup>[14]</sup> The electrospun material was calcined at 625 °C in a furnace to form metal oxide nanofiber fabrics. SEM images confirmed that the nanofibers had an average diameter of approximately 90 nm. The fabric also had a low BET area of approximately 20 m<sup>2</sup>g<sup>-1</sup>, which suggested that the nanofibers were dense and did not possess internal porosity. This fabric (20 mg) was

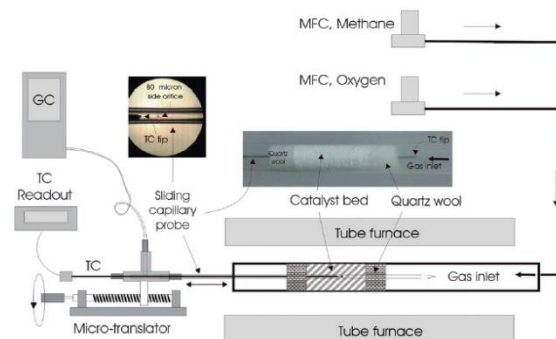


**Figure 1.** The reactor system used to acquire spatial temperature and concentration profiles. The reactor comprised a 6 mm diameter quartz tube packed with La<sub>2</sub>O<sub>3</sub>-CeO<sub>2</sub> nanofiber fabric catalyst (20 mg), which was sandwiched between quartz wool plugs (20 mg, right image). Gas samples were withdrawn from within the packed bed by using an 800  $\mu$ m closed-end capillary with an approximately 80  $\mu$ m side sampling orifice (left image) that was centrally inserted into the reactor. Gas analysis was accomplished by on-line gas chromatography (GC). Spatial profiles were generated by sliding the capillary within the packed bed by using a microtranslation device. Temperature profiles were measured by a 250  $\mu$ m diameter K-type thermocouple (TC) that was inserted into the capillary after the concentration profile measurements. The tip of the thermocouple was placed at the same location of the sampling orifice.

[a] B. Zohour, D. Noon, Prof. Dr. S. Senkan  
Department of Chemical and Biomolecular Engineering  
University of California  
Los Angeles CA 90095 (USA)

loosely packed into a 6 mm diameter quartz tube and sandwiched between quartz wool plugs (20 mg, Figure 1). The bulk density and void fraction of the bed were determined to be approximately  $0.3 \text{ g cm}^{-3}$  and 0.94, respectively. The reactor was placed inside a cylindrical tubular furnace, which preheated the feed gases and the catalyst bed. The total flow of reactant gases was maintained at  $160 \text{ cm}^3 \text{ min}^{-1}$  at standard temperature and pressure (STP) in all of the experiments by using electronic mass flow controllers (MFCs; MKS Billerica, MA). This flow rate corresponded to a nominal space time of approximately 60 ms. The experiments were performed at 101.3 kPa.

Gas sampling was accomplished by centrally inserting a conically tapered and closed-end quartz capillary tube ( $800 \mu\text{m}$ ; Friedrich and Dimock, Millville, NJ) into the packed bed followed by gas analysis by on-line gas chromatography (Varian 4900 Mini GC, with  $5 \text{ \AA}$  molecular sieves and Poraplot U columns). The capillary had an  $80 \mu\text{m}$  diameter orifice laser drilled on its side<sup>[12,13]</sup> to withdraw gases from within the bed (see inset in Figure 1). The location of the sampling orifice and the overall length of the probe were designed such that the capillary tip always remained outside the packed bed at any sampling position to avoid gas bypass. The capillary probe withdrew gas samples at a rate less than  $5 \text{ cm}^3 \text{ min}^{-1}$  at STP; thus, the flow within the reactor ( $160 \text{ cm}^3 \text{ min}^{-1}$  at STP) was minimally perturbed. Temperature measurements were performed by placing a thin ( $250 \mu\text{m}$  diameter) K-type thermocouple inside the capillary probe in the absence of gas withdrawal. The tip of the thermocouple was positioned at the sampling orifice. Capillary sampling lines as well as the GC injection system were heated to approximately  $100^\circ\text{C}$  to prevent water condensation in the transfer lines. The temperature and concentration profiles were obtained by moving the capillary (with and without the thermocouple) in the axial direction by using a micropositioning device (Velmex, Bloomfield, NY). Positional accuracy associated with the placement of the capillary probe within the reactor was estimated to be  $\pm 0.25 \text{ mm}$ . Similar uncertainty would be expected to exist between the temperature and concentration profiles as well.

In Figures 2, 3, and 4, the spatially resolved temperature and species mole percent profiles are presented for  $\text{CH}_4/\text{O}_2=7$ , 9, and 11, respectively, without the use of a diluent gas. A total of nine species were quantified:  $\text{CH}_4$ ,  $\text{O}_2$ ,  $\text{C}_2\text{H}_6$ ,  $\text{C}_2\text{H}_4$ ,  $\text{C}_3\text{H}_8/\text{C}_3\text{H}_6$  ( $\text{C}_3$ ),  $\text{H}_2$ ,  $\text{H}_2\text{O}$ ,  $\text{CO}$ , and  $\text{CO}_2$ . With the exception of the concentration of  $\text{H}_2\text{O}$ , which was calculated from oxygen atom balances, all of the species were quantified directly from GC measurements by using a multipoint GC calibration process performed before the OCM experiments. In Figure 5, the spatially resolved  $\text{CH}_4$  conversions and  $\text{C}_{2+}$  ( $\text{C}_2\text{H}_6 + \text{C}_2\text{H}_4 + \text{C}_3$ ) selectivities are also presented. As is evident from these figures, the spatial concentration and temperature profiles measured in the early parts of the catalytic bed provide information-rich data on the kinetics and mechanism of the OCM. In contrast, profiles are essentially featureless and contain very limited information towards the reactor exit.

In all of the figures, the location of the catalyst bed is indicated by vertical dashed lines; the catalyst packing starts at approximately 4 mm and ends at approximately 18 mm, which

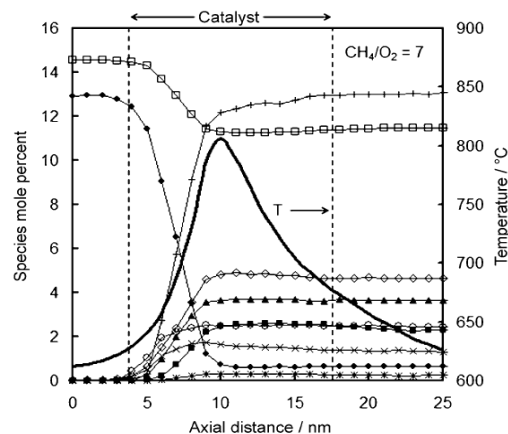


**Figure 2.** Spatial temperature and species mole percent profiles for a feed  $\text{CH}_4/\text{O}_2$  ratio of 7. Total gas flow rate was  $160 \text{ cm}^3 \text{ min}^{-1}$ , which corresponded to a nominal space time of approximately 60 ms. Furnace temperature was  $600^\circ\text{C}$ .  $\text{CH}_4/\text{O}_2$  ( $\square$ ),  $\text{O}_2$  ( $\blacklozenge$ ),  $\text{C}_2\text{H}_6$  ( $\blacktriangle$ ),  $\text{C}_2\text{H}_4$  ( $\blacksquare$ ),  $\text{C}_3$  ( $*$ ),  $\text{H}_2\text{O}$  ( $+$ ),  $\text{H}_2$  ( $\circ$ ),  $\text{CO}_2$  ( $\diamond$ ),  $\text{CO}$  ( $\times$ ),  $T$  (—).

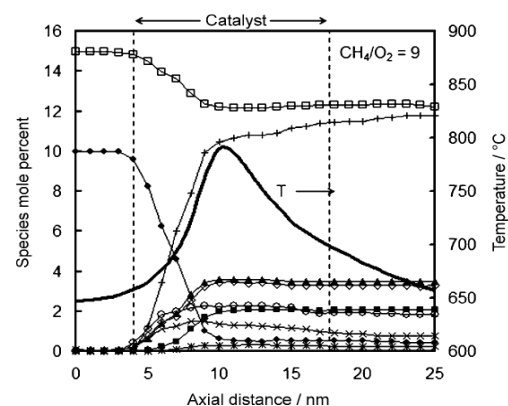


**Figure 3.** Spatial temperature and species mole percent profiles for a feed  $\text{CH}_4/\text{O}_2$  ratio of 9. Total gas flow rate was  $160 \text{ cm}^3 \text{ min}^{-1}$ , which corresponded to a nominal space time of approximately 60 ms. Furnace temperature was  $640^\circ\text{C}$ .  $\text{CH}_4/\text{O}_2$  ( $\square$ ),  $\text{O}_2$  ( $\blacklozenge$ ),  $\text{C}_2\text{H}_6$  ( $\blacktriangle$ ),  $\text{C}_2\text{H}_4$  ( $\blacksquare$ ),  $\text{C}_3$  ( $*$ ),  $\text{H}_2\text{O}$  ( $+$ ),  $\text{H}_2$  ( $\circ$ ),  $\text{CO}_2$  ( $\diamond$ ),  $\text{CO}$  ( $\times$ ),  $T$  (—).

corresponds to a bed depth of 14 mm. The feed temperature used (furnace temperature) for each  $\text{CH}_4/\text{O}_2$  ratio was different because of the different ignition temperatures that were exhibited. As expected, the feed temperature for ignition increased from  $600^\circ\text{C}$  for  $\text{CH}_4/\text{O}_2=7$  (Figure 2) to  $640^\circ\text{C}$  for  $\text{CH}_4/\text{O}_2=9$  (Figure 3) and to  $730^\circ\text{C}$  for  $\text{CH}_4/\text{O}_2=11$  (Figure 4). However, the peak reactor temperatures were relatively close to one another at  $810$ ,  $790$ , and  $840^\circ\text{C}$  for  $\text{CH}_4/\text{O}_2=7$ , 9, and 11, respectively. The temperature profiles as shown in these figures are direct thermocouple measurements. The possible presence of radial-temperature gradients was also explored by simultaneously placing multiple thermocouples at the same axial position but at different radial positions during the reaction. These measurements indicated maximum radial temperature differen-



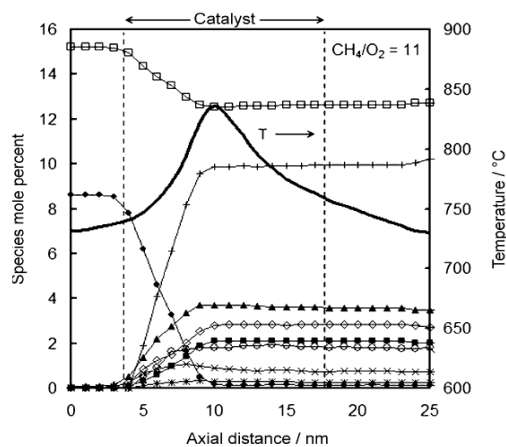


**Figure 4.** Spatial temperature and species mole percent profiles for a feed  $\text{CH}_4/\text{O}_2$  ratio of 11. Total gas flow rate was  $160 \text{ cm}^3 \text{ min}^{-1}$ , which corresponded to a nominal space time of approximately 60 ms. Furnace temperature was  $730^\circ\text{C}$ .  $\text{CH}_4/6$  ( $\square$ ),  $\text{O}_2$  ( $\blacklozenge$ ),  $\text{C}_2\text{H}_6$  ( $\blacktriangle$ ),  $\text{C}_2\text{H}_4$  ( $\blacksquare$ ),  $\text{C}_3$  ( $*$ ),  $\text{H}_2\text{O}$  ( $+$ ),  $\text{H}_2$  ( $\circ$ ),  $\text{CO}_2$  ( $\times$ ),  $\text{CO}$  ( $\times$ ),  $T$  (—)

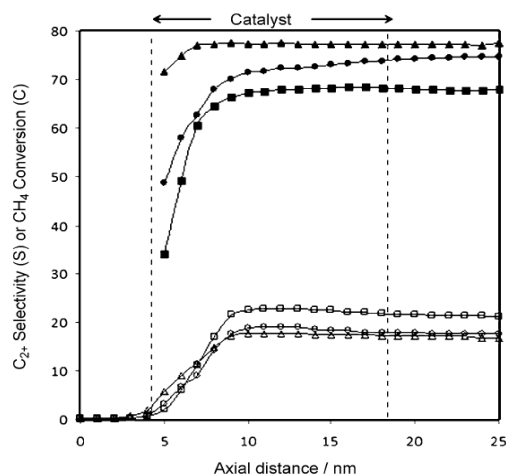


**Figure 5.** Spatial profiles for  $\text{CH}_4$  conversions and  $\text{C}_{2+}$  selectivities for the different  $\text{CH}_4/\text{O}_2$  ratio experiments. Total gas flow rate was  $160 \text{ cm}^3 \text{ min}^{-1}$ , which corresponded to a nominal space time of approximately 60 ms. S,  $\text{CH}_4/\text{O}_2 = 7$  ( $\blacksquare$ ); S,  $\text{CH}_4/\text{O}_2 = 9$  ( $\bullet$ ); S,  $\text{CH}_4/\text{O}_2 = 11$  ( $\blacktriangle$ ); C,  $\text{CH}_4/\text{O}_2 = 7$  ( $\square$ ); C,  $\text{CH}_4/\text{O}_2 = 9$  ( $\circ$ ); C,  $\text{CH}_4/\text{O}_2 = 11$  ( $\triangle$ ).

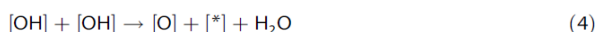
ces in the  $10\text{--}20^\circ\text{C}$  range at peak reactor temperatures of approximately  $800^\circ\text{C}$ . Consequently, the treatment of the reactor as quasi-1D appears to be a reasonable assumption.

At  $\text{CH}_4/\text{O}_2 = 7$  (Figure 2), the temperature sharply increased to its maximum of approximately  $800^\circ\text{C}$  at 6 mm into the catalyst bed (i.e., at 10 mm axial distance on the plot), which corresponds to a temperature increase of approximately  $200^\circ\text{C}$ , and it then decreased towards the exit of the reactor. Given that the reactor was not adiabatic, this temperature profile was expected and could be used directly in reactor simulations to de-

couple the energy balance equation from mole balance equations.<sup>[3,6]</sup>

The species profiles in Figure 2 exhibit both confirmatory and new information. First, the integral OCM performance was 23%  $\text{CH}_4$  conversion and 68% selectivity for  $\text{C}_{2+}$  products (see also Figure 5), an expected result. However, close examination of the profiles at the upstream part of the catalyst reveals intriguing new information. Most importantly, significant levels of  $\text{H}_2$  were produced very early in the catalytic zone, that is, prompt  $\text{H}_2$ ; a peak level of approximately 2.5 mol% was reached within 5 mm inside the catalyst bed (9 mm axial distance). Within this zone, the reactor temperature was still relatively low at  $625\text{--}675^\circ\text{C}$ ; thus,  $\text{H}_2$  formation is expected to be due to surface-catalyzed reactions. Hydrogen formation is closely followed up by  $\text{CO}_2$  (peak at  $\approx 5\%$ ) and  $\text{CO}$  ( $\approx 1.8\%$ ) formation and then by  $\text{C}_2\text{H}_6$  formation ( $\approx 3.5\%$ ). Hydrogen could be produced by surface reactions similar to those reported in the catalytic partial oxidation of methane to synthesize gas on Pt and Rh surfaces.<sup>[15,16]</sup> However, in our experiments the temperatures were lower and  $\text{CO}_2$  was formed in larger amounts than  $\text{CO}$ . Alternately, the catalytic water gas shift (WGS) reaction, that is,  $\text{H}_2\text{O} + \text{CO} = \text{CO}_2 + \text{H}_2$ , could be another potential route for hydrogen production. Analysis of the experimental data in Figure 2 indicates that the mole fraction ratio  $Y_{\text{CO}_2} \times Y_{\text{H}_2} / (Y_{\text{H}_2\text{O}} \times Y_{\text{CO}})$  was in the 0.5–0.6 range within 5 mm into the catalyst bed. These values are significantly lower than the WGS equilibrium constant of 1.5–2 at the prevailing temperatures; this indicates that  $\text{La}_2\text{O}_3\text{--CeO}_2$  is not a good WGS catalyst. These and other plausible surface reactions leading to  $\text{H}_2$  formation should be incorporated into current DCKMs to broaden their range of applicability and to increase their utility to predict OCM performance over a wide range of operating conditions.<sup>[4,6,7]</sup>

The measured concentration profiles for  $\text{C}_2\text{H}_6$  and  $\text{H}_2\text{O}$  are consistent with the well-established elementary reactions leading to their formation. Surface oxygen species [O] are widely accepted to be responsible for  $\text{CH}_4$  activation, which leads to the formation of  $\text{CH}_3$  radicals and surface [OH].<sup>[4,5,7]</sup> The  $\text{CH}_3$  radicals then diffuse away from the catalyst surface and recombine in the gas phase to produce  $\text{C}_2\text{H}_6$ . Regeneration of the active sites is also well accepted to occur through the formation and desorption of  $\text{H}_2\text{O}$ .<sup>[4,5]</sup> The vacated active sites are then rapidly repopulated by  $\text{O}_2$  chemisorption. These events are summarized by the following elementary reaction set [Eqs. (1)–(4)]:



in which [\*] represents a vacant catalytic surface site for oxygen chemisorption. It is likely that a dynamic equilibrium exists between gaseous  $\text{O}_2$  and the various forms of surface oxygen, for example, chemisorbed and lattice oxygen. Unde-

sired catalytic and gas-phase reactions of CH<sub>3</sub> with O<sub>2</sub> and [O] can also lead to the formation of CO<sub>2</sub> and CO (CO<sub>x</sub>).<sup>[4,5]</sup> C<sub>2</sub>H<sub>4</sub> is then produced by the oxidative or catalytic dehydrogenation of C<sub>2</sub>H<sub>6</sub>. As a consequence, the formation of C<sub>2</sub>H<sub>4</sub> exhibits significant lag relative to that of C<sub>2</sub>H<sub>6</sub>, which is clearly observed in Figure 2. Ethylene levels peaked at 2.5% at 8 mm (12 mm axial distance) into the catalyst bed. Once formed, both C<sub>2</sub>H<sub>6</sub> and C<sub>2</sub>H<sub>4</sub> can also interact with [O] and create additional paths for the formation of CO<sub>x</sub>.<sup>[4,5]</sup> Figure 2 also shows the early formation and rapid rise in the concentration of H<sub>2</sub>O concomitant with a decrease in the concentration of O<sub>2</sub>. It is well recognized that the steady-state rate of the OCM reaction is controlled not by the activation of CH<sub>4</sub> and the formation of C<sub>2</sub>H<sub>6</sub> but by the reactions that lead to the formation of H<sub>2</sub>O (e.g., reaction 4). This is because of the requirement to close the catalytic cycle.<sup>[4,5]</sup> The data presented in Figure 2 are in harmony with this argument, for which sharp changes in species mole fraction profiles cease only after O<sub>2</sub> is largely consumed, that is, at an axial distance of approximately 10–11 mm. Peak H<sub>2</sub>O concentrations reached in this system (CH<sub>4</sub>/O<sub>2</sub>=7) were approximately 13%. Notably, in spite of the presence of an excess amount of CH<sub>4</sub>, some O<sub>2</sub> slipped through the reactor. This is likely caused by the sharp decrease in the temperature, as seen in Figure 2.

In Figure 3, the spatial profiles are presented for CH<sub>4</sub>/O<sub>2</sub>=9. Prompt H<sub>2</sub> formation was also noted in this case, albeit at a slightly lower peak level of approximately 2.2%. The production of CO<sub>2</sub> decreased and reached only 3.5%, whereas C<sub>2</sub>H<sub>6</sub> production increased to a peak level of approximately 3.5%. As before, C<sub>2</sub>H<sub>4</sub> formation lagged behind C<sub>2</sub>H<sub>6</sub> formation and increased to a peak level of approximately 2.1%. The integral CH<sub>4</sub> conversions and C<sub>2+</sub> selectivities were approximately 19 and 72%, respectively (Figure 5). Water formation leveled off at approximately 11–12%. Oxygen slippage was less in this system than in the system with CH<sub>4</sub>/O<sub>2</sub>=7.

The spatial profiles obtained at the highest ratio, CH<sub>4</sub>/O<sub>2</sub>=11, exhibited new trends, as shown in Figure 4. Most importantly, C<sub>2</sub>H<sub>6</sub> was formed very early in the catalyst bed, and significantly, C<sub>2</sub>H<sub>6</sub> production surpassed H<sub>2</sub> production, which is in stark contrast to the experiments for lower CH<sub>4</sub>/O<sub>2</sub> ratios discussed above (i.e., Figure 2). Hydrogen levels peaked at approximately 1.9%. Ethane also became the most abundant product (peak at ≈4%), surpassing CO<sub>2</sub> (peak at ≈3%). However, ethylene levels remained surprisingly similar to those of previous experiments and exhibited a peak concentration of only 2.2%, although the temperatures were significantly higher. As seen in Figure 4, C<sub>2</sub>H<sub>4</sub> production abruptly ceased at 6 mm into the catalyst bed (10 mm axial distance), at which point O<sub>2</sub> was entirely consumed and the temperature peaked at 840 °C. This result is consistent with the generally accepted mechanism that oxidative dehydrogenation of C<sub>2</sub>H<sub>6</sub> is the primary path for C<sub>2</sub>H<sub>4</sub> formation in OCM experiments. Similar observations were made in experiments in which lower CH<sub>4</sub>/O<sub>2</sub> ratios were studied (Figures 2 and 3). Maximum water concentration of approximately 10% was also reached at 6 mm into the catalyst bed. Exit CH<sub>4</sub> conversions were lowest at approxi-

mately 17%, whereas C<sub>2+</sub> selectivities were the highest at 77% among the three CH<sub>4</sub>/O<sub>2</sub> ratios investigated.

In conclusion, comprehensive spatial species and temperature profiles were reported for the first time in an oxidative coupling of methane (OCM) fixed-bed reactor. Profiles presented at different CH<sub>4</sub>/O<sub>2</sub> ratios provided information-rich data necessary for the refinement and rigorous validation of detailed chemical kinetic mechanisms for this important process. The measurements revealed new insights into the kinetics and mechanism of the OCM reaction. In particular, the formation of significant levels of prompt H<sub>2</sub> deserve further investigation, as catalytic H<sub>2</sub> formation has not been addressed fully in the OCM literature. Such reactions should be incorporated in future detailed chemical kinetic mechanisms to broaden their range of applicability and to increase their utility in predicting OCM performance over a wide range of operating conditions.

### Acknowledgements

We thank Laboratory Catalyst Systems (LLC) for the use of their facilities and database. B.Z. acknowledges the University of California, Los Angeles (UCLA) Graduate Division Fellowship. D.N. acknowledges the National Science Foundation (NSF) MCTP - DGE-0654431.

**Keywords:** heterogeneous catalysis • kinetics • microprobe sampling • oxidative coupling • reaction mechanisms

- [1] M. C. Alvarez-Galvan, N. Mota, M. Ojeda, S. Rojas, R. M. Navarro, J. L. G. Fierro, *Catal. Today* **2011**, *171*, 15–23; C. Hammond, S. Conrad, I. Hermans, *ChemSusChem* **2012**, *5*, 1668–1686.
- [2] U. Zavyalova, M. Holena, R. Schlögl, M. Baerns, *ChemCatChem* **2011**, *3*, 1935–1947.
- [3] J. W. Thybaut, J. Sun, L. Olivier, A. C. Van Veen, C. Mirodatos, G. B. Marin, *Catal. Today* **2011**, *159*, 29–36; J. Sun, J. W. Thybaut, G. B. Marin, *Catal. Today* **2008**, *137*, 90–102.
- [4] M. Y. Sinev, Z. T. Fattakhova, V. I. Lomonosov, Y. A. Gordienko, *J. Nat. Gas Chem.* **2009**, *18*, 273–287.
- [5] Z. Stansch, L. Mleczko, M. Baerns, *Ind. Eng. Chem. Res.* **1997**, *36*, 2568.
- [6] J. H. J. B. Hoebink, P. M. Couwenberg, G. B. Marin, *Chem. Eng. Sci.* **1994**, *49*, 5453–5463.
- [7] S. Senkan, *Advances in Chemical Engineering*:18, Academic Press, New York, **1992**, 95.
- [8] R. M. Fristrom, A. A. Westenberg, *Flame Structure*, McGraw-Hill, New York, **1965**, 177.
- [9] A. Granada, S. B. Karra, S. Senkan, *Ind. Eng. Chem. Res.* **1987**, *26*, 1901–1905.
- [10] S. B. Karra, S. Senkan, *Combust. Sci. Technol.* **1987**, *54*, 333–347.
- [11] R. Horn, K. A. Williams, N. J. Degenstein, L. D. Schmidt, *J. Catal.* **2006**, *242*, 92–102.
- [12] R. Horn, O. Korup, M. Geske, U. Zavyalova, I. Oprea, R. Schlögl, *Rev. Sci. Instrum.* **2010**, *81*, 064102.
- [13] O. Korup, S. Maylyankariyev, M. Geske, C. F. Goldsmith, R. Horn, *Chem. Eng. Process.* **2011**, *50*, 998–1009.
- [14] D. Noon, A. Seubsai, S. Senkan, *ChemCatChem* **2013**, *5*, 146–149.
- [15] D. A. Hickman, L. D. Schmidt, *Science* **1993**, *259*, 343–346.
- [16] D. Dalle Nogare, N. J. Degenstein, R. Horn, P. Canu, L. D. Schmidt, *J. Catal.* **2011**, *277*, 134–148.

Received: May 27, 2013

Published online on September 18, 2013

A2. Spatial Concentration and Temperature Profiles in Dual-Packed-Bed Catalytic Reactors:  
Oxidative Coupling of Methane

# Spatial Concentration and Temperature Profiles in Dual-Packed-Bed Catalytic Reactors: Oxidative Coupling of Methane

Bahman Zohour, Daniel Noon, and Selim Senkan<sup>\*[a]</sup>

Oxidative coupling of methane (OCM) is a complex surface catalysis and gas-phase reaction process to transform methane into ethane, ethylene and higher molecular weight hydrocarbons ( $C_{2+}$ ). However, the  $C_{2+}$  product yields in single-pass fixed-bed reactors have been limited by the intrusion of gas-phase combustion reactions. To remedy this problem, a dual-bed OCM reactor configuration was explored in which the  $O_2$  feed was distributed between two sequential packed bed reactors with interstage cooling using  $La_2O_3$ - $CeO_2$  nanofiber fabric catalysts. At the overall  $CH_4/O_2$  feed ratio of 4.0, the dual-bed reactor configuration with split  $O_2$  introduction resulted in the ultimate  $C_{2+}$  product yield of 21%, which is significantly higher than the 16% observed in the single-bed OCM reactor. In addition, spatially resolved species concentration and temperature profiles along the entire length of the dual-bed reactor were also acquired by using in situ microprobe sampling.

Oxidative coupling of methane (OCM) is a complex surface catalysis and gas-phase reaction process to convert natural gas into ethane and ethylene, which are valuable intermediates for the chemical industry.<sup>[1,2]</sup> In spite of decades-long research and many OCM catalysts reported,<sup>[2]</sup> no commercially viable catalyst has been developed. There appears to be an upper limit of  $C_{2+}$  yield of approximately 25% per reactor pass, which has been attributed to the intrusion of gas-phase combustion reactions at high temperatures.<sup>[3]</sup> Therefore, catalyst design alone may not be sufficient to result in the breakthrough needed for the commercialization of the OCM process. Consequently, a combined effort, both in catalyst development and in novel reactor systems and operating schemes are needed to advance the field.<sup>[4]</sup>

Early reactor simulations that used global OCM reaction kinetics were particularly encouraging, as they suggested the feasibility for attaining yields for  $C_{2+}$  products as high as +50% if the  $O_2$  feed was distributed along the reactor, that is, by using membrane-type reactors.<sup>[5-7]</sup> Although these predictions may not be realistic, as the global reaction models used are well recognized to be of limited predictive value, they nevertheless create optimism regarding the future of the OCM process. More realistic and accurate predictions of the attainable yields can be accomplished by using detailed chemical ki-

netic mechanisms (DCKM). DCKM comprise a comprehensive description of chemical transformations in terms of irreducible chemical events or elementary reactions. DCKM, in conjunction with transport models, are crucial not only to correlate available experimental data but also to predict performance well outside the ranges of parameters investigated, including conditions under which the acquisition of the experimental data may be infeasible, for example, higher pressures and temperatures. However, the development and validation of DCKM require experimental data of high information content because of the presence of a large number of species participating in an even larger number of elementary reactions.

Recently, we reported spatial temperature and species concentration profiles in a packed-bed OCM reactor acquired by microprobe sampling.<sup>[8]</sup> This information-rich data, in addition to being particularly useful for DCKM work, revealed the early, that is, prompt, formation of  $H_2$  in the OCM process, even before the formation of  $C_2H_6$ . This discovery suggested that the existing DCKM for the OCM processes<sup>[9,10]</sup> clearly must be revised to render them useful for predictive purposes. Our previous work<sup>[8]</sup> also demonstrated a significant weakness of using traditional integral reactor data, that is, reactor exit measurements, to develop reaction mechanisms.

Herein, we report for the first time spatially resolved species concentration and temperature profiles in a dual fixed-bed OCM reactor with interstage  $O_2$  injection by using microprobe sampling<sup>[8]</sup> and demonstrate that the yields of  $C_{2+}$  products in the OCM can significantly be increased by distributed  $O_2$  feed, as noted earlier.<sup>[5-7]</sup> The information-rich spatial profiles also provide new quantitative insight into the close coupling of the formation of  $C_{2+}$  products and  $O_2$  levels in OCM reactors and, as such, should be valuable for the improvement and validation of predictive models.

## Experimental Section

Experiments were performed by using a dual fixed-bed tubular reactor system, as shown in Figure 1. The reactor was sequentially packed with  $La_2O_3$ - $CeO_2$  nanofiber fabric catalysts that were prepared by electrospinning a viscous solution of polyvinylpyrrolidone (PVP, 0.60 g, 1.3 MDa), water/ethanol ( $\approx 1:1$  w/w, 9.5 g) into which the metal precursor (0.35 g), as  $La(NO_3)_3 \cdot 6H_2O$  and  $Ce(NO_3)_3 \cdot 6H_2O$ , were dissolved having a La/Ce weight ratio of 3.<sup>[11]</sup> The electrospun material was calcined at 625 °C in a furnace to form metal-oxide nanofiber fabrics. SEM images confirmed that the nanofibers had an average diameter of approximately 90 nm. The fabric also had a low BET area of approximately  $20 \text{ m}^2 \text{ g}^{-1}$ , which suggested that the nanofibers were dense and did not possess internal porosity.

[a] B. Zohour, D. Noon, Prof. Dr. S. Senkan  
Department of Chemical and Biomolecular Engineering  
University of California, Los Angeles CA 90095 (USA)



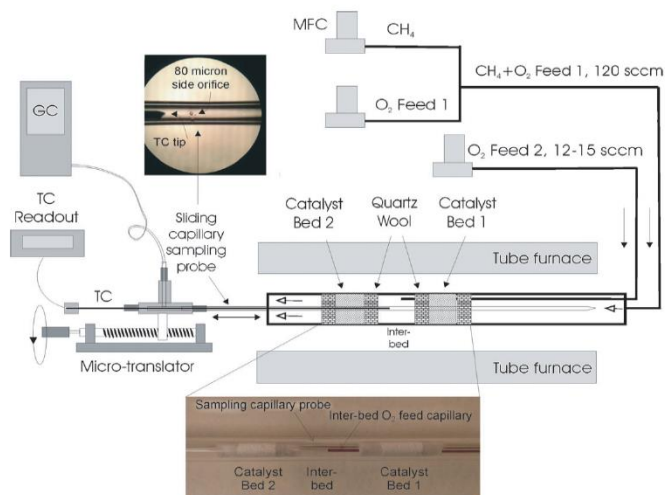


**Figure 1.** The reactor system used to acquire spatial temperature and concentration profiles. The reactor is a 6 mm diameter quartz tube packed with two 20 mg  $\text{La}_2\text{O}_3\text{-CeO}_2$  nanofiber fabric catalyst beds (10 mm deep). Each bed is sandwiched between 20 mg quartz-wool plugs (5 mm deep), with an interbed spacing of 15 mm. The reactants are fed to the first reactor at a rate of  $120 \text{ mL s}^{-1}$  STP. A second  $\text{O}_2$  feed is introduced to the middle of the interbed through a capillary tube at a rate of  $12\text{--}15 \text{ mL s}^{-1}$  STP. Gas samples were withdrawn from within the packed bed by using an  $800 \mu\text{m}$  closed-end capillary tube with four approximately  $80 \mu\text{m}$  side sampling orifices that was centrally inserted into the reactor bed. Gas analysis was accomplished by on-line gas chromatography. Spatial profiles were generated by sliding the capillary within the packed bed by using a microtranslation device. Temperature profiles were measured by a  $250 \mu\text{m}$  diameter K-type thermocouple (TC) that was inserted into the capillary in separate experiments. The tip of the thermocouple was placed at the same location of the sampling orifice. Close-up images of the packed reactor (bottom) and the capillary sampling probe (top) are also shown.

As shown in Figure 2, two sections each with 20 mg of this fabric was loosely packed into a 6 mm diameter quartz tube ( $\approx 10$  mm bed depth) and sandwiched between two 20 mg quartz wool plugs ( $\approx 5$  mm bed depth). The interbed spacing was approxi-

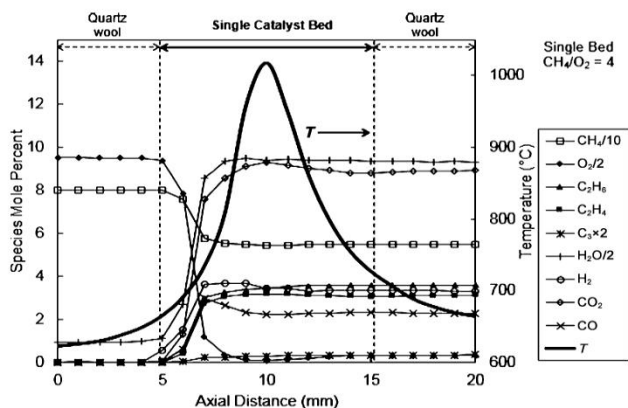


**Figure 2.** Spatial temperature and species mole percent profiles for a feed  $\text{CH}_4/\text{O}_2$  ratio of 4. Total gas flow rate was  $120 \text{ cm}^3 \text{ min}^{-1}$ , which corresponds to a nominal space time of approximately 70 ms (SB1).

mately 15 mm long. The bulk density and void fraction of the catalytic beds were determined to be approximately  $0.3 \text{ g cm}^{-3}$  and 0.94, respectively. The dual-bed reactor was placed inside a cylindrical tubular furnace to preheat the feed gases. In all experiments, the flow rate of the reactant gases to the first bed was maintained at  $120 \text{ cm}^3 \text{ min}^{-1}$  at STP ( $\text{mL min}^{-1}$ ) by using electronic mass flow controllers (MFC, MKS Billerica, MA). This flow rate corresponds to a nominal space time of approximately 60 ms per bed. The interstage  $\text{O}_2$  was introduced at the middle of the interspace, that is, at approximately 27–28 mm by using a quartz capillary feed tube ( $800 \mu\text{m}$ , Friedrich and Dimock, Millville, NJ) at a rate of  $12\text{--}15 \text{ mL min}^{-1}$  (see Figure 2). The experiments were performed at 101.3 kPa.

Gas sampling was accomplished by centrally inserting a conically tapered and closed end quartz capillary tube into the packed beds followed by gas analysis by on-line gas chromatography (Varian 4900 Mini GC, with molecular sieve 5A and Poraplot U columns). The sampling capillary had four perpendicularly oriented  $80 \mu\text{m}$  diameter orifices laser drilled on its side<sup>[12,13]</sup> to withdraw gases from within the bed (see inset in Figure 1). The location of the sampling orifice and the overall length of the probe were designed such that the capillary tip remained well outside both packed beds at any sampling position to avoid gas bypass within the beds. The sampling capillary probe withdrew gases at a rate less than  $5 \text{ mL min}^{-1}$ , which thus minimally perturbed the flow within the reactor (total flow  $\approx 120\text{--}135 \text{ mL min}^{-1}$ ). This sampling rate corresponded to an average gas velocity of  $50\text{--}100 \text{ cm s}^{-1}$  within the capillary (depending on the temperature), which enabled the rapid removal of the gas samples from within the reactor. The fact that the measured concentration profiles remained flat, that is, did not change with axial position within the quartz wool, the interstage section, and reactor exits further supports the notion that reactions inside the sampling capillary were unimportant in our experiments. Temperature measurements were performed by placing a thin ( $250 \mu\text{m}$  diameter) K-type thermocouple inside the sampling capillary in the absence of gas withdrawal. The tip of the thermocouple was positioned at the sampling orifice. The possible presence of radial-temperature gradients was also explored by simultaneously placing multiple thermocouples at the same axial position but at different radial positions during the reaction. These measurements indicated maximum radial temperature differences in the  $10\text{--}20^\circ\text{C}$  range at peak reactor temperatures of  $800\text{--}1000^\circ\text{C}$ . Consequently, treatment of the reactor as quasi 1D appears to be a reasonable assumption.<sup>[8]</sup> Capillary sampling lines outside the reaction furnace as well as GC injection system were heated to approximately  $100^\circ\text{C}$  to prevent water condensation in the transfer lines. Water subsequently was condensed out by using an ice bath before GC analysis. Temperature and concentration profiles were obtained by moving the capillary (with and without the thermocouple) in the axial direction by using a micropositioning device (Velmex, Bloomfield, NY). Positional accuracy associated with the placement of the capillary probe within the reactor was estimated to be  $\pm 0.25 \text{ mm}$ . Similar uncertainty would also be expected to exist between the temperature and concentration profiles.



## Results and Discussion

To demonstrate the improvements provided by the split introduction of O<sub>2</sub> on the yields of C<sub>2+</sub> products, two sets of experiments were performed. First, a single-bed experiment (SB1) was performed in which methane and oxygen were fed at a CH<sub>4</sub>/O<sub>2</sub> ratio of 4.0 at 120 mL min<sup>-1</sup> (≈60 ms space time). In the first dual-bed experiment (DB1), the first reactor feed was at 120 mL min<sup>-1</sup> having a CH<sub>4</sub>/O<sub>2</sub> ratio of 9.0, followed by 12 mL min<sup>-1</sup> O<sub>2</sub> addition into the interstage zone, which thereby maintained the overall CH<sub>4</sub>/O<sub>2</sub> ratio of 4.0.

An additional dual-bed experiment was also performed at the overall CH<sub>4</sub>/O<sub>2</sub> ratio of 4.4 (DB2 experiment) to assess the impact of the CH<sub>4</sub>/O<sub>2</sub> ratio on reactor performance. In this case, the feed flow rate to the first reactor feed was kept at 120 mL min<sup>-1</sup> with a CH<sub>4</sub>/O<sub>2</sub> ratio of 11.0, followed by the introduction of 15 mL min<sup>-1</sup> O<sub>2</sub> to the interstage zone. Notably, in the dual-bed experiments (DB1, DB2) both of the catalyst beds were kept inside one tubular furnace (Figure 1).

In Figure 2, the spatially resolved temperature and species mole percent profiles are presented for the single-bed reactor experiments (SB1). In Figures 3 and 4, the same profiles are presented for the dual-bed reactor experiments DB1 and DB2, respectively. A total of nine species were quantified: CH<sub>4</sub>, O<sub>2</sub>, C<sub>2</sub>H<sub>6</sub>, C<sub>2</sub>H<sub>4</sub>, C<sub>3</sub>H<sub>8</sub>/C<sub>3</sub>H<sub>6</sub> (C<sub>3</sub>), H<sub>2</sub>, H<sub>2</sub>O, CO, and CO<sub>2</sub>. With the exception of H<sub>2</sub>O concentration, which was calculated from oxygen atom balances, all the species were quantified directly from GC measurements by using multipoint GC calibration process performed before the OCM experiments. In Figure 5, the CH<sub>4</sub> conversion and C<sub>2+</sub> (C<sub>2</sub>H<sub>6</sub>+C<sub>2</sub>H<sub>4</sub>+C<sub>3</sub>) selectivity profiles are presented for the SB1, DB1, and DB2 experiments. Methane conversions and C<sub>2+</sub> selectivities were determined from Equations (1) and (2):

$$\text{CH}_4 \text{ conversion [\%]} = \frac{[(\text{CH}_4)_{\text{in}} - (\text{CH}_4)_{\text{out}}]}{[(\text{CH}_4)_{\text{in}}]} \times 100 \quad (1)$$

$$\text{C}_{2+} \text{ selectivity [\%]} = \frac{[2(\text{C}_2\text{H}_6 + \text{C}_2\text{H}_4) + 3(\text{C}_3\text{H}_6)]}{[2(\text{C}_2\text{H}_6 + \text{C}_2\text{H}_4) + 3(\text{C}_3\text{H}_6) + \text{CO}_2 + \text{CO}]} \times 100 \quad (2)$$

In all the figures, the locations of the various sections of the reactor system are indicated by vertical dashed lines; the first La<sub>2</sub>O<sub>3</sub>-CeO<sub>2</sub> nanofiber fabric catalyst packing starts at approximately 5 mm and ends at approximately 15 mm, which corresponds to a bed depth of approximately 10 mm. The first 5 mm in the graphs correspond to the quartz-wool packing. The first bed is followed by another 5 mm of quartz packing, followed by 15 mm of interspace (no packing). The quartz packing for the second bed starts at approximately 35 mm followed by approximately another 10 mm La<sub>2</sub>O<sub>3</sub>-CeO<sub>2</sub> nanofiber

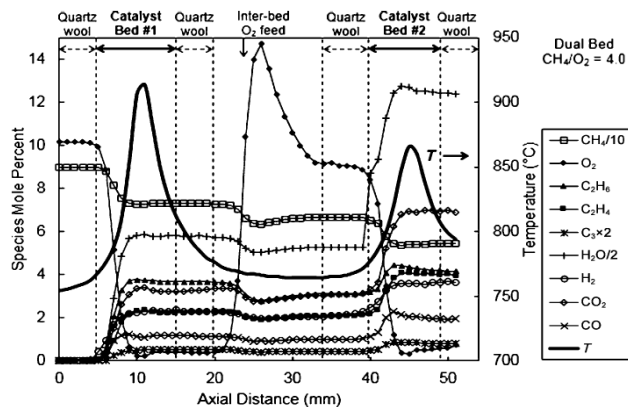


Figure 3. Spatial temperature and species mole percent profiles for the dual-bed reactor system (DB1). Feed to first reactor was 120 cm<sup>3</sup> s<sup>-1</sup> STP at CH<sub>4</sub>/O<sub>2</sub>=9. Interbed O<sub>2</sub> flow rate was 12 cm<sup>3</sup> s<sup>-1</sup> STP, which rendered overall CH<sub>4</sub>/O<sub>2</sub>=4.0.

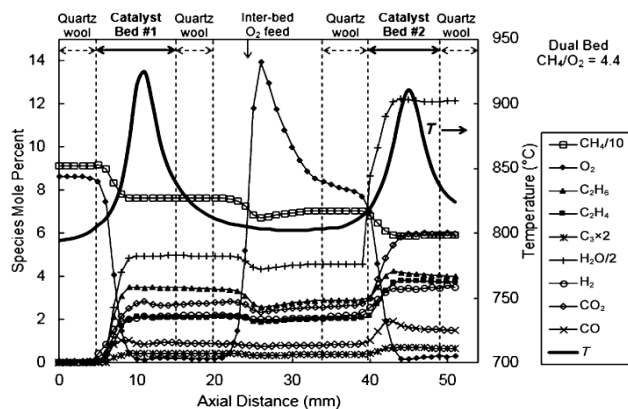


Figure 4. Spatial temperature and species mole percent profiles for the dual-bed reactor system (DB2). Feed to first reactor was 120 cm<sup>3</sup> s<sup>-1</sup> STP at a CH<sub>4</sub>/O<sub>2</sub>=11. Interbed O<sub>2</sub> flow rate was 15 cm<sup>3</sup> s<sup>-1</sup> STP, which rendered overall CH<sub>4</sub>/O<sub>2</sub>=4.4.

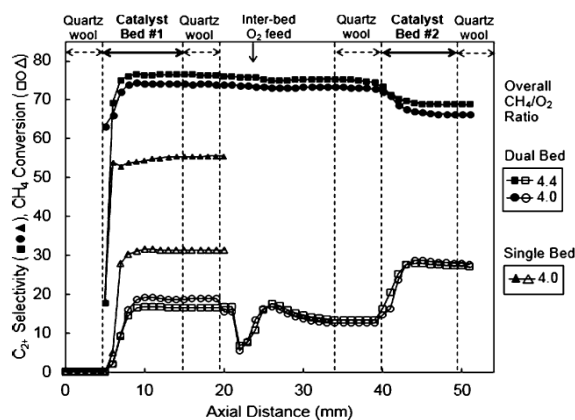


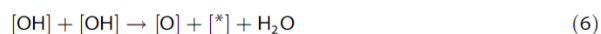
Figure 5. Spatial profiles for CH<sub>4</sub> conversions and C<sub>2+</sub> selectivities for the single-bed (SB1) and dual-bed (DB1, DB2) experiments.

fabric catalyst and 5 mm of quartz-wool packing. The secondary O<sub>2</sub> injection point was at approximately 25 mm, as indicated by an arrow pointing down. Other than the interspace concentration profiles, the location of the O<sub>2</sub> injection point had no discernible effect on the performance of the second reactor.

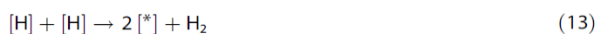
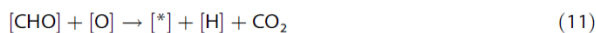
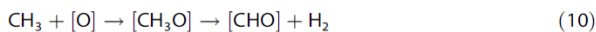
The spatial concentration and temperature profiles for the single-bed experiment (SB1) with a CH<sub>4</sub>/O<sub>2</sub> ratio of 4 were acquired at a furnace temperature (*T<sub>f</sub>*) of 600 °C, which was sufficient to achieve ignition. As seen in Figure 2, the maximum bed temperature reached approximately 1015 °C at approximately 10 mm (i.e., 5 mm within the catalyst zone), concomitant with the near-complete consumption of O<sub>2</sub> and approximately 30% CH<sub>4</sub> maximum conversion and 55% C<sub>2+</sub> selectivity (see also Figure 5). These values represent a C<sub>2+</sub> yield of approximately 16%.

Close examination of the profiles at the upstream part of the catalyst bed reveals significant levels of H<sub>2</sub> production early in the catalytic zone, that is, prompt H<sub>2</sub>; a peak level is reached at approximately 3.7 mol% within 3 mm inside the catalyst bed (8 mm axial distance). Within this zone, the reactor temperature is still relatively low at 650–725 °C; thus, H<sub>2</sub> formation is expected to be due to surface-catalyzed reactions. Hydrogen formation precedes H<sub>2</sub>O formation (peak 19%) and is closely followed up by CO<sub>2</sub> (9.31%) and CO (≈3%) and then by C<sub>2</sub>H<sub>6</sub> (3.6%).

The measured concentration profiles for C<sub>2</sub>H<sub>6</sub> and H<sub>2</sub>O are consistent with the well-established elementary reactions leading to their formation. Surface oxygen species [O] are widely accepted to be responsible for CH<sub>4</sub> activation leading to the formation of CH<sub>3</sub> radicals and surface [OH].<sup>[14–16]</sup> The CH<sub>3</sub> radicals then diffuse away from the catalyst surface and recombine in the gas phase to produce C<sub>2</sub>H<sub>6</sub>. Regeneration of the active sites is also well accepted to occur through the formation and desorption of H<sub>2</sub>O.<sup>[14,15]</sup> The vacated active sites are then rapidly repopulated by O<sub>2</sub> chemisorption. These events are summarized by the following elementary reaction set [Eqs. (3)–(6)]



in which [\*] represents a vacant catalytic surface site for oxygen chemisorption. It is known that a dynamic equilibrium exists between gaseous O<sub>2</sub> and the various forms of surface oxygen, for example, chemisorbed and lattice oxygen. The early formation of H<sub>2</sub>, which is also accompanied by H<sub>2</sub>O, CO<sub>2</sub>, and CO, could be attributed to surface reactions similar to those reported in the catalytic partial oxidation (CPO) of methane to synthesis gas on Pt and Rh surfaces,<sup>[17,18]</sup> or by reactions such as the following [Eqs. (7)–(13)]:



Undesired gas-phase reactions of CH<sub>3</sub> with O<sub>2</sub>, O, and OH can also lead to CO<sub>2</sub> and CO (CO<sub>x</sub>) formation, but at higher temperatures. Ethylene is then produced by the oxidative or catalytic dehydrogenation of C<sub>2</sub>H<sub>6</sub>. As a consequence, C<sub>2</sub>H<sub>4</sub> formation exhibits significant lag relative to C<sub>2</sub>H<sub>6</sub> formation, which is clearly observed in Figure 2. Ethylene levels peaked at 3.1% at 4 mm into the catalyst bed. Once formed, both C<sub>2</sub>H<sub>6</sub> and C<sub>2</sub>H<sub>4</sub> can also interact with [O] and result in the formation of CO<sub>x</sub> as a result of both gas-phase and surface reactions.<sup>[14,15]</sup> Figure 2 also shows the early formation and rapid rise of H<sub>2</sub>O concomitant with a decrease in the O<sub>2</sub> concentration. It is well recognized that the steady-state rate of the OCM reaction is controlled not by the activation of CH<sub>4</sub> and C<sub>2</sub>H<sub>6</sub> formation, but by the reactions that lead to the formation of H<sub>2</sub>O [e.g., Eq. (6)]. This is because of the requirement to close the catalytic cycle.<sup>[14,15]</sup> The data presented in Figure 2 are in harmony with this argument, for which sharp changes in species mole fraction profiles cease only after O<sub>2</sub> is completely consumed and H<sub>2</sub>O formation level off.

The spatial concentration and temperature profiles for the dual-bed operation (DB1) for the OCM reaction at the overall CH<sub>4</sub>/O<sub>2</sub> ratio of 4 as presented in Figure 3 reveal several important features. First, the feed CH<sub>4</sub>/O<sub>2</sub> ratio of 9 used in the first catalyst bed necessitated the use of a higher *T<sub>f</sub>* of approximately 750 °C for ignition. As seen in Figure 3, the bed temperatures rapidly increased within the catalytic zones and reached maximum bed temperatures of 920 °C in the first bed and 866 °C in the second bed, both at approximately 5 mm within the catalyst zones, which corresponds to complete conversion of O<sub>2</sub>. This trend of temperature profile is similar to the SB1 experiment presented in Figure 2 and yet gives us additional insight into the effects of temperature on C<sub>2+</sub> yields in OCM. For example, the peak temperatures in each bed for the dual-bed experiments are significantly lower than those in the single-bed experiment. This was the consequence of the split introduction of oxygen and heat removal realized within the interstage zone, which collectively decreased the maximum temperature attained in the OCM reactors, in spite of the higher ignition temperature. As seen in Figure 5, a C<sub>2+</sub> selectivity of 70% and an ultimate C<sub>2+</sub> yield of 21% was achieved in the DB1 experiment; the latter is a value significantly higher than the 16% yield observed in the single-bed experiment at the same overall CH<sub>4</sub>/O<sub>2</sub> ratio of 4. This clearly demonstrates that distributing the oxygen feed with interstage cooling is a good strategy to increase CH<sub>4</sub> conversion, whereas adverse effects on the selectivity of C<sub>2+</sub> products are minimized. These comparative results are also presented in Table 1.



**Table 1.** Reaction conditions and reactor exit values for conversions, selectivities, and yields.<sup>[a]</sup>

	$T_f$	Overall	$T_{\text{peak}}$	Feed 1	Exit 1	Exit 1	Exit 1	$T_{\text{interbed}}$	$T_{\text{peak 2}}$	Exit 2	Exit 2	Exit 2
	[°C]	CH <sub>4</sub> /O <sub>2</sub>	[°C]	CH <sub>4</sub> /O <sub>2</sub>	CH <sub>4</sub>	C <sub>2+</sub> sel.	C <sub>2+</sub> yield [%]	[°C]	[°C]	CH <sub>4</sub>	C <sub>2+</sub> sel.	C <sub>2+</sub> yield [%]
		ratio		ratio	conv. [%]	[%]	[%]			conv. [%]	[%]	[%]
SB1	600	4	1015	4	30	55	16	–	–	–	–	–
DB1	750	4	920	9	17	77	13	755	866	30	70	21
DB2	780	4.4	930	11	19	74	14	800	910	28	67	19

[a] 1 and 2 refer to catalyst beds.

Second, although the mixing of the secondary O<sub>2</sub> feed with the reactor gases was not instantaneous, as evidenced by the presence of a steep axial oxygen concentration profile, a uniform composition was achieved within the interbed zone close to the upstream quartz-wool packing of the second reactor. Third, the concentrations of all the species decreased upon O<sub>2</sub> introduction (i.e., dilution), but remained virtually unchanged along the interbed zone and within the quartz-wool packing. Furthermore, the temperature in the interbed zone remained at approximately 755 °C, close to the furnace temperature. These measurements clearly indicate both the absence of any gas-phase reactions and the inert nature of the quartz wool. This is a surprising result, as packets of high O<sub>2</sub> concentrations would be expected to cause gas-phase combustion at the indicated interbed temperatures especially if H<sub>2</sub> is present. The OCM reaction commenced once the gases entered the second catalytic bed at approximately 40 mm.

As seen in Figure 3, CO exhibited peak concentrations of 1.2% at 9 mm in the first bed and of 2.2% at 43 mm in the second bed, which ultimately leveled off at 2.0% at the reactor exit. Hydrogen levels were 2.3 and 3.6% at the exits of beds 1 and 2, respectively. Carbon dioxide and water levels reached 3.4 and 11.5% in bed 1, respectively, and became 7 and 25.5% at the exit of the dual-bed reactor, respectively.

Hydrocarbon products generally increased monotonically within the catalytic zones with increasing methane conversions and ceased to change if O<sub>2</sub> was consumed. At the exit of the first bed, the following levels were reached: C<sub>2</sub>H<sub>6</sub> 3.7%, C<sub>2</sub>H<sub>4</sub> 2.23%, and C<sub>3</sub>H<sub>6</sub> 0.25%, whereas CH<sub>4</sub> conversion was 17%. Under these conditions, C<sub>2+</sub> selectivities corresponded to 76.6%, which represents a yield of 13%. However, at the exit of the second bed the species concentrations became: C<sub>2</sub>H<sub>6</sub> 4.4%, C<sub>2</sub>H<sub>4</sub> 4.1%, and C<sub>3</sub>H<sub>6</sub> 0.41%, whereas CH<sub>4</sub> conversion increased to approximately 30%, with a small reduction in the C<sub>2+</sub> selectivities and, hence, a 21% yield at the end of the dual-bed reactor.

Temperature and species concentration profiles within the second catalytic zone were qualitatively similar to those within the first bed, and the reactions ceased immediately after the exhaustion of O<sub>2</sub>. This is an interesting result because unlike the first reactor, the feed to the second catalyst bed possessed significant levels of H<sub>2</sub>, CO, CO<sub>2</sub>, and H<sub>2</sub>O, together with C<sub>2+</sub> products. Considering the fact that with complete consumption of oxygen in the second bed, H<sub>2</sub> and H<sub>2</sub>O production levels are consistent with our expectations from the OCM reaction and there is no sign of H<sub>2</sub>O consumption in the second

bed. Therefore, as apparent from the species concentration profiles in the second bed, even in the presence of an excess amount of steam produced in the first bed, La<sub>2</sub>O<sub>3</sub>-CeO<sub>2</sub> does not promote the steam reforming of methane reaction. Moreover, the excess amounts of carbon dioxide and water fed to the second bed did not cause

any apparent deactivation of the OCM catalyst.

Analysis of the experimental data of Figures 2 and 3 also indicate that the catalytic water gas shift (WGS) reaction, that is, H<sub>2</sub>O + CO = CO<sub>2</sub> + H<sub>2</sub>, can be ruled out. For example, the mole fraction ratios  $Y_{\text{CO}_2} \times Y_{\text{H}_2} / (Y_{\text{H}_2\text{O}} \times Y_{\text{CO}})$  were in the 0.4–0.6 range within the 5 mm in the catalyst beds in all the experiments. These values are significantly lower than those of the WGS reaction equilibrium constants that are in the 1.5–2.0 range under the prevailing conditions in the reactor beds.

The profiles for the DB2 experiment at the overall CH<sub>4</sub>/O<sub>2</sub> ratio of 4.4 as presented in Figure 4 are in harmony with the DB1 experiment at CH<sub>4</sub>/O<sub>2</sub> = 4.0 (Figure 3), which thereby gives us confidence regarding the validity of our measurements. In the DB2 experiment, the feed CH<sub>4</sub>/O<sub>2</sub> ratio of 11 used in the first catalyst bed necessitated the use of a higher  $T_f$  of approximately 780 °C for ignition, and the maximum bed temperatures reached 930 and 910 °C in the first and second beds, respectively. These values are significantly lower than the single-bed temperature peak of 1015 °C (Figure 2). Again, the location of the maximum temperatures corresponds to the complete conversion of O<sub>2</sub>. Moreover, the interbed temperature remained relatively constant at approximately 800 °C.

From Figure 4 it can be seen that CO exhibited a peak concentration of 1.0% at 5 mm within the first bed, and ultimately reached 1.6% at the exit of the second catalyst bed. Hydrogen levels were 2.2 and 3.5% at the exits of beds 1 and 2, respectively. Carbon dioxide and water levels reached 2.8 and 10% in bed 1, respectively, and became 6 and 24.2% at the exit of the second bed, respectively.

In the DB2 experiment, the hydrocarbon products also exhibited similar trends, which generally increased within the catalytic zones with increasing methane and oxygen conversions and which ceased to change after the complete conversion of O<sub>2</sub>. At the exit of the first bed, the following levels were recorded: C<sub>2</sub>H<sub>6</sub> 3.52%, C<sub>2</sub>H<sub>4</sub> 2.1%, and C<sub>3</sub>H<sub>6</sub> 0.21%, whereas CH<sub>4</sub> conversion was 19%. Under these conditions, C<sub>2+</sub> selectivities would be 74%, which represents a yield of 14%. At the second bed exit, the concentration levels became C<sub>2</sub>H<sub>6</sub> 4.1%, C<sub>2</sub>H<sub>4</sub> 3.8%, and C<sub>3</sub>H<sub>6</sub> 0.35%, with a maximum CH<sub>4</sub> conversion of approximately 28%. These results correspond to a C<sub>2+</sub> selectivity of 67% and represent a final yield of approximately 19%. This value is slightly lower than the 21% yield obtained in the DB1 experiment yet higher than the 16% yield of the single-bed experiment (see Table 1).

## Conclusions

The microprobe sampling technique as applied to dual-packed-bed catalytic reactors for the oxidative coupling of methane (OCM) demonstrated that distributing the O<sub>2</sub> feed can significantly increase the yields of the C<sub>2+</sub> products. By using La<sub>2</sub>O<sub>3</sub>-CeO<sub>2</sub> nanofiber fabric catalyst beds, the C<sub>2+</sub> products were obtained in an ultimate yield of 21% in a double-bed OCM reactor with split O<sub>2</sub> introduction, which is significantly higher than the 16% yield observed in the single-bed experiment at the same overall CH<sub>4</sub>/O<sub>2</sub> ratio of 4. The dual-bed configuration with interstage cooling increases the yield of the C<sub>2+</sub> products primarily by increasing CH<sub>4</sub> conversion and by maintaining the C<sub>2+</sub> product selectivity levels.

## Acknowledgements

We thank LCS for the use of their facilities and database. B.Z. acknowledges the National Science Foundation (NSF) GRFP Support Grant No. DGE1144087 and the University of California, Los Angeles (UCLA) Graduate Division Fellowship. D.N. acknowledges NSF MCTP-DGE-0654431 Fellowship.

**Keywords:** gas-phase reactions · microreactors · nanostructures · oxidation · surface chemistry

- [1] M. C. Alvarez-Galvan, N. Mota, M. Ojeda, S. Rojas, R. M. Navarro, J. L. G. Fierro, *Catal. Today* **2011**, *171*, 15–23.
- [2] U. Zavyalova, M. Holena, R. Schlögl, M. Baerns, *ChemCatChem* **2011**, *3*, 1935–1947.
- [3] S. Sahebdehfar, M. T. Ravanchi, M. Gharibi, M. Hamidzadeh, *J. Nat. Gas Chem.* **2012**, *21*, 308–313.
- [4] C. Hammond, S. Conrad, I. Hermans, *ChemSusChem* **2012**, *5*, 1668–1686.
- [5] E. Esche, H. Arellano-Garcia, L. T. Biegler, *AIChE J.* **2014**, *60*, 170–180.
- [6] S. Jašo, H. R. Godini, H. Arellano-Garcia, M. Omidkhan, G. Wozny, *Chem. Eng. Sci.* **2010**, *65*, 6341–6352.
- [7] E. V. Kondratenko, U. Rodemerck, *ChemCatChem* **2013**, *5*, 697–700.
- [8] B. Zohour, D. Noon, S. Senkan, *ChemCatChem* **2013**, *5*, 2809–2812.
- [9] a) J. W. Thybaut, J. Sun, L. Olivier, A. C. Van Veen, C. Mirodatos, G. B. Marina, *Catal. Today* **2011**, *159*, 29–36; b) J. Sun, J. W. Thybaut, G. B. Marina, *Catal. Today* **2008**, *137*, 90–102.
- [10] J. H. J. B. Hoebink, P. M. Couwenberg, G. B. Marin, *Chem. Eng. Sci.* **1994**, *49*, 5453–5463.
- [11] D. Noon, A. Seubsai, S. Senkan, *ChemCatChem* **2013**, *5*, 146–149.
- [12] R. Horn, O. Korup, M. Geske, U. Zavyalova, I. Oprea, R. Schlögl, *Rev. Sci. Instrum.* **2010**, *81*, 064102-1-6.
- [13] O. Korup, S. Maylyankariev, M. Geske, C. F. Goldsmith, R. Horn, *Chem. Eng. Process.* **2011**, *50*, 998–1009.
- [14] M. Y. Sinev, Z. T. Fattakhova, V. I. Lomonosov, Y. A. Gordienko, *J. Nat. Gas Chem.* **2009**, *18*, 273–287.
- [15] Z. Stansch, L. Mleczko, M. Baerns, *Ind. Eng. Chem. Res.* **1997**, *36*, 2568.
- [16] S. Senkan, *Advances in Chemical Engineering: 18*, Academic Press, New York, **1992**, 95.
- [17] D. A. Hickman, L. D. Schmidt, *Science* **1993**, *259*, 343–346.
- [18] D. Dalle Nogare, N. J. Degenstein, R. Horn, P. Canu, L. D. Schmidt, *J. Catal.* **2011**, *277*, 134–148.

Received: June 3, 2014

Published online on August 27, 2014

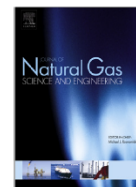
### A3. Oxidative Coupling of Methane with $\text{La}_2\text{O}_3\text{-CeO}_2$ Nanofiber Fabrics: A Reaction Engineering Study





Contents lists available at ScienceDirect

## Journal of Natural Gas Science and Engineering

journal homepage: [www.elsevier.com/locate/jngse](http://www.elsevier.com/locate/jngse)

# Oxidative coupling of methane with $\text{La}_2\text{O}_3\text{--CeO}_2$ nanofiber fabrics: A reaction engineering study



Daniel Noon, Bahman Zohour, Selim Senkan\*

Department of Chemical Engineering, University of California, Los Angeles, CA 90095, USA

## ARTICLE INFO

## Article history:

Received 29 January 2014

Received in revised form

6 April 2014

Accepted 7 April 2014

Available online 23 April 2014

## Keywords:

OCM

Natural gas processing

Nanofiber catalyst

Electrospinning

Exothermic reactions

Rare earth oxide catalysts

## ABSTRACT

The effects of changes in various operating conditions were explored on the performance of an oxidative coupling of methane (OCM) reaction using  $\text{La}_2\text{O}_3\text{--CeO}_2$  nanofiber fabric catalysts in a packed bed reactor. The operating conditions were: 1 atm pressure,  $\text{CH}_4/\text{O}_2$  ratio 4–7, feed flow rate 80–320 sccm, catalyst loading 5–20 mg, feed gas temperature 300–620 °C. These studies revealed that the rates of the OCM reaction is largely dominated by mass transfer limitations as evidenced by increases in reactor bed temperatures with increasing feed flow rates.  $\text{C}_{2+}$  selectivities and yields of up to 70% and 18% respectively were also attained. Experiments with different catalyst loadings indicated that short catalytic beds are preferred for increasing  $\text{C}_{2+}$  selectivities in OCM reactors.

© 2014 Elsevier B.V. All rights reserved.

## 1. Introduction

The direct utilization of methane, the main component of natural gas (NG), as an alternate chemical feedstock to petroleum, has been a highly desirable but difficult goal in industrial catalysis (Alvarez-Galvan et al., 2011). Many direct and indirect methods have been studied for  $\text{CH}_4$  conversion into more useful products, including olefins (e.g.  $\text{C}_2\text{H}_4$ ,  $\text{C}_3\text{H}_6$ ), higher molecular weight hydrocarbons and liquids (e.g. benzene and gasoline), as discussed in a recent review (Alvarez-Galvan et al., 2011). The production of ethylene from NG represents a particularly significant opportunity because of its massive worldwide use as an intermediate in the production of plastics, such as polyethylene and polyvinyl chloride. In addition, ethylene can be oligomerized into liquid hydrocarbons, such as alpha olefins, thereby enabling the efficient utilization of NG in remote parts of the world. At present, ethylene is primarily produced by the steam cracking of naphtha, a petroleum product. All indirect NG conversion routes utilize the high temperature, endothermic and costly steam reforming as a first step, where synthesis gas ( $\text{H}_2/\text{CO}$  mixtures) is produced. This is followed by the synthesis of useful products via various catalytic processes (Alvarez-Galvan et al., 2011). Although direct methods avoid use of

costly syngas steps, they remain uneconomical due in part to low  $\text{C}_{2+}$  yields, high temperatures and low throughputs. High temperatures are particularly detrimental since they result in catalyst deactivation and create materials problems for reactors.

In the oxidative coupling of methane (OCM),  $\text{CH}_4$  is directly converted to  $\text{C}_2\text{H}_6$ ,  $\text{C}_2\text{H}_4$  and  $\text{H}_2\text{O}$  in the presence of  $\text{O}_2$  and a suitable catalyst (Alvarez-Galvan et al., 2011). The first step involves the abstraction of H from  $\text{CH}_4$  by the catalyst to form methyl radicals ( $\text{CH}_3\bullet$ ) (Zavyalova et al., 2011; Lunsford, 1995). The coupling of two  $\text{CH}_3\bullet$  then creates  $\text{C}_2\text{H}_6$ , followed by its dehydrogenation to  $\text{C}_2\text{H}_4$ . Some  $\text{C}_3$  hydrocarbons also form by addition of  $\text{CH}_3\bullet$  to  $\text{C}_2\text{H}_4$  (Conway et al., 1991). However, undesirable surface and gas phase combustion reactions also lead to CO and  $\text{CO}_2$  ( $\text{CO}_x$ ). Since high temperatures promote homogeneous gas phase free radical reactions detrimental for  $\text{C}_{2+}$  products, the development of new catalysts that can operate at low temperatures is crucial for the economic viability of OCM. We recently reported promising results in OCM using catalytic nanofiber fabrics of  $\text{La}_2\text{O}_3\text{--CeO}_2$  (Noon et al., 2013). This material was found to be advantageous over analogous powders previously reported in the literature (Dedov et al., 2003, 2005; Makhlin et al., 2009), especially in terms of the feed gas temperature required to activate methane (Noon et al., 2013). The  $\text{CeO}_2$  is well recognized to promote  $\text{La}_2\text{O}_3$  with regard to the OCM reaction (Dedov et al., 2003, 2005; Makhlin et al., 2009).

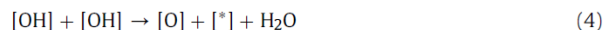
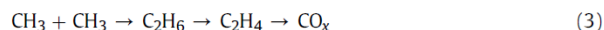
There are two prevailing OCM mechanisms in relation to  $\text{La}_2\text{O}_3$  surfaces: the idea that a lattice oxygen is responsible for activation

<http://dx.doi.org/10.1016/j.jngse.2014.04.004>

1875-5100/© 2014 Elsevier B.V. All rights reserved.

of the C–H bond on CH<sub>4</sub> either through a Mars–van Krevelen mechanism or through the dissociative adsorption of CH<sub>4</sub>, where the fragments CH<sub>3</sub> and H bind to the surface oxide (Mleczko and Baerns, 1995; Li and Metiu, 2012; Hu et al., 2011); the dissociative adsorption of O<sub>2</sub> first onto the catalyst's oxide covered surface, forming a peroxy-type species that is responsible for subsequently activating the C–H bond (Palmer et al., 2002a, 2002b). Most of the remaining reactions occur in the gas phase, though it is suggested that CO<sub>2</sub> can be created by oxidation of an adsorbed methyl group in addition to through multiple gas phase routes. The difficulty in OCM is in isolating the products C<sub>2</sub>H<sub>4</sub> and C<sub>2</sub>H<sub>6</sub>, which are susceptible to further oxidation, ultimately to CO<sub>x</sub>.

The critical overall steps accepted to occur in the OCM mechanism, leading up to the formation of C<sub>2</sub>H<sub>6</sub>, are summarized in Eqs. (1)–(4):



where [\*] is a vacant catalytic surface site. The direct oxidation of CH<sub>4</sub> to CO<sub>2</sub> as well as the oxidative dehydrogenation of C<sub>2</sub>H<sub>6</sub> to C<sub>2</sub>H<sub>4</sub> are also well accepted pathways in the OCM process. Additionally, there may be surface occupation by CO<sub>2</sub> as in Eq. (5):



which may block active sites from participating in OCM (Arndt et al., 2011; Xu et al., 1992; Istadi and Amin, 2006; Papa et al., 2011). The coupling of methyl radicals in Eq. (3) occurs in the gas phase while the formation of C<sub>2</sub>H<sub>4</sub> and CO<sub>x</sub> may either be catalytic or in the gas phase. The remaining reactions listed occur on the catalyst. In a highly exothermic catalytic reaction such as OCM, mass transfer limitations can be critical in determining reactor performance. This will be particularly important for the case of the limiting reactant O<sub>2</sub> in the current studies. At high temperatures, adsorption, surface reaction and desorption rates exceed mass diffusion rates (Mleczko and Baerns, 1995), rendering the latter as the rate determining process. Since mass transfer rates increase with increasing Reynolds number, the reactor bed temperatures would be expected to increase with increasing gas flow. However, the overall performance of the OCM reactors will be determined as a result of the competition between increased rates of reaction and shortened residence times with increased flow through the reactor.

Here, we report a follow-up study detailing some of the OCM reaction engineering aspects of the La<sub>2</sub>O<sub>3</sub>–CeO<sub>2</sub> catalyst developed in our laboratories. Reactor temperature profiles as well as reactor exit conversion and product selectivities are presented as a function of feed temperature, feed flow rate and composition.

## 2. Materials and methods

### 2.1. Electrospinning

Nanofibers are prepared by electrospinning (Tan et al., 2007). In a typical preparation, polyvinylpyrrolidone (PVP; 1.3 MDa) is mixed with a solvent containing water and ethanol (~1:2 weight ratio). To this solution, La(NO<sub>3</sub>)<sub>3</sub>·6H<sub>2</sub>O and Ce(NO<sub>3</sub>)<sub>3</sub>·6H<sub>2</sub>O are added. Water is necessary to allow for the mutual solubility of PVP and the metal salts while ethanol is used primarily to lower the surface tension of the solution, allowing it to be electrospun into fibers. The

final solution is 6 wt% PVP with a metal-to-polymer weight ratio of 0.20.

The electrospinning setup in Fig. 1 features a syringe loaded with the spinning solution being pumped through a metal needle collector, which has aluminum foil wrapped tightly around it. The syringe pump is programmed to then pump the fluid at a fixed rate of 1.0 mL/h. The material collected on the aluminum foil comprises nanofibers of PVP and the embedded La and Ce metal salts. After a sufficient amount of material is collected, the foil then is placed inside an oven for air calcination at 625 °C. This temperature allows for the fiber sample to be calcined without melting the foil. The La/Ce weight ratio of the material studied in this work is 3/1.

### 2.2. Catalytic performance testing

The nanofiber catalyst is packed in a 4 mm ID quartz tube, sandwiched between two quartz wool plugs and placed inside a temperature controlled tube furnace (Thermolyne® 21100). The reactor pressure is 1 atm. Inlet gas flow rates are regulated by electronic mass flow controllers (MKS, Burlington, MA). In this work, flow rates of 80–320 standard cubic centimeters per minute (sccm), catalyst weights of 5–20 mg (0.94 void fraction) and feed temperatures of 300–620 °C are examined. The inlet is a binary gas of CH<sub>4</sub> and O<sub>2</sub> with 75–87.5 mol% CH<sub>4</sub>. Reaction products are sampled by a 300 micron ID capillary tubing and analyzed by on-line gas chromatography (Varian 4900 Micro-GC, with Molecular sieve X and Porapak U columns).

### 2.3. Temperature profiles

In separate experiments, a 0.25 mm diameter thermocouple (K-Type, Omega Engineering, CT) is placed inside the catalytic zone to measure the axial temperature profiles. The thermocouple is inserted tightly into a quartz capillary, the combination of which is placed on a micro-translation device that allows for precise incremental changes in the axial position of the thermocouple along the reactor (Zohour et al., 2013). In these experiments, 20 mg catalyst loading is used to form a bed depth of ~1.4 cm to improve the spatial resolution of the axial temperature profiles.

## 3. Results and discussion

### 3.1. Nanofibers

Shown in Fig. 2 is an SEM image of the calcined La<sub>2</sub>O<sub>3</sub>–CeO<sub>2</sub> nanofiber fabric. First and foremost, the fibers show considerable uniformity in diameter (~70 nm) and dispersion. BET area is about 25 m<sup>2</sup>/g, suggesting the nanofibers are dense and do not possess internal porosity. Second, the fibers appear individually well

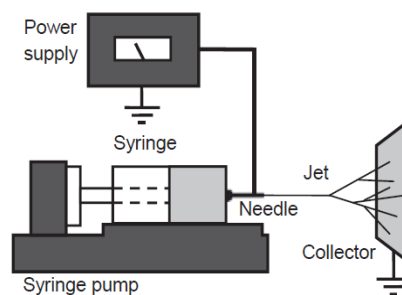


Fig. 1. Electrospinning setup used in the synthesis of La<sub>2</sub>O<sub>3</sub>–CeO<sub>2</sub> nanofibers.



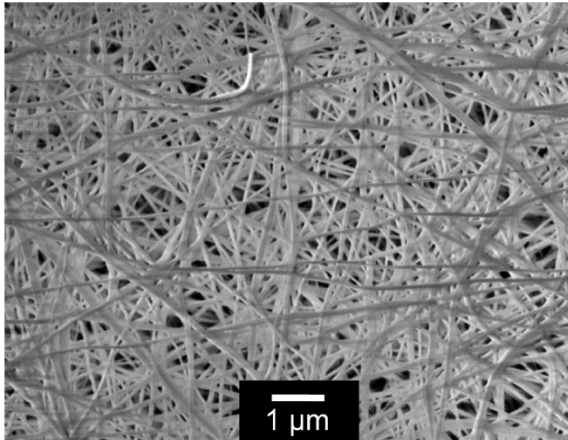


Fig. 2. SEM image of electrospun and subsequently calcined  $\text{La}_2\text{O}_3\text{-CeO}_2$  fibers (diameter  $\sim 70$  nm; magnification 13,000; working distance 6.7 mm; 4.0 kV).

exposed with little clustering, concomitant with the large and uniform interfiber space and a void fraction of 0.94. Although these features provide rapid access to and from active sites, which should be advantageous in improving the selectivity for labile products in partial oxidation reactions, they also promote homogeneous gas phase reactions. In contrast, co-precipitated  $\text{La}_2\text{O}_3\text{-CeO}_2$  particles exhibit a high degree of agglomeration in which a significant fraction of  $\text{La}_2\text{O}_3\text{-CeO}_2$  remain inaccessible or are accessible only through pores, concomitant with pore diffusion limitations and associated problems. Previously we demonstrated that  $\text{La}_2\text{O}_3\text{-CeO}_2$  nanofiber fabric catalysts exhibit lower ignition temperatures and broader operating windows than the corresponding powder catalysts (Noon et al., 2013).

### 3.2. Feed temperature hysteresis

Before results are presented, it should be pointed out that the major  $\text{C}_2$  products observed over  $\text{La}_2\text{O}_3\text{-CeO}_2$  catalysts are  $\text{C}_2\text{H}_6$  and  $\text{C}_2\text{H}_4$ , with the  $\text{C}_2\text{H}_6/\text{C}_2\text{H}_4$  ratio being in the 1–2 range. In addition, some  $\text{C}_3\text{H}_6$  is also formed constituting 5–8% of the  $\text{C}_{2+}$  products. Furthermore, some  $\text{C}_4$  products were also consistently detected under OCM conditions, though in significantly lower amounts compared to the other products. The major undesirable products were  $\text{CO}_2$  and  $\text{CO}$ .

In Fig. 3, the axial temperature profiles are presented for a  $\text{CH}_4/\text{O}_2$  feed ratio of 5 and at a feed gas flow rate of  $F = 160$  sccm with  $m_{\text{cat}} = 20$  mg of catalyst packed into the bed at various feed gas temperatures  $T_f$ . Filled symbols represent the temperature profiles measured when the furnace temperature was stepwise heated up, while empty symbols were obtained during the stepwise cooling process. The temperature profile measurements were acquired while the reactant gases were flowing. The embedded thermocouple was used to monitor the establishment of the steady state bed temperature. Once the steady state temperature was reached ( $\sim 30$  min during heating and  $\sim 60$  min during cooling), the temperature profile was measured by axially moving the thermocouple. After data acquisition, the furnace temperature was readjusted to its new set point. As seen in Fig. 3, the difference between the peak temperature in the catalytic zone and feed temperature  $T_f$  ranges between  $\sim 300$  and  $400$  °C. This difference is at its largest at the lowest feed temperature  $T_f = 390$  °C. However the locations of the peaks were noted to shift downstream during the cooling experiments, i.e. at values for  $T_f$  that are lower than the

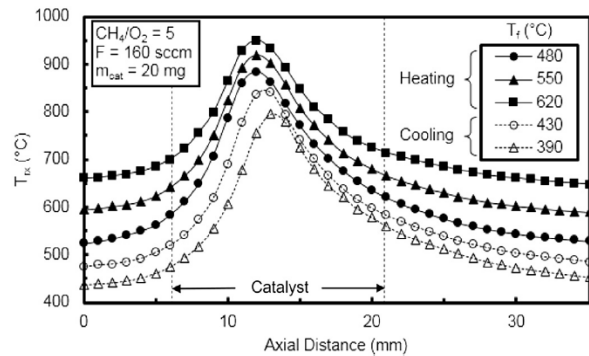


Fig. 3. Reactor temperature  $T_{rx}$  as a function of axial distance within and near the catalytic zone while increasing and decreasing the feed temperature  $T_f$  [480 (●), 550 (▲), 620 (■), 430 (○), 390 (△) °C] with the following fixed:  $\text{CH}_4/\text{O}_2$  feed ratio of 5, catalyst weight of  $m_{\text{cat}} = 20$  mg, flow rate of  $F = 160$  sccm.

ignition temperature  $T_{ig}$ . This could also be due to insufficient cooling period (60 min) to attain steady state during the cooling process.

In Fig. 4, the accompanying reactor exit  $\text{CH}_4$  conversions and  $\text{C}_{2+}$  selectivities are presented while Fig. 5 shows the  $\text{O}_2$  conversions and  $\text{C}_2\text{H}_6/\text{C}_2\text{H}_4$  ratios, both as a function of feed gas temperature  $T_f$ . As seen in Figs. 3 and 4, the onset of catalyst ignition was at  $450$  °C when increasing  $T_f$ , with a  $\text{C}_{2+}$  selectivity of 55% at 28%  $\text{CH}_4$  conversion. Oxygen was completely consumed and the  $\text{C}_2\text{H}_6/\text{C}_2\text{H}_4$  ratio was about 1 at the ignition point. For  $T_f > T_{ig}$ , the catalyst performance is limited by the exhaustion of  $\text{O}_2$ , with no change in the location of the peak bed temperature. As evident from Figs. 3 and 4, a hysteresis window was noted. On the decreasing  $T_f$  path, the high  $\text{C}_{2+}$  selectivity of 52–59% extended down to about  $300$  °C. Both the  $\text{CH}_4$  and  $\text{O}_2$  conversions steadily decreased and the  $\text{C}_2\text{H}_6/\text{C}_2\text{H}_4$  ratio increased with decreasing  $T_f$  below the ignition temperature. These results are consistent with the lower catalyst peak temperature with decreasing  $T_f$  (Fig. 3).

### 3.3. Effect of feed flow rate and $\text{CH}_4/\text{O}_2$ ratio

In Fig. 6, the effects of feed gas flow rate on the spatial temperature profiles are presented at a  $\text{CH}_4/\text{O}_2$  ratio of 5 and feed gas temperature of  $570$  °C. As evident from this figure, increasing feed gas flow rate dramatically increases the reactor temperature, while

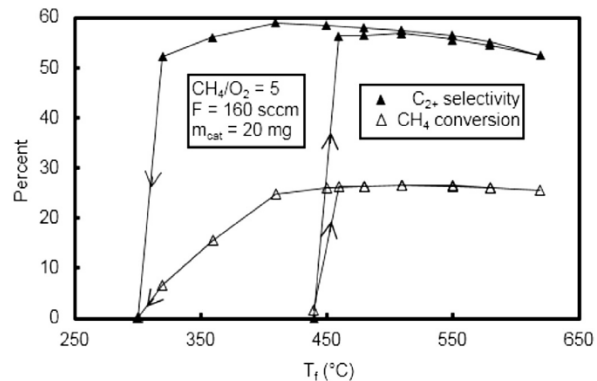


Fig. 4.  $\text{C}_{2+}$  selectivity (▲) and  $\text{CH}_4$  conversion (Δ) as a function of feed temperature  $T_f$ , where the arrows indicate the increasing or decreasing path for  $T_f$ , with:  $\text{CH}_4/\text{O}_2$  feed ratio of 5, catalyst weight of  $m_{\text{cat}} = 20$  mg, flow rate of  $F = 160$  sccm.



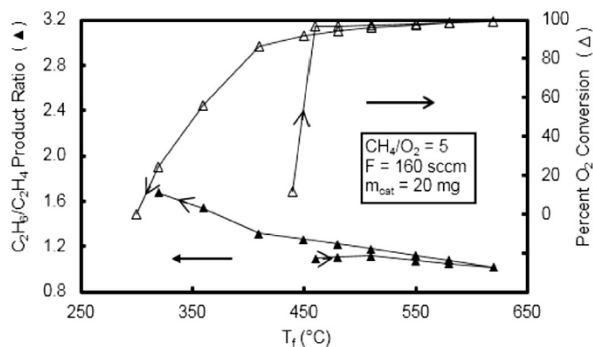


Fig. 5. Ethane-to-ethylene product ratio (left ordinate,  $\blacktriangle$ ) and percent  $O_2$  conversion (right ordinate,  $\triangle$ ) as a function of feed temperature  $T_f$ , where the arrows indicate the increasing or decreasing path for  $T_f$ , with:  $CH_4/O_2$  feed ratio of 5, catalyst weight of  $m_{cat} = 20$  mg, flow rate of  $F = 160$  sccm.

only slightly shifting the location of the maximum temperature. For example, at 80 sccm flow, the peak temperature is 825 °C at  $\sim 12$  mm within the bed. In contrast, at 200 sccm, the peak temperature reached 960 °C at  $\sim 11$  mm. These results indicate that the rate of the OCM process in the experiments was significantly under the mass transfer limited conditions (Dalle Nogare et al., 2011). That is, the increased flow rates increased mass transfer coefficients and thus transport rates to the catalyst surface, thereby increasing the rates of the OCM reaction and thus heat generation rates. Increases in temperature results in the establishment of steeper temperature gradients which then lead to increased heat conduction both to upstream and downstream of the hot spot. On the other hand, increases in gas flow rates would decrease the residence times as well as convectively pushing the hot gases downstream. As a consequence of the complex combination of these conduction, convection and reaction processes, the peak temperatures can shift either upstream or downstream. Clearly, performing a detailed modeling work involving both the chemical kinetics and transport phenomena of the OCM process is called for.

Another possible contributor to the observed shifts in peak temperature locations in the OCM reactors is heat conduction in along thermocouple wires placed into the bed. Due to their higher thermal conductivity, metal thermocouples can transfer heat more efficiently than gases and the solid catalysts. As a result, thermocouples only provide spatially averaged readings, averaged along

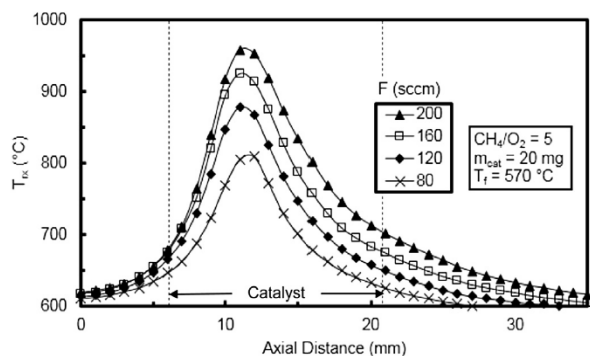


Fig. 6. Reactor temperature  $T_{rx}$  as a function of axial distance in the catalytic zone for various flow rates  $F = 80$  ( $\times$ ), 120 ( $\blacklozenge$ ), 160 ( $\square$ ), 200 ( $\blacktriangle$ ) sccm, with the following fixed:  $CH_4/O_2$  feed ratio of 5, catalyst weight of  $m_{cat} = 20$  mg, feed temperature of  $T_f = 570$  °C.

few bead or fiber diameters, especially when steep temperature gradients are present. Ideally, thermocouples should be placed perpendicular to gas flow, in order to accurately determine axial temperature profiles. However, such an option is not readily available for most catalytic reactor studies, including this work. In our experiments thermocouples were placed from the downstream side of the reactor.

In Fig. 7 the effect of  $CH_4/O_2$  ratio on reactor temperature is shown. As can be seen, decreasing the  $CH_4/O_2$  ratio from 7 to 4 increases the peak reactor temperature from 850 °C to 980 °C, while also resulting in a shift of the peak location from 12 mm to 10.8 mm. The increase in reactor bed temperature is the expected consequence of decreased methane dilution in the feed gas based on the overall OCM as well as combustion reaction stoichiometries.

In Figs. 8 and 9,  $CH_4$  and  $O_2$  conversions,  $C_{2+}$  selectivities and  $C_2H_6/C_2H_4$  ratios are presented as a function of feed gas flow rate and  $CH_4/O_2$  ratio at a feed gas temperature of  $T_f = 570$  °C. An inspection of Fig. 8 reveals several interesting trends. First, increasing gas flow rates and decreasing  $CH_4/O_2$  ratios have an adverse effect on  $C_{2+}$  selectivity, which reaches as high as 70% at a  $CH_4/O_2$  feed ratio of 7 and feed flow rate of  $F = 160$  sccm. The only exception to this trend is seen at the  $CH_4/O_2$  ratio of 7 at low gas flow rates, which can be attributed to greater mass transfer limitations. Additionally, the depth of the catalyst bed could be a significant factor in creating low  $C_{2+}$  selectivities for low flow rates for the high  $CH_4/O_2$  ratio. In a previous work when using an 8 mg  $La_2O_3-CeO_2$  bed, a  $T_f$  hysteresis plot similar to that of Fig. 4 here was constructed (Noon et al., 2013). It was found that for a  $CH_4/O_2$  feed ratio of 4 that  $C_{2+}$  selectivities reached their highest at the quench temperature of  $T_f = 230$  °C. In Fig. 4 at the quench temperature, the  $C_{2+}$  selectivity is at one of its lowest observed values. A key difference between these two experiments is the bed depth, which clearly explains why  $C_{2+}$  selectivities are sacrificed at very low flow rates at  $CH_4/O_2 = 7$ . Over our OCM catalyst, we have previously shown that  $O_2$  was completely consumed at about one-third of the 20 mg  $La_2O_3-CeO_2$  bed (Zohour et al., 2013). This would not necessarily occur within a shallow 5 mg bed. That is, products of OCM with a deep bed are being exposed to the catalyst at low temperatures, that could lead to the destruction of  $C_{2+}$  products.

Second, methane conversions consistently increase with decreasing  $CH_4/O_2$  ratio as a consequence of increased bed temperature caused by decreased methane dilution, reaching as high as 33% at a  $CH_4/O_2$  feed ratio of 4 and the lowest feed rate examined of  $F = 80$  sccm. Third, the effect of gas flow rates on methane conversions is complex. Methane conversion decreases with increasing

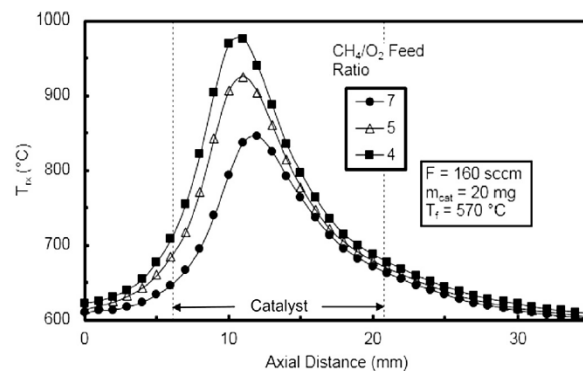


Fig. 7. Reactor temperature  $T_{rx}$  as a function of axial distance in the catalytic zone for the various feed  $CH_4/O_2$  ratios of 4 ( $\blacksquare$ ), 5 ( $\triangle$ ), 7 ( $\bullet$ ), with the following fixed: feed flow rate of  $F = 160$  sccm, catalyst weight of  $m_{cat} = 20$  mg, feed temperature of  $T_f = 570$  °C.

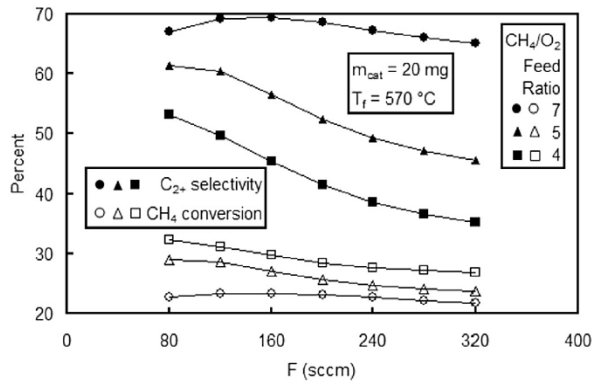


Fig. 8. C<sub>2+</sub> selectivity (● ▲ ■) and CH<sub>4</sub> conversion (○ △ □) as a function of flow rate and the CH<sub>4</sub>/O<sub>2</sub> feed ratios of 4 (■ □), 5 (▲ △), 7 (● ○) with the following fixed: catalyst weight of m<sub>cat</sub> = 20 mg, feed temperature of T<sub>f</sub> = 570 °C.

gas flow rate for CH<sub>4</sub>/O<sub>2</sub> ratios of 4 and 5, but the reverse trend is observed for 7. For the CH<sub>4</sub>/O<sub>2</sub> ratios of 4 and 5 decreases in CH<sub>4</sub> conversions with increase in gas flow rate can readily be accounted for by the decreases in contact/reaction times since under these conditions the catalyst is at a sufficiently high temperature. Also, CO<sub>x</sub> selectivities tend to be higher at larger flow rates due to higher temperatures. Since pathways that produce CO<sub>x</sub> consume more O<sub>2</sub>, less CH<sub>4</sub> will be converted at the end. From Fig. 9, the variation in oxygen conversion with respect to flow rate is less significant than for methane conversion, consistent with the argument that increasing CO<sub>x</sub> selectivities with flow rates being the primary reason for the decreasing CH<sub>4</sub> conversions as opposed to reduced contact times. For the CH<sub>4</sub>/O<sub>2</sub> ratio of 7 at 80 sccm, the catalyst temperature evidently is not hot enough resulting in increase in methane conversion slightly with increase in gas flow rate. This result is also in harmony with the results noted above.

Third, O<sub>2</sub> conversions uniformly increased with increasing gas flow and leveled off at higher flow rates for all CH<sub>4</sub>/O<sub>2</sub> ratios (Fig. 9). Interestingly, O<sub>2</sub> conversions leveled off earlier and to a slightly lower level at the CH<sub>4</sub>/O<sub>2</sub> ratio of 7. Fourth, C<sub>2</sub>H<sub>6</sub>/C<sub>2</sub>H<sub>4</sub> ratios exhibited trends that consistently decreased with increasing gas flow rates and decreasing CH<sub>4</sub>/O<sub>2</sub> ratios, an expected result based on increased reactor bed temperatures. The C<sub>2</sub>H<sub>6</sub>/C<sub>2</sub>H<sub>4</sub> ratios were significantly higher (i.e. 1.3–1.6) at the CH<sub>4</sub>/O<sub>2</sub> ratio of 7. For the

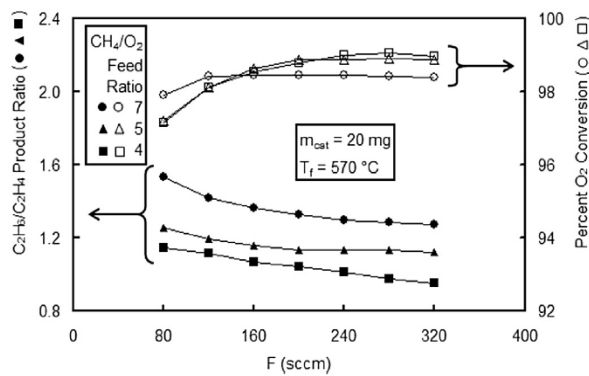


Fig. 9. Ethane-to-ethylene product ratio (left ordinate, ● ▲ ■) and percent O<sub>2</sub> conversion (right ordinate, ○ △ □) as a function of feed flow rate and the CH<sub>4</sub>/O<sub>2</sub> feed ratios of 4 (■ □), 5 (▲ △), 7 (● ○), with the following fixed: catalyst weight of m<sub>cat</sub> = 20 mg, feed temperature of T<sub>f</sub> = 570 °C.

CH<sub>4</sub>/O<sub>2</sub> ratio of 4, the C<sub>2</sub>H<sub>6</sub>/C<sub>2</sub>H<sub>4</sub> ratio decreased from 1.15 at 80 sccm to 0.95 at 320 sccm. Carbon dioxide, an abundant by-product in OCM, has also been documented as a catalyst poison and has strong binding affinity for highly basic materials (Papa et al., 2011). Consequently, under certain conditions CO<sub>2</sub> could limit the rates of the OCM reaction.

### 3.4. Effect of bed depth and space velocity

In order to better assess the importance of transport limitations relative to surface reactions, the performances of three reactors having 5, 10 and 20 mg catalyst loadings were investigated as a function of space velocity (i.e.  $F/m_{cat} = [\text{Feed gas flow rate (sccm)}] / [\text{Catalyst weight (mg)}]$ ). In Figs. 10 and 11, CH<sub>4</sub> and O<sub>2</sub> conversions, and C<sub>2+</sub> selectivities and C<sub>2</sub>H<sub>6</sub>/C<sub>2</sub>H<sub>4</sub> ratios are presented respectively, as a function of space velocity for each of these packed beds. The CH<sub>4</sub>/O<sub>2</sub> ratio was kept at 5 and the feed gas temperature was 570 °C in all of this set of experiments. An inspection of Fig. 10 reveals several trends. First, both the C<sub>2+</sub> selectivities and methane conversions decreased with space velocity for all the three beds. Second, neither the methane conversion nor the C<sub>2+</sub> selectivity profiles overlapped, clearly indicating that mass transfer rates were the limiting process in the OCM reaction. As seen in Fig. 10, C<sub>2+</sub> selectivities were dramatically different, with the smaller packed bed reactor performing the best. For example, at the 15 sccm/mg space velocity, the C<sub>2+</sub> selectivities were 64%, 55% and 45%, for the 5, 10 and 20 mg catalyst bed reactors, respectively. These results indicate that deeper bed reactors are detrimental in OCM as they result in the subsequent destruction of C<sub>2+</sub> products once formed in the early part of the bed. Consequently, shallow bed reactors are desirable to maximize C<sub>2+</sub> selectivities.

From Fig. 11, it can be seen that O<sub>2</sub> conversions in the shorter 5 mg bed were consistently lower at 85–93% than others both of which exhibited near complete oxygen consumption (>95%). Evidently, the 5 mg bed utilizes the reactants more efficiently towards OCM products while the other, i.e. deeper, beds lead to the subsequent combustion of C<sub>2+</sub> products. These results are consistent with the higher C<sub>2+</sub> selectivity of the 5 mg bed with its similar methane conversion (Fig. 10) and the lower C<sub>2+</sub> selectivities of deeper beds.

The trends exhibited by the C<sub>2</sub>H<sub>6</sub>/C<sub>2</sub>H<sub>4</sub> ratios were all similar, decreasing with increasing space velocity as a result of increasing reactor temperatures. However unlike C<sub>2+</sub> selectivities, the deeper bed reactors were more beneficial for ethylene production. For

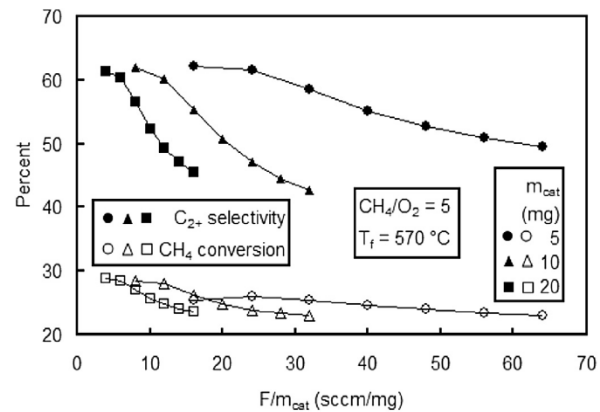


Fig. 10. C<sub>2+</sub> selectivity (● ▲ ■) and CH<sub>4</sub> conversion (○ △ □) as a function of space velocity  $F/m_{cat}$  and the catalyst weights of m<sub>cat</sub> = 5 (● ○), 10 (▲ △), 20 (■ □) mg with the following fixed: CH<sub>4</sub>/O<sub>2</sub> feed ratio of 5, feed temperature of T<sub>f</sub> = 570 °C.



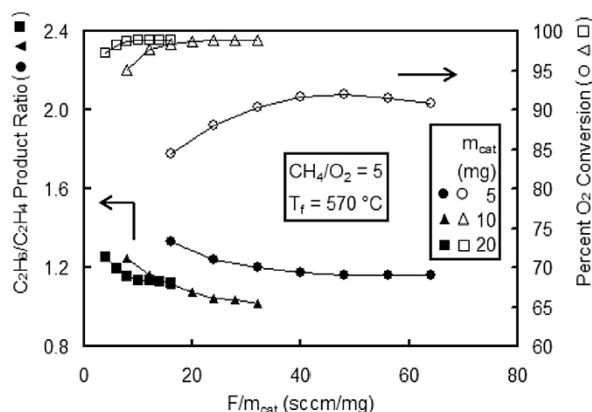


Fig. 11. Ethane-to-ethylene product ratio (left ordinate, ● ▲ ■) and percent O<sub>2</sub> conversion (right ordinate, ○ △ □) as a function of space velocity  $F/m_{\text{cat}}$  and the catalyst weights of  $m_{\text{cat}} = 5$  (● ○), 10 (▲ △), 20 (■ □) mg with the following fixed: CH<sub>4</sub>/O<sub>2</sub> feed ratio of 5, feed temperature of  $T_f = 570$  °C.

example, at space velocity of 20 sccm/mg, the C<sub>2</sub>H<sub>6</sub>/C<sub>2</sub>H<sub>4</sub> ratios were 1.3 and 1.05 for the 5 mg and 10 mg beds, respectively. This appears to be due to increased rates of surface mediated ethane dehydrogenation through the deeper catalyst bed. If gas phase dehydrogenation processes were responsible, then the C<sub>2</sub>H<sub>6</sub>/C<sub>2</sub>H<sub>4</sub> ratios would have been expected to be similar. These results are also consistent with a previous work in which concentration profiles in a similar reactor showed a delayed production of C<sub>2</sub>H<sub>4</sub> relative to C<sub>2</sub>H<sub>6</sub> (Zohour et al., 2013). Such a lag is expected since C<sub>2</sub>H<sub>4</sub> is understood to be produced by the sequential catalytic dehydrogenation of C<sub>2</sub>H<sub>6</sub>.

### 3.5. Time on stream

In Fig. 12, the time on stream performance of the La<sub>2</sub>O<sub>3</sub>–CeO<sub>2</sub> nanofiber fabric catalyst is presented for over a 10 h continuous operation. The experimental conditions were: feed gas flow rate 80 sccm, 20 mg catalyst CH<sub>4</sub>/O<sub>2</sub> ratio of 5, feed temperature 570 °C. As evident from Fig. 12, the La<sub>2</sub>O<sub>3</sub>–CeO<sub>2</sub> exhibits an excellent performance, showing no deterioration in activity and selectivity, rendering it a promising practical OCM catalyst.

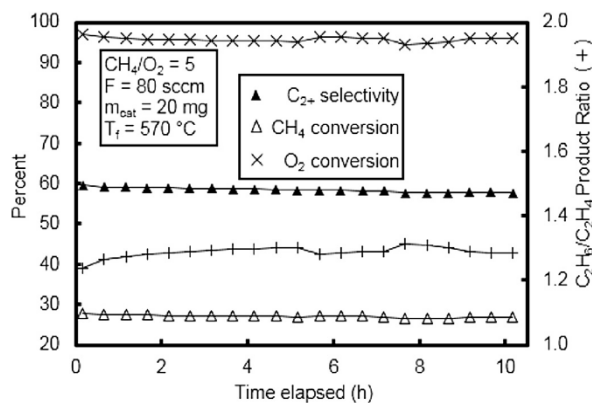


Fig. 12. Time on stream showing C<sub>2+</sub> selectivity (▲), CH<sub>4</sub> conversion (△) and O<sub>2</sub> conversion (×) as a function of time with the following fixed: CH<sub>4</sub>/O<sub>2</sub> feed ratio of 5, feed flow rate of  $F = 80$  sccm, catalyst weight of  $m_{\text{cat}} = 20$  mg, feed temperature of  $T_f = 570$  °C.

## 4. Conclusions

In conclusion, the reaction engineering aspects of a La<sub>2</sub>O<sub>3</sub>–CeO<sub>2</sub> nanofiber fabric catalyst have been evaluated using packed bed reactors over a broad range of operating conditions. These studies indicated that the rates of the OCM reaction is largely dominated by mass transfer limitations, evidenced by the increases in the bed temperature with increasing feed flow rates. Our studies also revealed that short catalytic beds are preferred for increasing C<sub>2+</sub> selectivities in OCM reactors. C<sub>2+</sub> selectivities and yields of up to 70% and 18% respectively were also attained in this study.

## Acknowledgments

We thank Laboratory Catalyst Systems (LCS) for use of its facilities and database. Daniel Noon acknowledges the NSF IGERT: Materials Creation Training Program (MCTP) – DGE-0654431 and the California NanoSystems Institute. Bahman Zohour acknowledges the University of California, Los Angeles (UCLA) Graduate Division Fellowship.

## References

- Alvarez-Galvan, M.C., Mota, N., Ojeda, M., Rojas, S., Navarro, R.M., Fierro, J.L.G., 2011. Direct methane conversion routes to chemicals and fuels. *Catal. Today* 171, 15.
- Arndt, S., Laugel, G., Levchenko, S., Horn, R., Baerns, M., Scheffler, M., Schlogl, R., Schomacker, R., 2011. A critical assessment of Li/MgO-based catalysts for the oxidative coupling of methane. *Catal. Rev.* 53, 424.
- Conway, S.J., Wang, D.J., Lunsford, J.H., 1991. Selective oxidation of methane and ethane over Li<sup>+</sup>-MgO-Cl-catalysts promoted with metal oxides. *Appl. Catal. A* 79, 11.
- Dalle Nogare, D., Degenstein, N.J., Horn, R., Canu, P., Schmidt, L.D., 2011. Modeling spatially resolved data of methane catalytic partial oxidation on Rh foam catalyst at different inlet compositions and flowrates. *J. Catal.* 277, 134.
- Dedov, A.G., Loktev, A.S., Moiseev, I.I., Aboukais, A., Lamonier, J.-F., Filimonov, I.N., 2003. Oxidative coupling of methane catalyzed by rare earth oxides – unexpected synergistic effect of the oxide mixtures. *Appl. Catal. A* 245, 209.
- Dedov, A.G., Moiseev, I.I., Loktev, A.S., Kuznetsov, N.T., Ketsko, V.A., Parkhomenko, K.V., Kartashev, I Yu., 2005. Catalytic synthesis of basic petrochemical products from C<sub>1</sub> – C<sub>4</sub> alkanes. *Chem. Tech. Fuels Oils* 41, 131.
- Hu, Z., Li, B., Sun, X., Metiu, H., 2011. Chemistry of doped oxides: the activation of surface oxygen and the chemical compensation effect. *J. Phys. Chem. C* 115, 3065.
- Istadi, Amin, N.A.S., 2006. Synergistic effect of catalyst basicity and reducibility on performance of ternary CeO<sub>2</sub>-based catalyst for CO<sub>2</sub> OCM to C<sub>2</sub> hydrocarbons. *J. Mol. Catal. A-Chem.* 259, 61.
- Li, B., Metiu, H., 2012. DFT studies of oxygen vacancies on undoped and doped La<sub>2</sub>O<sub>3</sub> surfaces. *J. Phys. Chem. C* 114, 12234.
- Lunsford, J.H., 1995. The catalytic oxidative coupling of methane. The catalytic oxidative coupling of methane. *Angew. Chem. Int. Ed.* 34, 970.
- Makhlin, V.A., Podlesnaya, M.V., Dedov, A.G., Loktev, A.S., Tel'pukhovskaya, N.O., Moiseev, I.I., 2009. Oxidative dimerization of methane: kinetics, mathematical modeling, and optimization with La/Ce catalysts. *Russ. J. Gen. Chem.* 79, 2016.
- Mleccko, L., Baerns, M., 1995. Catalytic oxidative coupling of methane – reaction engineering aspects and process schemes. *Fuel Process. Technol.* 42, 217.
- Noon, D., Seubsai, A., Senkan, S., 2013. Oxidative coupling of methane by nanofiber catalysts. *ChemCatChem* 5, 146.
- Palmer, M.S., Neurock, M., Olken, M.M., 2002a. Periodic density functional theory study of the dissociative adsorption of molecular oxygen over La<sub>2</sub>O<sub>3</sub>. *J. Phys. Chem. B* 106, 6543.
- Palmer, M.S., Neurock, M., Olken, M.M., 2002b. Periodic density functional theory study of methane activation over La<sub>2</sub>O<sub>3</sub>: activity of O<sup>2-</sup>, O<sup>-</sup>, O<sub>2</sub><sup>-</sup>, oxygen point defect, and Sr<sup>2+</sup>-doped surface sites. *J. Am. Chem. Soc.* 124, 8452.
- Papa, F., Luminata, P., Osiceanu, P., Birjega, R., Akane, M., Balint, I., 2011. Acid-base properties of the active sites responsible for C<sub>2</sub> and CO<sub>2</sub> formation over MO-Sm<sub>2</sub>O<sub>3</sub> (M = Zn, Mg, Ca and Sr) mixed oxides in OCM reaction. *J. Mol. Catal. A-Chem.* 346, 46.
- Tan, S., Huang, X., Wu, B., 2007. Mini review – some fascinating phenomena in electrospinning processes and applications of electrospun nanofibers. *Polym. Int.* 56, 1330.
- Xu, M.T., Shi, C.L., Yang, X.M., Rosynek, M.P., Lunsford, J.H., 1992. Effect of carbon dioxide on the activation energy for methyl radical generation over lithium/magnesia catalysts. *J. Phys. Chem.* 96, 6395.
- Zavalyova, U., Holena, M., Schlogl, R., Baerns, M., 2011. Statistical analysis of past catalytic data on oxidative methane coupling for new insights into the composition of high-performance catalysts. *ChemCatChem* 3, 1935.
- Zohour, B., Noon, D., Senkan, S., 2013. New insights into the oxidative coupling of methane from spatially resolved concentration and temperature profiles. *ChemCatChem* 5, 2809.

A4. Key Mechanistic Insight into the Direct Gas-Phase Epoxidation of Propylene by the RuO<sub>2</sub>-CuO-NaCl/ SiO<sub>2</sub> Catalyst

# Key Mechanistic Insight into the Direct Gas-Phase Epoxidation of Propylene by the RuO<sub>2</sub>-CuO-NaCl/SiO<sub>2</sub> Catalyst

Anusorn Seubsai,<sup>\*[a]</sup> Bahman Zohour,<sup>[b]</sup> Daniel Noon,<sup>[b]</sup> and Selim Senkan<sup>[b]</sup>

The discovery of the RuO<sub>2</sub>-CuO-NaCl/SiO<sub>2</sub> catalyst for the direct gas-phase epoxidation of propylene to propylene oxide created a potentially promising path towards developing a high-performing catalyst of substantial commercial value and opened a new challenge in catalysis research. In this work, studies following up this discovery are presented to reveal critical insight into the catalytic mechanism on the trimetallic catalyst. Small crystalline CuO particles, in close proximity of RuO<sub>2</sub>, were determined from temperature-programmed reduction and high-resolution transmission electron microscopy studies to be the site for propylene oxide synthesis. In addition, the presence of NaCl was confirmed to suppress the formation of CO<sub>2</sub>.

Propylene oxide (PO) is widely used in the preparation of various textiles and plastics<sup>[1]</sup> with over 8 million pounds of propylene-derived PO produced annually.<sup>[2]</sup> However, because some of the current production methods result in environmentally hazardous chlorinated byproducts that entail significant costs,<sup>[3]</sup> the search for an alternative method to achieve a high production rate of PO on an industrial scale has intensified. Although the direct gas-phase epoxidation of propylene to PO by molecular oxygen with the use of heterogeneous catalysts under atmospheric pressure is still, in theory, the most promising route, it has proven to be the most challenging production method thus far, as no breakthrough has yet been made.<sup>[3]</sup>

Several research groups have been exploring a number of alternatives, such as silver-based catalysts,<sup>[4]</sup> gold particles on titania with H<sub>2</sub> as a co-reactant,<sup>[5]</sup> titania-based catalysts,<sup>[6]</sup> molten salts of metal nitrates,<sup>[7]</sup> O<sub>3</sub> and nitrous oxide as reactants,<sup>[8]</sup> and copper-modified catalysts.<sup>[9,10]</sup> All of these methods suffer from low PO selectivities,<sup>[10–12]</sup> low propylene conversions,<sup>[5,10–14]</sup> short catalyst lifetimes,<sup>[6]</sup> high pressure requirements,<sup>[15]</sup> or costly co-reactants.<sup>[13,16]</sup> Consequently, no econom-

ically viable catalysts are currently available for the direct gas-phase epoxidation of propylene to PO by molecular oxygen.

Recently, we reported the discovery of RuO<sub>2</sub>-CuO<sub>x</sub>-NaCl/SiO<sub>2</sub> catalysts for the direct gas-phase epoxidation of propylene to PO that were prepared by the co-impregnation method.<sup>[17]</sup> It was shown that the catalyst system delivered a promising combination of PO selectivities (in the 40–50% range) and propylene conversions (10–20%) between 240 and 270 °C at atmospheric pressure. The best PO yield was obtained at a Ru/Cu/Na ratio of 4:2:1 at 12.5 wt% total metal loading on SiO<sub>2</sub>. Although the catalyst deactivated over time, as a result of the loss of chlorine content, we found that adding a small amount of a chlorocarbon (1–100 ppmv) such as chloroethane or 1,2-dichloroethane prevented deactivation by replenishing the chlorine content of the catalyst.<sup>[18]</sup> The chlorinated additives were found to play a critical role in maintaining high PO selectivities for at least 10 h under the conditions owing to geometric/ensemble and electronic effects, as well as gas-phase kinetic effects.

Herein, we report a critical key in understanding the mechanism of the epoxidation of propylene to PO facilitated by the SiO<sub>2</sub>-supported RuO<sub>2</sub>-CuO-NaCl catalyst by using oxygen as the only co-reactant. The desired propylene epoxidation reaction is shown in Equation (1).




However, the deep oxidation products CO<sub>2</sub> and H<sub>2</sub>O were also formed with the use of the title catalyst. Other detected trace byproducts included acetone (AT), acetaldehyde (AD), acrolein (AC), and propanal.

In earlier studies, the copper oxide phase was denoted as CuO<sub>x</sub>. However, recent XRD studies showed no evidence of Cu<sub>2</sub>O, which indicated the sole presence of CuO in the RuO<sub>2</sub>-CuO<sub>x</sub>-NaCl system. Given that the SiO<sub>2</sub>-supported RuO<sub>2</sub>-CuO-NaCl catalyst has multiple phases and contains more than one active metal, to understand the mechanism of propylene epoxidation to PO, the key active site for the formation of PO must first be identified. As reported earlier,<sup>[17]</sup> of the single catalyst systems (RuO<sub>2</sub>/SiO<sub>2</sub>, CuO/SiO<sub>2</sub>, and NaCl/SiO<sub>2</sub>), only CuO/SiO<sub>2</sub> produced detectable amounts of PO under the testing conditions, whereas the RuO<sub>2</sub>/SiO<sub>2</sub> catalyst led to complete combustion, and the NaCl/SiO<sub>2</sub> catalyst generally exhibited no activity. This implied that the CuO site may also be the key site for PO synthesis in our RuO<sub>2</sub>-CuO-NaCl system. To confirm this hypothesis, various catalytic materials were prepared and tested. The selectivity–conversion results of these catalysts are pre-

[a] Dr. A. Seubsai  
Department of Chemical Engineering, Faculty of Engineering  
Kasetsart University  
Ladyao, Jatujak, Bangkok, 10900 (Thailand)  
Fax: (+66)02-561-4621  
E-mail: fengasn@ku.ac.th

[b] B. Zohour, D. Noon, Prof. Dr. S. Senkan  
Department of Chemical Engineering  
University of California  
Los Angeles, CA 90095 (USA)

 Supporting information for this article is available on the WWW under <http://dx.doi.org/10.1002/cctc.201301009>.

**Table 1.** Product selectivities and propylene conversions for the different catalysts studied.

Catalyst #	Catalyst supported on SiO <sub>2</sub> <sup>[a]</sup>	Selectivity [%]					C <sub>3</sub> H <sub>6</sub> conversion [%]	PO yield [%]
		PO	AC	AT	AD	CO <sub>2</sub>		
ref.cat.	RuO <sub>2</sub> + CuO + NaCl	48	0	0	0	52	10.00	4.80
1	*RuO <sub>2</sub> + CuO + NaCl	40	0.5	0	0	60	6.25	2.48
2	*RuO <sub>2</sub> + CuO + Na <sub>2</sub> O	0	0	0	0	+ <sup>[b]</sup>	0.40	0
3	*RuO <sub>2</sub> + CuO	28	0.3	0	0	71.7	5.88	1.65
4	CuO + NaCl	0	0	0	0	+ <sup>[b]</sup>	0.05	0
5	CuO + Na <sub>2</sub> O	0	0	0	0	+ <sup>[b]</sup>	0.07	0
6	*RuO <sub>2</sub> + NaCl	1	0	0	0	99	5.39	0.04
7	*RuO <sub>2</sub> + Na <sub>2</sub> O	0	0	0	0	+ <sup>[b]</sup>	0.38	0
8	Na <sub>2</sub> O	0	0	0	0	+ <sup>[b]</sup>	0.08	0
9	NaCl	0	0	0	0	+ <sup>[b]</sup>	0.06	0

[a] Precursor: RuO<sub>2</sub> = (NH<sub>4</sub>)<sub>2</sub>RuCl<sub>6</sub>, \*RuO<sub>2</sub> = Ru(NO)(NO<sub>3</sub>)<sub>3</sub>, CuO = Cu(NO<sub>3</sub>)<sub>2</sub>·2.5H<sub>2</sub>O, NaCl = NaCl, Na<sub>2</sub>O = Na(NO<sub>3</sub>), weight ratio of Ru or \*Ru/Cu/Na/SiO<sub>2</sub> = 7.14:3.57:1.78:87.5. [b] In these very low C<sub>3</sub>H<sub>6</sub> conversion experiments, CO<sub>2</sub> was the only product observed. Measurements were taken with no chlorinated hydrocarbon co-feed after 2 h of startup if the catalyst performance remained in a pseudo-steady-state.

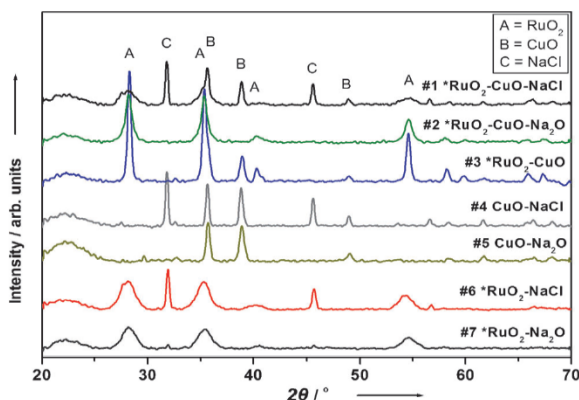


Figure 1. XRD spectra of the various catalysts investigated in this study.

sented in Table 1, and their XRD patterns are shown in Figure 1. The reference catalyst (ref.cat.) in Table 1 was prepared by using (NH<sub>4</sub>)<sub>2</sub>RuCl<sub>6</sub> as the RuO<sub>2</sub> precursor. To avoid residual chloride in the catalytic materials after calcination, Ru(NO)(NO<sub>3</sub>)<sub>3</sub> (denoted as \*RuO<sub>2</sub>, which has chemical activity similar to that of RuO<sub>2</sub>) was used as the source of Ru.

These results revealed several important aspects of this catalytic system, including the following:

- 1) Na<sub>2</sub>O (catalyst #8) and NaCl (catalyst #9) on SiO<sub>2</sub> were inactive for propylene reactions
- 2) The reference catalyst (ref.cat.) prepared from the (NH<sub>4</sub>)<sub>2</sub>RuCl<sub>6</sub> precursor provided a higher yield of PO than catalyst #1 prepared from the Ru(NO)(NO<sub>3</sub>)<sub>3</sub> precursor, because the excess amount of Cl (in the form of NaCl) promoted the formation of PO<sup>[18]</sup>
- 3) Importantly, Cl-free catalyst #2 exhibited very little reactivity with no PO formation. Comparison of the XRD spectra of catalysts #1 and #2 (Figure 1) also showed that the crystalline CuO phase (indicated by B) in catalyst #1 was absent in

catalyst #2, which was Cl free. This is important evidence that suggests that CuO crystals are the key catalytic sites for the synthesis of PO in this system

- 4) Comparison of the XRD spectra of catalysts #1, #2, #4, and #5 revealed that only catalyst #2 did not show the crystalline CuO phase peak at 2θ = 39°. This suggests that in the absence of Cl ions but in the presence of Ru, Cu, and Na ions, the Na ions block the formation of CuO crystals

- 5) Comparison of the reactivity results in Table 1 for catalysts #2, #5, and #7 revealed that Na<sub>2</sub>O strongly inhibited the reaction. Na ions also appear to have reduced the particle size of RuO<sub>2</sub>, as seen by comparing the XRD spectrum of catalyst #3 to the spectra of #1, #2, #6, and #7 at approximately 26–28°. However, because the \*RuO<sub>2</sub> peaks become broader, especially for catalyst #1, this appears also to improve the PO selectivity
- 6) Comparison of catalysts #6 and #7 in Table 1 revealed that NaCl is important not only to suppress the formation of CO<sub>2</sub><sup>[18]</sup> but also to initiate the reaction. Catalyst #6 gave higher conversions of propylene than catalyst #7, but the product was primarily CO<sub>2</sub>
- 7) Comparison of catalysts #4 and #6 revealed that NaCl plays a critical role only in the presence of both \*RuO<sub>2</sub> and CuO. This indicates that \*RuO<sub>2</sub> is also an active catalytic site but for the complete combustion
- 8) Comparison of catalysts #1 and #6 revealed that these two samples exhibited similar conversions of propylene but visibly different PO selectivities, which clearly points to CuO as an important site for the transformation of propylene into PO after initial activation over \*RuO<sub>2</sub> crystals. This indicates a cooperative effect between \*RuO<sub>2</sub> and the CuO crystals. In contrast, catalyst #3 indicates that even in the absence of the Cl source, CuO and RuO<sub>2</sub> may cooperate and convert propylene into PO, but with lower PO selectivity.

In summary, for the SiO<sub>2</sub>-supported RuO<sub>2</sub>-CuO-NaCl catalysts, crystalline CuO is implicated as the main catalytic site for the formation of PO with promotion by crystalline RuO<sub>2</sub> and CO<sub>2</sub> suppression by NaCl. To test this hypothesis, a series of experiments were performed to study the effects of the NaCl loading on the RuO<sub>2</sub>-CuO/SiO<sub>2</sub> catalysts. The catalysts were prepared by using (NH<sub>4</sub>)<sub>2</sub>RuCl<sub>6</sub>, Cu(NO<sub>3</sub>)<sub>2</sub>·2.5H<sub>2</sub>O, and Na(NO<sub>3</sub>) as precursors, followed by impregnation on SiO<sub>2</sub>, drying, and calcination as described earlier. It was also assumed, for calculation purposes, that all Na atoms would form crystalline NaCl in the final materials as a result of the excess amount of the Cl source. The performance test results of this series of catalysts are shown in Figure 2.



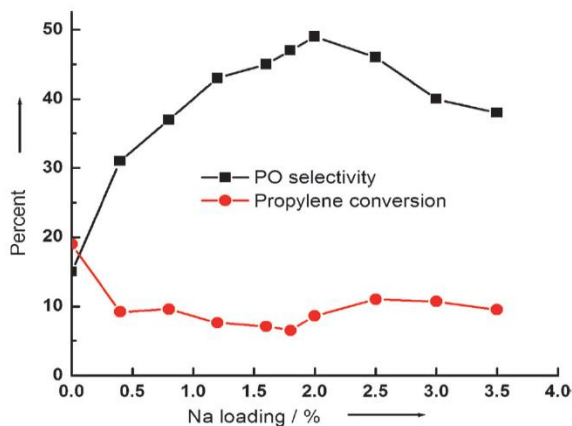


**Figure 2.** Results of the RuO<sub>2</sub>-CuO/SiO<sub>2</sub> catalysts at different Na loadings. Precursor: RuO<sub>2</sub> = (NH<sub>4</sub>)<sub>2</sub>RuCl<sub>6</sub>, CuO = Cu(NO<sub>3</sub>)<sub>2</sub>·2.5H<sub>2</sub>O, Na<sub>2</sub>O = Na(NO<sub>3</sub>), weight ratio Ru/Cu = 7.14:3.57, SiO<sub>2</sub> and Na were varied. Measurements were taken with no chlorinated hydrocarbon co-feed after 2 h of startup if the catalyst performance remained in a pseudo-steady-state.

As seen in Figure 2, in the absence of Na loading, propylene conversion was approximately 19% with a PO selectivity of 15%. Increasing the Na loading to 2% increased the PO selectivity to a maximum of approximately 49%, whereas the conversion of propylene decreased to approximately 9%. At higher Na loadings, the PO selectivity started to decrease, whereas the conversion of propylene remained relatively constant at approximately 10%.

At low Na loadings, the NaCl crystals are expected to be well dispersed and small, and they could even be incorporated into the solid structure. They also primarily occupy highly acidic sites on the catalysts, which causes CO<sub>2</sub> suppression. This initially results in lower conversions of propylene, but increased PO selectivity owing to electronic effects.<sup>[18]</sup> After all of the highly acidic sites are capped, however, the remaining Na (as NaCl) forms larger NaCl crystals and/or aggregates. After a certain point (≈2% Na loading in our experiments, Figure 2), the excess amount of NaCl leads to the formation of larger crystals, which then separate from the RuO<sub>2</sub>-CuO clusters; this lowers the PO selectivity, whereas the conversion of propylene remains approximately the same. The XRD spectra of this group of catalysts confirmed this explanation (see the Supporting Information).

A temperature-programmed reduction (TPR) experiment was also performed to gain insight into the nature and interaction of the surface sites, especially for \*RuO<sub>2</sub> and CuO (see Figure 3). The TPR profile of CuO/SiO<sub>2</sub> shows a single broad peak at 423 °C, whereas that for catalyst #4 shows two peaks: a main peak at 423 °C and a shoulder at approximately 330 °C. The peak at 423 °C is due to the reduction of bulk CuO, and the lower-temperature peak corresponds to the reduction of the highly dispersed copper species (e.g., small 2D or 3D clusters), including isolated Cu<sup>2+</sup> ions that interact with the SiO<sub>2</sub> support.<sup>[19]</sup> As seen in Figure 3, all \*RuO<sub>2</sub>-containing catalysts exhibit two TPR peaks. The peak at the lower temperature (be-

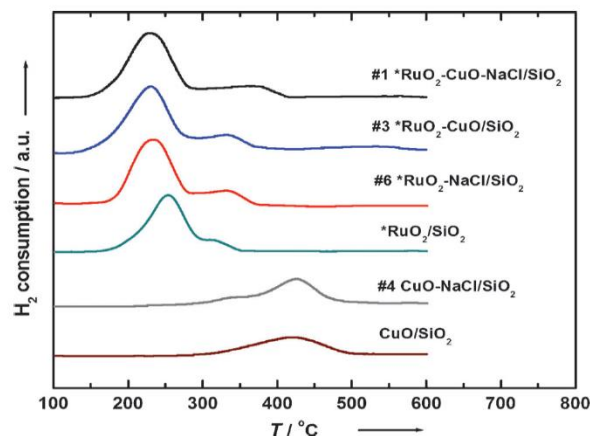


**Figure 3.** TPR profiles of all combinations of \*RuO<sub>2</sub>, CuO, and NaCl on SiO<sub>2</sub>. Each catalyst had a weight percent of Ru, Cu, and Na on SiO<sub>2</sub> of 7.19, 3.57, and 1.79%, respectively.

tween 230 and 250 °C) corresponds to the complete reduction of Ru<sup>4+</sup> to Ru<sup>0</sup>, and the shoulder (≈320 °C) corresponds to the ruthenium species interacting with the support.<sup>[20]</sup> Mass spectrometric monitoring of the effluent gases during the TPR experiments revealed no CO<sub>x</sub> or CH<sub>4</sub>.<sup>[21]</sup> This suggests that the above explanations for the observed TPR shoulders are likely correct.

A close inspection of the TPR profiles in Figure 3 revealed that the maximum peak for catalysts #1 and #6 was shifted towards lower temperatures relative to that of \*RuO<sub>2</sub>/SiO<sub>2</sub>, that is, from 253 to 230 °C. In contrast, the shoulder was shifted towards higher temperatures, that is, from 310 °C for the \*RuO<sub>2</sub>/SiO<sub>2</sub> catalyst to 370 and 350 °C for catalyst #1 and #6, respectively. These shifts may be due to a decrease in the size of the \*RuO<sub>2</sub> particle in the presence of Na. A similar trend was also observed for the TPR profile of catalyst #3 relative to that of \*RuO<sub>2</sub>/SiO<sub>2</sub>. In this case, a combination of effects may be responsible for the observed TPR shifts. First, the particle size of \*RuO<sub>2</sub> in catalyst #3 is smaller than that in \*RuO<sub>2</sub>/SiO<sub>2</sub> as a consequence of the presence of CuO.<sup>[17]</sup> Second, the observed shifts can be due to the presence of strong interactions between \*RuO<sub>2</sub> and the CuO crystals.

As mentioned above, the main TPR peaks were at 423 °C for CuO in catalyst #4 and CuO/SiO<sub>2</sub>. However, such peaks were absent in other CuO-containing catalysts such as catalysts #1 and #3. This is because both \*RuO<sub>2</sub> and CuO were reduced simultaneously in catalysts #1 and #3 owing to a spillover effect induced by the rapid reduction of RuO<sub>2</sub>. That is, at lower temperatures the RuO<sub>2</sub> TPR peak becomes larger, which is caused by a larger consumption of H<sub>2</sub><sup>[22]</sup> by the combined reduction of RuO<sub>2</sub> and CuO, concomitant with the loss of the individual CuO peak at higher temperatures. This phenomena was also observed in the study of the Ru-Cu system for butane hydrogenolysis.<sup>[20]</sup> That study concluded that CuO was well spread on the surface of RuO<sub>2</sub> and that RuO<sub>2</sub> and CuO were in very close proximity. Our TPR results presented in Figure 3 are in



harmony with this picture. A close inspection of the TPR profile for catalyst #3 revealed the presence of a very small and broad peak at approximately 500 °C. This could be due to some isolated CuO clusters that remained on the SiO<sub>2</sub> surface that were distant from the RuO<sub>2</sub> crystals in the absence of Na.

Shown in Figure 4 is a high-resolution transmission electron microscopy (HR-TEM) image in support of the TPR experiments. Although it is difficult to identify the small CuO crystals (3–5 nm) on the surface of the RuO<sub>2</sub> crystals ( $\approx 10 \times 30$  nm), the use of a crystal plane unique (fast Fourier transform) to RuO<sub>2</sub> and CuO can identify these components. The TEM images also

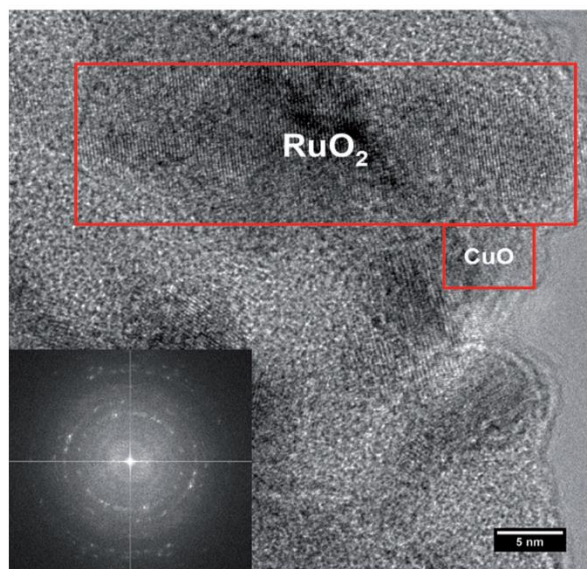


**Figure 4.** HR-TEM image of the SiO<sub>2</sub>-supported RuO<sub>2</sub>-CuO-NaCl catalyst. The RuO<sub>2</sub>+CuO clusters are in close proximity. Fast Fourier transform of the HR-TEM image was used to identify crystal planes unique to RuO<sub>2</sub>, CuO, and NaCl.

confirmed that CuO and RuO<sub>2</sub> were distinct crystal structures that were in close proximity. Notably, NaCl crystals were also present as cubic structures ( $\approx 30$  nm) but are not shown in this particular TEM image.

By taking into account all of the aforementioned findings, a model for the RuO<sub>2</sub>-CuO-NaCl/SiO<sub>2</sub> catalyst and a plausible mechanism for the epoxidation of propylene over this catalyst system may be formulated. The proposed model and mechanism are shown in Figure 5a,b. According to this mechanism, an O<sub>2</sub> molecule first adsorbs (chemisorption) onto an active center on the RuO<sub>2</sub> surface and dissociates into two surface O atoms (O<sub>s</sub>). The O<sub>s</sub> migrates across the surface to a neighboring CuO site, which is in close proximity, to form CuO-O. Gas-phase propylene then interacts with CuO-O ultimately to form PO through the formation of relevant intermediates such as an oxametallocycle and other species.<sup>[23]</sup>

In conclusion, a mechanism for the direct epoxidation of propylene by O<sub>2</sub> over a SiO<sub>2</sub>-supported RuO<sub>2</sub>-CuO-NaCl cata-

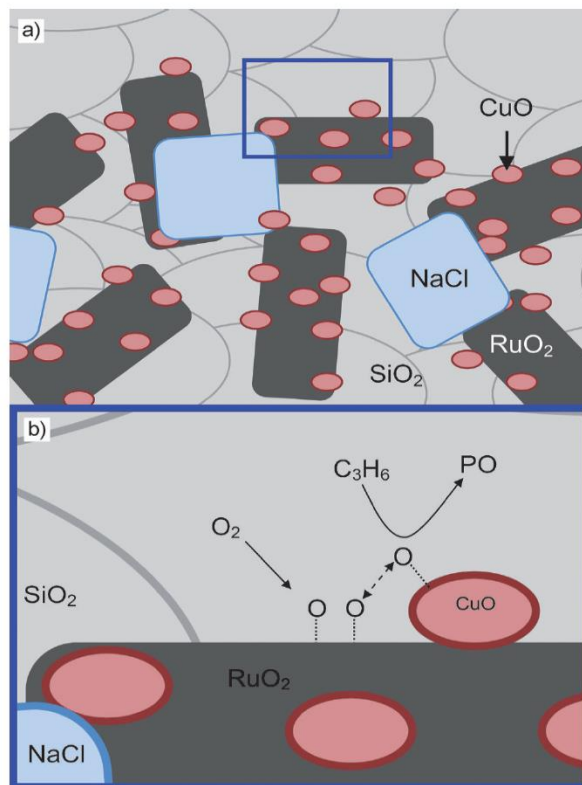


**Figure 5.** a) Schematic structure of the RuO<sub>2</sub>-CuO-NaCl/SiO<sub>2</sub> catalyst. b) Proposed mechanism for the epoxidation of propylene, showing the dissociative adsorption of O<sub>2</sub> onto the RuO<sub>2</sub> surface, surface migration of adsorbed oxygen to CuO surface, and the formation of PO.

lyst, previously discovered in our laboratories, was developed. The trimetallic catalyst at 12.5 wt% total metal loading was characterized by using powder XRD, HR-TEM, and TPR techniques. These studies confirmed that this catalyst system consists of distinct nanocrystals of RuO<sub>2</sub>, CuO, and NaCl. Furthermore, the crystalline RuO<sub>2</sub> and CuO particles are in close proximity, and the CuO particles are generally smaller than the RuO<sub>2</sub> particles with the result that the CuO particles are likely to be positioned on the surface of the RuO<sub>2</sub> structures. In investigations of the effects of Na and Cl, Na<sub>2</sub>O showed itself to be a strong inhibitor of PO synthesis, whereas NaCl played two important roles: it reduced the RuO<sub>2</sub> crystal size, which favored PO activity,<sup>[17]</sup> and suppressed CO<sub>2</sub> combustion, which led to higher PO selectivity. A critical finding ascertained from comparing the XRD patterns and the performance test results of single and bimetallic subsets of the RuO<sub>2</sub>-CuO-NaCl/SiO<sub>2</sub> catalyst, along with chlorinated and unchlorinated variants, indicated that the active site of the catalyst is likely the CuO crystal. A mechanism was therefore proposed in which RuO<sub>2</sub> adsorbs diatomic oxygen from the gas phase; then, the adsorbed oxygen undergoes surface migration onto CuO, from which it is transferred to propylene to form PO. Further improvements of this



catalyst thus could be made by precise arrangement of the crystalline RuO<sub>2</sub>, CuO, and NaCl phases on the SiO<sub>2</sub> support.

## Experimental Section

SiO<sub>2</sub>-supported mono-, bi-, and trimetallic heterogeneous catalysts were prepared by co-impregnation. For the monometallic catalysts, the metal salt aqueous solutions with aqueous solution mixtures of Ru [(NH<sub>4</sub>)<sub>2</sub>RuCl<sub>6</sub>, Aldrich or Ru(NO)(NO<sub>3</sub>)<sub>3</sub>, Alfa Aesar, Ru 31.3% min], Cu [Cu(NO<sub>3</sub>)<sub>2</sub>·2.5H<sub>2</sub>O, Alfa Aesar, ACS, 98.0–102.0%], and Na (NaNO<sub>3</sub>, Alfa Aesar, ACS, 99.0% or NaCl, Alfa Aesar ACS, 99%)<sup>[24]</sup> were prepared to achieve a predetermined weight percent (by metal atomic weight) loading on the SiO<sub>2</sub> support powder (SiO<sub>2</sub>, Alfa Aesar, surface area 145 m<sup>2</sup> g<sup>-1</sup>). Each metal salt solution was introduced to SiO<sub>2</sub> and left to penetrate the support for 24 h in air. The resulting materials were dried (120 °C, until dry) and calcined (500 °C, 12 h) in air.

These materials (≈5.0 mg) were investigated for their catalytic performance by using previously developed high-throughput heterogeneous catalysis screening tools.<sup>[25]</sup> The array channel reactor was used to test 80 different catalysts in a single experiment by using a computer-controlled system. All experiments were performed under atmospheric pressure at a gas hourly space velocity of 20000 h<sup>-1</sup> controlled by using mass flow controllers (MKS, Andover, MA). The feed gas consisted of 1 vol% propylene (C<sub>3</sub>H<sub>6</sub>), 4 vol% O<sub>2</sub>, and balance He at a reactor temperature of 250 °C. Data analysis was conducted by an online Micro-Gas Chromatograph (Varian, CP-4900) equipped with a thermal conductivity detector (TCD), Porapak U (10 μm), and 5 Å molecular sieves (10 μm). The detected products were propylene oxide, acetone, acetaldehyde, CO<sub>2</sub>, and acrolein. The propylene conversion, product selectivity, and yield (calculated as selectivity of a product × propylene conversion) of the products were determined on the basis of carbon balance. The reproducibility of the experiments was within ±10%.

Powder XRD patterns were obtained with an X-ray powder diffractometer (Panalytical X'Pert Pro) by using CuK<sub>α</sub> radiation, 45 kV, and 40 mA to identify different phases. TEM studies were performed by using a FEI Titan 80-300 TEM. For high-resolution TEM imaging a field emission gun operating at 300 kV was used.

TPR measurements were made by using an apparatus developed in the laboratory.<sup>[26]</sup> Each TPR run was performed by passing a H<sub>2</sub>-He mixture (5% H<sub>2</sub>) over the catalyst (160 mg) placed in a quartz reaction tube (0.8 cm in diameter and 45 cm long) positioned in a furnace (Vulcan 3–550) at a total gas flow rate of 20 mL min<sup>-1</sup>. A heating rate of 10 °C min<sup>-1</sup> was set by using the furnace's programmable temperature controller (PID). Hydrogen consumption was monitored online by a quadrupole mass spectrometer (QMS, RGA 200, Stanford Research System, Santa Clara, CA) from 100 to 600 °C. Prior to the TPR measurements, the catalysts were treated in situ by flowing He at 20 mL min<sup>-1</sup> from RT to 200 °C at a heating rate of 10 °C min<sup>-1</sup> and maintaining these conditions for an additional 1 h, after which it was cooled down to 100 °C.

## Acknowledgements

We thank the Laboratory Catalyst Systems, LLC, for providing access to their facilities, for the use of their catalytic materials discovery library, and for financial support. A.S. acknowledges the Faculty of Engineering, Kasetsart University for financial support.

B.Z. acknowledges the University of California, Los Angeles (UCLA) Graduate Division Fellowship. D.N. acknowledges the National Science Foundation MCTP-DGE-0654431.

**Keywords:** copper oxide · epoxidation · propylene oxide · ruthenium oxide · supported catalysts

- [1] D. Kahlich, U. Wiechern, J. Lindner, *Propylene Oxide. In Ullmann's Encyclopedia of Industrial Chemistry*, Wiley, 2000, pp. 1–25.
- [2] F. Cavani, J. H. Teles, *ChemSusChem* 2009, 2, 508–534.
- [3] T. A. Nijhuis, M. Makkee, J. A. Moulijn, B. M. Weckhuysen, *Ind. Eng. Chem. Res.* 2006, 45, 3447–3459.
- [4] R. A. Vansanten, C. P. M. Degroot, *J. Catal.* 1986, 98, 530–539.
- [5] T. Hayashi, K. Tanaka, M. Haruta, *J. Catal.* 1998, 178, 566–575.
- [6] K. Murata, Y. Kiyozumi, *Chem. Commun.* 2001, 1356–1357.
- [7] T. A. Nijhuis, S. Musch, M. Makkee, J. A. Moulijn, *Appl. Catal. A* 2000, 196, 217–224.
- [8] a) S. Yang, W. Zhu, Q. Zhang, Y. Wang, *J. Catal.* 2008, 254, 251–262; b) X. X. Wang, Q. H. Zhang, S. F. Yang, Y. Wang, *J. Phys. Chem. B* 2005, 109, 23500–23508.
- [9] a) W. M. Zhu, Q. H. Zhang, Y. Wang, *J. Phys. Chem. C* 2008, 112, 7731–7734; b) H. Chu, L. Yang, Q. H. Zhang, Y. Wang, *J. Catal.* 2006, 241, 225–228; c) Y. Wang, H. Chu, W. Zhu, Q. Zhang, *Catal. Today* 2008, 131, 496–504.
- [10] O. P. H. Vaughan, G. Kyriakou, N. Macleod, M. Tikhov, R. M. Lambert, *J. Catal.* 2005, 236, 401–404.
- [11] Z. Song, N. Mimura, J. J. Bravo-Surez, T. Akita, S. Tsubota, S. T. Oyama, *Appl. Catal. A* 2007, 316, 142–151.
- [12] J. H. Huang, T. Akita, J. Faye, T. Fujitani, T. Takei, M. Haruta, *Angew. Chem. Int. Ed.* 2009, 48, 7862–7866; *Angew. Chem.* 2009, 121, 8002–8006.
- [13] T. Hayashi, L. B. Han, S. Tsubota, M. Haruta, *Ind. Eng. Chem. Res.* 1995, 34, 2298–2304.
- [14] a) B. S. Uphade, M. Okumura, S. Tsubota, M. Haruta, *Appl. Catal. A* 2000, 190, 43–50; b) A. K. Sinha, S. Seelan, S. Tsubota, M. Haruta, *Angew. Chem. Int. Ed.* 2004, 43, 1546–1548; *Angew. Chem.* 2004, 116, 1572–1574.
- [15] H. Orzesek, R. P. Schulz, U. Dingerdissen, W. F. Maier, *Chem. Eng. Technol.* 1999, 22, 691–700.
- [16] M. Daté, Y. Ichihashi, T. Yamashita, A. Chiorino, F. Boccuzzi, M. Haruta, *Catal. Today* 2002, 72, 89–94.
- [17] A. Seubsai, M. Kahn, S. Senkan, *ChemCatChem* 2011, 3, 174–179.
- [18] A. Seubsai, S. Senkan, *ChemCatChem* 2011, 3, 1751–1754.
- [19] Z. L. Wang, Q. S. Liu, J. F. Yu, T. H. Wu, G. J. Wang, *Appl. Catal. A* 2003, 239, 87–94.
- [20] S. Galvagno, C. Crisafulli, R. Maggiore, G. R. Tauszik, A. Giannetto, *J. Therm. Anal.* 1985, 30, 611–618.
- [21] D. E. Damiani, E. D. P. Millan, A. J. Rouco, *J. Catal.* 1986, 101, 162–168.
- [22] M. G. Musolino, C. V. Caia, C. Busacca, F. Mauriello, R. Pietropaolo, *Appl. Catal. A* 2009, 357, 106–113.
- [23] a) L. J. Broadbelt, R. Q. Snurr, *Appl. Catal. A* 2000, 200, 23–46; b) D. Torres, N. Lopez, F. Illas, R. M. Lambert, *Angew. Chem. Int. Ed.* 2007, 46, 2055–2058; *Angew. Chem.* 2007, 119, 2101–2104.
- [24] A. C. Kizilkaya, S. Senkan, I. Onal, *J. Mol. Catal. A* 2010, 330, 107–111.
- [25] a) S. Duan, S. Senkan, *Ind. Eng. Chem. Res.* 2005, 44, 6381–6386; b) S. M. Senkan, S. Ozturk, *Angew. Chem. Int. Ed.* 1999, 38, 791–795; *Angew. Chem.* 1999, 111, 867–871; c) S. Senkan, K. Krantz, S. Ozturk, V. Zengin, I. Onal, *Angew. Chem. Int. Ed.* 1999, 38, 2794–2799; *Angew. Chem.* 1999, 111, 2965–2971; d) S. Senkan, M. Kahn, S. Duan, A. Ly, C. Leidhom, *Catal. Today* 2006, 117, 291–296; e) S. Senkan, *Angew. Chem. Int. Ed.* 2001, 40, 312–329; *Angew. Chem.* 2001, 113, 322–341.
- [26] A. Miller, B. Zohour, A. Seubsai, D. Noon, S. Senkan, *Ind. Eng. Chem. Res.* 2013, 52, 9551–9555.

Received: November 28, 2013

Revised: January 20, 2014

Published online on April 1, 2014

## A5. Spatial Profiles in RuO<sub>2</sub>-CuO-NaCl/SiO<sub>2</sub> Packed-Bed Propylene Epoxidation Reactors



## Spatial Profiles in RuO<sub>2</sub>–CuO–NaCl/SiO<sub>2</sub> Packed-Bed Propylene Epoxidation Reactors

Bahman Zohour,<sup>†</sup> Daniel Noon,<sup>†</sup> Anusorn Seubsai,<sup>‡</sup> and Selim Senkan<sup>\*,†</sup>

<sup>†</sup>Department of Chemical Engineering, University of California, Los Angeles, California 90095, United States

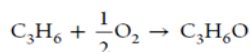
<sup>‡</sup>Department of Chemical Engineering, Kasetsart University, Bangkok, Thailand 10900

**ABSTRACT:** The spatially resolved species concentration and temperature profiles in a catalytic fixed-bed propylene epoxidation reactor were determined for RuO<sub>2</sub>–CuO–NaCl/SiO<sub>2</sub> catalysts, using microprobe sampling and online gas chromatography. Experiments were performed at furnace temperatures of 250 and 270 °C and feed gas compositions of 1 mol % C<sub>3</sub>H<sub>6</sub>, 4 mol % O<sub>2</sub>, and 1<sup>2</sup>/<sub>3</sub> mol % C<sub>3</sub>H<sub>6</sub>, 3<sup>1</sup>/<sub>3</sub> mol % O<sub>2</sub>, both with 95 mol % He dilution. The pressure was atmospheric, and the gas hourly space velocity (GHSV) was ~30 000 h<sup>-1</sup>. The spatial profiles indicated that propylene oxide (PO) and acetone production exhibited well-defined induction periods. In contrast, acrolein (AC) formation was prompt and occurred early in the catalyst bed. These findings point to two different mechanisms associated with the formation of PO/AT and AC, respectively. The absence of any measurable propanal in the product mix suggests that C2 oxametallacycle propylene (C2OMMP) may be the preferred route for PO formation in this catalytic system. The spatial profiles reported represent information-rich data that are of significant utility for the development and validation of detailed chemical kinetic mechanisms for propylene partial oxidation in general and epoxidation in particular.

### INTRODUCTION

Propylene oxide (PO) is an important intermediate for the production of a large variety of valuable consumer products such as polyurethane foams, propylene glycol, cosmetics, food emulsifiers, fumigants, and insecticides.<sup>1,2</sup> Over eight million tons of PO are produced annually, mostly via the chlorohydrin and peroxidation processes.<sup>1,2</sup> Recently, a process using H<sub>2</sub>O<sub>2</sub> has also been commercialized.<sup>1,3</sup> However, the direct synthesis of PO from propylene and oxygen remains an important goal in industrial catalysis. The technology, the economics, and the environmental impacts of current as well as alternate propylene epoxidation processes were reviewed by Cavani and Teles in 2009<sup>1</sup> and Nijhuis et al. in 2006.<sup>2</sup>

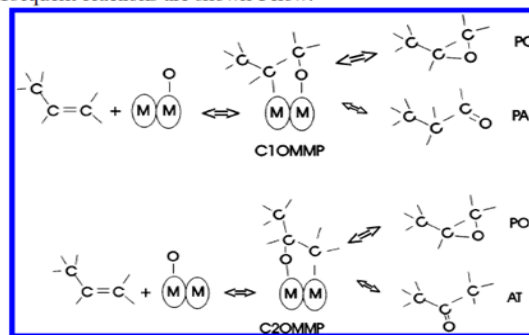
The direct epoxidation of propylene by oxygen involves the following overall stoichiometry:



However, besides PO, the partial oxidation of propylene can also form a variety of byproducts, such as acetone (AT), acrolein (AC), propionaldehyde (propanal, PA), acetaldehyde (AA), and formaldehyde (FA), together with deep oxidation products of CO and CO<sub>2</sub>. Earlier research on direct PO formation involved the use of Ag-based catalysts in an attempt to produce the commercial success of ethylene oxide (EO) production.<sup>1,2,4</sup> Many other catalytic materials and techniques were also explored for PO synthesis, including silica-supported Cu,<sup>5</sup> various single and mixed metal oxides,<sup>6,7</sup> Au-based catalysts with H<sub>2</sub><sup>8</sup> or H<sub>2</sub>O<sup>9</sup> as co-reactants, titania-based catalysts,<sup>10</sup> and molten salts of metal nitrates,<sup>2</sup> in addition to the use of O<sub>3</sub><sup>11</sup> and nitrous oxide<sup>2</sup> as reactants. PO synthesis by Ag<sub>3</sub> clusters deposited on thin alumina films prepared via molecular beam techniques was also performed.<sup>12</sup> Recently, we reported the discovery of a new class of silica-supported multimetallic RuO<sub>2</sub>–CuO–NaCl catalysts for the direct epoxidation of propylene by O<sub>2</sub> under atmospheric pressure.<sup>13</sup> This trimetallic catalyst, prepared via co-impregnation,

exhibits PO selectivities of 40%–50% with propylene conversions of 10%–20% at 240–270 °C and 1 atm.<sup>13</sup> It is important to note that all the aforementioned prior research involved measurements of reactor exit conditions, which provide data of limited information content.

PO is believed to occur via the formation of an oxametallacycle propylene intermediate (OMMP, where M represents a general surface metal atom) similar to that proposed for ethylene epoxidation.<sup>14,15</sup> However, the presence of the methyl group in propylene results in the formation of two distinct OMMP structures, which lead to different products. For example, C1-OMMP formation (i.e., surface O is bonded to the =CH<sub>2</sub>) can directly form PO by cyclization and, via C1 to C2 H atom transfer, PA. Similarly, C2-OMMP formation (i.e., surface O is bonded to the =CHCH<sub>3</sub>) can also produce PO and, via C2 to C1 H atom transfer, AT. These OMMP structures and plausible subsequent reactions are shown below:



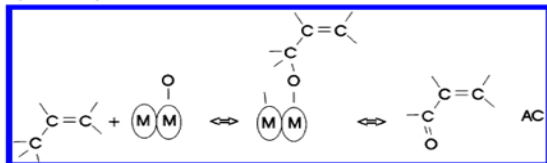
Received: July 26, 2013

Revised: February 27, 2014

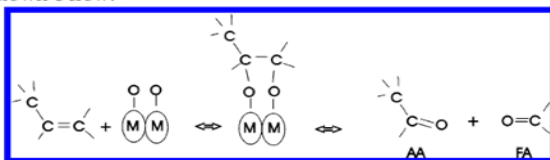
Accepted: March 19, 2014

Published: March 19, 2014

Based on this representation, the relative amounts of PA and AT produced can indicate the dominant OMMP structure expected to be present in a given catalytic system. On the other hand, the formation of AC requires O insertion into the methyl group (C3) of propylene, which is an entirely different pathway, and, as such, could involve a different surface metal atom M.



It should be recognized that the products PO, AT, and PA can also undergo subsequent isomerizations and related reactions.<sup>16</sup> Similarly, the formation of CH<sub>3</sub>CHO and HCHO could be taken into account by the formation of a C1OMMOC2 structure, as shown below:



Propylene, as well as all partial oxidation products, can undergo further oxidations, ultimately forming CO<sub>2</sub> and H<sub>2</sub>O.

As evident from the above discussion, propylene partial oxidation involves a highly complex network of parallel and sequential reactions. Consequently, to better control and optimize the propylene epoxidation reaction, detailed chemical kinetic mechanisms (DCKM) of the underlying surface reactions (as well as possible gas-phase reactions) must be developed and validated over a broad range of conditions. DCKM comprise a comprehensive description of chemical transformations in terms of *irreducible* chemical events or *elementary reactions* for which independent rate coefficient parameters, frequently expressed in the form  $k = AT^n \exp[-E/(RT)]$ , are either available from direct measurements or estimated from theoretical considerations.<sup>17</sup> DCKM are then combined with transport models for the simulation and optimization of propylene partial oxidation reactors.<sup>17</sup> However, the validation of DCKM require experimental data of high information content, because of the presence of a large number of species participating in an even larger number of elementary reactions.<sup>17</sup> In this regard, reproducing only the reactor exit concentrations will not be a particularly demanding test for mechanism validation. On the other hand, the prediction of the absolute *concentration profiles*, i.e., shapes, of all the major and minor species within the catalytic packed beds represents a more rigorous test for DCKM validation. It can be argued that traditional experiments in which reactor exit measurements at different gas flow rates and/or catalyst loadings are performed can be used to obtain similar data. However, traditional approaches rapidly become very tedious and extremely time-consuming especially when data of high information content are needed. Consequently, the development and use of new experimental techniques that allow for the rapid acquisition of spatial profiles in reactors is desirable. In an earlier study, Wong et al.<sup>18</sup> proposed a DCKM for the catalytic partial oxidation of propylene to AC and acrylic acid, together with the formation of numerous byproducts. Although these authors did not explicitly consider PO formation pathways in their

mechanism, their work represents a good starting point for the development of DCKM for propylene epoxidation.

Here, we report, for the first time, the spatially resolved species concentration and temperature profiles in a catalytic fixed-bed propylene epoxidation reactor using microprobe sampling for the RuO<sub>2</sub>-CuO-NaCl/SiO<sub>2</sub> catalyst discovered recently in our laboratories.<sup>13</sup> Although microprobe sampling techniques have long been used in high-temperature flame combustion research to obtain spatial temperature and concentration profiles,<sup>19</sup> their adaptation to and use in heterogeneous catalysis is relatively recent. Earlier applications of microprobe sampling to catalysis include the catalytic partial oxidation (CPO) of methane producing CO and H<sub>2</sub><sup>20</sup> and the oxidative coupling of methane (OCM) to form C<sub>2</sub>H<sub>6</sub> and C<sub>2</sub>H<sub>4</sub>.<sup>21</sup>

## EXPERIMENTAL SECTION

Experiments were performed using a fixed-bed tubular reactor system, as shown in Figure 1. The silica-supported multimetallic

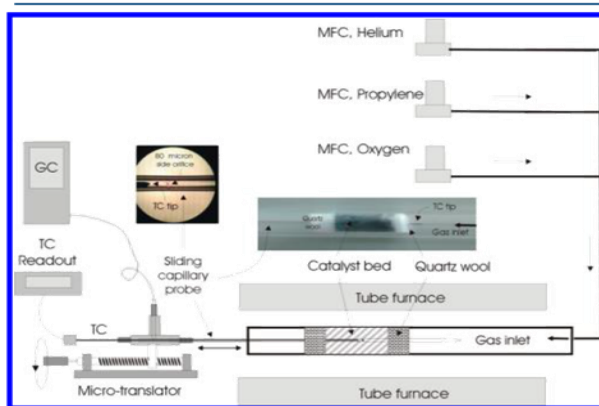


**Figure 1.** Schematic of the mass flow control system, heated quartz tube reactor setup, capillary sampling probe and gas chromatography, and temperature measurement system. Photographic images of the packed-bed reactor, magnified capillary probe, 80  $\mu\text{m}$  sampling orifice, and inserted thermocouple are also shown.

RuO<sub>2</sub>-CuO-NaCl catalyst was prepared via the *co-impregnation* method described previously.<sup>13</sup> Briefly, predetermined weights of amorphous fumed silica powder (SiO<sub>2</sub>, Alfa Aesar, surface area of 145 m<sup>2</sup>/g, bulk density of powder  $\approx$  0.2 g/cm<sup>3</sup>) were mixed with an aqueous solution of ruthenium [(NH<sub>4</sub>)<sub>2</sub>RuCl<sub>6</sub>, Aldrich], copper [Cu(NO<sub>3</sub>)<sub>2</sub>, Alfa Aesar, ACS, 98.0%–102.0%], and sodium [NaCl, Alfa Aesar, 99.99% (metals basis)]. The metal salt solution was then allowed to impregnate the support for 24 h in air. The resulting material was then heated at 165 °C until dried, and calcined at 480 °C for 6 h in air. The catalyst used in the experiments had a Ru:Cu:Na metal ratio of 4:2:1 (weight ratio, or  $\sim$ 3:4:4 atomic ratio) at 12.5 wt % total metal loading maximized the PO selectivity.<sup>22</sup> Fifty milligrams (50 mg) of this catalyst was packed into a 6-mm-diameter quartz tube and sandwiched between two quartz wool plugs, each weighing 10 mg (Figure 1). The bulk density and void fraction of the bed were determined to be about 0.27 g/cm<sup>3</sup> and 0.90, respectively, assuming nonporous SiO<sub>2</sub> nanoparticles having a solid density of 2.65 g/cm<sup>3</sup>. The reactor was placed inside a cylindrical tubular furnace, which also preheated the feed gases. Using electronic mass flow controllers (MFC, MKS Billerica, MA), the total flow



of reactant gases was maintained at 100 cm<sup>3</sup>/min at STP in all of the experiments.

Gas sampling was accomplished by centrally inserting a conically tapered and closed-end quartz capillary tube (800 μm, Friedrick and Dimock, Millville, NJ) into the packed bed, followed by gas analysis using online gas chromatography (Varian 4900 mini GC, with molecular sieve 5A and PoraPLOT U columns). The capillary had several 80-μm-diameter orifices laser-drilled on its side to withdraw gases from within the bed (see inset in Figure 1). The location of the sampling orifice and the overall length of the probe were designed such that the capillary tip always remained well outside the packed bed at any sampling position to avoid channeling and gas bypass. That is, the probe body always remained inserted into the entire bed length, including the quartz wool plugs. If the probe tip were moved into the bed during measurements, channeling would occur through the hole created. The capillary probe withdrew gas samples at a rate of ~5 cm<sup>3</sup>/min at STP, thus minimally perturbing the gas flow within the reactor, which was flowing at a rate of 100 cm<sup>3</sup>/min at STP. At this sampling rate, the residence time of the gases in the capillary probe can be estimated to be in the range of 25–50 ms. Temperature measurements were performed by placing a thin (250-μm-diameter) K-type thermocouple inside the capillary probe in the absence of gas withdrawal. The tip of the thermocouple was positioned at the sampling orifice. Temperature and concentration profiles were obtained by moving the capillary (with and without the thermocouple) in the axial direction using a micropositioning device (Velmex, Bloomfield, NY). Positional accuracy associated with the placement of the capillary probe within the reactor is estimated to be ±0.25 mm. Similar uncertainty also would be expected to exist between the temperature and concentration profiles.

The experiments were carried out at two distinct furnace temperatures of 250 and 270 °C under a pressure of 1 atm and at a gas hourly space velocity (GHSV) of ~30 000 h<sup>-1</sup>. Two feed gas compositions were explored: 1 mol% C<sub>3</sub>H<sub>6</sub> (Matheson, 99%), 4 mol% O<sub>2</sub> (Matheson, 99.9%), and 95 mol% He (Matheson 99.99%); and 1<sup>2</sup>/<sub>3</sub> mol% C<sub>3</sub>H<sub>6</sub>, 3<sup>1</sup>/<sub>3</sub> mol% O<sub>2</sub> and 95 mol% He. These feed streams correspond to O<sub>2</sub>/C<sub>3</sub>H<sub>6</sub> ratios of 4 and 2, respectively.

The propylene conversions and product selectivities were calculated on the basis of carbon atom balances. GC calibrations for propylene, oxygen, and CO<sub>2</sub> were performed using mass flow controllers (MKS) and He as a carrier gas. Calibrations for PO, AC, AT, and PA were performed by vaporizing known quantities of the liquid in a heated, evacuated 2250 cm<sup>3</sup> stainless steel tank and using He as a carrier gas.<sup>13</sup> All calibrations yielded linear five-point curves with a correlation factor of at least R<sup>2</sup> = 0.995, using the peak area as the basis for GC calculations.

## RESULTS AND DISCUSSION

Before presenting the results, several properties of the RuO<sub>2</sub>–CuO–NaCl/SiO<sub>2</sub> catalyst should be noted. First, this catalyst is well-documented to require ~1 h of activation;<sup>13</sup> consequently, the results reported here were obtained after this period. Second, this catalyst is also known to exhibit deactivation after 6 h of continuous operation, because of the loss of chlorine.<sup>13</sup> Although co-feeding chlorinated hydrocarbons at a parts per million level remedies this problem,<sup>22</sup> we did not implement this method. Instead, experiments were performed during the initial 2–5 h age period of the catalysts, after which the catalysts were replaced.

In Figures 2 and 3, the spatially resolved temperature and species mole percent profiles are presented for the feed O<sub>2</sub>/C<sub>3</sub>H<sub>6</sub>

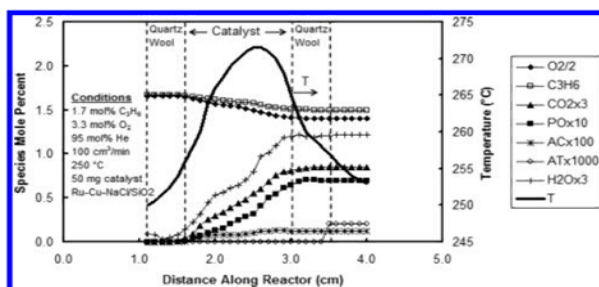


**Figure 2.** Species concentration profiles, including O<sub>2</sub>, propylene (C<sub>3</sub>H<sub>6</sub>), CO<sub>2</sub>, propylene oxide (PO), acrolein (AC), acetone (AT), and H<sub>2</sub>O and temperature profile for a feed of 1<sup>2</sup>/<sub>3</sub> mol % C<sub>3</sub>H<sub>6</sub>, 3<sup>1</sup>/<sub>3</sub> mol % O<sub>2</sub>, and 95 mol % He at 250 °C.

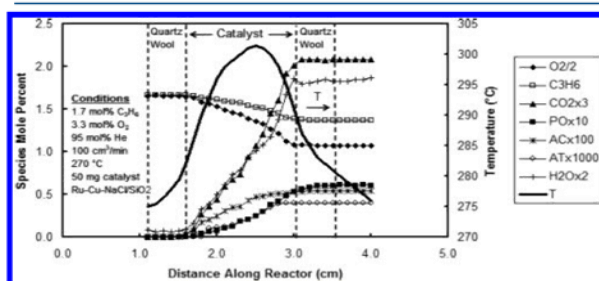


**Figure 3.** Species concentration profiles, including O<sub>2</sub>, propylene (C<sub>3</sub>H<sub>6</sub>), CO<sub>2</sub>, propylene oxide (PO), acrolein (AC), acetone (AT) and H<sub>2</sub>O and temperature profile for a feed of 1<sup>2</sup>/<sub>3</sub> mol % C<sub>3</sub>H<sub>6</sub>, 3<sup>1</sup>/<sub>3</sub> mol % O<sub>2</sub>, and 95 mol % He at 270 °C.

ratio of 2 at furnace temperatures of 250 and 270 °C, respectively. A total of seven species were quantified: O<sub>2</sub>, C<sub>3</sub>H<sub>6</sub>, PO, AT, AC, H<sub>2</sub>O, and CO<sub>2</sub>. Concentrations of other likely products (e.g., PA and AA) were too low for detection using the GC system with any appreciable accuracy. With the exception of the H<sub>2</sub>O concentrations, which were calculated from oxygen atom balances, all the species were quantified directly from GC measurements, using a multipoint GC calibration process performed before the experiments. In Figures 4 and 5, the corresponding spatial profiles for the PO and CO<sub>2</sub> selectivities and C<sub>3</sub>H<sub>6</sub> conversions are presented.

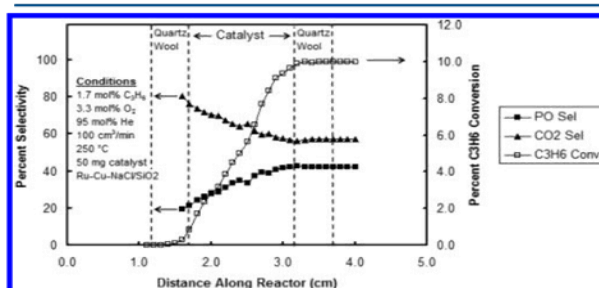


**Figure 4.** Propylene oxide (PO) selectivity, CO<sub>2</sub> selectivity, and propylene (C<sub>3</sub>H<sub>6</sub>) conversion profiles for a feed of 1<sup>2</sup>/<sub>3</sub> mol % C<sub>3</sub>H<sub>6</sub>, 3<sup>1</sup>/<sub>3</sub> mol % O<sub>2</sub>, and 95 mol % He at 250 °C.

In all the figures, the positions of the catalyst bed and quartz wool packing are indicated by vertical dashed lines; the catalyst

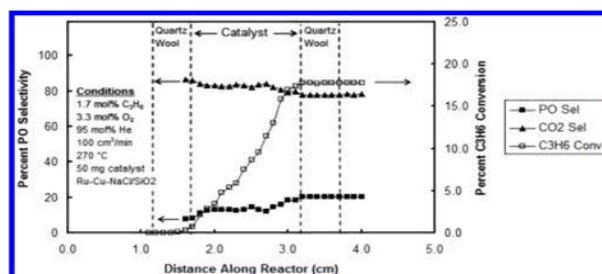


**Figure 5.** Propylene oxide (PO) selectivity, CO<sub>2</sub> selectivity, and propylene (C<sub>3</sub>H<sub>6</sub>) conversion profiles for a feed of 1<sup>2</sup>/<sub>3</sub> mol % C<sub>3</sub>H<sub>6</sub>, 3<sup>1</sup>/<sub>3</sub> mol % O<sub>2</sub>, and 95 mol % He at 270 °C.

packing starts at ~1.5 cm and ends at ~3.0 cm, corresponding to a bed depth of 1.5 cm. As evident from Figures 2 and 3, the spatial concentration and temperature profiles measured within the bed provide information-rich data on the kinetics and mechanism of the propylene and oxygen reaction. In contrast, the profiles at the catalyst exit were essentially featureless and contain very limited information.

As seen in Figure 2, the temperature increased to a maximum of ~272 °C at 1.1 cm into the catalyst bed (i.e., at a distance of 2.6 cm along the reactor), corresponding to a temperature rise of ~22 °C, then decreased toward the exit of the reactor. Since the reactor was not adiabatic, this temperature profile is expected for an exothermic reaction. The possible presence of radial temperature gradients was also explored by placing multiple thermocouples at different radial positions at the same axial position. These studies indicated radial temperature differences that were within measurement errors of 2–5 °C, which suggests that the treatment of the reactor as being quasi one-dimensional appears to be a reasonable assumption. The temperature decreases observed in the later stages of the catalytic bed are indicative of the increased importance of product adsorption on the title reaction. As product concentrations increase in the gas phase, their desorption rates from the catalyst surface should decrease, thereby decreasing the overall rate of the reaction. Consequently, decreases in the heat generation rate can no longer exceed heat losses into the furnace (at 250 °C), resulting in a net decrease in reactor temperature at increased propylene conversions.

An important issue that must also be considered in the acquisition of accurate temperature profiles in reactors is the thermal conduction along the thermocouple wires. Conduction can result in temperature smoothing and profile shifts, especially when large temperature gradients (e.g., >100s °C/mm, as seen in flames) exist.<sup>19</sup> However, in the current experiments, such effects appear to be relatively insignificant.

The species profiles shown in Figure 2 at a feed temperature of 250 °C show both confirmatory and new features. First, the integral (i.e., exit) reactor performance was ~10% C<sub>3</sub>H<sub>6</sub> conversion and 42% PO and 58% CO<sub>2</sub> selectivities, consistent with the O<sub>2</sub>/C<sub>3</sub>H<sub>6</sub> ratio of 2 (see also Figure 4) and previous experiments.<sup>13</sup> Second, the quartz wool packing had no catalytic activity, with respect to either propylene or the products, as all the concentration profiles remained flat prior to and after the catalyst bed. Third, reactions outside the catalyst bed can also be ruled out under the prevailing conditions. The fact that the measured concentration profiles remained flat (i.e., did not change with axial position within the quartz wool and reactor exit) supports the notion that reactions inside the sampling capillary were

unimportant in our experiments. Fourth, the entire catalyst bed depth was actively utilized in creating the integral results (i.e., PO levels monotonically increased with distance along the reactor until the end of the catalyst bed). Finally, there was a sudden increase in the AT concentration at 3.4 mm (i.e., within the quartz wool packing), which can be attributed to the detection limits of the GC. Evidently, at the lower temperatures associated with the downstream quartz wool section and beyond, the increased gas density was sufficient to bring AT levels above the detection limits of the GC.

From Figure 2, it can be seen that PO formation started early in the catalytic bed and steadily increased with distance along the reactor, reaching a peak level of ~0.075%. On the other hand, CO<sub>2</sub> formation rate was faster, ultimately reaching a peak level of 0.25% at the exit, concomitant with the formation of H<sub>2</sub>O (peaking at 0.38%). The higher CO<sub>2</sub> formation rate is not surprising, since 3 moles of CO<sub>2</sub> are produced per mole of C<sub>3</sub> species combusted. The profiles presented in Figure 4 reveal that PO selectivity also steadily increased and that for CO<sub>2</sub> decreased with increasing residence time in the reactor. These results clearly present useful trends that can be exploited for the design and operation of packed-bed reactors to improve PO selectivities. For example, increasing residence time can be beneficial in improving PO selectivity under the prevailing conditions.

The corresponding spatial profiles along the reactor at 270 °C feed temperature are shown in Figure 3. In this case, the temperature peak of 301 °C occurred at a distance of 2.6 cm along the reactor (i.e., 1.1 cm within the catalyst bed). Under these conditions, propylene conversion expectedly increased to a value of ~17.5%, as shown in Figure 5. This increase corresponds to an apparent activation energy of ~11 kcal/mol. However, the higher feed temperature of 270 °C had a significant detrimental effect on PO formation, both with respect to concentration (Figure 3) and selectivity (Figure 5). For example, the peak PO levels were only 0.06%, while CO<sub>2</sub> levels increased to 0.65%. The apparent activation energy for CO<sub>2</sub> levels formation corresponds to ~15 kcal/mol. Similarly, the PO selectivity only reached 20% (Figure 5), in contrast to 80% for CO<sub>2</sub>. At 270 °C, the spatial profile for PO selectivity also exhibited a weak increasing trend, with respect to the distance along the reactor, in marked contrast with the results at 250 °C (Figure 4).

As noted earlier, trace levels of AC and AT were also produced in the current experiments, the profiles of which are shown in Figures 2 and 3. AC clearly was more abundant than AT under the conditions investigated. The absence of any measurable PA in the product mix may suggest that C2OMMP is the major route for PO formation, which also produces AT. However, the subsequent destruction of PA cannot be ruled out without a detailed chemical kinetic analysis. At a feed temperature of 250 °C (Figure 2), the peak levels of AT and AC were ~0.2 × 10<sup>-3</sup> % and ~0.1 × 10<sup>-2</sup> %, respectively. That is, AC levels were a factor of ~5 higher. It is interesting to note an abrupt increase in AT levels at the exit of the catalyst bed in Figure 2. This is related to the insensitivity of the GC to the low concentrations of AT early in the reactor. That is, sampling probe artifacts can be ruled out, since at slightly higher concentrations (i.e., at 270 °C, Figure 3), AT profiles exhibit the expected trends. Unlike PO, increasing the feed temperature to 270 °C increased the AT and AC peak levels to 0.4 × 10<sup>-3</sup> % and 0.5 × 10<sup>-2</sup> %, respectively (see Figure 3). Concentrations reported on Figures 2 and 3 suggest apparent activation energies of ~11 and ~30 kcal/mol for AT and AC formation reactions, respectively. The higher-temperature sensitivity of AC formation is also consistent with the relatively weaker allylic C–H bonds.



In addition to their magnitudes, the shapes of the concentration profiles presented in Figure 3 also provide new insights on the kinetics and mechanisms of formation of AC, AT, and PO. For example, AC formation can be seen to be prompt, exhibiting its highest rate at the entrance to the catalytic bed. In contrast, AT and PO exhibited a well-defined induction period. These results are consistent with the two different mechanisms associated with the formation of AC and PO/AT, respectively, as discussed earlier.

In order to quantify the effects of feed gas composition on species concentration profiles, experiments were also performed at the  $O_2/C_3H_6$  ratio of 4 and at a feed temperature of 250 °C, and these results are presented in Figure 6. The corresponding

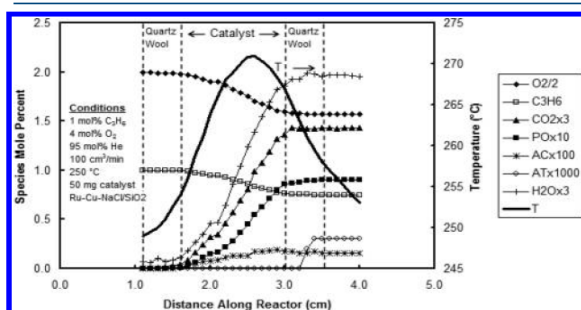


**Figure 6.** Species concentration profiles, including  $O_2$ , propylene ( $C_3H_6$ ),  $CO_2$ , propylene oxide (PO), acrolein (AC), acetone (AT), and  $H_2O$ , and temperature profile for a feed of 1 mol %  $C_3H_6$ , 4 mol %  $O_2$ , and 95 mol % He at 250 °C.

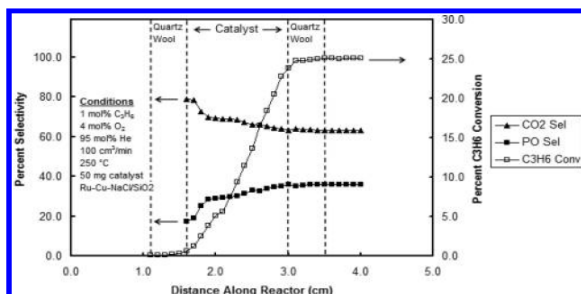


**Figure 7.** Propylene oxide (PO) selectivity,  $CO_2$  selectivity, and propylene ( $C_3H_6$ ) conversion profiles for a feed of 1 mol %  $C_3H_6$ , 4 mol %  $O_2$ , and 95 mol % He at 250 °C.

profiles for propylene conversion and PO and  $CO_2$  selectivities are presented in Figure 7. The peak temperature was  $\sim 271$  °C, a 21 °C temperature increase, where the peak is positioned at a distance of  $\sim 2.5$  cm along the reactor (i.e., 1.0 cm within the catalyst bed). From Figure 6, peak PO,  $CO_2$ , and  $H_2O$  levels were 0.09%, 0.50%, and 0.63%, respectively. A comparison of these results to Figure 2 indicate that increasing  $O_2$  increases the degree of propylene total combustion to  $CO_2$ , relative to epoxidation, which is an expected result. As seen in Figure 7, although propylene conversions increased and exhibited a peak level of  $\sim 25\%$ , the maximum PO selectivity decreased to 38%, with  $CO_2$  selectivity increasing to 62%. The PO selectivity also increased modestly with increasing residence time in the catalytic bed, in sharp contrast to the experiments at the  $O_2/C_3H_6$  ratio

of 2 (Figure 4). Significantly higher levels of AT and AC were also produced at the  $O_2/C_3H_6$  ratio of 4, with peak concentrations of  $\sim 0.3 \times 10^{-3}\%$  and  $\sim 0.2 \times 10^{-2}\%$ , respectively. These levels are  $\sim 50\%$  higher than those observed in Figure 2.

## CONCLUSIONS

Detailed species concentration and temperature profiles have been obtained for the first time in a propylene epoxidation fixed-bed reactor packed with  $RuO_2-CuO-NaCl/SiO_2$  catalysts. These profiles reveal significant new insights on the catalytic kinetics and mechanism of propylene epoxidation. In particular, spatial profiles indicate that acrolein (AC) formation was prompt and occurred early in the catalyst bed. In contrast, both acetone (AT) and propylene oxide (PO) production exhibited well-defined induction periods. These findings point to two different mechanisms associated with the formation of AC and AT/PO, respectively. The absence of any measurable propanal (PA) in the product mix also suggests that C2OMMP may be the preferred route for PO formation in this catalytic system. The spatial profiles reported represent information-rich data that are of significant utility for the development and validation of detailed chemical kinetic mechanisms for propylene partial oxidation in general and epoxidation in particular.

## AUTHOR INFORMATION

### Corresponding Author

\*E-mail: ssenkan@gmail.com.

### Notes

The authors declare no competing financial interest.

## ACKNOWLEDGMENTS

We thank the Laboratory Catalyst Systems, LLC for providing access to their facilities, for the use of their catalytic materials discovery library and for financial support. B.Z. and D.N. acknowledge the support of the UCLA Graduate Division Fellowship and the NSF IGERT: Materials Creation Training Program (MCTP) (No. DGE-0654431) and the California NanoSystems Institute, respectively.

## REFERENCES

- (1) Cavani, F.; Teles, J. H. Sustainability in Catalytic Oxidation: An Alternative Approach or a Structural Evolution? *ChemSusChem* **2009**, *2*, 508–534.
- (2) Nijhuis, T. A.; Makkee, M.; Moulijn, J. A.; Weckhuysen, B. M. Production of Propene Oxide: Catalytic Processes and Recent Developments. *Ind. Eng. Chem. Res.* **2006**, *45*, 3447–3459.
- (3) Tullo, A. H.; Short, P. L. Propylene Oxide Routes Take Off. *Chem. Eng. News* **2006**, *84*, 22–23.
- (4) Monnier, J. R. The direct epoxidation of higher olefins using molecular oxygen. *Appl. Catal., A* **2001**, *221*, 73–91.
- (5) Vaughan, O. P. H.; Kyriakou, G.; Macleod, N.; Tikhov, M.; Lambert, R. M. Copper as a selective catalyst for the epoxidation of propene. *J. Catal.* **2005**, *236*, 401–404.
- (6) Song, Z. X.; Mimura, N.; Bravo-Suarez, J. J.; Akita, T.; Tsubota, S.; Oyama, S. T. Gas-phase epoxidation of propylene through radicals generated by silica-supported molybdenum oxide. *Appl. Catal., A* **2007**, *316*, 142–151.
- (7) Orzesek, H.; Schulz, R. P.; Dingerdissen, U.; Maier, W. F. Selective Oxidation of Propene with Air to Propylene Oxide, a Case Study of Autoxidation Versus Catalytic Oxidation with AMM-Catalysts. *Chem. Eng. Technol.* **1999**, *22*, 691–700.
- (8) (a) Hayashi, T.; Han, L. B.; Tsubota, S.; Haruta, M. Formation of Propylene Oxide by the Gas-Phase Reaction of Propane and Propene Mixture with Oxygen. *Ind. Eng. Chem. Res.* **1995**, *34*, 2298–2304.

A6. Discovery of Superior Cu-GaO<sub>x</sub>-HoO<sub>y</sub> Catalysts for the Reduction of Carbon Dioxide to Methanol at Atmospheric Pressure



# Discovery of Superior Cu-GaO<sub>x</sub>-HoO<sub>y</sub> Catalysts for the Reduction of Carbon Dioxide to Methanol at Atmospheric Pressure

Bahman Zohour,<sup>[a]</sup> Iskender Yilgor,<sup>[b]</sup> Mehmet A. Gulgun,<sup>[c]</sup> Ozgur Birer,<sup>[b]</sup> Ugur Unal,<sup>[b]</sup> Craig Leidholm,<sup>[d]</sup> and Selim Senkan<sup>\*,[a]</sup>

Catalytic conversion of carbon dioxide to liquid fuels and basic chemicals by using solar-derived hydrogen at, or near, ambient pressure is a highly desirable goal in heterogeneous catalysis. If realized, this technology could lead to a more sustainable society together with decentralized power generation. A novel class of holmium-containing multi-metal oxide Cu catalysts, discovered through the application of high-throughput methods, is reported. In particular, ternary systems of Cu-GaO<sub>x</sub>-HoO<sub>y</sub> > Cu-CeO<sub>x</sub>-HoO<sub>y</sub> > Cu-LaO<sub>x</sub>-HoO<sub>y</sub> supported on γ-Al<sub>2</sub>O<sub>3</sub> exhibited superior methanol production (10×) with less CO formation than previously reported catalysts at 1 atm pressure. Holmium was shown to be highly dispersed as few-atom clusters, suggesting that the formation of trimetallic sites could be the key for the promotion of methanol synthesis by Ho.

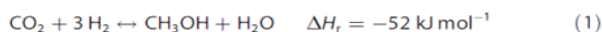
Efficient catalytic reduction of carbon dioxide, the primary product of the combustion of fossil fuels and an increasing atmospheric greenhouse gas, to methanol represents an important step towards the creation of a sustainable society. Methanol has been proposed both as a chemical feedstock as well as a convenient liquid medium of energy storage.<sup>[1–4]</sup> Although the CO<sub>2</sub> reduction process requires molecular hydrogen, it can easily be obtained by the electrolysis of water by using electricity obtained from photovoltaic cells or wind turbines.<sup>[5–8]</sup>

Once produced, methanol can be transformed into a wide range of useful chemicals, such as dimethyl ether (DME), ethylene, gasoline, diesel, and others by using established technologies.<sup>[1–3]</sup> In addition, methanol can also be used directly in

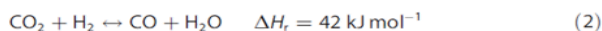
combustion engines and fuel cells, thereby allowing the continuous generation of electricity and enabling energy sustainability.

Currently, methanol is produced exclusively from syngas (CO/CO<sub>2</sub>/H<sub>2</sub>) obtained from the reforming of fossil fuels in centralized facilities, over Cu-ZnO catalysts promoted by Al<sub>2</sub>O<sub>3</sub> at 50–100 bar (1 bar = 0.1 MPa) and 200–300 °C.<sup>[9–15]</sup> This catalyst is also active for the water-gas-shift reaction.<sup>[16–19]</sup> Owing to the practical importance of this technology, catalysts for methanol synthesis have been studied extensively and optimized for use with syngas at high pressures. Most catalysts investigated to date for the title reaction are based on the Cu-ZnO-Al<sub>2</sub>O<sub>3</sub> system modified by metals such as Zr, Ga, Si, Al, B, Cr, V, Ti, and others.<sup>[20]</sup> Although high methanol yields have been reported at a pressure of 360 bar,<sup>[21]</sup> Cu-ZnO-Al<sub>2</sub>O<sub>3</sub> system could not be used efficiently for neat CO<sub>2</sub> reduction at low pressures.<sup>[22]</sup> This finding demonstrated the need for the discovery and optimization of new and more active catalysts for methanol synthesis. Recently, a Ni-Ga/SiO<sub>2</sub> system prepared by the standard impregnation technique was reported to give methanol yields that were comparable to the traditional Cu-ZnO-Al<sub>2</sub>O<sub>3</sub> catalysts prepared by co-precipitation at atmospheric pressure.<sup>[22]</sup> In another recent report, also at 1 atm, CeO<sub>x</sub> deposited on Cu(111) and Cu-CeO<sub>x</sub> co-deposited on TiO<sub>2</sub>(110) surfaces (by chemical vapor deposition) produced significantly more CH<sub>3</sub>OH than the Cu-ZnO(0001) surfaces.<sup>[23]</sup> A hybrid oxide catalyst comprising MnO<sub>x</sub> nanoparticles supported on mesoporous Co<sub>3</sub>O<sub>4</sub> was also recently reported to exhibit significant CH<sub>3</sub>OH production at a higher pressure of 4 bar, together with CO and hydrocarbon products.<sup>[24]</sup>

Methanol formation from carbon dioxide and hydrogen proceeds via the following reaction:



This reaction is often accompanied by the reverse water-gas-shift reaction (RWGS):



In the presence of acidic surfaces, for example, H-ZSM5 or γ-Al<sub>2</sub>O<sub>3</sub>, the CH<sub>3</sub>OH produced is readily converted to DME, which is also a desirable product, by dehydration:<sup>[9, 10, 25]</sup>



Herein, we report the discovery of a series of superior and novel holmium-containing catalytic materials for the low-pressure reduction of CO<sub>2</sub> to CH<sub>3</sub>OH and DME. By using impregna-

[a] B. Zohour, Prof. Dr. S. Senkan  
Department of Chemical Engineering  
University of California  
Los Angeles, CA (USA)  
E-mail: ssenkan@gmail.com

[b] Prof. Dr. I. Yilgor, Prof. Dr. O. Birer, Prof. Dr. U. Unal  
Department of Chemistry, KUYTAM  
Koc University  
Sariyer, Istanbul (Turkey)

[c] Prof. Dr. M. A. Gulgun  
Department of Material Science and Engineering  
Sabanci University  
Tuzla, Istanbul (Turkey)

[d] C. Leidholm  
Laboratory Catalyst Systems, LLC  
Los Angeles, CA (USA)

Supporting Information for this article can be found under <http://dx.doi.org/10.1002/cctc.201600020>.

tion and high-throughput (HT) catalyst-screening technologies developed in our laboratories,<sup>[26,27]</sup> we systematically investigated the oxides of single, binary, and ternary combinations of 27 metals (total metal atom loading of 20 wt%) with several support materials in over 3000 experiments. Our studies led to the discovery of  $\gamma$ -Al<sub>2</sub>O<sub>3</sub>-supported Cu-GaO<sub>x</sub>-HoO<sub>y</sub>, as well as Cu-CeO<sub>x</sub>-HoO<sub>y</sub> and Cu-LaO<sub>x</sub>-HoO<sub>y</sub> systems, which exhibit superior methanol production and less CO formation than other materials reported in the literature. The observed higher activity and selectivity of the Cu-Ga-Ho system could be related to the formation of trimetallic active sites.

Initial screening experiments led to the determination of a number of binary systems that exhibited catalytic activity for CH<sub>3</sub>OH synthesis mostly over the  $\gamma$ -Al<sub>2</sub>O<sub>3</sub> support. These binary systems, in decreasing order of CH<sub>3</sub>OH production at 260 °C were: Cu-Ga<sup>[14,28]</sup> > Cu-La<sup>[29]</sup> ~ Cu-Ce<sup>[23]</sup> > Cu-Ho ~ Cu-Zr<sup>[15]</sup> > Ga-Ni/SiO<sub>2</sub><sup>[22]</sup> ~ Cu-Zn<sup>[10,12,13]</sup> ~ Ga-Ho ~ Cu-Mg > Zn-Ir, which are consistent with the literature. The validity of our experimental approach is supported by the observation that the relative performances of our as-prepared Cu-Zn/Al<sub>2</sub>O<sub>3</sub> and Ga-Ni/SiO<sub>2</sub> catalysts are similar to one another, a finding that is identical to results reported by Studt et al. who used co-precipitation to synthesize the traditional Cu-Zn-Al<sub>2</sub>O<sub>3</sub> catalysts.<sup>[22]</sup> The higher-performing binary systems were then used as the basis to explore the ternary systems at different loadings and temperatures. In Figure 1, the reactor exit mole percentages for CH<sub>3</sub>OH ( $\times 10^4$ ), DME ( $\times 10^4$ ), and CO ( $\times 0.5 \times 10^3$ ) are presented for the Ho-containing ternary catalysts with the best performance together with selected binary systems for comparison. The values presented in Figure 1 correspond to the average of three different sets of experiments that were within 10% of each other. It should be noted that CO<sub>2</sub> conversions, thus product mole fractions, were small because of the high gas velocities used (GHSV  $\approx 200\,000\text{ h}^{-1}$ ). The high gas velocities allowed the catalysts to remain isothermal, which enabled the undertaking of rigorous comparisons of their intrinsic activities. The results reported herein must be studied in greater detail to better understand the catalyst structures, activities, selectivities, reaction mechanisms, and optimization of their performances.

From Figure 1 a it can be seen that our HT experiments produced the following order for CH<sub>3</sub>OH production for some of the previously reported catalysts at 260 °C: Cu-Ga<sub>2</sub>O<sub>3</sub> (3)<sup>[14,28]</sup> > Cu-La<sub>2</sub>O<sub>3</sub> (9)<sup>[29]</sup> > Cu-CeO<sub>2</sub> (11)<sup>[23]</sup> > Cu-Zn-(Zr-Al<sub>2</sub>O<sub>3</sub>) (7)<sup>[15,30]</sup> > Cu-ZrO<sub>2</sub> (6)<sup>[15]</sup> > Ga-Ni/SiO<sub>2</sub> (13)<sup>[22]</sup> ~ MnO<sub>x</sub>/m-Co<sub>3</sub>O<sub>4</sub> hybrid (16)<sup>[24]</sup> ~ Cu-ZnO<sub>2</sub>/Al<sub>2</sub>O<sub>3</sub> (1)<sup>[10,12,13]</sup>. Unlike the reported high performance at 4 bar, the methanol production of the hybrid MnO<sub>x</sub>/m-Co<sub>3</sub>O<sub>4</sub> catalyst (16)<sup>[24]</sup> was surprisingly poor at 1 atm, only on par with the as-prepared Cu-Zn/Al<sub>2</sub>O<sub>3</sub> (1) ~ Ga-Ni/SiO<sub>2</sub> (13) systems (see Figure 1 a); nevertheless, 16 was a very active catalyst producing very high levels of CO and CH<sub>4</sub> along with some C<sub>2</sub>H<sub>4</sub> and higher hydrocarbons (C<sub>3+</sub>).

As evident from Figure 1, our  $\gamma$ -Al<sub>2</sub>O<sub>3</sub>-supported ternary Cu-GaO<sub>x</sub>-HoO<sub>y</sub> catalyst (4), Cu-Ga-Ho at 8-8-4 metal wt%) together with the Cu-LaO<sub>x</sub>-HoO<sub>y</sub> (10, Cu-La-Ho at 10-5-5 metal wt%) and Cu-CeO<sub>x</sub>-HoO<sub>y</sub> (12, Cu-Ce-Ho at 10-5-5 metal wt%) systems significantly outperform the previously reported systems.

For example, at 260 °C (Figure 1 a), the Cu-GaO<sub>x</sub>-HoO<sub>y</sub> catalyst (4) produced CH<sub>3</sub>OH at  $1.14 \times 10^{-4}\%$ , which is about a factor of 10 higher than the Cu-Zn/Al<sub>2</sub>O<sub>3</sub> system (1) of  $0.112 \times 10^{-4}\%$ , while producing similar levels of CO. It is also important to note that catalyst 4 also produced significant levels of DME. In fact, if we were to combine the yields for DME ( $2 \times 0.42 \times 10^{-4} = 0.84 \times 10^{-4}$ ) and CH<sub>3</sub>OH ( $1.14 \times 10^{-4}$ ) (4), at 260 °C, the performance of catalyst 4 would be a factor of 17 higher than that of catalyst 1 and 13. These results correspond to a CH<sub>3</sub>OH + DME selectivity of 48% for the Cu-GaO<sub>x</sub>-HoO<sub>y</sub> (4) catalyst at 260 °C. The turnover frequency (TOF) of catalyst 4 was estimated to be approximately  $1.6 \times 10^{-4}\text{ s}^{-1}$  at 260 °C (Figure 1 a) for the combined production of CH<sub>3</sub>OH and DME; this was calculated by assuming  $\approx 7\text{ nm}$  diameter spherical Cu metal clusters ( $\approx 20\,000$  Cu atoms) and  $\approx 3000$  surface atoms exposed for reaction and 10% reactant gas utilization.<sup>[27]</sup> Similar considerations for the Cu-Zn/Al<sub>2</sub>O<sub>3</sub> catalyst (1) result in a TOF value of  $0.45 \times 10^{-5}\text{ s}^{-1}$ , which is in agreement with the values reported in literature.<sup>[22,24]</sup>

Holmium also had a dramatic promotional effect on some of the reported binary CH<sub>3</sub>OH catalyst systems. For example, both CH<sub>3</sub>OH and DME production increased significantly by the Ho doping of catalyst 1 by more than a factor of two (2) at 300 °C. For the case of the Cu-CeO<sub>2</sub> (11), Ho doping was also influential, increasing CH<sub>3</sub>OH levels by approximately a factor of two (12) at 260 °C. However, Ho did not promote CH<sub>3</sub>OH formation in the Ga-Ni/Al<sub>2</sub>O<sub>3</sub> system (15), although it significantly increased CO and CH<sub>4</sub> (not included in Figure 1) production.

Increasing the temperature from 260 to 280 °C significantly increased CH<sub>3</sub>OH production for the Cu-GaO<sub>x</sub>-HoO<sub>y</sub> (4) catalyst. However, increasing the temperature further from 280 to 300 °C resulted in a smaller increase in CH<sub>3</sub>OH formation. This result is not surprising in view of the equilibrium considerations of this exothermic reaction [Eq (1)].<sup>[31]</sup> On the other hand, increasing the temperature increased the CO production substantially, clearly demonstrating the need to develop low-temperature catalysts for the synthesis of CH<sub>3</sub>OH from CO<sub>2</sub>.

Rapid decreases in CH<sub>3</sub>OH production were observed within few hours with the Cu-Zn/Al<sub>2</sub>O<sub>3</sub> (1) catalyst. None of the  $\gamma$ -Al<sub>2</sub>O<sub>3</sub>-supported Cu-GaO<sub>x</sub>-HoO<sub>y</sub> (4), Cu-LaO<sub>x</sub>-HoO<sub>y</sub> (10), or Cu-CeO<sub>x</sub>-HoO<sub>y</sub> (12) exhibited any significant deactivation or change in methanol selectivity during  $\approx 10\text{ h}$  of continuous runs or after repeated reduction–reaction cycles. The time-on-stream performance of the Cu-GaO<sub>x</sub>-HoO<sub>y</sub> (4) catalyst presented in Figure 2 at 260 °C shows that the combined selectivities for CH<sub>3</sub>OH and DME remained at approximately 48% for the entire 10 h testing period.

In the Cu-Zn/Al<sub>2</sub>O<sub>3</sub> system (1), the metallic copper clusters are accepted to be the sites for methanol synthesis, whereas ZnO has been proposed to act both as a physical promoter (i.e., to assist in the formation of a larger number of surface Cu sites) and as a promoter for the Cu-ZnO synergy.<sup>[11]</sup> The same Cu-ZnO sites are also believed to be catalysts for the RWGS reaction. It is also widely accepted that CH<sub>3</sub>OH production from CO<sub>2</sub> over Cu-ZnO catalysts occurs via the formation of surface formates  $\text{HCOO-M} \rightarrow \text{HCOOH-M} \rightarrow \text{CH}_3\text{O}_2\text{-M} \rightarrow \text{CH}_2\text{O-M} \rightarrow \text{CH}_3\text{O-M} \rightarrow \text{CH}_3\text{OH-M}$ .<sup>[31]</sup>



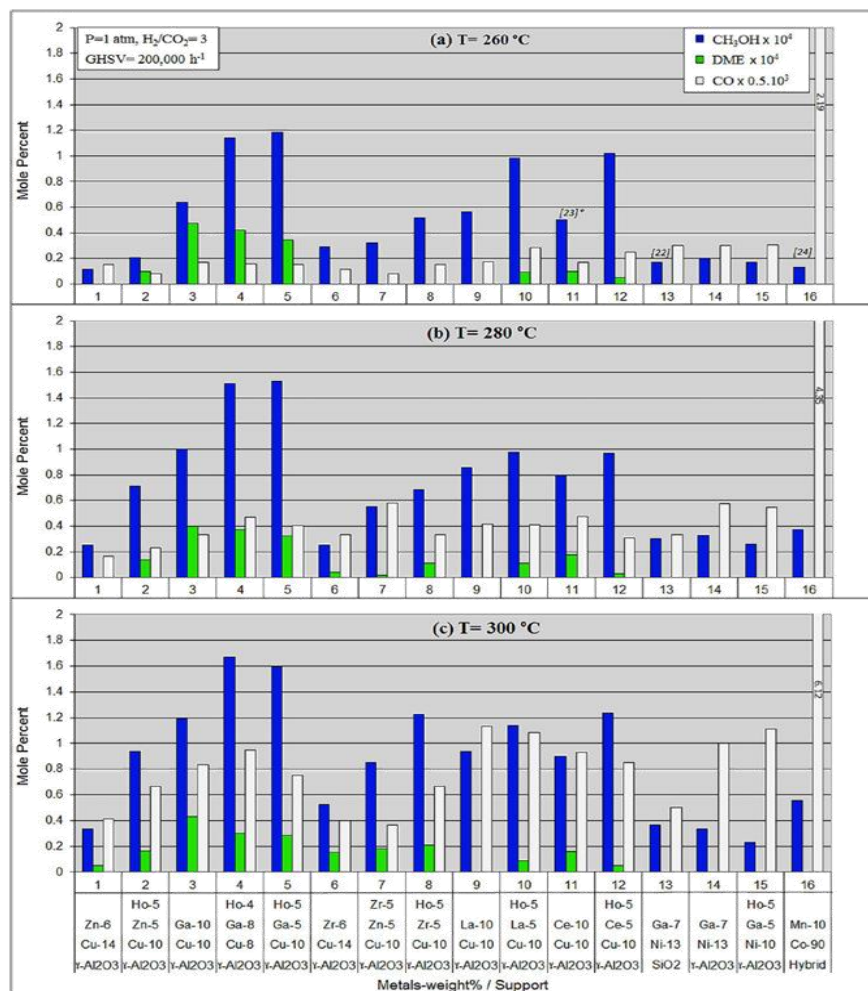


**Figure 1.** Reactor exit CH<sub>3</sub>OH, DME, and CO mol% levels for the high-performing Ho-containing catalysts together with some previously reported catalytic systems at a) 260 °C, b) 280 °C, and c) 300 °C. Significant amounts of CH<sub>4</sub> were also produced with the Ni-containing catalysts (13, 14, 15) and for 16, but are not presented for clarity. [n]\* refers to catalytic materials reported recently in the literature at low pressures.

For the Ni-Ga/SiO<sub>2</sub> system (13), the Ga-rich sites have been reported to facilitate methanol synthesis, whereas the Ni-rich sites have been suggested to be responsible for the RWGS and methanation reactions.<sup>[22]</sup> Consequently, the superior performance of the Cu-GaO<sub>x</sub>-HoO<sub>y</sub> system (4), which contains both Cu and Ga sites, can be due, in part, to their mutual physical and chemical promotion (3). The remarkable effect of Ho in the promotion of methanol synthesis could be attributed to the formation of very small clusters that are highly dispersed. As discussed in the characterization section below, STEM images of catalyst 4 showed the presence of few-atom (1–3 atom) Ho clusters. Some of these clusters also appear to be

positioned along the Cu and Ga cluster interfaces or on the surfaces of their alloys, creating trimetallic sites that could be the key for the promotion of methanol synthesis by Ho. This representation is also supported by the experimentally observed order of activity of the CH<sub>3</sub>OH catalysts, that is, Cu-Ga-Ho (4) > Cu-Ga (3) > Cu-Ho > Ga-Ho.

The reduced Cu-GaO<sub>x</sub>-HoO<sub>y</sub> system was characterized (4, Cu-Ga-Ho at 8-8-4 metal wt% loading and 5.3/4.8/1 atom ratio) by using BET analysis (Micromeritics ASAP 2020 using N<sub>2</sub>), scanning transmission electron microscopy (STEM, JEOL, JEM-ARM200CFEG UHR, with EDS), X-ray diffraction (XRD) (Bruker Xflash 5010), and X-ray photoelectron (XPS) (ThermoScientific

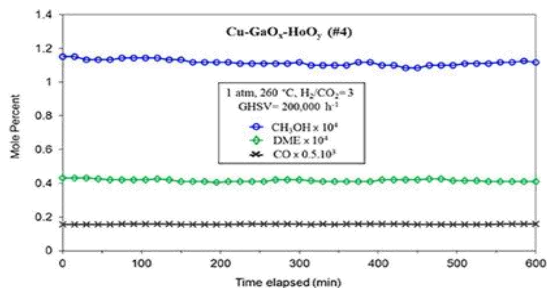


**Figure 2.** Time-on-stream behavior of the Cu-GaO<sub>x</sub>-HoO<sub>y</sub> (4) catalyst shows no significant performance change over a 10 h testing period.

K-Alpha) spectroscopy to develop insights on its structure and surface chemistry. BET analysis indicated a surface area of 142 m<sup>2</sup>g<sup>-1</sup> for the catalyst, consistent with the alumina support. The XRD spectra (see the Supporting Information) only showed the features of the Al<sub>2</sub>O<sub>3</sub> support, suggesting the presence of amorphous Cu, Ga, and Ho moieties or their nanosize crystallites. This finding was also confirmed by the high-resolution TEM studies (Figure 3); HR-TEM images of the reduced catalyst 4 (Cu-Ga-Ho at 8-8-4 wt% metal loading and atom ratios of 5.2/4.8/1) is provided in Figures 3a and 3b. Element mapping images obtained from STEM/EDS indicate the presence of 5–7 nm Ga (Figure 3e) and Cu (Figure 3f) clusters in close proximity to one another, which also suggests the possibility of some alloy formation. On the other hand the Ho map did not show the presence of larger particles (Figure 3c). The high angular annular dark field (HAADF) Z-contrast ( $-z^2$ ) image indicated that the heavy Ho ( $z=165$ ) is highly dispersed and exists only as few-atom (1–3 atom) clusters (Figure 3d).

Ex situ XPS studies of the reduced catalyst 4 indicated the presence of both Cu<sup>0</sup> and CuO, whereas only Ga<sub>2</sub>O<sub>3</sub> and Ho<sub>2</sub>O<sub>3</sub> were observed at the surface (see the Supporting Information). Some oxidation of Cu was observed because of exposure to the atmosphere during sample transfer to the XPS system. Consequently, Cu-Ga<sub>2</sub>O<sub>3</sub>-Ho<sub>2</sub>O<sub>3</sub> could be the correct representation of catalyst 4. It is interesting to note that the surface concentration of Ga was higher, whereas those for Cu and Ho were lower, than their nominal/bulk values for the Cu-Ga<sub>2</sub>O<sub>3</sub>-Ho<sub>2</sub>O<sub>3</sub> (4) catalyst. Further characterizations, as well as detailed kinetic and quantum modeling studies, are underway to better understand the nature of the active site(s) and to explain the mechanism of action of the novel Cu-Ga<sub>2</sub>O<sub>3</sub>-Ho<sub>2</sub>O<sub>3</sub> system in the promotion of CH<sub>3</sub>OH synthesis from CO<sub>2</sub> and H<sub>2</sub>.

In summary, high-throughput impregnation synthesis and reaction screening of the binary and ternary combinations of 27 metals and 5 supports for the hydrogenation of CO<sub>2</sub> to CH<sub>3</sub>OH under atmospheric pressure led to the discovery of a novel class of superior ternary catalytic materials containing holmium, while reproducing the trends for the relative performances of the already established binary catalytic systems from the literature. The Cu-Ga<sub>2</sub>O<sub>3</sub>-Ho<sub>2</sub>O<sub>3</sub>/γ-Al<sub>2</sub>O<sub>3</sub> system exhibited the highest CH<sub>3</sub>OH production together with significant levels of DME formation, and maintained its activity and selectivity over a long period of time. Considering the significant practical interest of these processes for a sustainable chemical industry and society in general, the newly discovered catalytic materials reported herein require further investigations to better understand the nature of the active sites, optimize their synthesis and operating conditions, including studies at higher pressures, to increase CH<sub>3</sub>OH and DME yields.

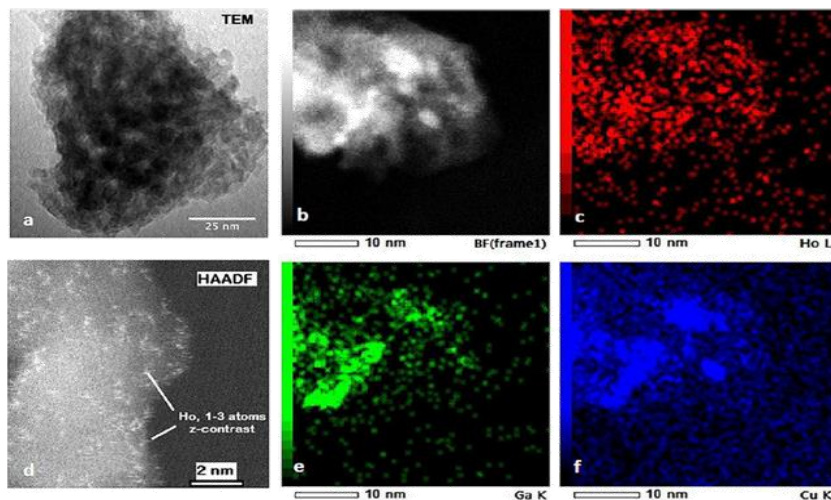


**Figure 3.** a, b) HR-TEM images of the reduced catalyst 4 (Cu-Ga-Ho at 8-8-4 wt% metal loading and atom ratios of 5.2/4.8/1). c, d) STEM-EDS images of the element maps of Ho, e) Ga, and f) Cu over  $\gamma$ -Al<sub>2</sub>O<sub>3</sub>.



## Experimental Section

The catalysts were prepared by impregnation of powders of  $\gamma$ - $\text{Al}_2\text{O}_3$ ,  $\text{CeO}_2$ ,  $\text{SiO}_2$ ,  $\text{TiO}_2$ , and  $\text{Y-ZrO}_2$  with single, binary, and ternary mixtures of aqueous (nitrate) salt solutions of 27 metals: Li, Na, Rb, Cs, Mg, Ca and Sr, Ga, V, Cr, Mn, Co, Ni, Cu, Zn, Zr, Ru, Ir, Ag, Au, La, Ce, Pr, Dy, Ho, Er, and Yb. Systematic consideration of different metal ratios and loadings necessitated the preparation of approximately 3000 distinct catalytic materials. For example, the best-performing trimetallic ( $\text{Cu-Ga}_x\text{-HoO}_y/\gamma\text{-Al}_2\text{O}_3$ , **4**) catalysts were prepared as follows: A predetermined amount of  $\gamma\text{-Al}_2\text{O}_3$  support (Alfa Aesar, surface area of  $\approx 150 \text{ m}^2 \text{ g}^{-1}$ ) was soaked in an aqueous solution of  $\text{Cu}(\text{NO}_3)_2 \cdot 2.5 \text{ H}_2\text{O}$ ,  $\text{Ga}(\text{NO}_3)_3 \cdot 6 \text{ H}_2\text{O}$ , and  $\text{Ho}(\text{NO}_3)_3 \cdot 5 \text{ H}_2\text{O}$  (Alfa Aesar) at concentrations previously determined to yield the desired metal loadings. The mixture was then dried at  $120^\circ \text{C}$  while stirring, followed by calcining in air at  $450^\circ \text{C}$  for 6 h. In addition, the recently reported hybrid  $\text{MnO}_x/\text{m-Co}_3\text{O}_4$  catalyst (**16**) was acquired and tested.<sup>[24]</sup>

Catalyst screenings were performed by using a high-throughput (HT) array channel microreactor system, which is shown in Figure 4, details of which have been described previously.<sup>[26,27]</sup> The system allows parallel screening of up to 80 catalytic materials. In array microreactors, reactant gases flow over the flat surfaces of compacted powders (20 mg of  $\gamma\text{-Al}_2\text{O}_3$ -based and 6 mg of  $\text{SiO}_2$ -based) of catalytic materials that are placed into the wells in each reactor channel (see Figure 4 top right inset). Consequently, the majority of the gases exit the reactor while only a small fraction ( $\approx 10\%$ ) participate in the catalytic reaction process.<sup>[27]</sup> This arrangement results in the establishment of identical flow rates or contact times in every channel, which enables the rapid comparison of the catalytic performances of up to 80 catalysts in a single experiment. The experiments were performed in the following manner: Firstly, the catalysts were reduced under  $\text{H}_2/\text{He}$  (50/50) flow at a temperature in the range of  $230\text{--}350^\circ \text{C}$  for 2 h. Catalysts were then cooled to the desired reaction temperature while still under  $\text{H}_2/\text{He}$  flow, and the gas flow was switched to the reactants. The experiments were performed at 260, 280, and  $300^\circ \text{C}$ , at 1 atm pressure and at gas hourly space velocity (GHSV) of approximately  $200\,000 \text{ h}^{-1}$ . The feed gas consisted of 25 vol%  $\text{CO}_2$  (Matheson,

99.9% purity) and 75 vol%  $\text{H}_2$  (Matheson, 99.99%). Gas sampling was accomplished by withdrawing reactor exit gases by using a passivated 200 micron ID capillary sampling probe that was sequentially positioned into each reactor channel, followed by on-line gas analysis either by mass spectrometry (MS, Stanford Research Systems, RGA-200) or by gas chromatography (Micro-GC Varian, CP-4900). The GC had dual Porapak U (10 m) and molecular sieve 13X (10 m) modules each equipped with individual thermal conductivity detectors (TCD). Using MS analysis the screening of the entire 80-catalyst library typically took 30 min or less depending on the sampling capillary dwell time inside and outside the reactor channels and the mass range and scan rate of the MS.<sup>[26,27]</sup> Consequently, MS analysis was used for initial screening to rapidly identify promising leads. The leads were then studied in greater detail by gas chromatography in smaller sets of 10 to 20 catalysts to better compare them under similar time-on-stream conditions. In the present work, each GC analysis took approximately 2.5 min for completion including a 30 s sampling time. The following products were detected and quantified:  $\text{CH}_3\text{OH}$ ,  $\text{CH}_3\text{OCH}_3$  (DME),  $\text{CO}$ ,  $\text{CH}_4$ ,  $\text{C}_2\text{s}$ , and  $\text{C}_3\text{s}$ . However, only  $\text{CH}_3\text{OH}$ ,  $\text{CH}_3\text{OCH}_3$  (DME), and  $\text{CO}$  were reported in Figure 1 for clarity.

## Acknowledgements

We thank Laboratory Catalyst Systems (LCS), LLC for funding and access to their high-throughput equipment and catalyst data base. We also thank Dr. Selim Alayoglu and Dr. Kwangjin An of the Lawrence Berkeley National Laboratory for providing the hybrid  $\text{MgO}_x/\text{CoO}$  catalyst. Author contributions: BZ, CL, and SS initiated and performed the original catalyst discovery work at LCS. IV, OB, and UU performed and interpreted the XRD and XPS analysis. MAG performed and interpreted the HRTEM analysis.

**Keywords:** carbon dioxide · dimethyl ether · heterogeneous catalysis · high-throughput testing · methanol synthesis

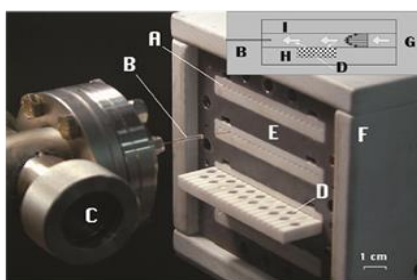


**Figure 4.** High-throughput microreactor catalyst screening system. A) Reactor bank with 20 parallel channels (4 banks, total 80 channels) micro-machined over a ceramic plate; B) Capillary gas-sampling probe; C) Gas analysis performed by mass spectrometer (MS) or gas chromatograph (GC); D) Wells for the placement of catalyst pellets or powders; E) Temperature-controlled heating block with a preheat zone (not shown); F) Insulation. The top right inset shows the schematic of the side view of a channel reactor: G) Reactant and product gases flow through the channel, which is embedded into the lower ceramic plate (H) and isolated by the cover plate (I). Gases flow over the catalyst bed (D) resulting in minimal pressure drop. The capillary probe (B) is also shown inserted into the channel for sampling.

- [1] G. A. Olah, *Angew. Chem. Int. Ed.* **2005**, *44*, 2636–2639; *Angew. Chem.* **2005**, *117*, 2692–2696.
- [2] G. A. Olah, A. Goepfert, G. S. Prakash, *J. Org. Chem.* **2009**, *74*, 487–498.
- [3] G. A. Olah, A. Goepfert, G. S. Prakash, *Beyond Oil and Gas: The Methanol Economy*, Wiley, Weinheim, **2009**.
- [4] G. A. Olah, *Angew. Chem. Int. Ed.* **2013**, *52*, 104–107; *Angew. Chem.* **2013**, *125*, 112–116.
- [5] N. S. Lewis, D. G. Nocera, *Proc. Natl. Acad. Sci. USA* **2006**, *103*, 15729–15735.
- [6] W. El-Khattam, M. M. A. Salama, *Electr. Power Syst. Res.* **2004**, *71*, 119–128.
- [7] G. Crabtree, J. Sarrao, *Phys. World* **2009**, *22*, 24–30.
- [8] M. Z. Jacobson, M. A. Delucchi, *Energy Policy* **2011**, *39*, 1154–1169.
- [9] G. Bozga, I. T. Apan, R. E. Bozga, *Recent Pat. Catal.* **2013**, *2*, 68–81.
- [10] F. Pontzena, W. Liebner, V. Gronemann, M. Rothaemel, B. Ahlers, *Catal. Today* **2011**, *171*, 242–250.
- [11] M. Behrens, F. Studt, I. Kasatkin, S. Kühl, M. Hävecker, F. Abild-Pedersen, S. Zander, F. Girgsdies, P. Kurr, B. L. Kniep, M. Tovar, R. W. Fischer, J. K. Nørskov, R. Schlögl, *Science* **2012**, *336*, 893–897.
- [12] M. M. Günter, T. Ressler, B. Bems, C. Büscher, T. Genger, O. Hinrichsen, M. Muhler, R. Schlögl, *Catal. Lett.* **2001**, *71*, 37–44.
- [13] M. Behrens, S. Zander, P. Kurr, N. Jacobsen, J. Senker, G. Koch, T. Ressler, R. W. Fischer, R. Schlögl, *J. Am. Chem. Soc.* **2013**, *135*, 6061–6068.
- [14] R. Ladera, F. J. Pérez-Alonso, J. M. González-Carbollo, M. Ojeda, S. Rojas, J. L. G. Fierro, *Appl. Catal. B* **2013**, *142*, 241–248.
- [15] S. G. Jadhav, P. D. Vaidya, B. M. Bhanage, J. B. Joshi, *Chem. Eng. Res. Des.* **2014**, *92*, 2557–2567.
- [16] F. S. Stone, D. Waller, *Top. Catal.* **2003**, *22*, 305–318.

## References

- [1] M. C.Alvarez, N. Mota and e. al, "Direct methane conversion routes to chemicals and fuels," *Catalysis today*, no. 171, pp. 15-23, 2011.
- [2] C. Hammond, S. Conrad and I. Hermans, "Oxidative Methane Upgrading," *ChemsusChem*, no. 5, pp. 1668-1686, 2013.
- [3] M. Yu.Sinev, Z. T.Fattakhova, V. I.Lomonosov and Y. A.Gordienko, "Kinetics of oxidative coupling of methane: Bridging the gap between comprehension and description," *Natural Gas Chemistry*, no. 18, pp. 273-287, 2009.
- [4] True and W. R., "Global ethylene capacity poised for major expansion," *Jornal of Oil and Gas*, no. 1, 2013.
- [5] "OECD SIDS Initial Assessment Profile- Ethylene," 2013. [Online]. Available: <http://www.inchem.org>.
- [6] O. S. P. Analytics, "Oil and Gas Industry: Process Analytics in Ethylene Production Plants," 2013.
- [7] M. Baerns, U. Zavyalova, M. Holena and R. Schlogl, "Statistical Analysis of past catalytic data on oxidative methane coupling for new insights into the composition of high-performance catalysts," *ChemCatChem*, pp. 1935-1947, 2011.
- [8] V. I.Alexiadis, J. W.Thybaut, P. N.Kechagiopoulos, M. Chaar and A. C. Veen, "Oxidative coupling of methane: catalytic behaviour assessment via comprehensive microkinetic modeling," *Applied catalysis*, vol. 150, pp. 496-505, 2014.
- [9] S. Arndta, G. Laugela, S. Levchenkob, R. Hornc, M. Baerns, M. Schefflerb, R. Schlöglc and R. Schomäckera, "A Critical Assessment of Li/MgO-Based Catalysts for the Oxidative Coupling of Methane," *Catalysis Reviews: Science and Engineering*, vol. 53, no. 4, pp. 424-514, 2011.
- [10] J. H.Lunsford, "The Catalytic Oxidative Coupling of Methane," *Angewandte Chemie*, vol. 34, no. 9, pp. 970-980, 1995.
- [11] L. Liangfeng, T. Xiaofeng, W. Wang, Y. Wang, S. Sun, F. Qi and W. Huang, "Methyl radicals in oxidative coupling of methane directly confirmed by synchrotron VUV photoionization mass spectroscopy," *Scientific reports*, no. 3, pp. 1-7, 2013.
- [12] M. S.Palmer, M. Neurock and M. M.Olken, "Periodic Density Functional Theory Study of Methane Activation over La<sub>2</sub>O<sub>3</sub>: Activity of O<sup>2-</sup>, O<sup>-</sup>, O<sub>2</sub><sup>2-</sup>, Oxygen Point Defect, and Sr<sup>2+</sup>-

- Doped Surface Sites," *Journal of the American Chemical Society*, vol. 124, no. 28, pp. 8452-8461, 2002.
- [13] B. Beck, V. Fleischer, S. Arndt, M. G.Hevia, A. Urakawa, P. Hugo and R. Schomacker, "Oxidative coupling of methane—A complex surface/gas phase mechanism with strong impact on the reaction engineering," *Catalysis Today*, vol. 228, pp. 212-218, 2014.
- [14] Z. Stansch, L. Mleczko and M. Baerns, "Comprehensive kinetics of oxidative coupling of methane over the  $\text{La}_2\text{O}_3/\text{CaO}$  catalyst," *Industrial & engineering chemistry research*, vol. 36, no. 7, pp. 2568-2579, 1997.
- [15] S. Senkan, *Advances in Chemical Engineering*, New York: Academic Press, 1992.
- [16] Nersessyan, "PhD Thesis," Institute of Chemical Physics, Moscow, 1979.
- [17] Nersessyan, I. A.Vardanyan, K. M.Kegeyan, L. Ya.Margolist and A. B.Nalbandyan, "Doklady Akademii Nauk SSSR," *Rep Acad Sci USSR, in Russian*, no. 3, p. 605, 1975.
- [18] L. H.Mitchell and H. R.Waghorne.US Patent 4 205 194, 1980.
- [19] T. Fang and C. Yeh, "Interactions of methane with  $\text{ThO}_2/\text{SiO}_2$  surface at 1073 K," *Journal of Catalysis*, no. 1, p. 227, 1981.
- [20] G. E.Keller and M. M.Bhasin, *Journal of Catalysis*, no. 1, p. 9, 1982.
- [21] M. Baerns and W. Hinsen, "Oxidative Coupling of Methane to  $\text{C}_2$ -Hydrocarbons in the Presence of Different Catalysts," *Chemiker-Zeitung*, vol. 107, no. 8, pp. 223-226, 1983.
- [22] T. Ito and J. H.Lunsford, "Synthesis of ethylene and ethane by partial oxidation of methane over lithium-doped magnesium oxide," *Nature*, pp. 721-722, 1985.
- [23] DeBoy, M. Jeffrey and R. F.Hicks, "Oxidative coupling of methane over alkaline earth promoted  $\text{La}_2\text{O}_3$ ," *Journal of the Chemical Society, Chemical Communications*, vol. 1, no. 14, pp. 982-984, 1988.
- [24] Y. Simon, F. Baronnet and P. Marquaire, "Kinetic Modeling of the Oxidative Coupling of Methane," *Ind. Eng. Chemistry*, no. 46, pp. 1914-1922, 2007.
- [25] K. Asami, T. Fujita, K. Kusakabe, Y. Nishiyama and Y. Ohtsuka, "Conversion of methane with carbon dioxide into  $\text{C}_2$  hydrocarbons over metal oxides," *Applied Catalysis*, vol. 126, no. 2, pp. 245-255, 1995.
- [26] Y. Wang, Y. Takahashi and Y. Ohtsuka, "Carbon Dioxide as Oxidant for the Conversion of Methane to Ethane and Ethylene Using Modified  $\text{CeO}_2$  Catalysts," *Journal of Catalysis*, vol. 186, no. 1, pp. 160-168, 1999.

- [27] Y. Y.Wang, "Mn-based binary oxides as catalysts for the conversion of methane to C<sub>2</sub> hydrocarbons with carbon dioxide as oxidant," *Applied Catalysis*, vol. 219, no. 1, pp. 183-193, 2001.
- [28] Y. Cai, L. Chou, S. Li, B. Zhang and J. Zhao, "Selective Conversion of Methane to C<sub>2</sub> Hydrocarbons Using Carbon Dioxide over Mn-SrCO<sub>3</sub> Catalysts," *Catalysis letters*, vol. 86, no. 4, pp. 191-195, 2003.
- [29] B. Li and H. Metiu, "DFT Studies of Oxygen Vacancies on Undoped and Doped La<sub>2</sub>O<sub>3</sub> Surfaces," *Journal of Physical Chemistry*, vol. 114, no. 28, pp. 12234-12244, 2010.
- [30] J. H.Hoebink, P. M.Couwenberg and G. B.Marin, "Fixed bed reactor design for gas phase chain reactions catalysed by solids: The Oxidative Coupling of Methane," *Chemical Engineering Science*, vol. 49, no. 1, pp. 5453-5463, 1994.
- [31] P. N.Kechgiopoulos, J. W.Thybaut and G. B.Marin, "Oxidative Coupling of Methane: A Microkinetic Model accounting for intraparticle surface-intermediates concentration profiles," *Industrial & Engineering Chemistry Research*, vol. 53, no. 1, pp. 1825-1840, 2014.
- [32] C. Tye, A. R.Mohamed and S. Bhatia, "Oxidative Coupling of Methane in a Catalytic Bed Reactor and a Membrane Reactor: Modeling and Simulation," *Journal of Industrial and Engineering Chemistry*, vol. 10, no. 5, pp. 834-844, 2004.
- [33] E. Esche, H. A.Garcia and L. T.Biegler, "Optimal Operation of a Membrane Reactor Network," *AIChE Journal*, vol. 60, no. 1, pp. 170-180, 2014.
- [34] M. H.Eghbal-Ahmadi, M. Zaerpour, M. Daneshpayeh and N. Mostoufi, "Optimization of Fluidized Bed Reactor of Oxidative Coupling of Methane," *International Journal of Chemical Reactor Engineering*, vol. 10, no. 2, pp. 1-20, 2012.
- [35] J. Y.Ying and W. H.Green, "Upper bound on the yield for oxidative coupling of methane," *Journal of Catalysis*, pp. 321-333, 2003.
- [36] D. Noon, A. Seubsai and S.Senkan, "Oxidative Coupling of Methane by Nanofiber Catalysts," *ChemCatChem*, no. 5, pp. 146-149, 2013.
- [37] X. Wu, Y. Salkovskiy and Y. A.Dzenis, "Modeling of solvent evaporation from polymer jets," *Applied Physics Letters*, no. 98, p. 223108, 2011.
- [38] D. Noon, B. Zohour and S. Senkan, "Oxidative coupling of methane with La<sub>2</sub>O<sub>3</sub>-CeO<sub>2</sub> nanofiber fabrics: A reaction engineering study," *Journal of Natural Gas Science and Engineering*, vol. 18, no. 1, pp. 406-411, 2014.



- [39] B. Zohour, D. Noon and S. Senkan, "New insights into the oxidative coupling of methane from spatially resolved concentration and temperature profiles," *ChemCatChem*, vol. 5, no. 10, pp. 2809-2812 (Front Cover page), 2013.
- [40] B. Zohour, D. Noon and S. Senkan, "Spatial Concentration and Temperature Profiles in Dual-Packed-Bed Catalytic Reactors: Oxidative Coupling of Methane," *ChemCatChem*, vol. 6, no. 10, pp. 2815-2820, 2014.
- [41] K. Otsuka, K. Jinno and A. Morikawa, "Active and selective catalysts for the synthesis of  $C_2H_4$  and  $C_2H_6$  via oxidative coupling of methane," *Journal of Catalysis*, vol. 100, no. 2, pp. 353-359, 1986.
- [42] K. D.Campbell, H. Zhang and J. H.Lunsford, "Methane activation by the lanthanide oxides," *The Journal of Physical Chemistry*, vol. 92, no. 3, p. 750-753, 1988.
- [43] A. G.Dedov, A. S.Loktev, I. I.Moiseev, A. Aboukais, J. F.Lamonier and I. N.Filimonov, "Oxidative coupling of methane catalyzed by rare earth oxides: Unexpected synergistic effect of the oxide mixtures," *Applied Catalysis A: General*, vol. 245, no. 2, pp. 209-220, 2003.
- [44] N. Imanaka, T. Masui and Y. Kato, "Preparation of the cubic-type  $La_2O_3$  phase by thermal decomposition of  $LaI_3$ ," *Journal of Solid State Chemistry*, vol. 178, no. 1, pp. 395-398, 2005.
- [45] C. Hu, Z. Zhang, H. Liu, P. Gao and Z. L.Wang, "Direct synthesis and structure characterization of ultrafine  $CeO_2$  nanoparticles," *Nanotechnology*, vol. 17, no. 24, pp. 5983-5987, 2006.
- [46] O. Deutschmann and L. D.Schmidt, "Two-dimensional modeling of partial oxidation of methane on rhodium in a short contact time reactor," *Symposium (International) on Combustion*, vol. 27, no. 2, p. 2283-2291, 1998.
- [47] F. Papa, P. Luminata, P. Osiceanu, R. Birjega, M. Akane and I. Balint, "Acid-base properties of the active sites responsible for  $C_{2+}$  and  $CO_2$  formation over  $MO-Sm_2O_3$ ," *Journal of molecular catalysis. A, Chemical*, vol. 346, no. 1-2, pp. 46-54, 2011.
- [48] D. A.Hickman and L. D.Schmidt, "Production of Syngas by Direct Catalytic Oxidation of Methane," *science*, vol. 259, no. 5093, pp. 343-346, 1993.
- [49] D. Dalle.Nogare, N. J.Degenstein, R. Horn, P. Canu and L. D.Schmidt, "Modeling spatially resolved data of methane catalytic partial oxidation on Rh foam catalyst at different inlet compositions and flowrates," *Journal of Catalysis*, vol. 277, no. 2, pp. 134-148, 2011.
- [50] S. Lacombe, H. Zanthof and C. Mirodatos, "Oxidative Coupling of Methane over Lanthana Catalysts: II. A Mechanistic Study Using Isotope Transient Kinetics," *Journal of Catalysis*, vol. 155, no. 1, pp. 106-116, 1995.

- [51] S. J.Huang, A. B.Walters and M. A.Vannice, "Adsorption and decomposition of NO on lanthanum oxide," *Journal of Catalysis*, vol. 192, no. 1, pp. 29-47, 2000.
- [52] S. Pak, P. Qiu and J. H.Lunsford, "Elementary reactions in the oxidative coupling of methane over Mn/Na<sub>2</sub>WO<sub>4</sub>/SiO<sub>2</sub> and Mn/Na<sub>2</sub>WO<sub>4</sub>/MgO catalysts," *Journal of Catalysis*, vol. 179, no. 1, pp. 222-230, 1998.
- [53] S. Sahebdehfar, M. T.Ravanchi, M. Gharibi and M. Hamidzadeh, "Rule of 100: An inherent limitation or performance measure in oxidative coupling of methane?," *Journal of Natural Gas Chemistry*, vol. 21, no. 3, pp. 308-313, 2012.
- [54] S. Jas̄o, H. R.Godini, H. Arellano-Garcia, M. Omidkhah and G. Wozny, "Analysis of attainable reactor performance for the oxidative methane coupling process," *Chemical Engineering Science*, vol. 65, no. 24, pp. 6341-6352, 2010.
- [55] V. E.Kondratenko and U. Rodemerck, "A Dual-Reactor Concept for the High-Yielding Conversion of Methane into Higher Hydrocarbons," *ChemCatChem*, vol. 5, no. 3, pp. 697-700, 2013.
- [56] H. Lee, D.-H. Lee, Y.-H. Song, W. C.Choi, Y. Park and D. H.Kim, "Synergistic effect of non-thermal plasma–catalysis hybrid system on methane complete oxidation over Pd-based catalysts," *Chemical Engineering Journal*, vol. 259, no. 1, pp. 761-770, 2015.
- [57] W. S.Kang, D. H.Lee, J. O.Lee, M. Hur and Y. H.Song, "Combination of Plasma with a Honeycomb-Structured Catalyst for Automobile Exhaust Treatment," *Environmental science & technology*, vol. 47, no. 19, p. 11358–11362, 2013.
- [58] R. Marques, S. D. Costa and P. D. Costa, "Plasma-assisted catalytic oxidation of methane: On the influence of plasma energy deposition and feed composition," *Applied Catalysis B: Environmental*, vol. 82, no. 1-2, p. 50–57, 2008.
- [59] S. Jo, T. Kim, D. H.Lee, W. S.Kang and Y. H.Song, "Effect of the electric conductivity of a catalyst on methane activation in a dielectric barrier discharge reactor," *Plasma Chemistry and Plasma Processing*, vol. 34, no. 1, pp. 175-186, 2014.
- [60] T. Kim, S. Jo, Y. H.Song and D. H.Lee, "Synergetic mechanism of methanol–steam reforming reaction in a catalytic reactor with electric discharges," *Applied Energy*, vol. 113, no. 1, p. 1692–1699, 2014.
- [61] P. Barbé, F. Battin-Leclerc and G. M.Côme, "Experimental and modelling study of methane and ethane oxidation between 773 and 1573 K," *Journal de chimie physique*, vol. 92, no. 9, pp. 1666-1692, 1995.
- [62] G. Olah, "Beyond oil and gas: the methanol economy," *Angewandte Chemie International Edition*, vol. 44, no. 18, pp. 2636-2639, 2005.

- [63] G. Olah, A. Goeppert and G. Prakash, "Chemical recycling of carbon dioxide to methanol and dimethyl ether: from greenhouse gas to renewable, environmentally carbon neutral fuels and synthetic hydrocarbons," *The Journal of organic chemistry*, vol. 74, no. 2, pp. 487-498, 2008.
- [64] G. Olah, A. Goeppert and G. Prakash, *Beyond oil and gas: the methanol economy*, John Wiley & Sons, 2011.
- [65] G. Olah, "Towards oil independence through renewable methanol chemistry," *Angewandte Chemie International*, vol. 52, no. 1, pp. 104-107, 2013.
- [66] N. Lewis and D. Nocera, "Powering the planet: Chemical challenges in solar energy utilization," *Proceedings of the National Academy of Sciences*, vol. 103, no. 43, pp. 15729-15735, 2006.
- [67] W. El-Khattam and M. Salama, "Distributed generation technologies, definitions and benefits," *Electric power systems research*, vol. 71, no. 2, pp. 119-128, 2004.
- [68] G. Crabtree and J. Sarrao, "The road to sustainability," *Physics World*, vol. 22, no. 10, pp. 24-30, 2009.
- [69] M. Jacobson and M. Delucchi, "Providing all global energy with wind, water, and solar power, Part I: Technologies, energy resources, quantities and areas of infrastructure, and materials," *Energy Policy*, vol. 39, no. 3, pp. 1154-1169, 2011.
- [70] G. Bozga, I. Apan and R. Bozga, "Design of novel hybrid catalysts for direct synthesis of Dimethyl ether from syngas," *Recent Patents on Catalysis*, vol. 2, pp. 68-81, 2013.
- [71] F. Pontzen, W. Liebner, V. Gronemann, M. Rothaemel and B. Ahlers, "CO<sub>2</sub>-based methanol and DME-Efficient technologies for industrial scale production," *Catalysis Today*, vol. 171, no. 1, pp. 242-250, 2011.
- [72] M. Behrens, F. Studt, I. Kasatkin, S. Köhl, M. Hävecker, F. Abild-Pedersen, S. Zander, F. Girgsdies, P. Kurr, B. Kniep and M. Tovar, "The active site of methanol synthesis over Cu/ZnO/Al<sub>2</sub>O<sub>3</sub> industrial catalysts," *Science*, vol. 336, no. 6083, pp. 893-897, 2012.
- [73] M. Günter, T. Ressler, B. Bems, C. Büscher, T. Genger, O. Hinrichsen, M. Muhler and R. Schlögl, "Implication of the microstructure of binary Cu/ZnO catalysts for their catalytic activity in methanol synthesis," *Catalysis Letters*, vol. 71, no. 1-2, pp. 37-44, 2001.
- [74] M. Behrens, S. Zander, P. Kurr, N. Jacobsen, J. Senker, G. Koch, T. Ressler, R. Fischer and R. Schlögl, "Performance improvement of nanocatalysts by promoter-induced defects in the support material: methanol synthesis over Cu/ZnO: Al," *Journal of the American Chemical Society*, vol. 135, no. 16, pp. 6061-6068, 2013.

- [75] R. Ladera, F. Pérez-Alonso, J. González-Carballo, M. Ojeda, S. Rojas, J. Fierro, F. Pérez-Alonso, J. González-Carballo, M. Ojeda, S. Rojas and J. Fierro, "Catalytic valorization of CO<sub>2</sub> via methanol synthesis with Ga-promoted Cu–ZnO–ZrO<sub>2</sub> catalysts," *Applied Catalysis B: Environmental*, vol. 142, pp. 241-248, 2013.
- [76] S. Jadhav, P. Vaidya, B. Bhanage and J. Joshi, "Catalytic carbon dioxide hydrogenation to methanol: A review of recent studies," *Chemical Engineering Research and Design*, vol. 92, no. 11, pp. 2557-2567, 2014.
- [77] F. Stone and D. Waller, "Cu–ZnO and Cu–ZnO/Al<sub>2</sub>O<sub>3</sub> catalysts for the reverse water-gas shift reaction. The effect of the Cu/Zn ratio on precursor characteristics and on the activity of the derived catalysts," *Topics in catalysis*, vol. 22, no. 3-4, pp. 305-318, 2003.
- [78] I. Nakamura, T. Fujitani, T. Uchijima and J. Nakamura, "The synthesis of methanol and the reverse water-gas shift reaction over Zn-deposited Cu (100) and Cu (110) surfaces: comparison with Zn/Cu (111)," *Surface science*, vol. 400, no. 1, pp. 387-400, 1998.
- [79] M. Ginés, N. Amadeo, M. Laborde and C. Apesteguia, "Activity and structure-sensitivity of the water-gas shift reaction over Cu Zn Al mixed oxide catalysts," *Applied Catalysis A: General*, vol. 131, no. 2, pp. 283-296, 1995.
- [80] M. Spencer, "The role of zinc oxide in Cu/ZnO catalysts for methanol synthesis and the water–gas shift reaction," *Topics in Catalysis*, vol. 8, no. 3-4, pp. 259-266, 1999.
- [81] Y. Hartadi, D. Widmann and R. Behm, "CO<sub>2</sub> Hydrogenation to Methanol on Supported Au Catalysts under Moderate Reaction Conditions: Support and Particle Size Effects," *ChemSusChem*, vol. 8, no. 3, pp. 456-465, 2014.
- [82] A. Bansode and A. Urakawa, "Towards full one-pass conversion of carbon dioxide to methanol and methanol-derived products," *Journal of Catalysis*, vol. 309, pp. 66-70, 2014.
- [83] F. Studt, I. Sharafutdinov, F. Abild-Pedersen, C. Elkjær, J. Hummelshøj, S. Dahl, I. Chorkendorff and J. Nørskov, "Discovery of a Ni-Ga catalyst for carbon dioxide reduction to methanol," *Nature Chemistry*, vol. 6, no. 4, pp. 320-324, 2014.
- [84] J. Graciani, K. Mudiyansele, F. Xu, A. Baber, J. Evans, S. Senanayake, D. Stacchiola, P. Liu, J. Hrbek, J. Sanz and J. Rodriguez, "Highly active copper-ceria and copper-ceria-titania catalysts for methanol synthesis from CO<sub>2</sub>," *Science*, vol. 345, no. 6196, pp. 546-550, 2014.
- [85] C. Li, G. Melaet, W. Ralston, K. An, C. Brooks, Y. Ye, Y. Liu, J. Zhu, J. Guo, S. Alayoglu and G. Somorjai, "High-performance hybrid oxide catalyst of manganese and cobalt for low-pressure methanol synthesis," *Nature communications*, vol. 6, pp. 1-5, 2015.
- [86] W. Chen, B. Lin, H. Lee and M. Huang, "One-step synthesis of dimethyl ether from the gas mixture containing CO<sub>2</sub> with high space velocity," *Applied energy*, vol. 98, pp. 92-101, 2012.

- [87] S. Senkan, "Combinatorial heterogeneous catalysis—a new path in an old field," *Angewandte Chemie International Edition*, vol. 40, no. 2, pp. 312-329, 2001.
- [88] S. Senkan, K. Krantz, S. Ozturk, V. Zengin and I. Onal, "High-Throughput Testing of Heterogeneous Catalyst Libraries Using Array Microreactors and Mass Spectrometry," *Angewandte Chemie International Edition*, vol. 38, no. 18, pp. 2794-2799, 1999.
- [89] J. Toyir, P. de-la-Piscina, J. Fierro and N. Homs, "Catalytic performance for CO<sub>2</sub> conversion to methanol of gallium-promoted copper-based catalysts: influence of metallic precursors," *Applied Catalysis B: Environmental*, vol. 34, no. 4, pp. 255-266, 2001.
- [90] D. Andriamasinoro, R. Kieffer, A. Kiennemann and P. Poix, "Preparation of stabilized copper-rare earth oxide catalysts for the synthesis of methanol from syngas," *Applied Catalysis A: General*, vol. 106, no. 2, pp. 201-212, 1993.
- [91] C. Li, X. Yuan and K. Fujimoto, "Development of highly stable catalyst for methanol synthesis from carbon dioxide," *Applied Catalysis A: General*, vol. 469, pp. 306-311, 2014.
- [92] L. Grabow and M. Mavrikakis, "Mechanism of methanol synthesis on Cu through CO<sub>2</sub> and CO hydrogenation," *ACS Catalysis*, vol. 1, no. 4, pp. 365-384, 2011.